Superconducting Properties of Nanostructured Cuprates, Nitrides and Bulk Iron Chalcogenides

A Thesis

Submitted for the Degree of

Doctor of Philosophy

by

SHIPRA RAI

CHEMISTRY AND PHYSICS OF MATERIALS UNIT
JAWAHARLAL NEHRU CENTRE FOR ADVANCED SCIENTIFIC RESEARCH

(A Deemed University)

Bangalore - 560 064

August 2011

DECLARATION

I hereby declare that the matter embodied in the thesis entitled **"Superconducting properties of nanostructured cuprates, nitrides and bulk Iron chalcogenides"** is the result of investigations carried out by me at the Chemistry and Physics of Materials Unit, Jawaharlal Nehru Centre for Advanced Scientific Research, Bangalore, India under the supervision of Prof. A. Sundaresan and it has not been submitted elsewhere for the award of any degree or diploma. In keeping with the general practice in reporting scientific observations, due acknowledgment has been made whenever the work described is based on the findings of other investigators.

_____

SHIPRA RAI

CERTIFICATE

I hereby certify that the matter embodied in this thesis entitled **"Superconducting properties of nanostructured cuprates, nitrides and bulk Iron chalcogenides"** has been carried out by Mrs. SHIPRA RAI at the Chemistry and Physics of Materials Unit, Jawaharlal Nehru Centre for Advanced Scientific Research, Bangalore, India under my supervision and it has not been submitted elsewhere for the award of any degree or diploma.

_____

Prof. A. Sundaresan

(Research Supervisor)

To my grand-parents

Acknowledgements

I am very much thankful to my research guide, Prof A. Sundaresan for his constant support and advices throughout my Ph.D. I am highly grateful to him for introducing me to superlattices. I really enjoyed full freedom provided by him to handle various instruments and perform different types of experiments in the lab.

My sincere regards to Prof. C.N.R Rao who has been a constant source of inspiration, not only to me but all the students who got an opportunity to work around him. It's a life time opportunity to be near to an exceptionally brilliant scientist. I am very much thankful to my research supervisors in Japan, Prof. Hirata and Prof. H. Takeya. I am also thankful to our collaborators, Prof. Tanaka and Prof. Terada for helpful discussions. I thank Prof. Shobhana, Prof. Chandrabhas, Prof. Waghmare, Prof. Narayanan, Prof. Eshwaramoorthy, Prof. Ranganathan, Prof. Swapan Pati, Prof. Shivaprasad, Prof. Kulkarni, Prof. Balasubramaniam, Dr. Vidyadhiraja and Dr. Datta for coursework and helpful discussions.

I am thankful to Selvi , Sirisha, Dr. Basavaraj, Er. Srinath, Er. Srinivas, Usha madam, Anil, Vasu, Arogyanathan for helping me with instruments. I express my thanks to all my lab-mates, batch-mates and friends at JNCASR and at previous institutes for creating friendly environment.

I express my sincere regards to all physics department faculties at IIT-Roorkee for being very supportive to me. I do not have words to express my obligations towards them for encouraging me so much. I am highly obliged to my B.Sc., as well as my school teachers. Believe it or not I had been a dear student to all my teachers from the very beginning even though never being a top-most scorer. I am very much grateful to my physics teacher Prof. M. M. R Akhtar and Er. Vikash Rahi for introducing me to graphical techniques in calculus.

I want to dedicate my thesis to my grandparents who took responsibility for my upbringing and education and because of their blessings only I am here. I am very much thankful to my husband for great support, trust and encouragement. I thank him for making me someone special. I also am thankful to my parents, in-laws and siblings for supporting and encouraging me both in good and bad times. I feel lucky to have such a

good family. I am also thankful to my dear friends Pooja and Rashmi for their much experienced suggestions

I am thankful to Department of Science and Technology (DST), India and Japan Science and Technology (JST) for providing the research fellowship and thus an opportunity to do the present work.

I am very much thankful to Lord Shiva for always pouring his blessings on me.

SHIPRA RAI

Preface

The thesis spans synthesis, structural analysis and investigations into various physical properties of nano-structured cuprate and nitride superconductors. A brief account of superconductivity in newly discovered Iron based superconductors is also presented. A study into the tuning of important length scales like coherence length (ξ) and penetration depth (λ) by controlling the primary particle and agglomerate size of the superconducting nano-material and disorder introduced in the system has been presented.

Chapter 1 gives an overview of various physical properties and parameters of superconductors.

Chapter 2 describes the experimental details involved in the synthesis of both nano-structured as well as bulk superconductors. It also describes the various techniques used for characterization of these materials.

Chapter 3 deals with the preparation and characterization of (Cu,C)$Ba_2CuO_{4\pm\delta}$ or (Cu,C)-1201 thin films. The main outcome of the study is that increasing substrate (deposition) temperature drives the relaxed thin film into a strained film. Apparently, superconductivity is observed only in the strained (Cu,C)-1201 thin films.

Chapter 4, discusses the preparation of superlattices with the help of (Cu,C)$Ba_2CuO_{4\pm\delta}$ and $CaCuO_2$ layers having the structural formula: (Cu,C)$Ba_2Ca_{n-1}Cu_nO_{2n+2\pm\delta}$, with n = 2 and 3.

Chapter 5 details the synthesis and characterization of agglomerated grains of $YBa_2Cu_3O_{7-\delta}$ superconductor. The effect of sub-micron size of grains on the magnetic properties of superconductors has been explored.

Chapter 6 describes the synthesis and characterization of δ- NbN superconducting clusters. Increase in the degree of agglomeration of nano-grains drives the system from insulating to superconducting regime.

Chapter 7 presents the investigations carried out on $FeSe_{1-x}Te_x$ superconductor. It presents an account on how doping can influence the transport properties in these multi-band superconductors.

List of Publications

- Shipra, A. Gomathi, A. Sundaresan and C. N. R. Rao, "*Room-temperature ferromagnetism in nanoparticles of superconducting materials"*, Solid State Communications **142,** 685 (2007)
- Shipra, Y. Tanaka and A. Sundaresan, "*Fabrication and characterization of superconducting (Cu,C)$Ba_2CuO_{4\pm\delta}$ thin films"*, Physica C **466,** 111 (2007)
- T. Yamamoto, K. Kikunaga, K. Obara, N. Terada, N. Kikuchi, Y. Tanaka, K. Tokiwa, T. Watanabe, A. Sundaresan and Shipra, *"Deposition of superconducting (Cu, C)-Ba-O films by pulsed laser deposition at moderate temperature"*, Supercond. Sci. Technol.**, 20**, 461 (2007).
- N. T. Mua, C. R. Serrao, Shipra, A. Sundaresan, T. D. Hien and N. K. Man, " *High critical current density in Ag-doped Bi-2212 thin films"*, Supercond. Sci. Technol., **21**, 105002 (2008).
- N. Varhese, K. Vinod, Shipra, A. Sundaresan and U. Syamaprasad, *"Burned Rice Husk: An Effective Additive for Enhancing the Electromagnetic Properties of MgB2 Superconductor"*, J. Am. Ceram. Soc, **93**, 732 (2010).
- R. Shipra, H. Takeya, K. Hirata and A. Sundaresan, "*Effect of Ni and Co doping on the physical properties of tetragonal $FeSe_{0.5}Te_{0.5}$ superconductor"*, Physica C **470**, 528 (2010)
- B. Loukya, P. Sowjanya, K. Dileep, R. Shipra, S. Kanuri, L. S. Panchakarla and Ranjan Datta, "*Controlling structural quality of ZnO thin film on c-plane sapphire during pulsed laser deposition*", Journal of Crystal Growth (2011) In press.
- R. Shipra, Nitesh Kumar and A Sundaresan, "*Synthesis and characterization of superconducting δ- NbN clusters*", submitted.
- R. Shipra and A. Sundaresan, "*Magnetic properties of sub-micron sized $YBa_2Cu_3O_{7-\delta}$ clusters"*, submitted.
- R. Shipra and A. Sundaresan, "*Substrate temperature induced strain and superconductivity in (Cu,C)$Ba_2CuO_{4\pm\delta}$ thin films"*, to be submitted.

List of presentations

- *"Effect of Ni and Co doping on the physical properties of tetragonal $FeSe_{0.5}Te_{0.5}$ superconductor"* Applied Superconductivity Conference (ASC-2010), Washington D.C ., USA, August 1st to 6th 2010: *Poster presentation*
- *"Structure and Properties of tetragonal FeSe superconductor"* Magnetic and Superconducting Materials (MSM), Kolkata, India, November 11th to 14th 2009: *Poster Presentation*
- "*Superconductivity in Metal-Oxide heterostructures*", Winter school on Chemistry and Physics of Materials, Bangalore, India, December 4th to 10th 2008: *Poster Presentation.*
- "*Surface ferromagnetism in nanoparticles of non-magnetic materials*", Bangalore-Nano-2007, Bangalore, India, December 6th to 7th 2007: *Poster presentation.*
- *"Surface effects in YBCO nano-crystallites"*, Third JNC research conference on chemistry of materials, Munnar, India, October 28th to November 1st 2007: *Oral and Poster presentation.*
- *"Fabrication and characterization of $(Cu,C)Ba_2CuO_{4\pm\delta}/(CaCuO_2)_n$ superlattices with n = 1, 2 and 3"*, International Conference on Advanced Materials under aegis of International Union of Materials Research Societies, Bangalore, India, October 8th to 13th 2007**:** *Oral presentation.*
- *"Fabrication and characterization of superconducting $(Cu, C)Ba_2CuO_{4\pm\delta}$ thin films"*, International Workshop on Physics of Disordered Materials, Indian Institute of Technology, Kanpur, India, December 4th to 8th, 2006**:** *Poster presentation.*

Contents

List of Abbreviations

BCS	Bardeen, Cooper and Schrieffer
HTSC	High Temperature Cuprate Superconductors
FeSC	Iron based Superconductors
WHH	Wethamer-Helfand-Hohenberg
RSM	Reciprocal Space Mapping
HRXRD	High Resolution X-Ray Diffraction
XRD	X-Ray Diffraction
FESEM	Field Emission Scanning Electron Microscopy
TEM	Transmission Electron Microscopy
ED	Electron Diffraction
VSM	Vibrating Sample Magnetometer
ZFC	Zero Field Cooling
FC	Field Cooling
PPMS	Physical Property Measurement System
DC	Direct Current
AC	Alternating Current
AHL	Ambegaokar, Halperin and Langer
Fe*Chs*	Iron based Chalcogenide Superconductor
SDW	Spin Density Wave

List of Symbols

B	Induced magnetic flux density
H	Applied magnetic field
χ	susceptibility (dc)
H_c	thermodynamic critical field
J or J_c	critical current density
λ	penetration depth
ξ	coherence length
Φ_0	flux quanta
T_c	superconducting transition temperature
$\Delta(T)$	BCS gap at temperature, T
θ_D	Debye temperature
$N(E_F)$	density of states at Fermi level
γ	Sommerfeld constant
F_P	flux pinning force density
Hc_2	Upper critical field
a, b, c	lattice parameters
T_s	substrate temperature
ρ	electrical resistivity
Λ	superlattice periodicity
R_H	Hall coefficient
ρ_{xy}	Hall resistivity
μ_H	Hall mobility
$\chi_n^{'}$	real part of n^{th} harmonic susceptibility
$\chi_n^{''}$	imaginary part of n^{th} harmonic susceptibility

Chapter 1

A general introduction on the various physical properties and parameters of superconductors

The courage of life is often a less dramatic spectacle than the courage of a final moment, but it is no less a magnificent mixture of triumph and tragedy. A man does what he must- in spite of personal consequences, in spite of obstacles and dangers and pressures-and that is the basis of all morality.

- John F. Kennedy

Summary

The present chapter deals mainly with the basic fundamentals of superconductivity. A brief introduction on copper and iron based superconductors is also discussed here. Short notes on flux pinning, grain size effects and Werthamer-Helfand-Hohenberg model is also presented in the chapter.

1.1. Superconductivity

1.1.1 The Phenomena

The year 2011 has witnessed the completion of 100 years of discovery of superconductivity. It was discovered in the year 1911 by H. K. Onnes in mercury while measuring its resistivity at low temperatures. He observed a sudden and massive drop in resistivity below 4.2 K that was immeasurable and coined the term 'superconducting state'. Since the discovery of superconductivity, it has not lost its fascination and has been an active area of research. The flow of electric current without friction amounts to the realization of age old human dream of 'perpetual motion'. The ratio of resistance in normal state and the superconducting state of a metal has been tested to exceed 10^{14} and thus there is every reason to assume the resistivity to be zero. Superconducting state is therefore a 'zero resistivity' state. However it is not just a resistance-less phenomena but also excludes magnetic fields from the bulk of the material. When magnetic field is removed from a perfect conductor, the Lenz law opposes the time dependent change in the magnetic field and the field is trapped in the material. However superconductors in the superconducting state show complete expulsion of magnetic and therefore also are perfect diamagnets.

$$B = \mu_0 (H + M) = 0$$
$$\chi = \frac{M}{H} = -1$$

B is the induced magnetic field while H is the applied magnetic field and M is the

magnetization of the sample. The magnetic susceptibility χ is -1 for a perfect diamagnet. The property of perfect diamagnetism in superconductors is called Meissner-Oschenfield after the name of its discoverers who first experimentally observed it in 1933. Meissner effect is one of the major hallmarks of superconductivity. On applying an external magnetic field, surface shielding currents are generated which create an induced magnetic field inside as well outside the superconductor [1-3]. The depth up to which the shielding current flows depends upon the penetration depth (λ) of the material at the measuring temperature. Outside the superconductor, the induced and applied fields add up while inside they cancel out each other inducing a perfect diamagnetic state. However superconducting state has a limited ability against application of a magnetic field and changes to normal state above a critical field (H_c). The energy gained by the material to switch from superconducting state to normal state is given by

$$G_s(T, H_c) = G_n(T,0)$$
$$G_n(T,0) - G_s(T,0) = \frac{1}{2}\mu_0 H_c^2$$

Where $G_s(T,H_c)$is the Gibb's free energy at a field H_c and is equal to the free energy in the normal state $G_n(T,0)$. $G_s(T,0)$ is the free energy in the superconducting state. The term H_c^2 is a consequence of Meissner effect where M/H = -1. The specific heat capacity shows a discontinuity at the superconducting transition temperature T_c and therefore superconducting to normal state transition is of second order. Meissner effect establishes superconductivity as a distinct equilibrium thermodynamic phase. In order to explain the Meissner effect, H. London and F. London, in 1935, propounded a phenomenological

theory based on the concept of a two fluid model. They proposed that of the total density n of electrons, there is a fraction of n_s that behaves in an abnormal way and represents superconducting electrons which are not scattered by impurities or phonons. The two famous London equations are:

1. $\vec{E} = \frac{\partial}{\partial t}\left(\lambda \vec{j}\right)$

2. $\vec{\nabla} \times \left(\lambda \vec{J}\right) = -\mu_0 \vec{H}$

Where λ is called the London penetration depth and is related to the superfluid density n_s as: $\lambda = \sqrt{\frac{m}{\mu_0 n_s e^2}}$, where m is the mass of the electron and e is the electronic charge. Figure 1.1 shows the interface of air and superconductor. The applied magnetic field decays to 1/e of its value at penetration depth. The penetration depth follows a empirical relation with temperature: $\lambda(T) = \lambda(0)\left[1 - \left(\frac{T}{T_c}\right)^4\right]^{-1/2}$

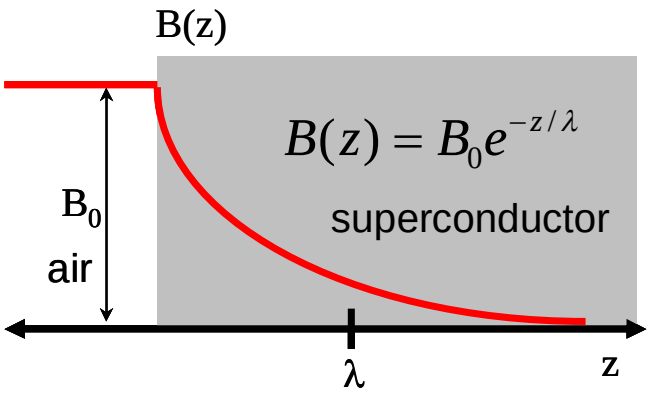

Figure 1.1 Interface of superconductor and air in applied magnetic filed. It should be noted that $B(z)=\mu_0 H$.

The London equations also give the concept of flux quantization inside a superconducting ring where the flux enters as an integral multiple of $\Phi_0 = h/2e = 2.07\text{x}10^{-15}$ T-m^2. Φ_0 is called the 'fluxon'. The London theory is not applicable to situations in which the number of superelectrons, n_s, varies; it does not link n_s with the applied field or current. Therefore we need a more general framework which relates *n*s to the external parameters. This is the approach of the Ginzburg-Landau theory, which uses the general (Landau) theory of second order phase transitions by introducing the corresponding an order parameter. Ginzburg and Landau have chosen to use a kind of a wave function, to describe the superconducting electrons which are given as:

$$\psi(\vec{r}) = |\psi(\vec{r})| \exp(i\phi(\vec{r}))$$

$\psi(\vec{r})$ is called the superconducting order parameter and has the following properties:

- Its modulus $|\psi(\vec{r})\psi^*(\vec{r})|$ can be interpreted as the number density of superconducting electrons *n*s at a point *r*.
- As in quantum mechanics, the phase $\phi(\vec{r})$ is related to the supercurrent that flows through the material below T_c .
- $\psi(\vec{r}) \neq 0$ in the superconducting state, but $\psi(\vec{r})$ = 0 in the normal state.

The two Ginzburg-Landau equations are given as:

$$\alpha\psi + \beta|\psi|^2\psi + \frac{1}{2m}\left(-i\hbar\vec{\nabla} - 2e\vec{A}\right)^2\psi = 0$$

$$\vec{J} = \frac{2e}{m}\text{Re}\left[\psi^*\left(-i\hbar\vec{\nabla} - 2e\vec{A}\right)\psi\right]$$

The first equation defines a characteristic length scale called the coherence length given as:

$$\xi^2(T) = \frac{\hbar^2}{2m|\alpha|} \propto \frac{1}{\left(1-\frac{T}{T_c}\right)}$$

It is the length scale at which the order parameter varies without costing free energy when a small perturbation is applied. There is no sharp boundary between the normal and the superconducting regions and transition between the two takes place over a length scale of ξ. The second equation gives another length scale called the penetration depth which is similar to the London penetration depth and is given as: $\frac{1}{\lambda^2} = 4\mu_0 e^2 \frac{|\psi|^2}{m}$.

1.1.2 Type I and type II superconductors

The ratio between ξ and λ is called the Ginzburg-Landau parameter, $\kappa = \frac{\lambda}{\xi}$. When

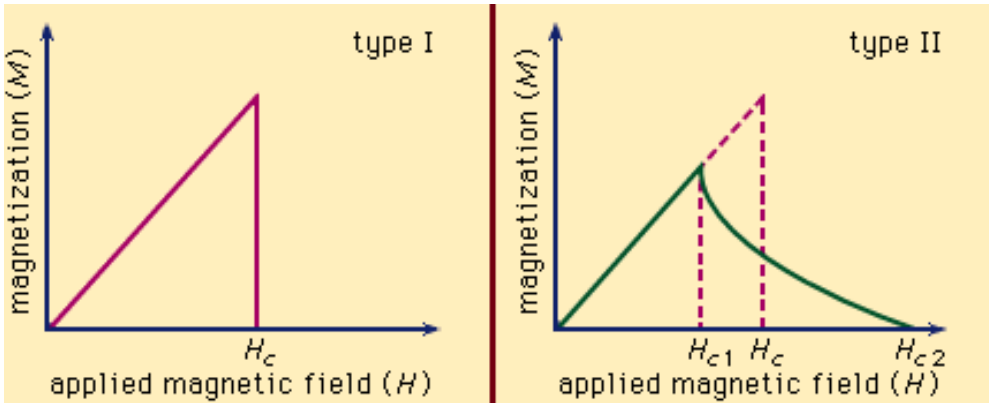

Figure 1.2 Magnetization versus applied field plots in type I and type II superconductors.

$\kappa < \frac{1}{\sqrt{2}}$, then the material is a type I superconductor $\kappa > \frac{1}{\sqrt{2}}$, then the material is a typeII superconductor. Type I superconductors completely expel magnetic fields less than H_c and show perfect diamagnetism with χ = -1. However type II superconductors have more complicated response to applied magnetic fields. The superconducting state in type II superconductor extends to an applied magnetic field (upper critical field, H_{c2}) much greater than the thermodynamic critical field (H_c). The field at which magnetic flux lines start nucleating on the surface (H_{c1}) is much lower than H_c in type II superconductors. In between H_{c1} and H_{c2}, magnetic flux enters into the superconductor in the form of a triangular array of flux tubes, each carrying a quantum of flux

$$\Phi_0 = \frac{hc}{2e} = 2.07 \times 10^{-7} G - cm^2 .$$

The vortex core has a diameter equal to the coherence length where the superconducting parameter goes to zero. The structure of an isolated vortex is shown in figure 1.3(a). It consists of a core with a radius equal to the coherence length ξ where the magnetic field suppresses superconductivity. Current vortices at a radius of λ, circulate around these normal cores to generate the flux within. The direction of this current is opposite to the main surface shielding current which makes the flux in the superconducting region zero. Each vortex is bound to carry only one flux quanta equal to Φ_0. According to Abrikosov, vortices arrange themselves inside a type II superconductor in a triangular lattice called the Abrikosov lattice in superconductors with smaller λ as observed in $NbSe_2$.

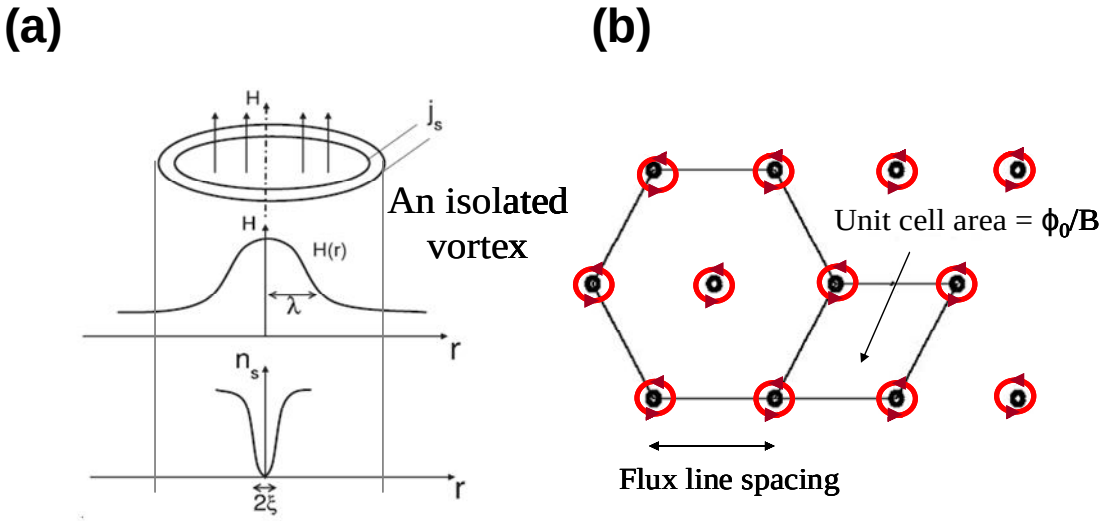

Figure 1.3(a) Structure of an isolated vortex. **(b)** Representation of the vortex lattice.

The zero resistivity state is maintained even in the presence of vortices in mixed state of type II superconductors. Below H_{c1}, type II superconductors also show perfect diamagnetism. As the field increases beyond H_{c1}, more vortices penetrate the material and at H_{c2}, the entire material is filled with the fluxons and the sample transits to the normal state as depicted in figure 1.4.

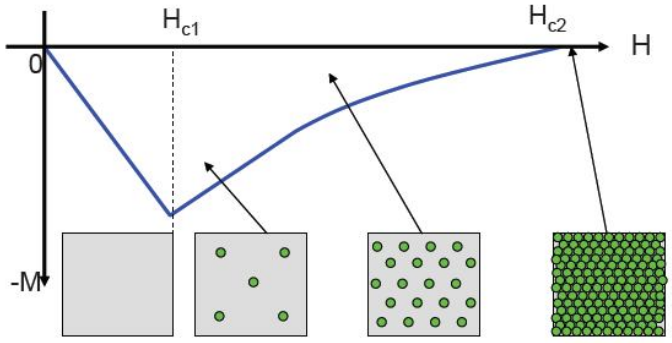

Figure 1.4 Schematic representation of the mixed state of a Type II superconductor. Below H_{c1} ,type II superconductors also show perfect diamagnetism. As the field increases beyond H_{c1}, more vortices penetrate the material and at H_{c2}, the entire material is filled with the fluxons and the sample transits to the normal state.

1.1.3 The BCS theory

In 1957 Bardeen, Cooper and Schrieffer proposed their celebrated electron-pairing theory of superconductivity, which explains completely this complex phenomenon for isotropic superconductors [1-4]. The basis of this theory is that even a very weak attractive interaction between electrons, mediated by phonons, creates a bound pair of electrons (called the Cooper pair) occupying states with equal and opposite momentum and spin (i.e. **k**↑, -**k**↓). The formation of the bound states creates instability in the ground state of the Fermi sea of electrons and a gap (Δ(T)) opens up at the Fermi level. The minimum energy *E*g required to break a Cooper pair to create two quasi-particle excitations is *E*g = 2Δ(*T*). This is shown schematically in figure 1.5(a). The formation of the Cooper pairs mediated by the phonons is illustrated in a simple cartoon in figure 1.5(b). An electron

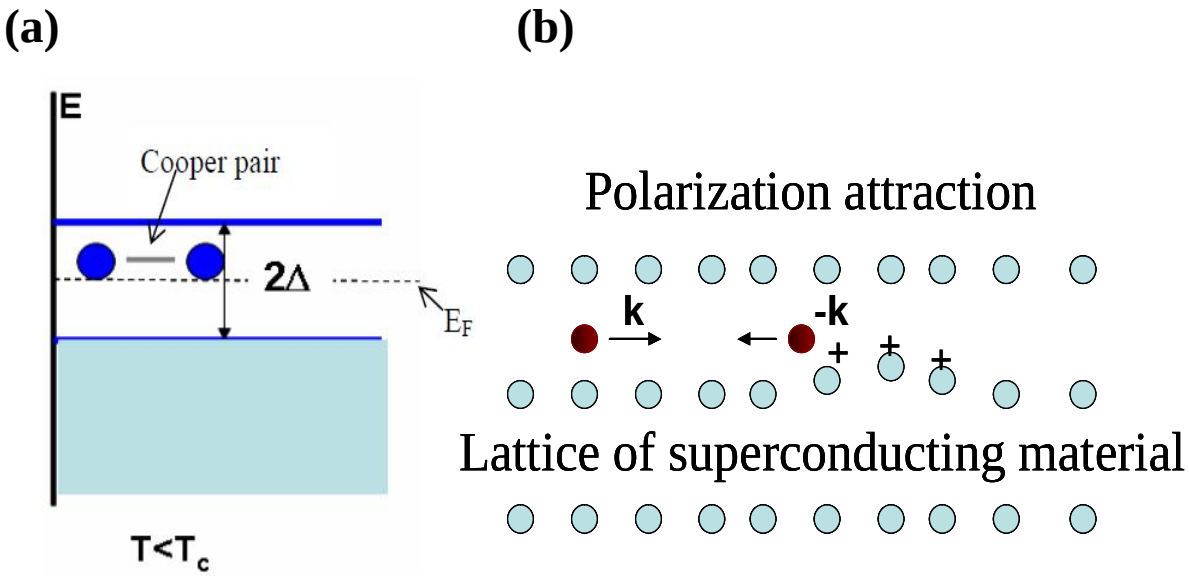

Figure 1.5 (a) Energy band diagram of a superconductor at T < *T*c. It shows the formation of cooper pairs condensing into the BCS state with a gap (Δ) opening at the Fermi level. (b) Simple cartoon depicting the formation of a cooper pair between twoelectrons traveling with momentum **k** and **–k,** mediated by the lattice.

with momentum **k** traveling through the lattice will polarize it, thereby creating a local positive charge. A second electron with momentum –**k** traveling through this lattice will be attracted to the local positive charge, thereby, getting attracted to the first electron. This leads to the formation of the Cooper pairs. The expression for the energy gap Δ(T) as calculated from the BCS theory is given by:

$$\Delta(T) = 2\hbar\omega_D e^{-1/N(E_F)V}, N(E_F)V < 1$$

Here, ω_D is the Debye frequency, $N(E_F)$ is the density of states at the Fermi energy and V is the attractive interaction potential. However, this equation is valid only for weak coupling superconductors with $N(E_F)V$ <1. The critical temperature (T_c) is the temperature at which $\Delta(T)\rightarrow 0$. The expression for T_c is given by:

$$k_B T_c = 1.14\theta_D e^{-1/N(E_F)V}$$

The maximum T_c predicted from this equation is only 25 K. Comparing the above two expressions, it can be seen that for a weak coupling superconductor: $\frac{2\Delta(0)}{k_B T_c} = 3.5$.

Experimentally, the values of 2Δ for different superconductors generally fall in the range from $3k_BT_c$ to $4.5k_BT_c$. Temperature dependence of the energy gap is shown in figure 1.6 and is given as:

$$\frac{\Delta(T)}{\Delta(0)} \approx 1.76\left(1 - \frac{T}{T_c}\right)^{1/2}$$

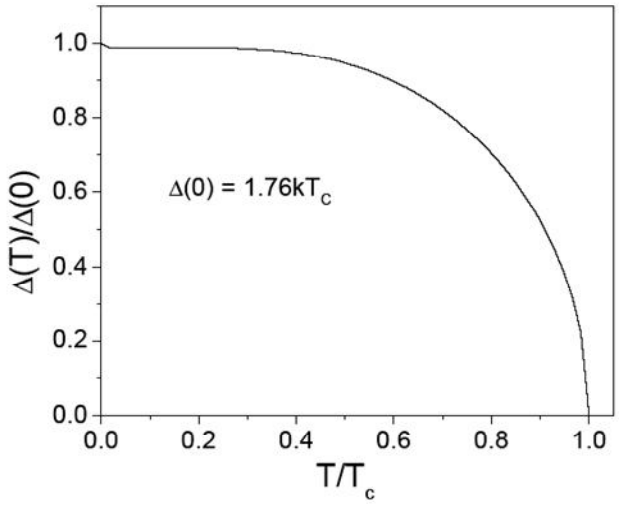

Figure 1.6 Variation of the reduced gap Δ(*T*)/Δ(0) *vs* the reduced temperature *T/Tc* from the BCS theory

Considering the repulsive screened Coulomb potential, μ^*, the coupling constant, $N(E_F)V = \lambda_{ele\text{-}ph} - \mu^*$, where $\lambda_{ele\text{-}ph}$ is the electron-phonon coupling constant. For transition metals μ^* is 0.13. In the strong coupling limit, the T_c is given by MacMillan equation:

$$T_c = \frac{\theta_D}{1.45}\exp\left[\frac{-1.04(1+\lambda)}{\lambda-\mu^*(1+0.62\lambda)}\right]$$

The BCS theory also predicts the magnitude of the electronic specific heat capacity jump at T_c with respect to the normal state value $C_{ele} = \gamma T$ and is given by:

$$\frac{C_s - \gamma T_c}{\gamma T_c} = 1.43$$

where C_s is the electronic specific heat in the superconducting state . Below T_c, the BCS theory predicts that C_s varies exponentially with inverse of temperature following the relation:

$$C_s = A\gamma T_c \exp\left(\frac{-1.76k_B T_c}{T}\right), \text{ where } A = constant = 8.5.$$

1.1.4 The Josephson effect

When two superconductors are brought into contact in such a way that the critical current in the contact region is much lower than that of the individual constituents, the contact is called a 'weak link'. Before contact is established the two superconducting constituents have independent wavefunctions, and therefore arbitrary and independent phases $\varphi(\vec{r})$. The Ginzburg-Landau wavefunction of each superconductor is:

$$\psi(\vec{r}) = |\psi(\vec{r})| \exp(i\phi(\vec{r}))$$

After establishment of weak link, coherence is established across the barrier with a phase difference $\Delta\varphi(\vec{r})$, causing interference between the previously independent wavefunctions and thus having a single wavefunction as a whole. The contact region then behaves as a superconductor. Weak links play a very important role in the magnetic properties of granular superconductors and it is always beneficial to remove them for a better superconducting properties. A typical realization of a weak link is a SIS tunnel junction. Brian Josephson in 1962 discovered that if two superconducting metals were separated by an oxide layer 1 to 2 nm thick, it is possible for electron pairs to pass through the barrier without resistance. This is known as the dc Josephson Effect. The current flowing through the junction, called the Josephson supercurrent, is given by:

$$I_s = i_c \sin\Delta\varphi(\vec{r})$$

Here, $\Delta\varphi$ is the phase difference of the GL wave function across the junction and i_c is the maximum supercurrent which the junction can support. Figure 1.7(a) and (b) show a Josephson junction and the *I-V* curve for such a junction. He further predicted that if a voltage difference V_0 is maintained across the junction, the phase difference $\Delta\varphi$ would

evolve according to the equation:

$$\frac{d\Delta\phi(\vec{r})}{dt} = \frac{2eV_0}{\hbar}$$

This is called the ac Josephson Effect, where the current is an alternating current of amplitude is I_c and frequency $\nu = 2eV_0/\hbar$. Both these predictions have been confirmed by many experiments.

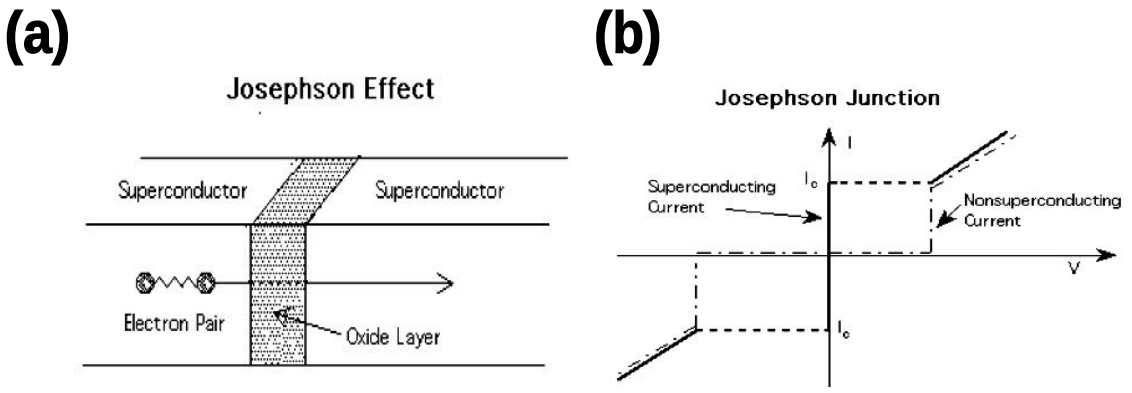

Figure 1.7 (a) Schematic of a Josephson junction showing two superconductors separated by a thin insulating layer. **(b)** The current-voltage characteristic of a single Josephson junction.

1.2. Superconductors

Superconductors range from simple metals to alloys and ceramics. The BCS theory limits the T_c to 25 K, however many other superconducting materials were discovered which do not follow this conventional theory of Cooper pairing and exhibited very high superconducting transition temperatures (T_c). Among the most exciting materials discovered are MgB_2, cuprate superconductors and the Fe-based superconductors. Figure 1.8 shows the development of the T_c with time for various superconductors.

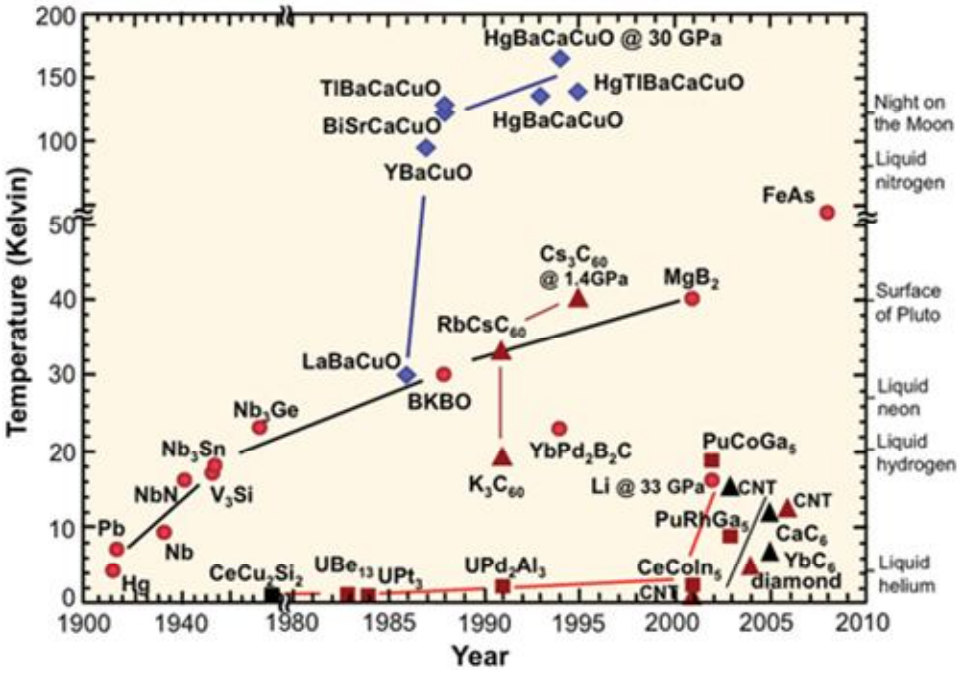

Figure 1.8 shows the development of the T_c with time for various superconductors.

1.2.1 Cuprate superconductors

Cuprate High Temperature Superconductors (HTSC) play an outstanding role in the scientific development and for the present understanding in superconductivity. The first cuprate superconductor was discovered in Ba doped La_2CuO_4 with T_c = 35 K in the year 1986 by Bednorz and Muller. A flurry of activity in the following years led to the identification of many more superconducting cuprates, with the highest T_c of 138 K found in $HgBa_2Ca_2Cu_3O_{8+\delta}$. A fluorinated sample of this phase showed an onset T_c of 166 ± 1 K at 23 GPa pressure which is the highest measured superconducting critical temperature to date. The essential structural features of cuprate superconductors are as

follows:

1. Copper oxide planes are essential. These have stoichiometry CuO_2 and a geometry like that found in the BO_2 planes of the ABO_3 perovskite structure. Hence cuprates are sometimes described as 'layered perovskites'. Maximum T_c is generally found for materials with blocks of three adjacent, hole-doped CuO_2 planes.
2. Electropositive cations, usually from the alkaline earth (Ca, Sr, Ba) or rare earth (La–Lu, Y) metals, act as layer separators in two distinctive structural roles. Large 'A' cations (typically Sr^{2+}, Ba^{2+} or La^{3+}) support additional coordination of a further oxygen to copper, and this can provide a connection to additional metal (M) oxide layers. Smaller electropositive 'B' cations (usually Ca^{2+} or a small rare earth) separate CuO_2 planes in multilayer cuprates without allowing intercalation of O between Cu in adjacent planes which is detrimental to superconductivity. Therefore 'n' number of CuO_2 planes require $(n - 1)$ B cation spacer layers.
3. Blocks of one or two covalent metal oxide layers, MO_x (M can be Cu, Ru, Hg, Tl, Pb, Bi) layers, are connected to CuO_2 planes *via* interplanar oxides in the AO layers. The MO_x layers are sometimes termed the 'charge reservoir' as they compensate for the doping of the CuO_2 planes although this can also achieved by non-aliovalent substitutions at the A or B sites.

Hence many cuprates have compositions $(MO_x)_m(AO)_2B_{n-1}(CuO_2)_n = M_mA_2B_{n-1}Cu_nO_z$, often abbreviated as $M - m2(n - 1)n$, *e.g.* the highest-T_c material $HgBa_2Ca_2Cu_3O_{8+\delta}$ is abbreviated as Hg-1223.

The undoped cuprates contain nine electrons in the copper 3*d*-shells resulting in Cu^{2+} ions within the CuO_2 sheets. Though band structure calculations predict a metallic behavior, they are actually antiferromagnetic insulators or Mott insulators due to strong correlation effects. The Cu^{2+} ion in the d^9 configuration which are octahedrally coordinated with oxygen ions (in case of La_2CuO_4), suffer strong Jahn-Teller distortion. The distorted octahedron makes the $d_{x^2-y^2}$ orbital as the only unoccupied orbital i.e. it accommodates the single hole. This unoccupied copper orbital hybridizes with the pσ orbital of the four neighboring oxygen atoms in the CuO_2 plane. Due to strong Coulomb repulsion these holes cannot move to neighboring Cu sites and thus the parent compounds are insulators. Virtual charge fluctuations generate superexchange interaction between Cu-O-Cu and favors antiparallel alignment of the neighboring spins. These results in long range antiferromagnetic ordering upto rather high Neel temperature; T_N = 250 – 400 K. Addition of charge carriers by either varying the oxygen content or by suitable substitution of cations relaxes the restrictions of spin alignment due to the interaction of these spin ½ particles with the spin lattice. Thus T_N is suppressed and the compound shows superconductivity. Figure 1.9 shows the phase diagram of electron and hole doped superconductors. The optimum number of excess holes or electron is 0.16 at which the superconductor shows the maximum T_c. Over-doping suppresses

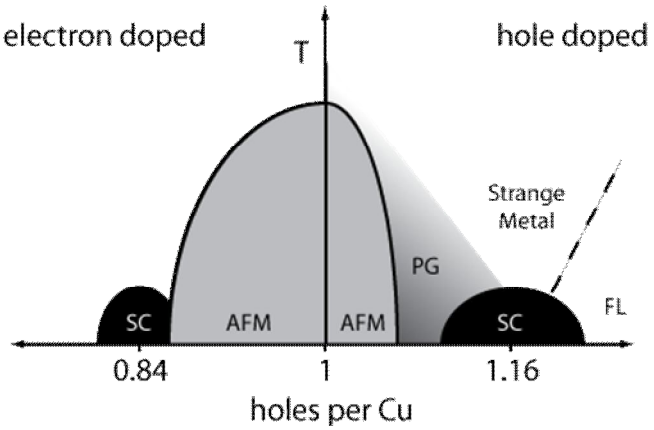

Figure 1.9 A generic phase diagram of electron and hole doped superconductor. The un-doped parent compound is in the antiferromagnetic (AFM) state. In the under-doped state pseudo-gap (PG) state develops in the normal state. At optimum doping, cuprates show superconductivity and in over-doped state, it behaves like a Fermi liquid.

superconductivity and the normal state behavior of hole doped compound shows Fermi liquid behavior. In addition to the doping level, structural features are also very important for optimizing T_c in the cuprates. Buckling of the Cu–O–Cu bridges in the CuO_2 sheets suppresses superconductivity and favors alternative charge and spin ordered insulating ground states, so large Ba^{2+} cations at the A type cation sites help to preserve flat CuO_2 planes and high T_c. Disorder arising from mixed A or B cations adjacent to the planes also suppresses superconductivity. Hence the highest reported T_c for single layer cuprates is 98 K for optimally doped $HgBa_2CuO_{4+\delta}$ (δ = 0.08) which has only Ba^{2+} cations adjacent to the CuO_2 planes, and relatively little additional strain and disorder from the small concentration δ of oxygen interstitials between the Hg sites. Coupling between nearby CuO_2 layers separated by B cation layers also enhances T_c; the highest values are found in the Hg-family where T_c increases up to 138 K for n = 3. T_c decreases for higher n most probably because the doping becomes non-uniform

across in-equivalent CuO_2 planes. The pairing mechanism for superconductivity in the cuprates remains unclear. The essential features for theoretical descriptions are the d-wave symmetry of the order parameter (the wavefunction describing the Cooper pairs has the symmetry of a $d_{x^2-y^2}$ atomic orbital), the presence of strong antiferromagnetic correlations, and the pseudogap feature. A plausible explanation is that antiferromagnetic fluctuations mediate the pairing instead of the electron–phonon coupling found in conventional BCS (Bardeen, Cooper and Schrieffer) type materials [5].

1.2.2 Fe-based superconductors

The credit of first Fe-based superconductors (FeSC) goes to LaOFeP which was discovered by Kamihara *et. al.*, in 2006 and showed a transition temperature of 4 K [6]. This compound resembles the structure of ZrCuSiAs which was introduced some 35 years back by Johnson and Jeitschko [7]. High transition temperature in FeSC were first reported in the electron-doped $LaFeAsO_{1-x}F_x$ [8] series and subsequent study of rare earth $RFeAsO_{1-x}F_x$ and oxygen-deficient $RFeAsO_{1-\delta}$ analogues led to discovery of the highest T_c = 56 K to date in $SmFeAsO_{1-\delta}$ [9]. Hole-doped materials are also superconducting; $La_{0.85}Sr_{0.15}FeAsO$ [10] has T_c = 25 K, and in the related AFe_2As_2 and AFeAs families, $Ba_{0.6}K_{0.4}Fe_2As_2$ has T_c = 38 K [11] and LiFeAs has T_c = 18 K [12]. Superconductivity is also observed in analogues where Fe or As are replaced by similar elements, but with lower T_c's. The binary phase $FeSe_{1-\delta}$ containing only the FeSe-type layers is superconducting with T_c = 9 K which increases to 37 K by applying hydrostatic

Pressure [13]. Non-Fe analogues such as LaNiPO and LaNiAsO, BaM_2As_2 (M = Cr, Mn, Co, Ni, Ru, Rh) and BaM_2P_2 (M = Ni, Rh, Ir), and LiFeP have T_c's < 5 K. The five different structural classes of FeSC have been found. These structures, shown in figure

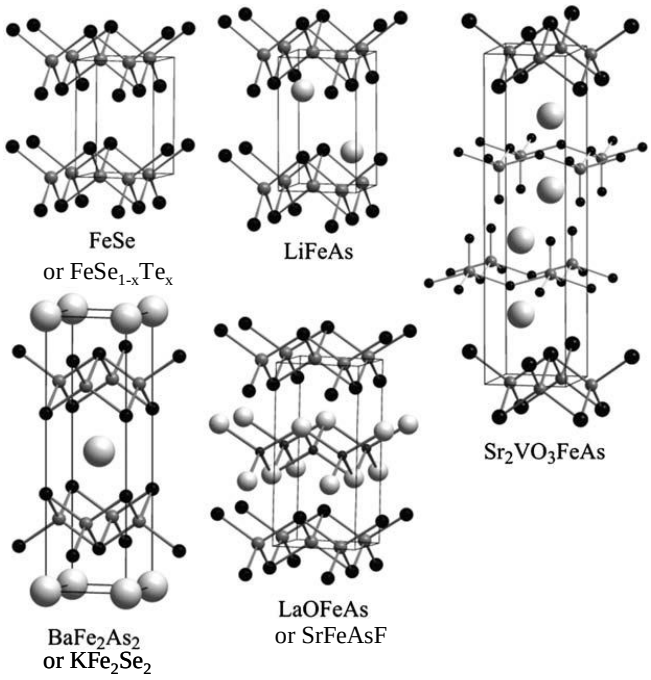

Figure 1.10. Five different structural classes in Fe-based superconductors. The basic structural motif is the presence of FeAs or FeSe layers.

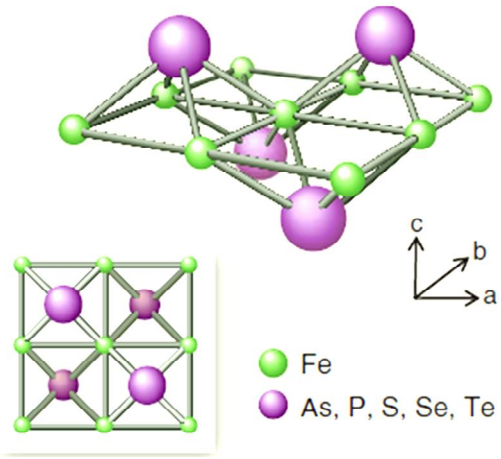

Figure 1.11. Structural motif of the FeSC. (Inset) Top view of the FeX (X = As, P, S, Se, Te) trilayer. The triad (a, b, and c) demonstrates the three crystallographic directions.

1.10, share a common layered structural motif consisting of a layer of FeX_4 (X = As, P, S, Se and Te) coordinated in a tetrahedral network (figure 1.11), with Fe atoms sitting at the centre forming a two dimensional (2D) square lattice. The chalcogen/pnictogen (X) atoms are located at the apical positions of the tetrahedron. These Fe-X layers stack in sequence separated by alkali, alkaline-earth or rare-earth and oxygen/fluorine `blocking layers [14]. It is now widely thought that the interaction that leads to the high temperature superconductivity originates within these common iron layers, similar in nature to the common copper-oxygen building block found in the copper oxide (cuprate) high-T_c superconductors. As in the cuprates, chemical substitution also plays a key role in inducing the superconducting phase in iron pnictides. However three key differences are found: (1) in the arrangement of pnictogen/chalcogen anions above and below the planar iron layer (figure 1.11) as opposed to the planar copper-oxygen structure of the cuprates; (2) in the ability to substitute or dope directly into the active pairing layer; and (3) in the

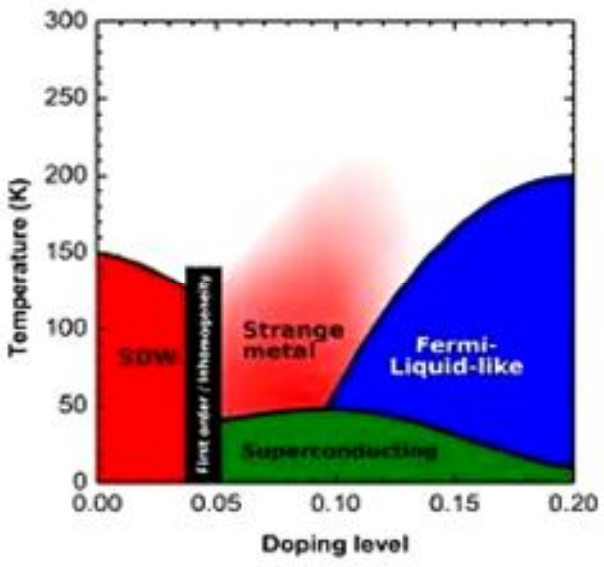

Figure 1.12. Phase diagram of electron doped Fe-based superconductors. In the un-doped state, the parent compound show spin density wave transitions along with structural transition. In the over-doped state, they also show Fermi-liquid behavior.

metallic (rather than insulating) multiband nature of the parent compounds. The electronic phase diagram for the high-T_c iron arsenide superconductors as shown in figure 1.12, appears similar to that of the cuprates, although an important difference is that the parent materials are metallic whereas the undoped cuprates are Mott insulators. The $3d^6$ electrons of Fe play an important role in the metallic nature of parent compounds of FeSC. The degenerate *d* levels split under the tetrahedral environment into low energy doublet ($3d_{3z^2-r^2}$ and $3d_{xy}$) belonging to *e* orbitals and high energy triplet ($3d_{x^2-y^2}$, $3d_{zx}$ and $3d_{yz}$) belonging to t_2 orbitals. The crystal field splitting energy is very small and almost all the bands cross the Fermi level. The Fermi surface of LaOFeAs in the paramagnetic phase consists a total of five sheets. Two quasi-two-dimensional (2D) hole cylinders at the Brillouin zone center (Γ), two electron cylinders at the zone corner (X(M)), and another 3D hole pocket at the top of the Brillouin zone (Z) are realized. The three hole sheets together contribute 80% of the total density of states near the Fermi level N(E_F) whereas 31% is realized from the electron pockets. DFT calculations together with experimental observations suggest that a nesting related (between hole pockets at Γ and electron pockets at X) spin density wave magnetic instability exists in the parent LaOFeAs [15, 16]. Superconductivity usually arises due to electron and hole doping leading to the change in size of the electron or hole cylinders by the suppression of spin density wave. The electronic properties of Fe based superconductors depend highly on the to lattice effects and is optimized when the As–Fe–As angle in the tetrahedral layers is close to the geometric ideal of 109.5° as shown in figure 1.13.

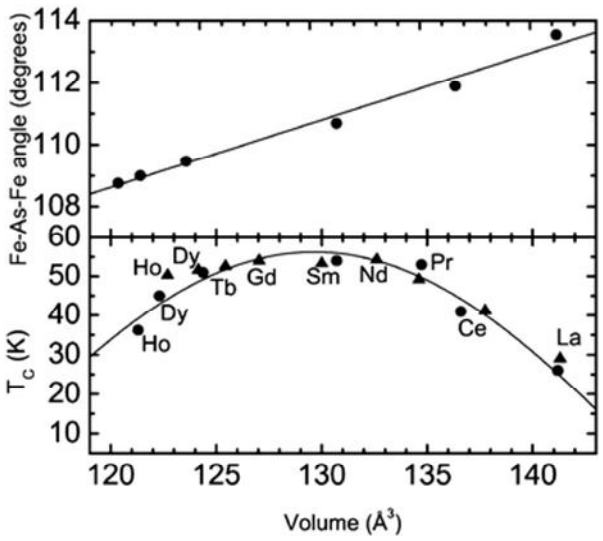

Figure 1.13 Dependence of T_c on the Fe-As-Fe angle in (RE)OFeAs (RE- rare earth metal) superconductors.

1.3. Flux Pinning

In extreme type II superconductor, the magnetic penetration depth i.e. the flux line is typically 100 times larger than the diameter of the vortex line. Hence the vortex line acts as a core and resides deep inside the flux line [2]. The flux within the core has the same direction as the applied field. Each vortex core is surrounded by persistent current which is having a direction opposite to that of diamagnetic shielding current flowing on the surface. Neighboring flux lines interact with each other and repel just like two parallel solenoids. As a consequence in a simple defect free type II superconductor the flux lines arrange themselves in to a triangular lattice so that each vortex is in a position of static equilibrium with respect to its neighboring flux line. The equilibrium gets disturbed when flux line lattice is subjected to an externally applied magnetic field. The flux lines

experience Lorentz force due to shielding currents that work opposite to the externally applied field leading to flux motion. The movement of flux causes the appearance of voltage and consequently no zero-resistance state is observed in the superconductor. In practical superconductors, the movement of flux lines is restricted due to pinning centers caused by defects, vacancies and grain boundaries and therefore a zero resistance can be achieved. However at non-zero temperature even a pinned flux lines can escape from its potential minimum at the pinned position to another pinning centre with the help of thermal activation. De-pinned flux creeps in order to relax the critical state gradient. However from engineering point of view, flux creep is not a serious problem as long as the voltage due to flux creep is small. Pinning of flux lines causes irreversibility effects in superconductors which in turn gives rise to hysteretic isothermal magnetization curves. In order to interpret the magnetic properties of irreversible type II superconductor, Bean introduced the idea of critical state model. The model assumes that the penetrated supercurrents flow with a density equal to the critical current density (J_c) in the regions of the sample which are exposed to a magnetic field. The Bean model is based on the two simple assumptions: first the J_c is independent of the internal magnetic field and second the flux penetration or exclusion happens through the surface.

When a field is applied parallel to the surface, then according to Ampere's law the force per unit volume on the vortex lattice is given by $\vec{F}_P = \vec{J}_c \times \vec{B}$, where J_c is the magnitude of total current density. This force will cause a continuous displacement of the vortex lattice and cause dissipation. In this case the superconductor will behave basically like a normal conductor. If we consider the maximum pinning force at which there is no

vortex motion as F_P, then it is given by $F_P = J_cB = BdH/dx$ (considering $\vec{H} = \hat{k}H$ and $\vec{J}_c = \hat{y}J_c$). In simplest form the Bean model proposes that the effect of vortex pinning is to determine the maximum gradient of the field [17]. This gradient is equal to the critical current J_c. Although Bean's model does not truly explain the dependence of J_c on B, but it explains the principle features of the magnetic hysteresis of a superconductor:

- The width of the hysteresis loop is a measure of J_c.
- A hysteresis with field-increasing and field decreasing branches almost symmetric.
- fast switching from the negative to positive branch of the hysteresis curve
- the slope of the reversing branch dependent on the sample shape only

While proposing Bean did not take into consideration the reversible magnetization nor the flux creep phenomena discussed earlier and therefore is valid only at low temperature

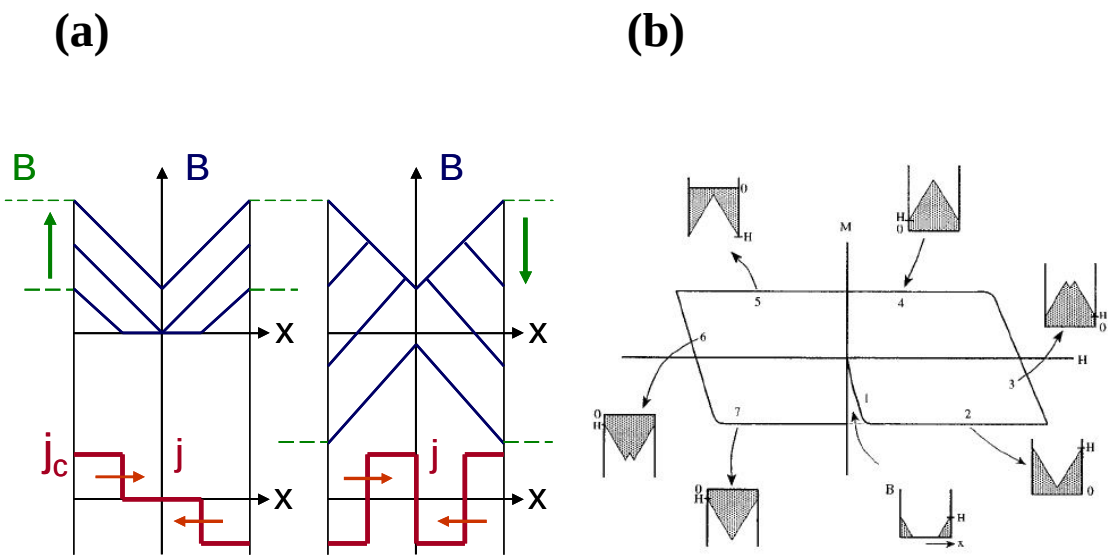

Figure 1.14 (a) Represents the variation of an applied magnetic field inside a superconductor with constant critical current density. **(b)** Isothermal magnetic hysteresis loop of a hard superconductor based on Bean's model.

and low magnetic fields. Below is a typical magnetic hysteresis curve predicted by Bean for a hard type II superconductor. Experimental hysteresis curves are very different in practical superconductors. We have observed that the current density once reaching the maximum value, decreases with increase in applied magnetic field and therefore is not a constant. Kim and Anderson modified the Bean's model by introducing another function such that $J_c(B)(B_0 + B) = C$, where C is a structure sensitive constant of the material and is having a temperature dependence explained on the basis of flux creep in the form of flux line bundles. B_0 is another constant which depends on the number of flux lines in the bundle. Following are the different models that discuss the dependence of critical current density on the induced magnetic field. .

- $J_c(B) = C.$ Bean's model
- $J_c(B)(B_0 + B) = C$ Kim and Anderson model
- $J_c(B)\, B^{1-\gamma} = C$ Irie model
- $J_c(B)B = C$ Silcox model
- $J_c(B)\, B^{-1/2} = C$ Yasukochi model
- $J_c(B) = C_1 exp(-B/C_2) + C_3$ Fietz *et al.* model

1.4. Grain size effects

Superconducting materials at the nano scale has received much attention due to their remarkably different properties from those of bulk superconductors. When the size of individual grains is reduced below their characteristic length scales such as penetration

depth (λ) or coherence length (ξ), the superconducting transition temperature (T_c) is greatly modified. In weak-coupled superconductors, the transition temperature is enhanced due to increase in the electron-phonon coupling constant which arises due to the presence of the low frequency soft phonons and their strong interaction with electrons. However for a strong-coupled BCS superconductor the T_c is lowered due to discretization of electronic energy bands imposed by "Anderson criterion". According to Anderson, superconductivity should cease to occur in nano-grains when the discrete energy level spacing becomes comparable to BCS superconducting gap (Δ). In bulk sample due to overlap of a large number of atomic orbitals, the energy levels are quite continuous and hence a large fraction of electrons are present near the Fermi level for condensation into BCS state and opening of the BCS gap. In nanoparticles, however the same is not true as the spacing between the energy levels increases which also weakens in the interaction among electrons thereby interfering with the BCS condensation. The critical diameter (d_c) of the particle below which superconductivity is absent, can be given as: $d_c = \Delta * N(E_F)$. For low dimensional superconductors, quantum fluctuations create "critical region" around T_c where superconducting properties still exists even though the superconducting

energy gap approaches zero [18]. Besides T_c, the size of superconducting grain also affects its magnetic properties like observation of "Little Parks" effect [19], paramagnetic Meissner effect [20, 21], flux jumps in the magnetic hysteresis [22] and pronounced observation of surface barriers [23]. Such size driven effects make it especially interesting to study strong-coupled type-II superconductor where magnetic vortices also show their distinct presence and dynamics.

1.5. Werthamer-Helfand-Hohenberg model

Generally, there exist two distinct ways to induce pair-breaking in type-II superconductors by an applied magnetic field, i.e., orbital and spin-paramagnetic effects. The former is related to an emergence of Abrikosov vortex lines and superconducting currents around vortex cores, which then reduce the condensation energy. The orbital limiting field refers to the critical field at which vortex cores begin to overlap and is given as: $H_{c2}^{orbital} = \Phi_0/2\pi\xi^2$ where ξ is the coherence length and Φ_0 is the flux quantum. For one-band BCS superconductors, $H_{c2}^{orb}(0)$ is commonly derived from the slope of the determined *H*-*T* phase boundary at T_c, which is given as: $H_{c2}^{orb}(0) = -0.69 \left.\frac{dH_{c2}}{dT}\right|_{T_c} T_c$ in the dirty limit and $-0.73 \left.\frac{dH_{c2}}{dT}\right|_{T_c} T_c$ in the clean limit [24]. The actual H_{c2} of real materials is generally influenced by the both orbital and spin-paramagnetic effects and their relative importance is discussed by Maki factor given as: $\alpha = \sqrt{2}\frac{H_{c2}^{orb}}{H_P^0}$, where H_P^0 is Pauli

limiting field [25]. However, in materials with a heavy electron mass or multiple small Fermi pockets, the spin paramagnetic effects are negligible as in case of High transition temperature iron based superconductors.

1.6. Applications

Unique properties of superconductors [26]:

- Zero resistance to direct current.
- Extreme high current carrying density.
- Extremely low resistance at high frequencies.
- High sensitivity to magnetic fields.
- Extremely low signal dispersion.
- Exclusion to externally high applied magnetic fields.
- Rapid single flux quantum transfer.
- Close to speed of light signal transmission.

Some of the technological applications of superconductivity include:

- the production of sensitive magnetometers based on Squids
- fast digital circuits (including those based on Josephson junctions and rapid single

- flux quantum technology), powerful superconducting electromagnets used in maglev trains, Magnetic Resonance Imaging (MRI) and Nuclear magnetic resonance (NMR) machines, magnetic confinement fusion reactors (e.g. tokamaks), and the beam-steering and focusing magnets used in particle accelerators.
- low-loss power cables
- RF and microwave filters (e.g., for mobile phone base stations, as well as military ultra-sensitive/selective receivers)
- fast fault current limiters
- high sensitivity particle detectors, including the transition edge sensor, the superconducting bolometer, the superconducting tunnel junction detector, the kinetic inductance detector, and the superconducting nanowire single-photon detector
- electric motors and generators

Challenges:

- Cost.
- Refrigeration.
- Reliability.

1.6. References

1. N. W. Ashcroft and N. D. Mermin, *Solid State Physics* (Hartcourt publishers, 1976).
2. K Fossheim and A. Sudbo, *Superconductivity, Physics and applications* (Wiley, 2004).
3. M. Cyrot and D. Pavuna, *Introduction to Superconductivity and High-T_c Materials* (World Scientific, 1992).
4. M. Tinkham, *Introduction to Superconductivity* (McGraw-Hill, 1996).
5. A. Narlikar, *Frontiers in Superconducting Materials* (Springer Verlag, Berlin, 2004).
6. Y. Kamihara, H. Hiramatsu, M. Hirano, R. Kawamura, H. Yanagi, T. Kamiya and H. Hosono, *J. Am. Chem.Soc.* 128 (2006) 10012.
7. V. Johnson, W. Jeitschko, *J. Solid State Chem*. **11** (1974) 161.
8. Y. Kamihara, T. Watanabe, M. Hirano and H. Hosono, *J. Am. Chem. Soc.* 130 (2008) 3296.
9. Z.A. Ren et al., *Eur. Phys. Lett.* **83** (2008) 17002.
10. Hai-Hu Wen, Gang Mu, Lei Fang, Huan Yang and Xiyu Zhu, *Euro. Phys. Lett.* **82** (2008) 17009.
11. M. Rotter, M. Tegel, D. Johrendt, *Phys. Rev. Lett.* **101** (2008) 107006.
12. J.H. Tapp, Z. Tang, B. Lv, K. Sasmal, B. Lorenz, P.C.W. Chu, A.M. Guloy, *Phys. Rev.B* **78** (2008) 060505.

13. S. Medvedev et al., *Nat. Mater.* **8** (2009) 630.

14. J. P. Paglione and R. L. Greene, *Nature Physics* **6** (2010) 645.

15. I. I. Mazin, D. J. Singh, M. D. Johannes, and M. H. Du, *Phys. Rev. Lett.* **101** (2008) 057003.

16. D. Lu, M. Yi, S.-K. Mo, J. Analytis, J.-H. Chu, A. Erickson, D. Singh, Z. Hussain, T. Geballe, I. Fisher, et al., *Physica C* **469** (2009) 452.

17. D. A. Cradwell and D. S. Ginley, *Handbook of Superconducting Materials: Volume 1; Superconductivity, Materials and Processes* (Institute of Physics, Bristol and Philadelphia, 2003).

18. S. Bose, A. M. García- García, M. M. Ugeda, J. D. Urbina, H. Christian M. I. Brihuega and K. Kern, *Nat. Mater.* **9** (2010) 550.

19. H. Vloebergs *et al.*, *Phys. Rev. Lett.* **69** (1992) 1268.

20. A. K. Geim, S. V. Dubonos, J. G. S. Lok, M. Henini and J. C. Mann, *Nature* **396** (1997) 144.

21. D. J. Thompson, L. E. Wenger and J. T. Chen, *Phys. Rev. B* **54** (1996) 16096.

22. A. K. Geim *et al.*, *Nature* **390** (1997) 259.

23. Alexander D. Hernández and D. Domínguez, *Phys. Rev. B* **65** (2002) 144529.

24. E. Helfand and N. R. Werthamer, *Phys. Rev.* **147** (1966) 288.

25. K. Maki, *Phys. Rev.* **148** (1966) 362.

26. Superconductivity; Present and Future Applications, *Coalition for the Commercial Applications of Superconductors* (CCAS/IEEE outreach, 2008).

Chapter 2

Experimental details for synthesis and characterization of superconductors

"A human being is a part of a whole, called by us _universe_, a part limited in time and space. He experiences himself, his thoughts and feelings as something separated from the rest... a kind of optical delusion of his consciousness. This delusion is a kind of prison for us, restricting us to our personal desires and to affection for a few persons nearest to us. Our task must be to free ourselves from this prison by widening our circle of compassion to embrace all living creatures and the whole of nature in its beauty."

- Albert Einstein

Summary

This chapter deals with the principles of operation of the various techniques used for the preparation and characterization of the samples. For the preparation of thin film and multilayers, a multitarget *rf* magnetron sputtering is used. The structural characterization of these films was carried out using Bruker D8 DISOVER high resolution X-ray diffractometer with the general 2θ/ω scans and reciprocal space mapping. Solid state reaction route was used for preparing sputtering targets and Fe-based chalcogenide superconductors. Sol-gel synthesis route was adopted to prepare $YBa_2Cu_3O_{7-\delta}$ sub-micron sized particles whereas urea-nitridation method was used to prepare δ-NbN nanoparticles. The as prepared samples were characterized using powder XRD, VSM magnetometry, AC magnetometry and four point probe resistivity. Hall measurements and heat capacity measurements were also performed on some of the samples.

2.1. Material preparation

2.1.1. Thin Film preparation

Since the discovery of superconductivity in LaBaCuO in 1986 (Bednorz and Muller 1986), research in fabricating high temperature superconductors (HTSCs) has grown extremely rapidly. From the very beginning, a significant effort has been put into the realization of epitaxial films of these oxide materials, motivated largely by the potential applications of thin films and by the possibility of using epitaxial films to study the anisotropic physical properties of these layered materials. Developments and improvements in thin film technology now allow one not only to grow very high-quality thin films, but also to achieve the growth of epitaxial oxide superlattices. Superlattices offer a promising way of growing HTSCs in an atomic layer-by-layer fashion. This multilayer approach takes advantage of the fact that the cuprate superconductor is based on stacked two-dimensional (*2D*) CuO_2 planes separated by layers that act as charge reservoirs [1]. A wide range of deposition techniques has been tested to prepare artificial oxide multilayers, including sputtering (DC and RF, on- and off-axis), laser ablation, laser molecular beam epitaxy (MBE), reactive electron beam evaporation, and thermal MBE [2]. All these techniques have been successfully used for growing oxides and multilayer oxide structures. Sputtering is one of the most commonly used methods for deposition of thin films and multilayers. Its advantage stems from the simplicity of the physical process involved, its versatility, and flexibility to alteration and the lost cost involved in its technology. Sputtering is a process where a solid surface is bombarded

with energetic particles such as accelerated ions, surface atoms of the solid are scattered backward due to collisions between the surface atoms and the energetic particles. A sputtering event is initiated by the first collision between incident ions and target surface atoms, followed by the second and third collisions between the target surface atoms. The displacement of target surface atoms may finally escape from the surface. Figure 2.1 shows the features of sputtering collision in the targets surface. The classical sputter

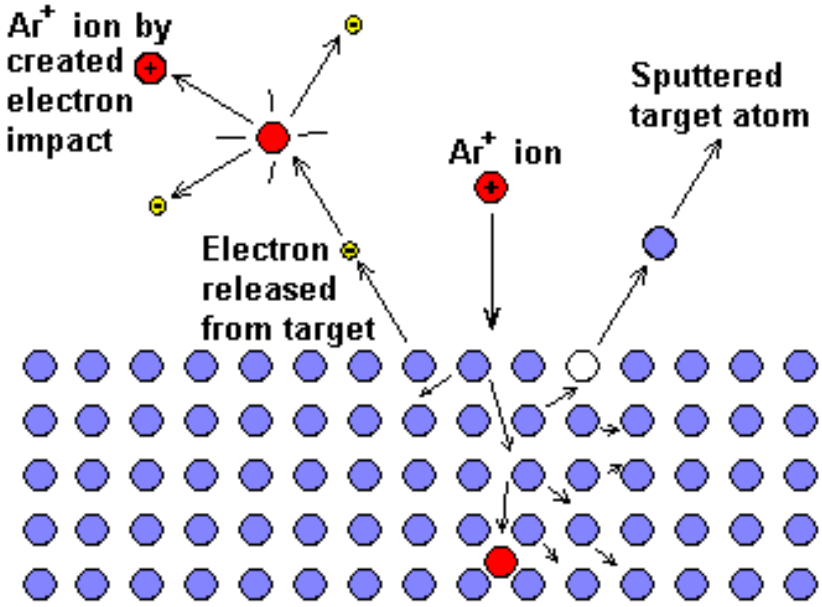

Figure 2.1 A schematic showing the working principle of sputtering. A highly energetic ion bombards the surface of the target material and the target atoms being removed due to the impact. Some of the Ar ions also get implanted in the target.

technologies range from simple dc glow discharge sputtering, which is limited to sputtering of conducting target material, through pulsed dc sputtering (typically at 10-200 kHz) preferentially used for reactive sputter deposition to *rf* (13.56 MHz) sputtering where any target regardless of its conductivity can be sputtered. Among these sputtering

systems, the simplest model is the dc diode sputtering system which is composed of a pair of planar electrodes. One of the electrodes is a cold cathode and the other is the anode. The front of the cathode is covered with target materials to be deposited. The substrate is placed at the anode. The sputtering chamber is filled with sputtering gas, typically argon gas. The glow discharge is maintained under the application of dc voltage between the electrodes. The Ar^+ ions generated in the glow discharge are accelerated at the cathode fall and sputter the target, resulting in the deposition of the thin films on the substrates. As mentioned above the dc sputtering is helpful only for metallic electrodes. But when there is an insulating target, then the sputtering discharge cannot be sustained because the immediate build up of a surface charge of positive ions on the front side of the insulator. To sustain the glow discharge with the insulator target, *rf* voltage is supplied to the target. The *rf* diode sputtering requires an impedance-matching network between the power supply and the discharge chamber. The impedance of the *rf* power supply is almost 50 Ω. The impedance of the glow discharge is on the order of 1 to 10 kΩ. A blocking capacitor is connected between the matching target and the target. The target area is much smaller than the grounded anode and the chamber wall. This asymmetric electrode configuration induces negative d bias on the target and these causes sputtering the rf system. The target and the inductance in the matching network are always cooled by water. The electrical resistivity of the cooling water should be high enough to serve as electrical insulation. In rf diode sputtering the cathode current density is given by:

$$i_s \cong C\frac{dV}{dt}$$

Where *C* is the capacitance between the discharge plasma and the target, and $\frac{dV}{dt}$ denotes the time variations of the target surface potential. This indicates that the increase in frequency increases the cathode ion currents. In practical systems, the frequency used is 13.56 MHz. In the *rf* discharge system, the operating pressure is lowered to as low as 1 mTorr, since the *rf* electrical field in the discharge chamber increases the collision probability between secondary electrons and gas molecules. To further increase the efficiency of sputter deposition, magnetron sputtering is used where a magnet is located behind the target, enhances the ionization and effectively directs the sputtered atoms towards the substrate. The applied magnetic field actually is superposed on the cathode

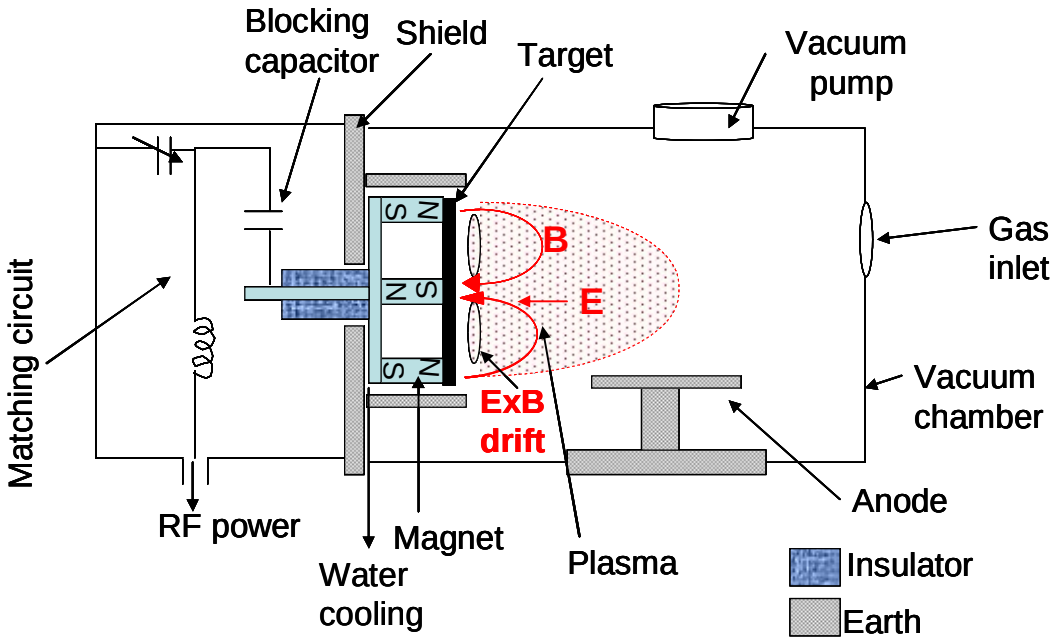

Figure 2.2 A schematic showing the working principle of rf magnetron sputtering. The rf circuit is attached to the target. Magnets are also attached to the target so that the plasma can form closed loop on the surface of the target.

and the glow discharge, which is parallel to the cathode surface. The electrons in the glow discharge show a cycloid motion and the centre of the orbit drifts in the direction of **E**x**B** with adrift velocity of E/B, where **E** and **B** denote the electric field vector in the discharge and the superposed transverse magnetic field vector respectively. The magnetic field is oriented such that the electrons are forced to drift in closed path. This increases the collision rate between the electrons and the sputtering gas molecules. Increase in the number of ionized atoms allows one to work at much lower gas pressures and thus increase their mean free path which is proportional to the partial gas pressure. The outcome is a higher amount of particles on the substrate at a lower pressure, which has a positive influence on the quality of deposition [3]. Figure 2.2 shows the schematic for a rf magnetron sputtering system in the off-axis configuration. Off-axis configuration is adopted to avoid re-sputtering of the grown film. The substrate is usually kept parallel to the axial direction of target that means the target surface is perpendicular to the substrate surface [4] as shown in figure 2.3.

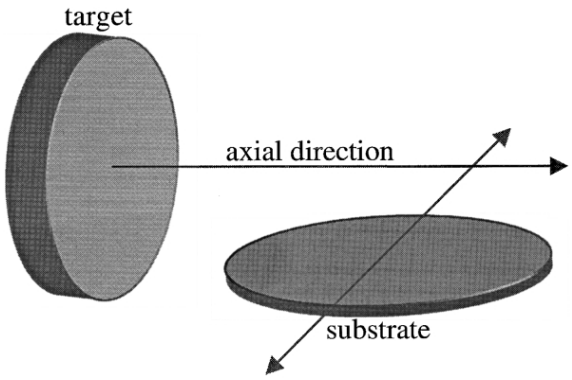

Figure 2.3. Off axis configuration where used in magnetron sputtering systems. The surface normal of the substrate and target are perpendicular directions.

Sputtering is mainly characterized by sputter yield *S*, which is defined as the mean number of atoms removed from the surface of a solid per incident ion and is given as

$$S = \frac{atoms \cdot removed}{incident \cdot ions}$$

Sputter yield is influenced by the following fators:

1. **RF power**:- *S* increases with increasing rf power as the ion bombardment energy as well as discharge current depends strongly on it. A threshold energy exists after which *S* is nearly constant and with further increase in energy, again decreases.
2. **Gas pressure**:- Sputter yield shows a maxima for optimized partial gas pressures. High pressures result in collision between the ions and also re-deposition of target material on the target itself.
3. **Target Material**:- The greater the binding energy of the target material, lower is its sputter yield.
4. **Effects of incidence angle**:- Since the sputter atoms mainly come from the surface of the target, so the angle of incidence of Ar^+ ions should be large with respect to the normal to the target surface. The sputter yield thus increases with increasing angle, shows a maximum for some range (mainly between 60º and 80º) and the increases rapidly with further increase.
5. **Target aging**:- For new targets, the ions impact with lower angles and therefore the sputter yield is less. Therefore it is recommended to functionalize the target before start depositing films. For a ceramic target this may take up to one week to functionalize. Since the most effective area on the target is influenced by the magnet, therefore circular regions called “race-tracks” are formed on the target.

These 'race-tracks' erode much faster than the other regions due to magnet. Therefore most of the target goes wasted [3]. The target composition also changes with time for compound thin films having more than two cations.

Figure 2.4 shows the schematic of the rf magnetron sputtering system that was used to deposit thin film as well as multilayers. The shutters as well as the switching of rf power was controlled and monitored by computer. To ensure uniform thickness of the deposited film, the substrate (that was glued on a silver holder and fixed on the top of heater) was rotated at the speed of 200 rpm. Inert Ar was employed as sputter gas while O_2 and CO_2 acted as reactive gases. For optimized growth the target to substrate distance was kept at 70 mm. The temperature of the substrate was monitored through pyrometer. Pumping of the sputtering chamber was done with the help of turbo pump. As we know that turbo

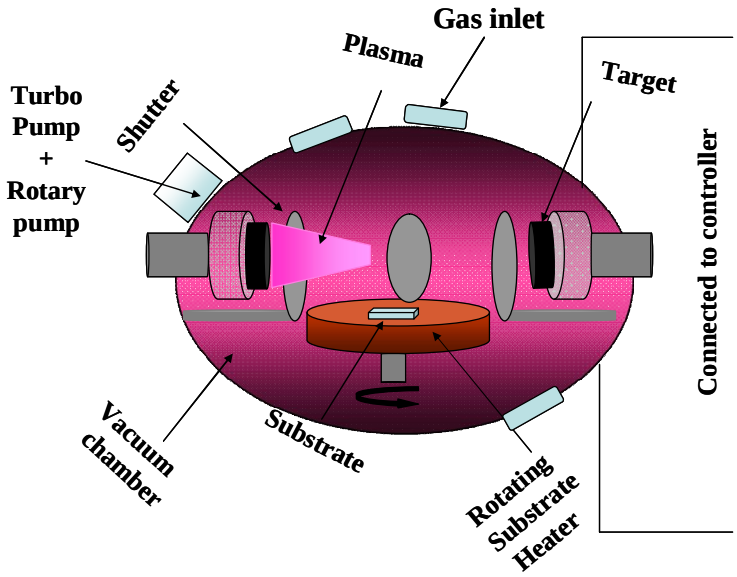

Figure 2.4. Schematic of the multitarget rf magnetron sputtering system that was used for making thin films and superlattices discussed in this thesis.

pumps work only when the pressure is reduced to 1 mTorr in the vacuum chamber. So it is connected to the rotary pump for required evacuation. After the vacuum chamber attains a high vacuum, the turbo pump was run in the 'low speed' mode so that the pressure of the flowing sputtering and reactive gases is maintained. The sputter deposition process of the film was performed in three steps. In the first part that is called pre-sputtering, the target was slowly energized with the shutter between the target and the substrate being closed. During this step the pressure inside the chamber increases due to a sudden increase in the number of charge carriers in the region. Once a steady state is reached, the gas pressure inside the chamber remains constant and here the normal deposition step follows. During multilayer deposition, the shutters that shadow the two targets as well as the *rf* power switches 'on' and 'off' one after the another depending upon the rates of deposition to form the superlattice. The targets are cooled by cold water.

2.1.2. Solid state reaction

The most widely used method for the preparation of polycrystalline solids is the direct heating of powdered reactants mixed in an appropriate ratio, referred as solid state reaction method [5]. The reaction temperatures are usually high and mainly depend upon the melting points of the starting reactants. If the reactants are sensitive to atmosphere, the heating process is usually done in sealed tubes either evacuated or filled with an inert gas. Both thermodynamic and kinetics factors are important in solid state reaction. Thermodynamic factors determine whether or not a particular reaction should occur by considering the change in free energy that are involved, whereas kinetic factors decide

the rate of reaction. In solid state reaction between two solids (powder), the actual reaction to form the product occurs at the interface of the particles and not on the atomic level. The target material is often trapped at the interface blocking further diffusion. Therefore it is very difficult to achieve chemical homogeneity in the end product. To ensure uniformity, re-grinding and re-heating is required to breakup the reactant/product interfaces and to bring fresh reactant surfaces into contact. As a result the synthesis process is very much prone to give secondary phases.

2.1.3. *Sol-gel* synthesis

The *sol-gel* process involves heating a gel formed from a colloidal suspension in order to get the appropriate solid phase. Since the reactants are mixed on an atomic scale into the gel, the reaction generally goes to completion in a short time and can be conducted at alower temperature as compared to the classical soli-state reaction route. The starting solution consists of a mixture of metal-containing compounds (such as metal alkoxides, acetylaetonates, soluble inorganic compounds like nitrates , acetates…), water as the hydrolysis agent or the solvent, acid or base as the catalyst and the organic solvent. In case of nitrates, complexing agent like citric acid is mixed and the pH can be adjusted with the help of ammonia or ethylenediamine. The *sol* consists of solid particles (with sizes varying between 1 nm and 1 μm) which upon continuous drying leads to the formation of an inorganic continuous network containing a liquid phase (*gel*). Formation of a metal oxide involves connecting the metal centers with oxo (M-O-M) or hydroxo (M-OH-M) bridges and therefore generating metal-oxo or metal-hydroxo polymers in

solution. The drying process serves to remove the liquid phase from the gel thus forming a porous material, then a thermal treatment (firing) may be performed in order to obtain metal oxide powders the desired product by the thermal decomposition of organic materials. The sol-gel process is very effective in producing particles with controlled morphology and degree of aggregation. This process offers an effective method for producing nanoparticles as well as thick or thin films of superconductors [6].

2.2. Characterization

2.2.1. Powder X-ray diffraction

X-rays interact almost exclusively with the electrons of the material, by means of scattering (coherent and incoherent) and absorption. Coherent scattering, which has exactly the same wavelength as the incident radiation, constitutes diffraction [7]. The most powerful and general principle in the diffraction theory for periodic objects such as crystals, is that developed by W. L. Bragg, which states that the lattice planes reflect radiation like mirrors. Maximum positive interference occurs when the path differences between reflections from successive lattice planes in a family is equal to an integer number of wavelengths, i.e.

$$n\lambda = 2d \sin\theta$$

Where 'n' is the order of reflection, λ is the wavelength, d is the lattice plane spacing and θ is the angle or incidence/reflection to the planes. To each family of the parallel planes

can be associated to a point in the reciprocal space, which all together forms a periodic lattice. The geometrical condition for diffraction to occur is that the reciprocal lattice point, defined by the vector $\boldsymbol{d}^*_{hkl}$,

$$|\boldsymbol{d}^*_{hkl}| = 1/d^*_{hkl} = 2\sin\theta/\lambda$$

lies on the surface of a sphere of radius 1/λ, called the Ewald sphere. Only lattice points located inside the sphere of radius $2/\lambda$ will be able to diffract. It should be noted that the wavelengths used for diffraction experiments must be of the same magnitude as the inter-planar distances in crystals ($\lambda \sim 0.5 - 2.5$ Å). The scattering amplitude of an atom is determined by summing the contributions from all its electrons. The ratio of the scattering amplitude of an atom to that of a single electron defines the atomic scattering factor, or the form factor '*f*'. At the diffraction angle zero, the scattering amplitude is equal to the number of electrons in the atom and the amplitude decreases rapidly with increasing diffraction angle. The atomic scattering factor is given by:

$$f = f_0 \exp\left[-B\left(\sin\theta/\lambda\right)^2 \right]$$

Where f_0 is the atomic scattering factor at absolute zero and B is the Debye-waller coefficient at the particular temperature at which the XRD patterns are obtained. The scattering amplitude of all the atoms in a unit cell is given by structure factor given by a a complex number:

$$F_{hkl} = \sum_{j=1}^{N} f_j \exp\left[2\pi i\left(hx_j + ky_j + lz_j\right)\right]$$

Where $2\pi(hx_j + ky_j + lz_j)$ is the phase angle of an atom with fractional coordinates x_j, y_j and z_j. The total number of atoms in the unit cell is N and *h, k, l* represents the miller

indices of the planes. For non-primitive Bravais lattice, there exists translational symmetry or rotation symmetry about a screw axis or reflection symmetry due to glide planes or a combination of the above within the unit cell may result in the absence of some potential reflections. The X-ray diffraction techniques are usually divided into single crystal and powder methods. For powder diffractometry, in the Bragg-Brentano geometry, a sample is mounted on a plate moves in steps of θ, whereas the detector turns by 2θ. The obtained patterns can give information about the following informations:

1. **Phase identification**:- The diffraction patterns obtained can be matched with the existing patterns in the Powder Diffraction File (PDF) of the International Centre for Diffraction Data. These databases are interfaced to a wide variety of diffraction analysis software and distributed globally. In multiphase patterns the relative intensities between the peaks can give a quantitative account of the two phases.
2. **Crystallinity**: X-ray diffraction produces pattern consist of series of sharp peaks due to the crystalline nature of the materials. In the case of amorphous materials (liquids, glasses etc.), it produces a background signal. The crystallinity percent in such compounds can be determined using powder XRD by comparing the integrated intensity of the background pattern to that of the sharp peaks.
3. **Lattice parameters**: The size and shape of the unit cell of crystalline phase determines the position of a diffaction peak. Each peak is characteristic of a certain lattice plane and therefore corresponds to a Miller index. Indexing the peaks for a high symmetry material, e.g. cubic or hexagonal, is quite easy even for

an unknown phase. Complex cases can be dealt with the indexing programs available, but if the unit cell is very large and the symmetry is low (triclinic), success is not always guaranteed.

4. **Crystal structure**: For unknown materials, Crystal structure determination from powder diffraction data is extremely challenging due to the overlap of reflections in a powder experiment, while comparing to that of single crystal analysis. Rietveld refinement can be carried out on the powder XRD data to obtain the refined crystal structural parameters of the material by using an initial structural model that is similar to the material under investigation.

Peak property	information
Peak position	Phase, structure, lattice parameter
Peak width	Crystallite size, strain, defects
Peak area or height ratio	Preferred orientation
Peak tails	Diffused scattering and point defects
Background	Amorphous content

Table I gives the summary of the information received from a powder XRD pattern

2.2.2. High resolution X-ray diffraction

The basic principles of crystallography are the same as that in powder and in this section,

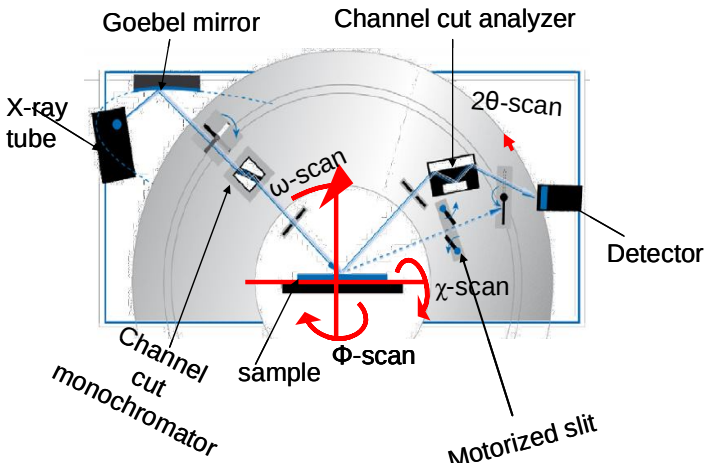

Figure 2.5. Schematic representation of the triple axis Bruker D8 discover diffractometer showing a 4 bounce monochromator for selecting Cu-$K_{\alpha 1}$ wavength. The monochromator gives a beam divergence of 0.0033º. The resolution of lattice constant determination is $\Delta d/d \approx 6 \times 10^{-5}$.

and the main focus will be on the various types of information acquired from the measurements. The high resolution X-ray diffraction (HRXRD) was performed for structural characterization of thin films. Figure 2.5 shows the triple axis geometry (an additional crystal analyzer is used to provide resolution on the 2θ axis) of the Bruker D8 DISCOVER high resolution X-ray diffractometer. In this set-up, the incident beam is fixed on to the reflecting plane of the single crystalline substrate or film whereas the sample holder and detector move. The desired symmetric plane is chosen with a set of rocking curves (Δω), detector scans (2θ-scan) and tilt (χ-scan). The alignment is sufficient for performing 2θ/ω scans that provide information about the planes that are strictly parallel to the aligned plane and in a single crystalline thin film gives information

about the out of plane lattice parameter. However the in-plane lattice parameter as well as the in-plane

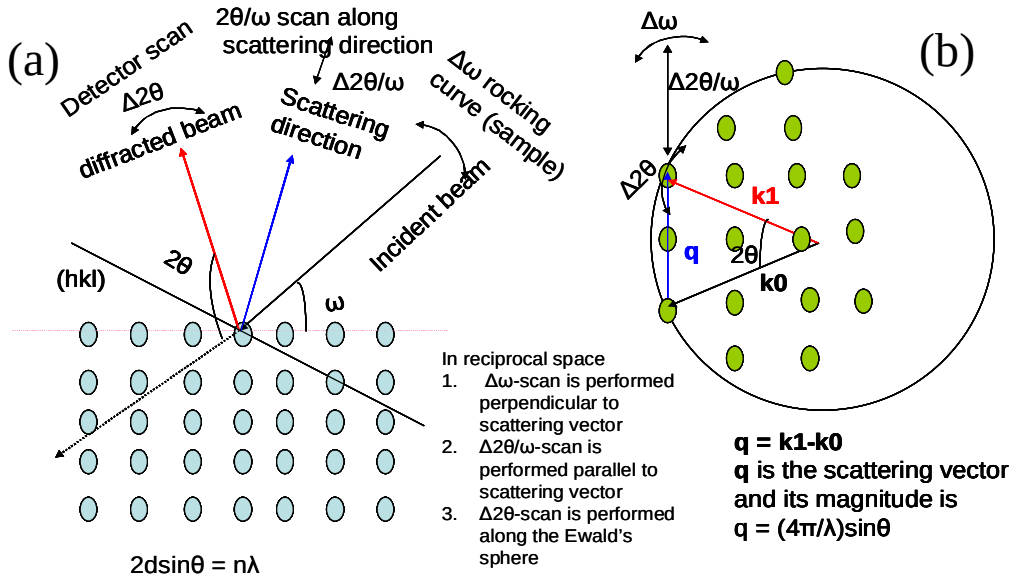

Figure 2.6. (a) shows the lattice plane in the real space and various types of HRXRD scanning modes. (b) shows the reciprocal lattice with Ewald sphere. The incident beam, diffracting beam and the sattering vector are shown. Information about various types of scans in reciprocal space are given in this figure.

surface quality of the film cannot be determined by this method. A more efficient method is to use reciprocal space maps (RSM) for such purpose. As discussed earlier that a lattice plane in real space represents a lattice point in reciprocal space. Figure 2.6 shows a schematic of the various types of scans that can be performed in the real as well as reciprocal space. RSM shows the map of a region in of reciprocal space in the vicinity of each (*hkl*) region. It can be accessed through a combination of 2θ/ω scan and rocking curves. By comparing the profile and position of the RSM of film and substrate, the information such as in-plane as well as out of plane lattice parameters, mosiacity, strain,

relaxation, layer tilt, coherency and curvature of the film can be obtained [8]. For a fully strained film, the matching of the in-plane lattice vector of the film to the substrate necessitates that the asymmetric reflections of the substrate and film lie vertically above each other in RSM. For fully relaxed layer the in-plane vector of the film is free of substrate constraints and so the film asymmetric reflection will lie on the radial line joing the substrate reflection and origin of the reciprocal space map as shown in figure 2.7.

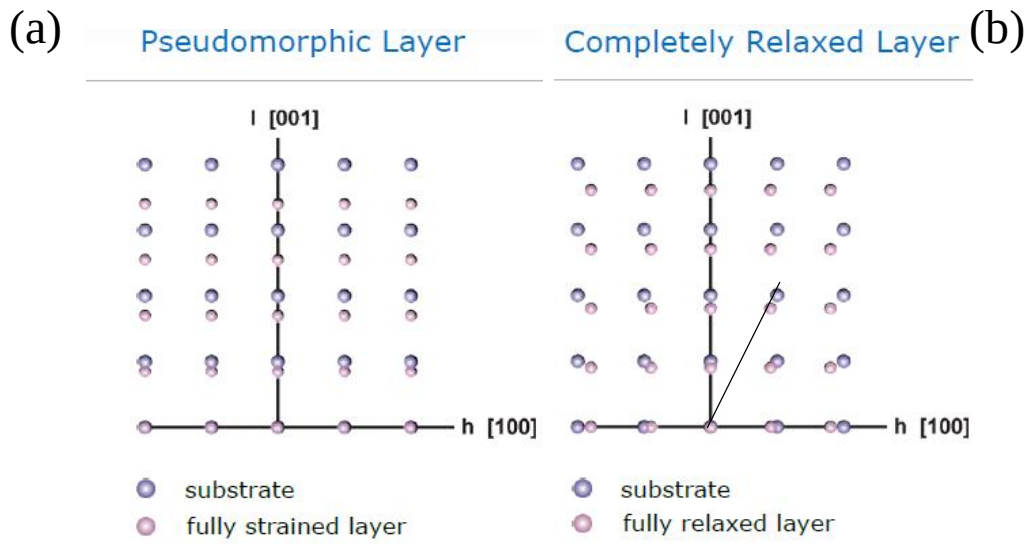

Figure 2.7. (a) shows the positions of a fully strained film with respect to substrate in the reciprocal space maps whereas (b) shows the position of a fully relaxed film.

The mosaicity in the sample can also be found from the shape of the film reflection in RSM. Figure 2.8 shows the RSM of a mosaic film and its profile. Thus we see that mosaicity or the spread of the film reflection becomes much broader for higher (*hkl*) values. Mosaicity of the film can also be determined by simply doing a rocking curve.

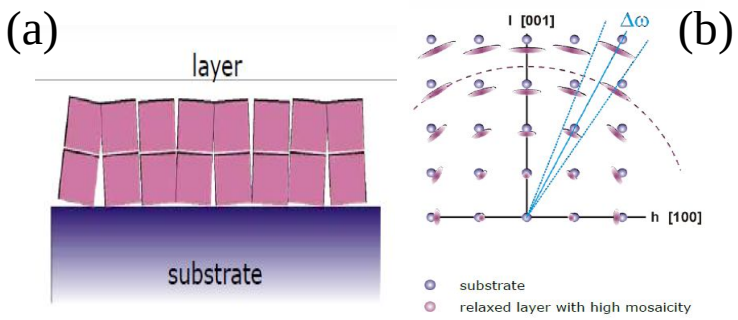

Figure 2.7. (a) In mosaic films, the grains are not oriented in a single direction but have a tilt. In the RSM (b), they appear to be smeared along the tangent to the circle with centre at the origin.

2.2.3. Scanning electron microscopy

Scanning electron microscope (SEM) is one of the most versatile and widely used tools of modern science as it allows the study of morphology and composition of the materials. By scanning an electron probe across a specimen, high resolution images of the morphology or topography of a specimen, with great depth of field, at very low or very high magnifications can be obtained. SEM uses a focused electron beam to scan small areas of solid samples. Secondary electrons emitted from the sample are collected to create an area map of the secondary emissions. Since the intensity of secondary emission is very dependent on local morphology, the area map is a magnified image of the sample. The SEM also produces images of high resolution, which means that closely spaced features can be examined at a high magnification. SEM consists of an electron gun, electron lenses, a scanning system and an electron detector [9]. The electron gun provides a source of electrons. In a typical SEM, an electron beam is thermionically emitted from an electron gun fitted with a tungsten filament cathode. Tungsten is normally used in

thermionic electron guns because it has the highest melting point and lowest vapour pressure of all metals, thereby allowing it to be heated for electron emission. Other types of electron emitters include are lanthanum hexaboride (LaB6) cathodes and field emission guns (FEG). FEG may be a cold-cathode type using tungsten single crystal emitters or a thermally-assisted Schottky type using emitters of zirconium oxide. Back-scattered electrons (BSE) are the electrons that are reflected from the sample by elastic scattering. BSE are often used in analytical SEM along with the spectra made from the characteristic x-rays. Because the intensity of the BSE signal is strongly related to the atomic number (Z) of the specimen, BSE images can provide information about the distribution of different elements in the sample. Characteristic x-rays are emitted when the electron beam removes an inner shell electron from the sample, causing a higher energy electron to fill the shell and release energy. These characteristic x-rays are used to identify the composition and measure the abundance of elements in the sample. For imaging in the conventional SEM, specimens must be electrically conductive, at least at the surface, and electrically grounded to prevent the accumulation of electrostatic charge at the surface. Nonconductive specimens tend to charge when scanned by the electron beam and especially in secondary electron imaging mode, this causes scanning faults and other image artifacts. They are therefore usually coated with an ultrathin electrically-conducting material, commonly gold, deposited on the sample. Coating prevents the accumulation of static electric charge on the specimen during electron irradiation. A field-emission cathode in the electron gun of a SEM provides narrower probing beams at low as well as high electron energy, resulting in both improved spatial resolution and minimized sample charging and damage. Field-emission scanning electron microscope

(FESEM) produces clearer, less electrostatically distorted images with spatial resolution down to 1.5 nm which is 3 to 6 times better than conventional SEM. Smaller-area contamination spots can be examined at electron accelerating voltages compatible with energy dispersive x-ray spectroscopy. Reduced penetration of low kinetic energy electrons probes closer to the immediate material surface. High quality and low voltage images are obtained with negligible electrical charging of samples (accelerating voltages range from 0.5 to 30 kV) and the need for placing conducting coatings on insulating materials is virtually eliminated.

2.2.4. Transmission electron microscopy

In a conventional transmission electron microscope, a thin specimen of the sample is illuminated by electron beam of uniform current density. Electrons are emitted in the electron gun by thermionic, Schottky or field emission. The transmission electron microscope offer both magnification as well as resolution with the help of a set of lenses. The lenses although serve the same purpose as in optical microscope, however they are different because of the charged electrons. Instead of the usual glass lenses, electromagnetic lenses are used that can deflect the electron beam and converge them to a single focal point. There are essentially three types of lenses used to form the final image in the TEM. These are the condenser, objective, and projector lenses. The main function of the condenser lens is to concentrate and focus the beam of electrons coming off of the filament onto the sample to give a uniformly illuminated sample. The objective lens and its associated pole pieces is the heart of the TEM and the most critical of all the lenses. It

forms the initial enlarged image of the illuminated portion of the specimen in a plane that is suitable for further enlargement by the projector lens. In order to eliminate the effect of scattered electrons from the image, an aperture is placed in the objective lens that will stop all those electrons that have deviated from the optical path. The smaller the aperture is, the better is the image contrast. Finally the projector lens projects the final image on a photographic screen. It is in the projector lens that the majority of the magnification occurs. Thus total magnification is a product of the objective and projector magnifications. For higher magnifications an intermediate lens is often added between the objective and projector lenses. This lens serves to further magnify the image. The transmission electron microscopy works under ultra-high vacuum conditions to avoid collision between electrons and gas molecules. Various types of information can be obtained in terms of electron diffraction (ED) patterns and high resolution transmission electron microscope images (HRTEM). The geometrical arrangement of the diffracted electrons is available on the back focal plane of the objective lens. The relative positions of the spots give information about the cell parameters, existing symmetry and orientation of the crystal. The bright field or the image due to transmitted beam from the sample forms the HRTEM image. It gives an idea about the microstructure and the defects present in the sample. The resolution of the image is limited by the image transfer function, determined by the instrumental parameters such as spherical aberration, defocus spread and beam divergence, the focus of the objective lens and the acceleration voltage.

Other analysis modes in TEM are electron dispersive spectroscopy (EDS) that provides the local chemical composition in the sample and electron energy loss spectroscopy (EELS) that provide information on light atoms like carbon, nitrogen or oxygen.

2.2.5. Vibrating sample magnetometry

Vibrating sample magnetometers (VSM), as introduced by Foner, have become widespread in studying magnetic and superconducting materials. The core of the VSM is a set of coils, which measure the alternating magnetic flux produced by the sample vibrating about the entre of the coil system [10]. The coil system is placed inside a magnet (either an electromagnet or a superconducting magnet for fields > 30 kOe) and the sample is attached to a motor that vibrates the sample. Depending upon the direction of vibration with respect to the applied field, the VSMs are referred to as axial (vibration parallel to the field) and transverse (vibration perpendicular to the field). The measurements that we have performed are axial. In contrast to the SQUID magnetometer which detects the flux itself, the VSM pick up coils detect the rate of change of magnetic flux. The voltage V measured across the sensing coils in a VSM can be expressed as the product of four contributing sources:

$$V = M \times A \times F \times S$$

where,

M = magnetic moment of the sample,

A = amplitude of vibration,

F = frequency of vibration and

S = sensitivity function of the sensing coils.

2.2.6. AC magnetometry

The basic unit for the measurement of AC susceptibility in PPMS contains an AC drive coil that provides alternating excitation field and a detection coil that inductively (according to Faraday's law) responds to the combined sample moment and excitation field. Both coils are concentric to the DC magnet of the PPMS. The drive coil is wound longitudinally around the detection coil set. The detection coils are arranged in first order

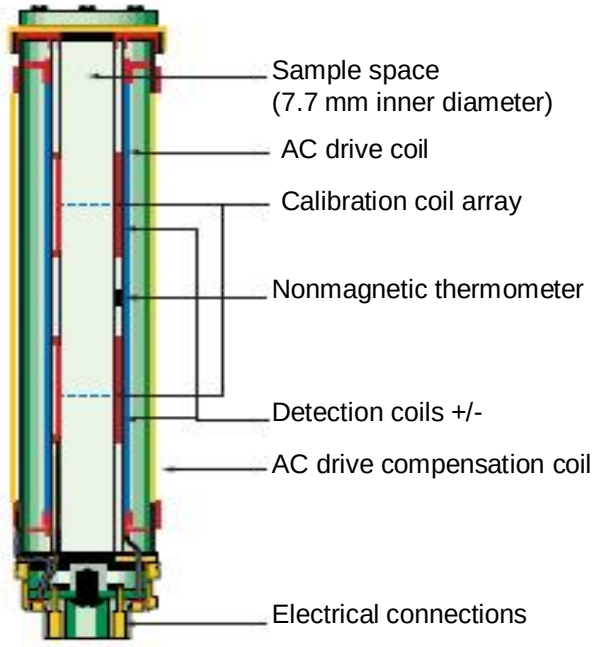

Figure 2.8. A schematic of the AC magnetic susceptibility option inbuilt in physical property measurement system (PPMS, Quantum Design).

gradiometer configuration to help isolate the sample's signal from uniform background noises. An AC compensation coil is wound around the AC drive coil ensures that the excitation field is confined to the volume of the coil set, thereby avoiding interaction with

any materials outside the region of measurement. This actively reduces environmental noise during AC measurements. To increase the accuracy of the phase and amplitude calibration during each measurement, a calibration coil array, situated in the middle of each of the two detection coils, is used. During AC measurements, an ac field is applied to the measurement region (under zero or a constant magnetic field) and the detection coils indicate how applied field is altered by the presence of the sample. The PPMS uses a digital signal processor (DSP) instead of a lock in amplifier [10]. An AC drive magnetic field (which is a time dependent magnetic field) is usually given as:

$$H(\omega t) = H_{ac}\,\mathrm{Re}[\exp(i\omega t)]$$

and the corresponding time dependent magnetization is given as:

$$M(\omega t) = H_{ac}\sum_{n=1}^{\infty}\mathrm{Re}[\chi_n \exp(i\omega t)]$$

Here we define χ_n as the harmonic ac magnetic susceptibility $\chi_n = \chi_n^{'} + i\chi_n^{''}$ (n = 1, 2, 3……) as the Fourier coefficients of the magnetization, where χ_1 is the fundamental ac susceptibility and others are higher harmonic susceptibilities. The susceptibility is calculated as: $\chi_n = dM(\omega t)/dH_{ac}$. AC susceptibility measurements have become popular mainly for characterizing superconductors and are very useful to study the dynamics of magnetic response of superconductors. It is a very sensitive tool as the ac susceptibility depends mainly on the minute changes in the applied field [7].

2.2.7. Resistivity measurements

In typical resistivity measurements, 4 electrical leads are attached to a rectangular sample

along a straight line (figure 2.9). A current is fed from contact A to contact B, and the voltage is measured across contacts C and D, which must be far away from the current contacts in order for the lines of current flow to be uniform and parallel between C and D. The resistance (R) of the sample can be derived from the voltage drop across contacts C and D, the applied current, and the geometry of the sample. Resistivity (ρ) of the sample can be calculated using the formula: $R = \frac{\rho L}{A}$ where L is the distance between the voltage probes and A is the area of the cross-section of the sample.

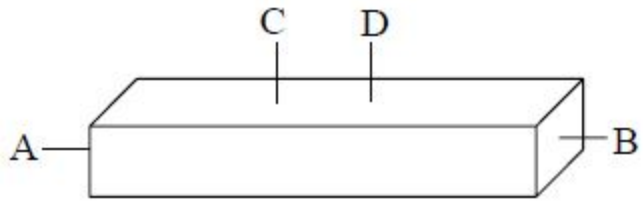

Figure 2.9. Ideal sample geometry and positions of the probes used for four probe resistivity measurements. The probes A and B are connected to a current source while probes C and D are connected at voltmeter.

If the current probes are not sufficiently far from the voltage probes then errors are introduced in the measurements due to non-uniformity of the electric field. In superconductors, this may give rise to the non-zero value of resistivity even at very low temperatures much below the superconducting transition temperature ($T_c(zero)$) of the sample. Below the onset temperature of superconductivity, the resistivity curves are highly dependent upon the magnetic field due to interaction of magnetic flux with vortices.

2.2.8. Hall measurements

The Hall effect is a direct consequence of the Lorentz force in electron transport in solids.

It was discovered in 1879 by Edward Hall. The geometry of Hall's experiment is shown in Figure 2.3. When a magnetic field **H (**H_z**)** is applied in a direction perpendicular to the direction of the current **j (**j_x**)**, then the charge carriers experience a force in the direction of **j x B** and get deposited near the edges of the sample. Positive and negative are deflected in the opposite direction and an electric field is developed in the direction perpendicular to both **j** and **B**. The field developed is called the Hall field and the voltage drop is called the Hall voltage. The quantity defined by the relation: $R_H = \frac{E_y}{j_x \mu_0 H}$ is called the Hall coefficient R_H. It is also inversely proportional to the charge carrier density through the relation: $R_H = -\frac{1}{ne}$, where e is the electronic charge. A quantitative description of the deflection of the charged particles is defined as the ratio of the mean free path (l) to the ratio of the curvature (r) of the carrier in magnetic field and is given by the relation: $\frac{l}{r} = \tan\theta_H = \frac{\rho_{xy}}{\rho_{xx}}$ where ρ_{xy} is the transverse resistivity (E_y/j_x), ρ_{xx} is the longitudinal resistivity (E_x/j_x) and θ_H is the Hall angle. The mobility of the majority charge carriers from Hall measurement can be calculated from the relation: $\mu_H = \frac{R_H}{\rho_{xx}}$.

Figure 2.10 shows a schematic of the Hall effect.

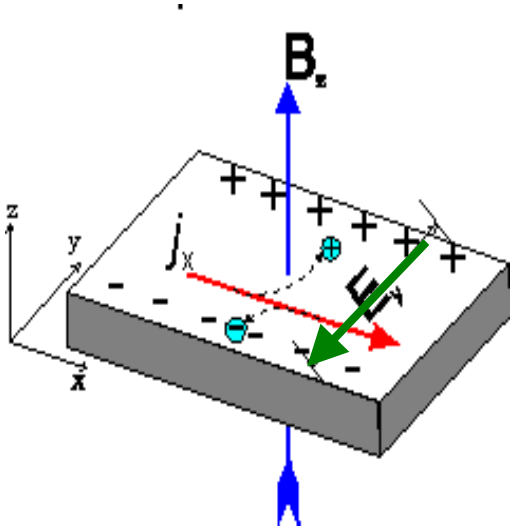

Figure 2.10. A standard geometry for the hall effect in which the sample with rectangular cross-section is placed in a magnetic field B_z along the z-direction. An electric field is applied along the x-direction which causes a current j_x. Due to Lorentz force, the electrons accumulate on one side of the sample and the excess positive ion on the opposite side. A transverse field is E_y is developed which cancels the Lorentz force.

Hall coefficient was measured using the AC transport option inbuilt in the physical property measurement system (PPMS, Quantum Design, U.S.A.). To measure only the potential difference due to the Hall potential, the voltage leads must delineate a perfect perpendicular to the bias field. However in real situations, there is always an additional longitudinal voltage (offset) superimposed on the transverse voltage which is dependent upon the sample resistance, electric bias field as well as magnetic field. This offset voltage is much larger than the actual Hall voltage. To nullify its effect, Hall resistivity corresponding to the Hall voltage was measured for both positive and negative applied magnetic fields. The actual Hall resistivity was calculated by subtracting the average of these two values from the measured resistivity at a particular magnetic field.

Another source of error is the sample shape. If the sample is not according to the above description, then for any arbitrary shaped sample with flat surface the probes can

be attached according to the Van der Paw method. But probes should fulfill the following conditions:

1. The contacts are at the circumference of the sample.
2. The contacts are sufficiently small.
3. The sample is homogeneous in thickness.
4. The surface of the sample is singly connected.

For a disc shaped sample, the error in Hall coefficient of the sample can be taken as:

$\frac{\Delta R_H}{R_H} = -\frac{6l}{\pi^2 d}$ where ΔR_H is the error in R_H, l is the length of the probe on the surface of the sample and d is the diameter of the disc [11].

2.2.9. Heat capacity measurements

Heat capacity measurements were carried out using Physical Property Measurement System (Quantum Design, USA). The Quantum Design Heat Capacity measures the heat capacity at constant pressure,

$$C_P = \left(\frac{dQ}{dT}\right)_P$$

As with other techniques for measuring heat capacity, the Quantum Design Heat capacity option controls the heat added to and removed from a sample while monitoring the resultant change in temperature. During a measurement, a known amount of heat is applied at constant power for a fixed time and then this heating period is followed by a cooling period of the same duration. In the heat capacity measurement puck a platform

heater and platform thermometer are attached to the bottom side of the sample platform (figure 2.11). Small wires provide the electrical connection to the platform heater and platform thermometer and also provide the thermal connection and structural support for the platform. The sample is mounted to the platform by using a thin layer of apiezon grease, which provides the required thermal contact to the platform. Sufficient vacuum is created so that thermal conductance between the sample platform and the thermal bath is totally dominated by the conductance of the wires. This gives a reproducible heat link to the bath with a corresponding time constant large enough to allow both the platform and sample to achieve sufficient thermal equilibrium during the measurement. Different measurement techniques [12] are optimized for different sample sizes and accuracy requirements. The Quantum Design Heat Capacity option uses a relaxation technique that combines the best measurement accuracy with robust analysis techniques. After each measurement cycle (which is a heating period followed by a cooling period), the heat capacity option fits the entire temperature response of the sample platform to a model that accounts for both the thermal relaxation of the sample platform to the bath temperature and the relaxation between the platform and the sample itself [13]. The effect of the relaxation between the sample platform and sample must be considered when the thermal

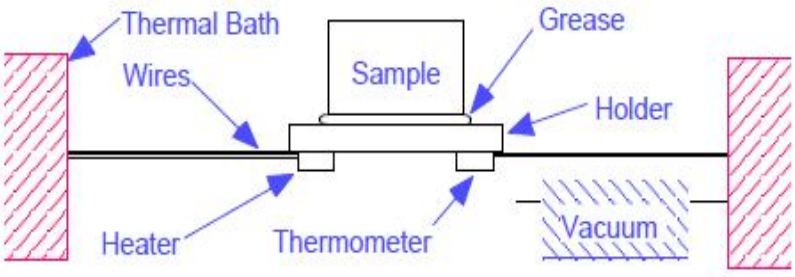

Figure 2.11. Thermal connections to sample and sample platform in the heat capacity measurement

connection shared by the sample and platform is poor. By modeling this effect, the software can report the correct heat capacity values despite such poor contact.

2.2.10. Infra-red spectroscopy

The infrared portion of the electromagnetic spectrum is divided into three regions; the near-, mid- and far- infrared, named for their relation to the visible spectrum. The far-infrared, approximately 400-10 cm^{-1} (30-1000 μm), lying adjacent to the microwave region, has low energy and may be used for rotational spectroscopy. The mid-infrared, approximately 4000-400 cm^{-1} (1.4-30 μm), may be used to study the fundamental vibrations and associated rotational-vibrational structure. The higher energy near-IR, approximately 14000-4000 cm^{-1} (0.8-1.4 μm), can excite overtone or harmonic vibrations. The names and classifications of these sub-regions are merely conventions. They are neither strict divisions nor based on exact molecular or electromagnetic properties.

The infra-red spectroscopy involves an exchange of energy between vibrational excitation and the photons, which obeys the energy conservation rule given by

$$\hbar\omega = \hbar\Omega$$

where $\hbar\omega$ and $\hbar\Omega$ are the photon and phonon energies. In the IR process, the photon couples to the polarization field set up by a phonon and are associated with the permanent dipole moment of the molecule. The interaction is zero unless there is phase coherence between the photon and the phonon. Because the wavelength of photon is large compared to the lattice constants, the requirement of phase coherence determines that only zone-

centre phonons are active participant. The resonant frequencies are determined by the masses of the atoms and by the associated vibronic coupling. In particular, in the Born-Oppenheimer and harmonic approximations, i.e. when the molecular Hamiltonian corresponding to the electronic ground state can be approximated by a harmonic oscillator in the neighborhood of the equilibrium molecular geometry, the resonant frequencies are determined by the normal modes corresponding to the molecular electronic ground state potential energy surface. Nevertheless, the resonant frequencies can be in a first approach related to the strength of the bond and the mass of the atoms at either end of it. Thus the frequency of the vibrations can be associated with a particular bond type.

2.3. References

1. H. Shaked, P.M. Keane, J. C. Rodrigues, F. F. Owen, R. L. Hitterman and J. D. Jorgensen, C*rystal structure of high T_c superconducting copper oxides* (Elsevier, Amsterdam, 1994).
2. Jean-Marc Triscone and Øystein Fischer, *Rep. Prog. Phys*. **60** (1997) 1673.
3. K. Wasa, M. Kitabatake and H. Adachi, *Thin Film Materials Technology: Sputtering of Compound Materials* (William Andrew, Springer, 2004).
4. J.C. Nie_, A. Sundaresan, A.K. Hayashi, Y. Ishiura, H. Ihara, *Thin Solid Films* **389** (2001) 261.
5. A. R. West, *Solid State Chemistry and Its Applications*. (Wiley, Singapore, 1984).
6. M. Kakihana, *Journal of Sol-Gel Science and Technology* **6** (1996) 7.
7. D. A. Cradwell and D. S. Ginley, *Handbook of Superconducting Materials: Volume 1;Superconductivity, Materials and Processes* (Institute of Physics, Bristol and Philadelphia, 2003).
8. P. F. Fewster, *Critical review in solid state and Materials sciences,* **22** (1997) 69.
9. J. I. Goldsteinand H. Yakowitz, *Practical Scanning Electron Microscopy*, (Plenum Press, New York, 1975).
10. Quantum Design, San Diego, CA 92121, USA. *Quantum Design. User manual of the physical property measurement system.*, 2 edition, (1999).
11. L. J. Van der Pauw, *Philips Technical Reports,* **20** (1958) 220.
12. G. R. Stewart, *Rev. Sci. Instrum.* **54** (1983) 1.
13. J. S. Hwang, K. J. Lin and C. Tien, *Rev. Sci. Instrum.* 68(1), 94{101 (1997).

Chapter 3

Preparation and characterization of superconducting (Cu,C)$Ba_2CuO_{4\pm\delta}$ or (Cu,C)-1201 thin films

The will to win, the desire to succeed, the urge to reach your full potential... these are the keys that will unlock the door to personal excellence.

- Confucius

Summary**

In this chapter we have studied the effects of substrate temperature in establishing superconductivity in carbon incorporated thin films of $BaCuO_{2+\delta}$ (IL) with a doubled *c* lattice parameter. Carbon in the form of CO_3^{2-} group modulates the IL structure into a superstructure with doubled *c* lattice parameter. The superstructure: (Cu,C)$Ba_2CuO_{4\pm\delta}$ ((Cu,C)-1201) shows superconductivity within a narrow window of *c* lattice parameters varying between 8.28 Å and 8.33 Å. Structural analysis of these thin films using reciprocal space maps (RSM) show that the *c*-axis expansion accompany pseudomorphic growth of the thin films. In plane lattice parameter (*a*) obtained for such films is 3.90 Å similar to the $SrTiO_3$ substrate. Growth temperature of these films under compressive strain is obtained at substrate temperatures varying between 530 °C and 560 °C. Relaxed films with *a* lattice parameter of 4.00 Å was obtained at deposition temperatures less than 500 °C. A small deviation in the substrate temperature led to the coexistence of strained and relaxed phases. Superconductivity was found to exist only in films under compressive strain. We are the first to report the above observation about the possibility of strain induced superconductivity in (Cu,C)-1201 thin films.

A paper based on the present study has been published in *Physica C* **466 (2007) 111-114 and other has been communicated to Appl. Phys. Lett.

3.1. Introduction

The structure of Infinite layer systems (ILs) consists of CuO_2 planes separated by alkaline metal ions (Ba^{2+}, Sr^{2+}, Ca^{2+}). This system forms the basic building block of all High Temperature Superconductors (HTSCs) where charge carriers are doped into the CuO_2 planes from the charge reservoir layers. Due to large size of Ba^{2+} – ion, $BaCuO_2$ can incorporate apical oxygen and carbon in the form of CO_3^{2-} group to form superstructure with a *c* lattice parameter double to that of the pure $BaCuO_2$ [1-4]. The structure of carbon incorporated $BaCuO_2$ or (Cu,C)-1201 can be regarded as the first member of $(Cu,C)Ba_2Ca_{n-1}Cu_nO_{2n+2\pm\delta}$ ((Cu,C)-12(n-1)n) superconducting systems with n = 1. The homologous series of this oxycarbonate family, where the superconducting transition temperature (T_c) is greater than 117 K for Cu-1234, can be obtained by high pressure synthesis route [5]. The bi-axial strain (hydrostatic pressure) not only stabilizes phases with desired cations and anions but also play an important role in enhancing the T_c of cuprate superconductors [6]. The pressure derivatives of T_c show that $dT_c/dp_a > 0$ and $dT_c/dp_c < 0$ (or negligible), where p_a and p_c denote the uniaxial pressure along the crystallographic *a* axis (parallel to the CuO_2 planes) and *c* axis (perpendicular to CuO_2 planes), respectively. However due to compensation there was not a big impact on T_c of the cuprate superconductor [7]. On the other hand, in most HTSCs it was found that uniaxial pressure can have a much better and clear impact on the T_c. Recently it was established that partial pressure derivative of T_c depends strongly on the lattice constant ratio *c*/*a* and increases with increasing *c*/*a* ratio [8]. These results suggest the possibility

of tuning the structure of HTSCs using epitaxial strain exploiting thin film deposition methods while choosing a proper substrate. A compressive strain decreases the in-plane lattice parameter while increasing the out-of-plane lattice parameter. A tensile strain however increases the in-plane lattice parameter while decreasing the out-of-plane lattice parameter. The misfit strain therefore distorts the structure of the film and may create voids that can accomodate oxygen during in-situ or post annealing. The degree of distortion (contraction or expansion) of the film's in-plane lattice parameter depends upon the elasticity of the film as well as choice of the substrate. Two fold increase in the T_c of $La_{1.9}Sr_{0.1}CuO_4$ thin film due to compressive epitaxial strain has already stimulated a great interest in superconducting thin film research [9, 10]. An Insulator - superconductor transition was observed in undoped strained thin films of La_2CuO_4 (LCO) deposited on $LaSrAlO_4$ (LSAO) single crystalline substrates [11]. The in plane lattice parameter of pseudo-tetragonal non-superconducting LCO (*space group: I4/mmm*) is ~ 3.8 Å while that of superconducting LSAO is 3.77Å [7]. Tensile strain induced by $SrTiO_3$ (STO) showed an adverse effect on the superconducting properties of hole doped LCO. The strain effect in LCO has been explained by the modulation of the CuO_2 plane-charge reservoir distance [12], and the suppression of the low-temperature tetragonal (LTT) phase [13, 14]. As undoped and lightly doped LCO are known to become superconducting when interstitial oxygen is inserted, it was also found that oxygenation plays an important role in the epitaxial strained thin films [11, 15]. The fact that hole doping relieves the crystallographic strain in bulk LCO, by shrinking the *a* lattice parameter while expanding the *c* lattice parameter [6], places compressive strain in thin

films on the same structural effects. It was argued that *c* axis expansion may lead to more space for interstitial sites in between LaO layers and therefore a much free movement for oxygen atoms [11]. Cross-sectional TEM images on such thin films illustrated the presence of shear defects which may lead to better oxygen diffusion [16].

In our study, we also suggest compressive strain induced Insulator – superconductor transition in thin films of (Cu,C)-1201. However in our case, the strain can be tuned by mere varying the deposition temperature. Low substrate temperature (T_s) provided relaxed films while at higher T_s, strained films were obtained. However a difference of 1.5% in the in-plane lattice parameters of relaxed and strained films could not alter the crystal structure. Annealing in oxygen showed a remarkable impact on the normal state resistivity of (Cu,C)-1201 thin films. Although a high partial pressure of oxygen during sputter deposition could not facilitate a much better difference and almost deteriorated the normal state transport. In this study we will present the relationship between deposition temperature, structure and superconductivity of (Cu,C)-1201 thin films.

3.2. Scope of present investigation

The in-plane lattice parameter of (Cu,C)-1201 thin films on $SrTiO_3$ substrates reported in literature is 3.96 Å which gives a lattice mismatch of 1.5% between the in-plane lattice parameters of $SrTiO_3$ and (Cu,C)-1201. For relieving the strain and smooth growth of film, it is therefore recommended to use a buffer layer whose lattice parameter lies in between the lattice parameters of STO and (Cu,C)-1201. The most favorable candidate is

$SrCuO_2$ with the same atomic arrangement and an in plane lattice parameter of 3.92 Å [17]. However, we show that the mismatch between (Cu,C)-1201 and STO can be nullified and tuned by choosing a suitable substrate temperature during the growth process of this thin film. At high growth temperature, the in-plane lattice of (Cu,C)-1201 experiences a compressive strain. Strained (Cu,C)-1201 thin film shows superconductivity whereas the relaxed film obtained at low growth temperature shows insulating behavior. Such an observation once again connotes charge carrier doping through epitaxial strain in cuprate superconductors. This work also highlights the uniqueness of (Cu,C)-1201 thin films in switching its growth mode from a relaxed growth to a pseudomorphic growth with increasing substrate temperature. Superconductivity in (Cu,C)-1201 thin films makes it a potential candidate for a charge reservoir layer in cuprate superlattices which forms the basis of the next chapter.

3.3. Experimental

3.3.1 Materials

Ceramic targets of the composition $BaCu_{0.75}O_y$ and $BaCu_{0.85}O_y$ were prepared by solid state reaction route from the starting materials, $BaCO_3$ and CuO. The starting mixture was calcined at temperatures 870 °C, 880 °C for and 890 °C for 36 h with intermittent grindings. The resultant powder was pressed into a disc of 50 mm diameter and then

sintered at 900 °C. X-ray Diffraction (XRD) pattern of the product indicated no stable compound formation but a mixture of $BaCuO_2$ and CuO with relative intensities roughly proportional to the expected ones based on stoichiometry. Thin films were deposited by rf magnetron sputtering on (100) $SrTiO_3$ single crystal substrate in the off-axis configuration using KE702-6 type sputtering machine (KScience, Japan). The substrates were glued to a silver–nickel substrate holder with silver paste and heated to a temperature range between of 470 °C - 560 °C which was measured by an optical pyrometer. The distance between the target surface and substrate was fixed at 75 mm. The deposition was carried out in a gas mixture of Ar, O_2 and CO_2 where the Ar : O_2 ratio was varied between 1 : 0.5 – 1 : 3 whereas the CO_2 partial gas pressure was varied between 1 - 3 $x10^{-3}$Torr. After deposition, films were cooled to room temperature in 1 atm O_2 pressure with a rate of 1 °C/min. The rf power to the target was kept constant at 25 W.

The as received substrates usually have an amorphous layer due to cutting and polishing. Annealing of such surfaces results in re-growth and improved crystallinity of the surface. However only annealing alone cannot remove the mixed termination of the $SrTiO_3$ surfaces. TiO_2 terminated surface can be prepared by buffer HF (BHF) etching. For most of our thin films we used the annealed substrates prepared by heating the as received substrate at 1000 °C. TiO_2 terminated substrates were also prepared by heating the substrates at 950 °C for 1 hour after etching them with BHF (pH = 5) for 3 minutes. Before etching the substrates were ultra-sonicated in de-ionized water for 30 minutes [18, 19]. The etched substrates showed steps of ~ 4 Å, with pits and precipitates on the surface [20]. This may have happened because of the high pH and low annealing temperature of

the substrate. Though the surface roughness of non-etched but annealed substrates was high, still we found them suitable for the growth of films.

3.3.2 Characterization

Structural characterization of these films was carried out using a four- circle Bruker D8 DISCOVER diffractometer equipped with a Cu-X ray tube, Göebel mirror, 4- bounce 022 Ge channel cut monochromator, (to select only the Cu $K_{\alpha 1}$ radiation) Eulerian cradle and a scintillation counter . The phase was identified using $2\theta/\omega$ coupled scan with 2θ ranging between 5° to 60°. Here 2θ is the angle between the incident and the diffracted X-ray beam and ω is the angle between the incident X-ray beam and the sample surface. Symmetry and texture of the epitaxial film were acknowledged via φ – scan around the [310] direction. A detailed structural analysis about the crystallinity and lattice parameters was obtained using reciprocal space mapping (RSM; i.e., a combination of several rocking curves at different diffraction angles, 2θ) was performed by high resolution X-ray diffraction (HRXRD). Symmetric mapping was done around the (100) and (200) Bragg reflections of STO while asymmetric mapping was performed around (310) Bragg reflection in the exit beam configuration. The surface of the annealed as well as etched substrate was characterized using AFM in the tapping mode. The surface morphology of the film was obtained by FESEM (NOVA NANO600 – FEI, The Netherlands). The thickness of the film was obtained through cross-setional FESEM

images. IR spectra of the thin films were obtained in the reflection geometry using Bruker IFS 66V/S spectrometer. All the films were prepared on rectangular cut substrates. Before attaching four point probe leads, 800 nm thick gold pads were deposited on the films masked by aluminium foils. Enamel removed thin Cu wires working as leads, were glued on these pads with the help of silver epoxy. DC resistivity was measured using the dc transport measurement option in physical property measurement system (PPMS). AC magnetic measurements to know about the onset of diamagnetic transition, were also performed in the PPMS. The applied ac field was kept constant at 1 Oe. Data was collected in the temperature range between 3 K and 50 K at three different frequencies (97 Hz, 997 Hz and 9997 Hz) respectively. AC susceptibility was sometimes measured up to the 3rd harmonic.

3.4 Results and discussion

3.4.1 Structure

Figure 3.1(a) shows the XRD pattern of $BaCuO_2$ thin film which was deposited without the presence of CO_2 gas in the sputtering environment. Two peaks corresponding to the (001) and (002) Bragg reflections can be observed before the substrate peaks. No other peaks related to any other phase or structure modulation was detected in the pattern. The *c* lattice parameter is equal to 4.18 Å and represents the tetragonal phase (S.G:- P4/mmm) of $BaCuO_2$. However the *c* lattice parameter is slightly larger than the usual reported

value of 4.02 Å [3, 4]. This phase is difficult to stabilize by usual solid state reaction route under normal pressure. Exploiting the stabilizing effects of an epitaxial growth, thin films of tetragonal $BaCuO_2$ up to a thickness of 30 nm can be deposited under a narrow range of deposition temperature (T_s = 530 °C) [20]. The asterisk (*) may be representing the cubic phase of $BaCuO_2$. Usually the cubic $BaCuO_2$ phase with a lattice constant of *a* = 18.3 Å forms easily with *a* axis orientation [3, 4]. Introduction of CO_2 gas into the sputtering chamber while deposition, modulated the structure of the film, that may be assumed to have an out of plane periodicity of "*2c*" to that of $BaCuO_2$ [3, 4, 21]. Figure 3.1(b) shows a typical XRD pattern of the superstructure where the (001) Bragg reflection peak corresponds to a *c* lattice parameter approximately equal to 8.3 Å. The

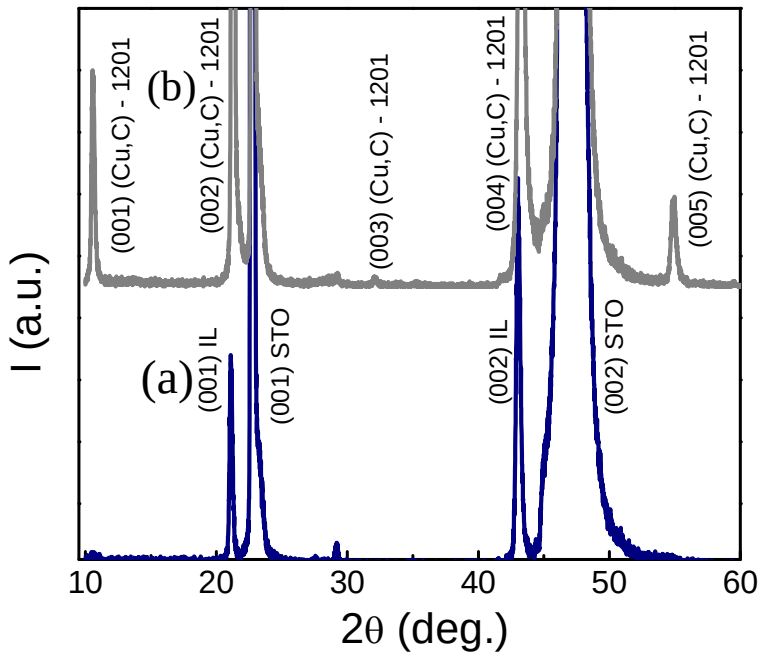

Figure 3.1. X-ray diffraction patterns of thin films prepared with and without CO_3 group in the structure. (a) shows the peak corresponding to the infinite layer $BaCuO_2$ with a *c* lattice parameter of 4.18 Å. (b) shows the modulated structure with doubled *c* length formed after incorporating CO_3 group in $BaCuO_2$. The (001) peak at 2θ ≈ 10.6° shows a lattice parameter of 8.3 Å.

doubling of the *c*- lattice parameter indicates formation of $Ba_2Cu_2O_4$ type structure. Due to large size of Ba^{2+}, Ba based IL stabilizes only through incorporation of oxygen into its layer. Oxygen present in carbon based CO_3 group, thus occupy the oxygen deficient sites in the Ba layer and therefore acts as bridge between the two IL $BaCuO_2$ unit cells forming a modulated structure with *c*- axis length appx. equal to 8.0 Å. However it has been found that most of the CO_3 sites are occupied by CuO_4 square planes. The CuO_4 planes have the same site occupancy as the chains present in $YBa_2Cu_3O_{7-\delta}$ (YBCO). Therefore the modulated compound is represented as (Cu,C)$Ba_2CuO_{4+\delta}$ or (Cu,C)-1201 and has two inequivalent Cu sites. Thus the arrangement of CO_3 and Cu-O chains in

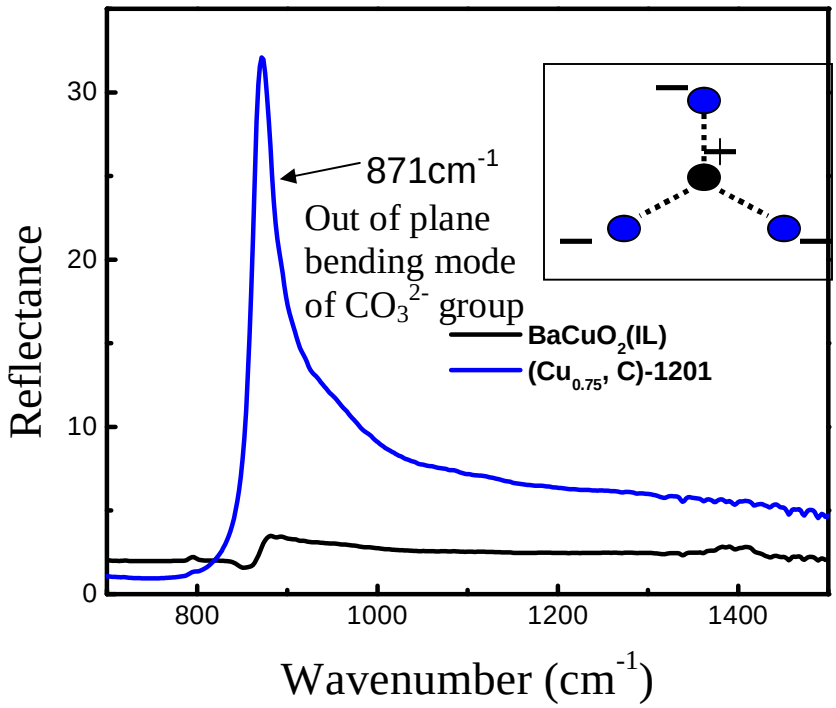

Figure 3.2. Infrared reflectance of films prepared in the absence and presence of CO_2 gas in the sputtering chamber. Presence of peak in the reflectance measurement of (Cu,C)-1201 thin film confirms the presence of CO_3 group in the structure. The wavenumber associated with the peak shows the out of plane bending mode of CO_3 group.

(Cu,C)-1201 is similar to that in carbon substituted YBCO [22]. It is a well known fact that carbon forms an essential constituent in bulk phases of (Cu,C)$Ba_2Ca_{n-1}Cu_nO_{2n+2\pm\delta}$ compounds. However if present in higher amounts, can deteriorate the superconducting properties as reported earlier [23, 24]. Therefore, it is advantageous to use minimum amount of carbon which can stabilize these phases. We will see later in this chapter that it indeed has an impact on the superconducting properties of (Cu,C)-1201 also. However due to a technical difficulty in controlling the CO_2 gas pressure in the sputtering chamber; we were not able to work at very low CO_2 gas pressures as reported by Wakamatsu *et. al*. [25]. In the present work, it was found that $1x10^{-3}$ Torr of CO_2 partial gas pressure can be controlled and is sufficient to stabilize this phase and therefore, has been fixed. Presence

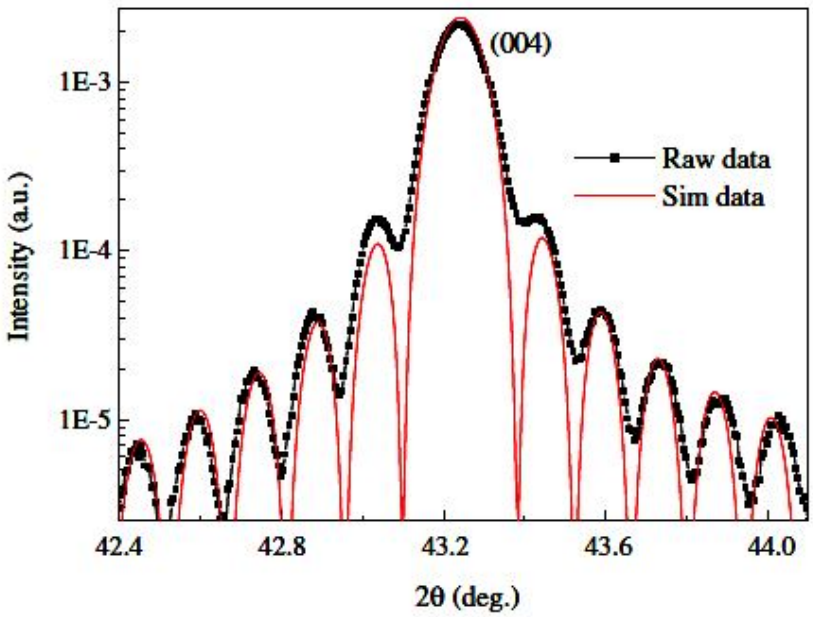

Figure 3.3. An enlarged view of the film peak obtained by slow and repeated scanning between a small range of 2θ values that include the (004) and (002) Bragg peaks of thin film and STO respectively. Laue fringes can be easily distinguished confirming the high quality crystallinity of the film. Thickness was calculated by matching the simulated data with the raw data.

of carbon in the form of CO_3^{2-} group was confirmed from IR spectra of (Cu,C) - 1201 thin film (figure 3.2). The peak at a wavenumber of 871 cm^{-1} represents out of plane bending mode of CO_3^{2-} group [26]. The infinte layered $BaCuO_2$ do not show any peak except the background. High quality epitaxial film with a *c*- axis lattice parameter of 8.3 Å was confirmed by the high resolution XRD pattern of (004) reflection with accompanying Laue oscillations (figure 3.3). Film thickness calculated by matching the experimental and simulated data was found to be around 80 nm which agreed well with the values obtained from cross-sectional FESEM images. Thickness of the film can also be calculated from the 2θ positions of oscillation fringes using the formula:

$$t = \frac{\lambda}{2\left|\sin\theta_0 - \sin\theta_{\pm 1}\right|}$$

where *t* is the thickness of the film, λ = 1.54 Å is the wavelength of X-ray, $2\theta_0$ is the angle of the central peak and $2\theta_{\pm 1}$ is the position of neighboring peaks nearest to the central peak.

The *c*- axis length corresponding to the (001) peak always varied between 7.83 Å and 8.4 Å. The main factors that we observed in our experiments are the substrate temperature and the O_2 gas partial pressure. It has been reported earlier that films grown under high CO_2 gas partial pressures usually have shorter *c*- axis lengths.. It was argued by Adachi *et. al.* that an increased intensity ratio between the (001) and (002) peaks of the film i.e. $\frac{I(001)}{I(002)}$ indicates a better CO_3 group ordering. [3]. Yamamoto *et. al.* [21] showed that a better ordering indeed takes places when the partial pressure of CO_2 gas

increases. It is also mentioned that at a fixed CO_2 partial gas pressures, the *c*- axis can be elongated and shortened by varying the substrate temperature during deposition [25] Figure 3.4 shows a comparison between the XRD patterns of films deposited on STO at 484 °C and 540 °C respectively. The O_2 partial gas pressure was $10x10^{-3}$ Torr and the CO_2 partial gas pressure was $1x10^{-3}$ Torr. The XRD pattern shows a peak shift from high values of 2θ to a low value of for the film deposited at higher temperature. The corresponding *c* lattice parameter of the film prepared at low substrate temperature is ~ 8.0 Å whereas that prepared at higher temperature shows a value of 8.3 Å. This agrees well with the above discussion and therefore it can be concluded that the *c*- axis expands with increasing substrate temperature. As we have discussed earlier that RSM using X-rays is an excellent reliable tool for performing non-destructive analysis of morphology

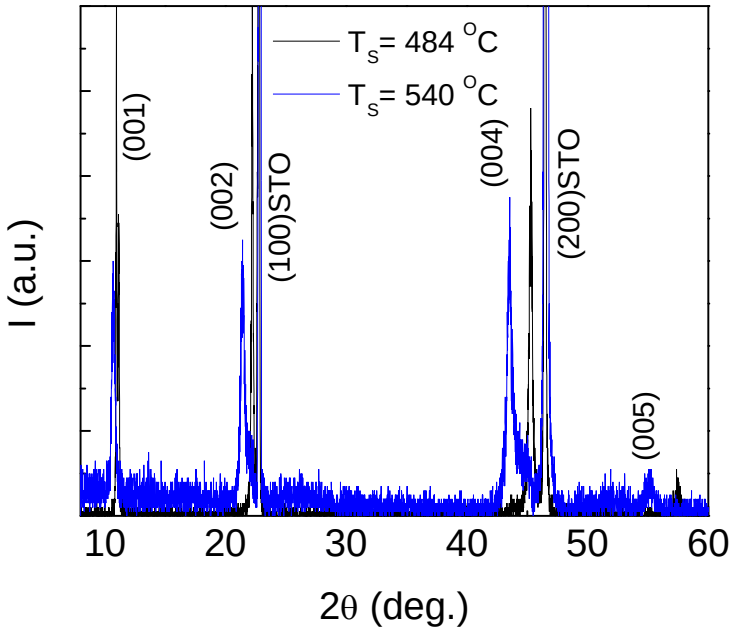

Figure 3.4. X-ray diffraction patterns of samples prepared at two different substrate temperatures. All peaks shift to lower 2θ angles for the (Cu,C)-1201 thin film prepared at higher temperature.

and structure of thin films. By comparing the shape and position of film and substrate reciprocal lattice points, we can get information regarding the strain, relaxation, mosaicity and lattice parameters of the film. Single crystalline STO substrate is oriented along the [*100*] direction while (Cu,C)-1201 grows along the [*001*] direction. Symmetrical scan about the (*100*) Bragg reflection will provide information on the crystal planes parallel to the substrate surface. Area scans in the reciprocal space about the general (*hkl*) reflections, known as asymmetric scan provides information about the planes inclined to the sample surface. If a film is strained, the film in-plane lattice matches exactly with that of the substrate, and the symmetric as well as asymmetric reciprocal lattice points lie vertically above each other. However for a fully relaxed film, the film and substrate reflection lie along a radial line originating from the centre of limiting sphere of radius (2/λ). Utilizing the above mentioned technique we calculated the *c* lattice parameter from the symmetric mapping around the *(l00)* reflection, while in plane lattice parameter was calculated from asymmetric RSM around the (310) reflection. Before performing the measurements, the substrate and the detector were aligned for the corresponding Bragg peak to be measured using a set of rocking curves (Δω), chi (χ) scan and detector (2θ) scans. For measuring the asymmetric reflections, azimuthal (φ) scan was performed for the best alignment of the selected peak. Figure 3.5 shows the symmetric scan of the film, prepared at T_s = 484 °C. By comparing the position of (002) reflection of film with that of the (100) reflection of STO, the out of plane lattice parameter is calculated to be 8.08 Å. As (Cu,C)-1201 shows a double-perovskite structure so its *c* lattice parameter can be given by the following formula:

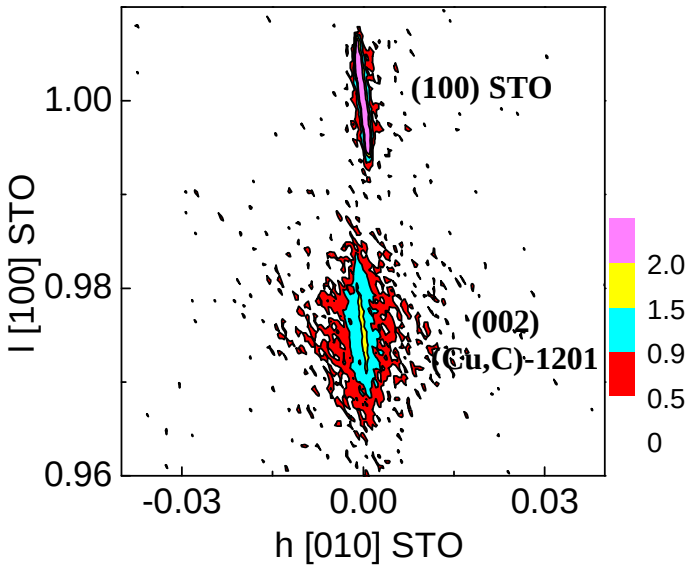

Figure 3.5. Symmetrical RSM around the (*100*) Bragg reflection of the substrate**.** The color bar is in log scale. The out of plane lattice parameter calculated from the RSM for the film is 8.08 Å. The film was synthesized at a substrate temperature of 484 °C. The intensities are in log-scale

.

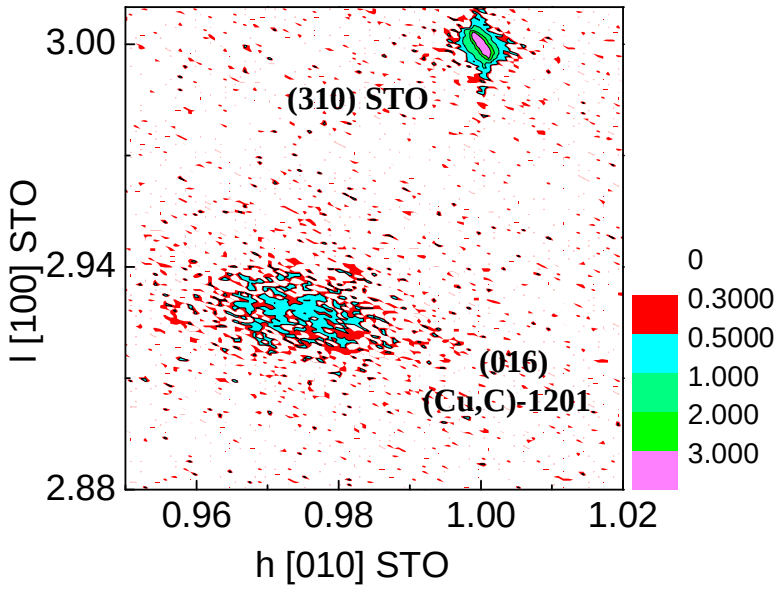

Figure 3.6. Asymmetrical RSM of (Cu,C)-1201 thin film prepared at T_s = 484 °C in semi-log scale. Film Bragg reflection point lie on the radial line joining the origin and (*310*) reflection of substrate. The in-plane lattice parameter is ~ 4.00 Å.

$$c(\,film) = \frac{2 \times c(STO)}{l(\,film)}$$

Here l(film) = 0.975 and c(STO) = 3.905 Å.

Lateral spread of film (*002*) reflection shows the inherent granularity in the film. Information about the in plane as well as out of plane lattice parameter of the film was calculated by comparing the asymmetric reciprocal lattice point of the film and the substrate. The detector was aligned for the (*310*) reflection of STO substrate. Other asymmetric reflections were not very clear due to low intensity. The position of (*016*) asymmetric reflection of the film gives information about the in plane lattice parameter (figure 3.6). As there is no doubling of the lattice along *a* or *b* (tetragonal symmetry) axes of the film, so using the formula:

$$b(\,film) = \frac{b(STO)}{h(\,film)}$$

in plane lattice parameter of the film was calculated to be 4.00 Å which is little higher than the 3.96 Å reported in literature. Here h(film) is 0.977. The out of plane lattice parameter was calculated to be equal to 7.99 Å which is almost equal to the value obtained from symmetrical scan. We also observe that the Bragg reflection points of both the film and the substrate lie on the radial line passing through the origin. Thus the film is relaxed. Figure 3.7 shows the symmetric RSM of the film prepared at T_s = 540 °C. The out of plane lattice parameter is calculated to be appx. 8.35 Å. As we can see the lateral spread earlier observed in relaxed film is lost here. This shows that the crystallinity of the film improved by increasing substrate temperature prior to deposition. In the asymmetric

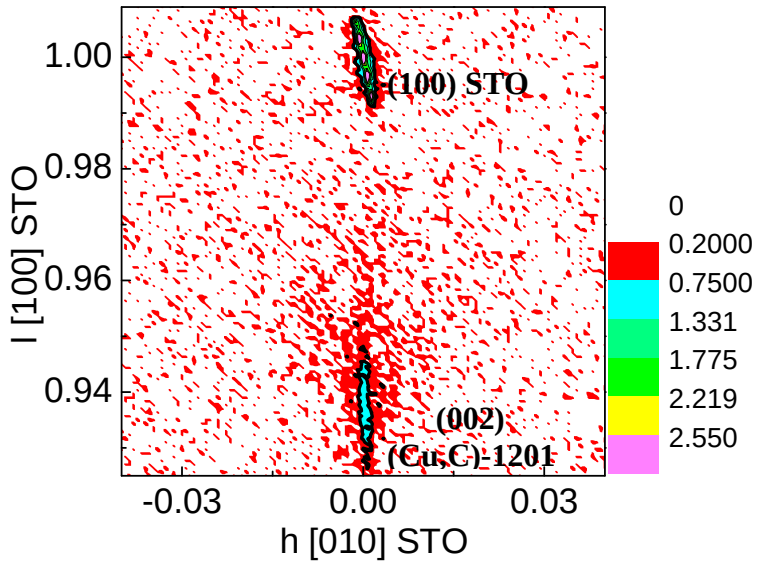

Figure 3.7. Symmetrical RSM of (Cu,C)-1201 thin film prepared at T_s = 540 °C. The out of plane lattice parameter is calculated as 8.35 Å. The narrow spread along [*010*] shows highly crystalline nature of the film. The iso-intensity regions are in log-scale

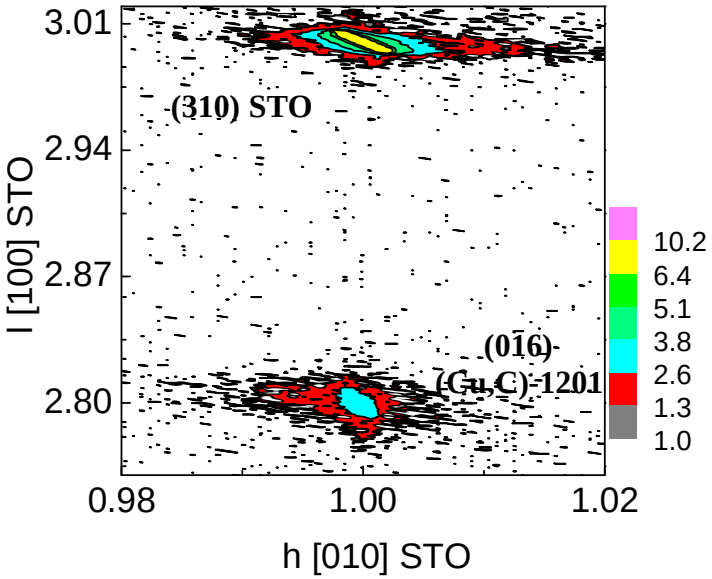

Figure 3.8. Asymmetrical RSM of (Cu,C)-1201 thin film prepared at T_s = 540°C. Substrate (*310*) reflection lies vertically above the film (*016*) reflection. The in-plane lattice parameter is 3.905 Å. Same colored regions are in log-scale.

RSM (figure 3.8), we observe that the substrate (*310*) reflection lies vertically above the film (*016*) reflection. As previously discussed, the film is completely strained and therefore the in-plane lattice parameter should equal to 3.90 Å (same as that of STO). The film is therefore experiencing an in plane compressive strain along the in-plane axis while the out of plane axis elongates simultaneously. The out of plane lattice parameter calculated is 8.36 Å. The epitaxial nature of the films was maintained throughout the temperature range for the deposition of thin films as observed in the pole figure of strained as well as relaxed thin films. Figures 3.9 (a) and (b) shows the in plane azimuthal (φ) scan of substrate and the strained film. Recurrence of peaks at an interval of 90° confirms the

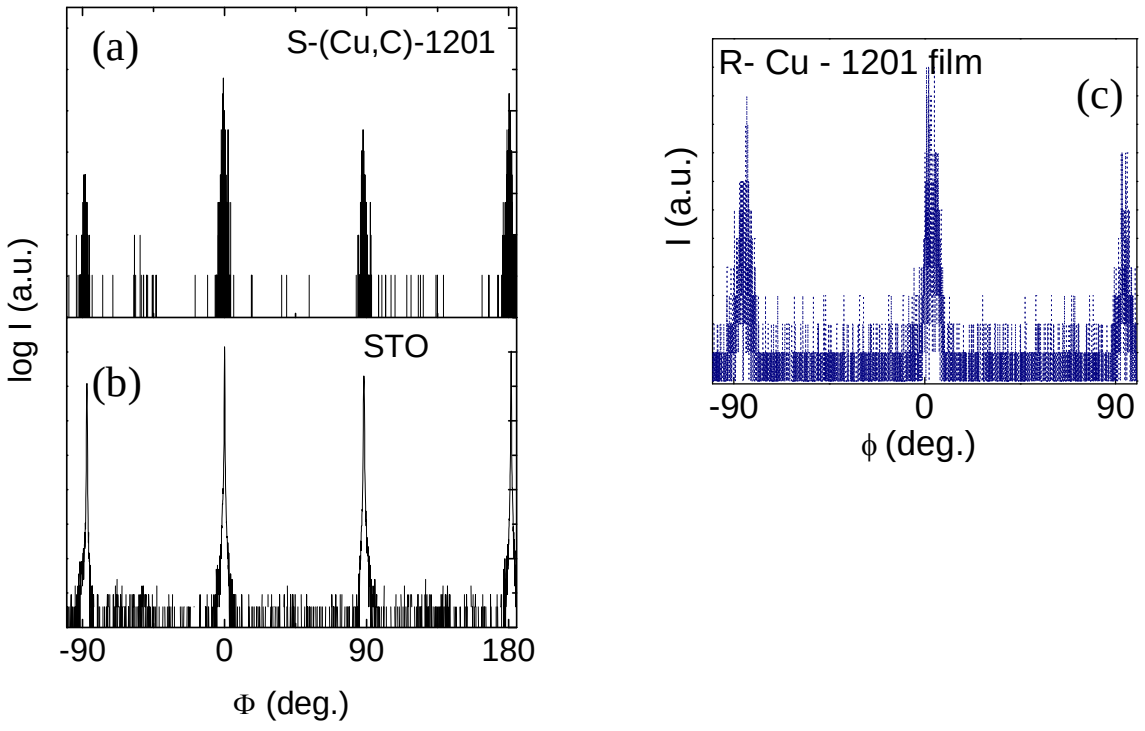

Figure 3.9. (a) shows the φ- scan of $SrTiO_3$ substrate about the (310) reflection. (b) and (c) shows the φ- scan of strained and the relaxed films deposited at 540 °C and 484 °C respectively.

four fold symmetry of the thin films. Absence of any other peak in the middle shows the presence of (*001*) oriented texture. The relaxed film in (c) also shows the same symmetry and texture. The stability of a completely relaxed or completely strained film requires very strict growth conditions. A small difference in the substrate temperature is sufficient to give the presence of both the phases in the film.

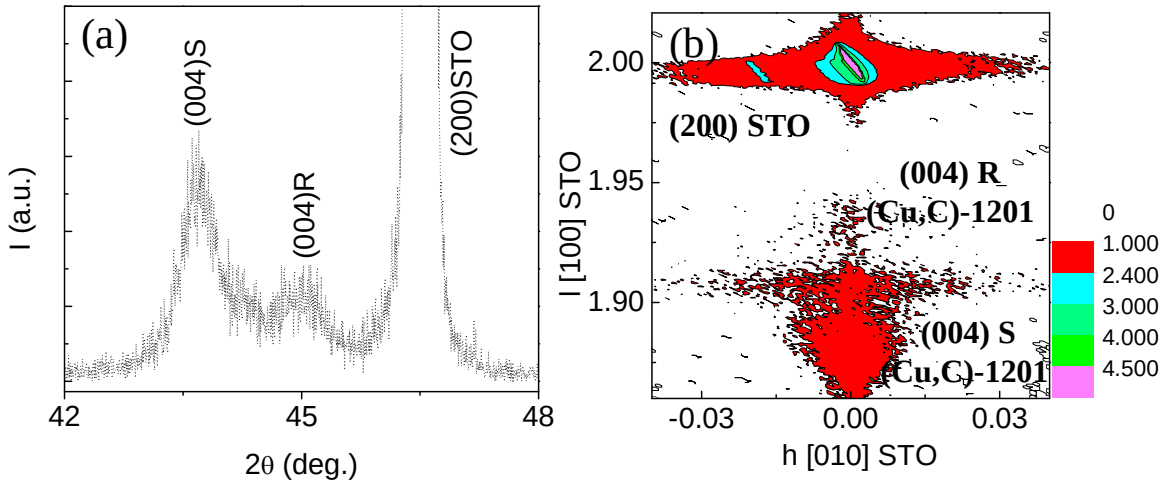

Figure 3.10. (a) shows the presence of both relaxed as well strained film around the (*200*) peak of SrTiO3 . The film was deposited at 504 °C. (b) shows the symmetric RSM. (*200*) reflection is selected to give a much better splitting the peaks.

Figure 3.10(a) shows the XRD pattern of the film where two peaks are present together for the film deposited at T_s = 504 °C. The splitting between the two peaks are clear in the RSM (figure 3.10(b)). So the temperature should be monitored properly in order to get a single phase. From here we conclude that strained films show much better crystallinity. Slight modification in the *c*- lattice parameter can also occur by the variation of oxygen gas partial pressure during the growth of the thin film. Crystallograhically these

variations may not be much important, however superconductivity is observed only in films having a very narrow range of *c* lattice parameters as mentioned earlier.

3.4.2 Transport

Figure 3.11(a) shows shift in the 2θ values of (001) peak of the (Cu,C)-1201 thin films deposited at various temperature. Resistivity versus temperature (ρ - *T*) plots of the corresponding films. The normal state resistivity decreases with increasing substrate temperature. The partial gas pressures for O_2 and CO_2 were $10x10^{-3}$ Torr and $1x10^{-3}$ Torr respectively. A general speculation about the decrease in resistivity may point towards the increasing *c* lattice parameter. It can also be due to the increasing crystallinity of the film. Once the desired lattice parameter was obtained, superconductivity was easily

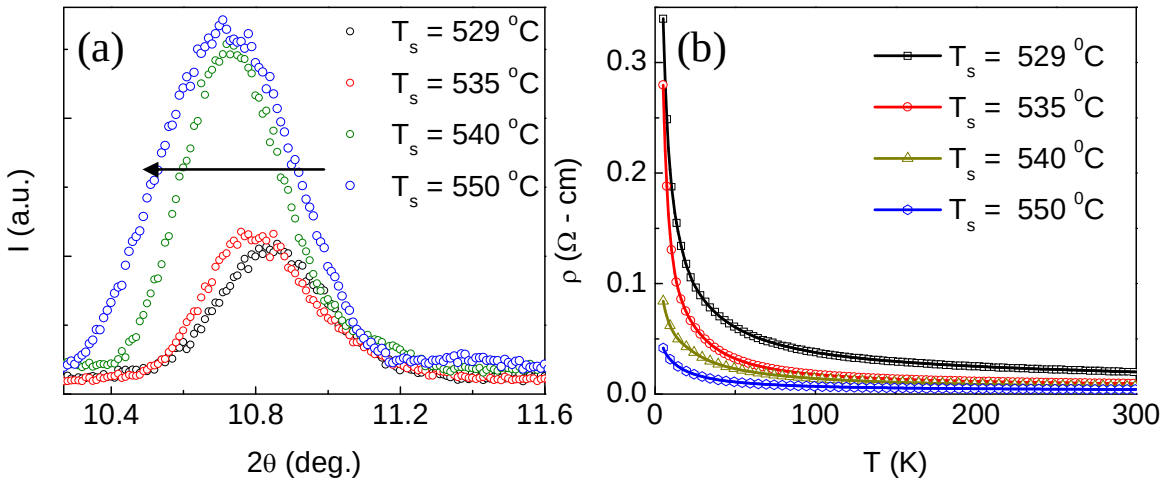

Figure 3.11. (a) Enlarged view of X-ray diffraction pattern showing the (001) peak of films prepared at various reaction temperatures with peaks shift to lower angles with increasing deposition temperature. (b) shows the ρ-T plots of the films associated with the films shown in (a).The normal state resistivity decreases with increasing substrate temperature.

induced in the films by decreasing the oxygen partial pressure as shown in figure 3.12 (a). The film was deposited at T_s = 540 °C. The film deposited under low oxygen pressure showed a superconducting transition at around 40 K. The transition width (ΔT_c = T_c (onset) - T_c (zero)) was ~ 15 K while normal state resistivity (ρ) showed a semiconducting behavior indicating carrier localization (figure 3.13(b)). A small increase in the growth temperature, induced semiconductor – metal transition in the

(a) *Oxygen partial pressure*	*'c' lattice parameter*
10x10^{-3} Torr	*8.269 Å*
7.5x10^{-3} Torr	*8.285 Å*
5.0x10^{-3} Torr	*8.308 Å*

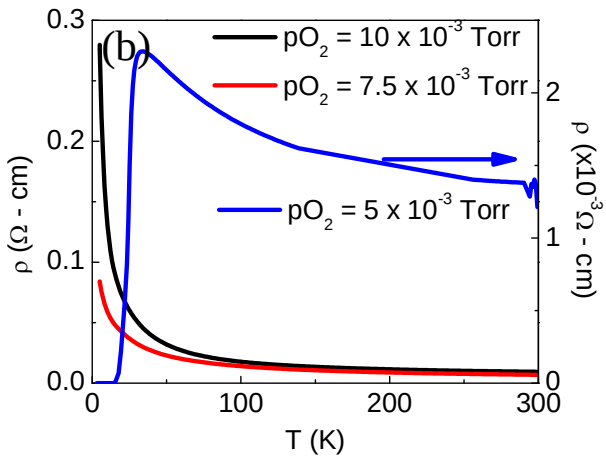

Figure 3.12. (a) tabulates the variations in the *c* lattice parameter corresponding to the films deposited under various O_2 partial pressures. The films were prepared around T_s = 540 °C under 1 mTorr CO_2 partial gas pressure. (b) is the ρ – T plots for the same films. A superconducting transition was observed for the film grown under 5 mTorr O_2 partial gas pressure.

normal state of the thin film. We also observed a very positive effect of the use of etched STO (ES) substrates as superconductivity was observed for *c*- axis lengths as low as 8.26 Å, however on un-etched substrates (NS), superconductivity was observed only between 8.29 Å – 8.33 Å. Figure 3.13(a) shows the comparison between the XRD patterns of thin films deposited on an un-etched and an etched substrate. The films were deposited at T_s =

545 °C with an oxygen partial pressure of $5x10^{-3}$ Torr. The Crystallinity of both the films are good as observed from the Laue oscillations in the (001) peaks of figure 3.13(a). Under the same growth conditions, film grown on ES showed an order of decrease in the normal state resistivity (figure 3.13(b)). It may be because of the single layer termination of the substrate which is desired for more homogeneous layer and interface properties. However we avoided using vicinal substrates as pits and precipitates were formed during the wet-etching process.

Most of the (Cu,C)-1201 thin films showed semiconducting behavior in the normal state. The resistivity curves shown in figure 3.11(b) showed a simple T^{α} dependence, where α varied between 0.6 to 0.9. However few films, as in figure 3.13(b) (for film grown on NS), showed a transition from non-metallic state to metallic state with positive ρ - T curvature in the normal state. It also shows a cusp just below 100 K before showing a superconducting transition.

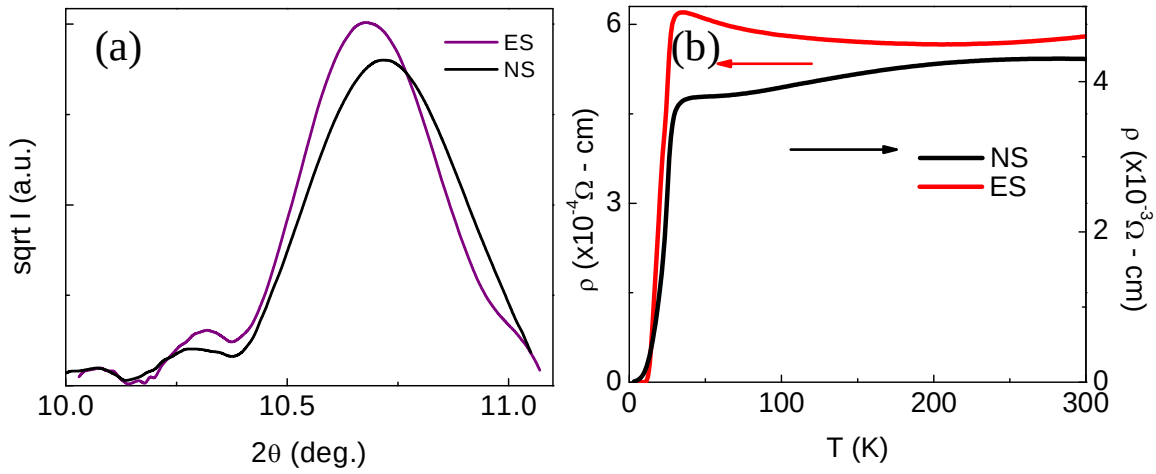

Figure 3.13. (a) X-ray diffraction patterns of samples prepared on etched (ES) as well as un-etched substrate (NS). (b) is the ρ-T plots of the corresponding films grown under same conditions. The normal state resistivity of film grown on ES is an order less than that grown on NS.

In figure 3.14, we observe a linear T dependence between 150 K – 300 K.

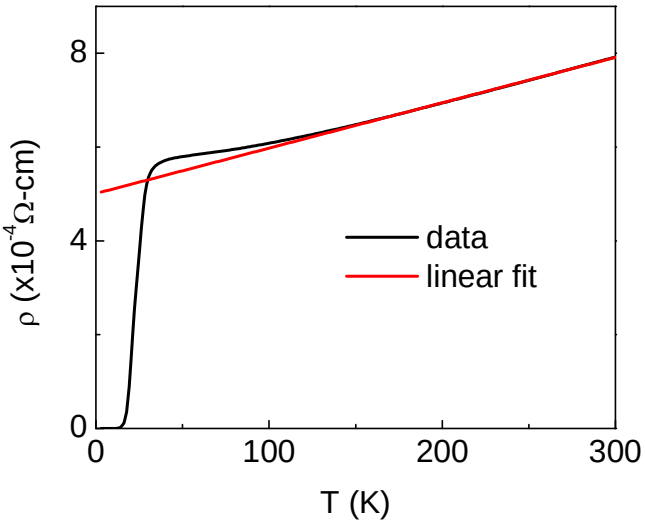

Figure 3.14. *ρ-T* plot of film prepared at T_s = 545 °C and 2.5 mTorr O_2 partial pressure with 1 mTorr CO_2 partial gas pressures.

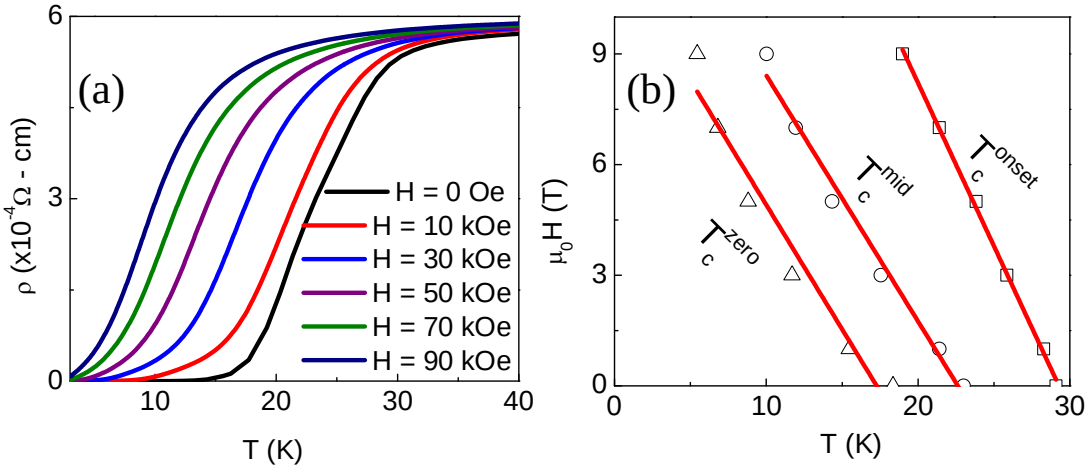

Figure 3.15. (a) shows the *ρ-T* plots at various applied magnetic fields. (b) shows the intial slopes of *H-T* diagram obtained from the magnetic field dependence of in-plane resistivity plots in (a) for 90% (onset), 50% (mid) and 10%(zero) drops in the resistivity from the value obtained at *T* = 50 K.

Difficulty in controlling the experimental parameters hindered with the systematic study of these thin films. Although substrate temperature played a very important role in the origin of superconductivity in these thin films, T_s beyond 560 °C introduced a double step superconducting transition. The upper critical field corresponding to 90% decrease in resistivity was calculated from the WHH (Werthamer-Helfand-Hohenberg) model [28]:

$$\mu_0 H_{C2}(0) = -0.69 T_c \left. \frac{d\mu_0 H_{c2}}{dT} \right|_{T_c}$$

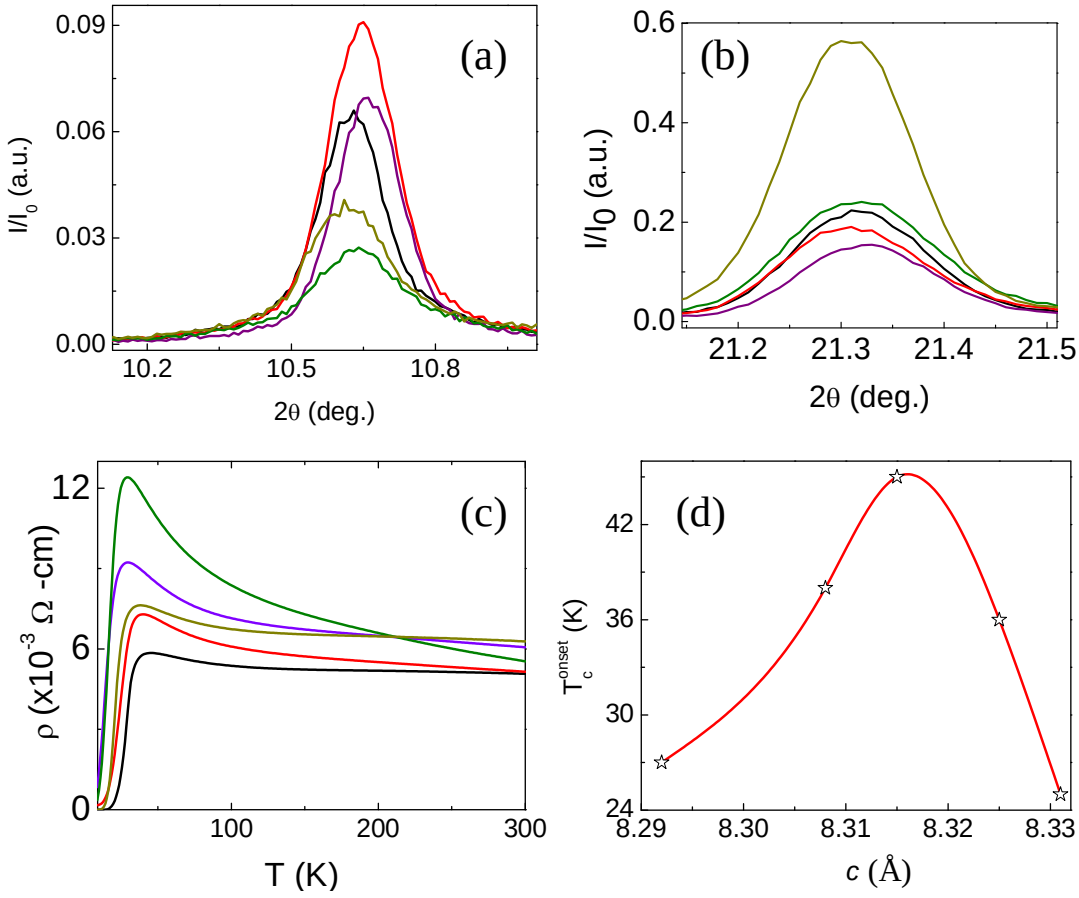

Figure 3.16. (a) shows a comparison between the intensities of the (001) peaks of (Cu,C)-1201 thin films deposited under various conditions. (b) shows the (002)peak intensities of the same Films. (c) In-plane ρ – T plots of these films show that normal state resistivity mainly depended upon the *c*-axis length irrespective of the intensity ratios of the (001) peak with respect to (002) peak. The highest T_c was observed for films having a *c*-axis length around 8.315 Å (d).

Figure 3.15(a) shows the temperature dependent resistivity below T_c at various magnetic fields and figure 3.15(b) is the *H-T* diagram. Using T_c^{onset} = 29 K and $\left.\frac{d\mu_0 H_{c2}}{dT}\right|_{T_c}$ (*onset*) = -0.88 T/K, we obtained the upper critical field in the dirty limit to be 17.6 T. The coherence length from this value was calculated to be ~ 4 Å using the formula:

$$\xi^2 = \frac{\phi_0}{2\pi\mu_0 H_{c2}(0)}$$

Although the above discussions on the dependence of superconductivity show some trend, however due to various experimental restrictions, the reproducibility of the same results was very difficult for the same deposition conditions. Figure 3.16 (a) and (b) shows normalized intensity ratios for (001) and (002) peaks. As discussed earlier a higher value of (001) peak with respect to (002) peak shows better ordering for the CO_3 group which in turn should deteriorate the superconduting properties. However in figure 3.16 (c) the resistivity seems to be mainly dependent upon the *c* lattice parameter irrespective of the intensity ratios. Proposed models and experimental observations indicate a statistical ordering of CO_3 group which may impede the probability of getting the same ordering of the group. We found a very consistent trend between the highest T_c^{onset} observed and the *c*- axis length. T_c^{onset} always showed a maxima (figure 3.16(b))for an out of plane lattice parameter of 8.315 Å which has also been observed by other groups [3, 21, 25].

3.4.3 AC susceptibility

Earlier in this chapter we assumed that a large (001) peak with respect to the (002) peak may indicate a higher amount of CO_3^{2-} group incorporation. However in the discussions

we were not able to relate the peak intensity with the transport properties as other factors like the *c* lattice parameter also played a prominent role. Resistivity measurement does not account for the whole sample as it is a one dimensional measurement probe. However magnetic measurements can give a clear a description of the whole sample volume. As the films are thin, ac susceptibility is a suitable for technique for studying the film diamagnetic response. We performed ac susceptibility measurements by applying 1 Oe ac field with varying frequency.

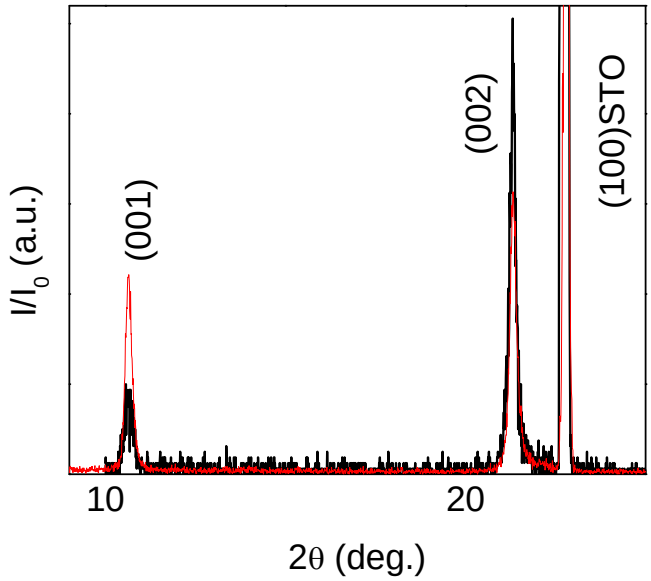

Figure 3.17. Normalized intensity ratio for the (001) and (002) peaks of the films prepared under same deposition conditions. The film with large (001) peaks indicate a much better CO_3 group ordering in the structure.

No dc field was applied. Figure 3.17 shows the normalized intensity ratios for films prepared at the same time under same conditions. The O_2 partial pressure was $5x10^{-3}$ Torr while the CO_2 gas pressure was $0.5x10^{-3}$ Torr. Films were deposited at a substrate

temperature of 550 °C. One of the films was glued at the centre of the heater whereas the other was kept beside it (a little away from the centre). XRD patterns of both the films do not show any peak shift that means their *c*-axis lengths are same.

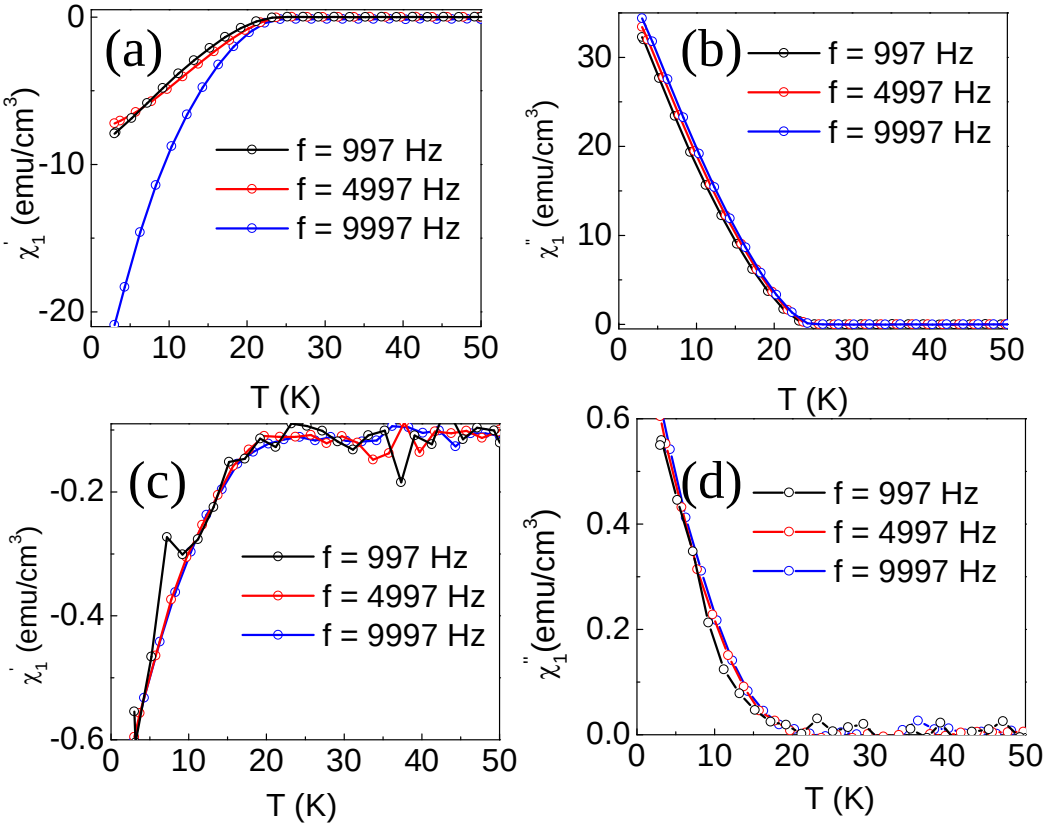

Figure 3.18. (a) shows the frequency dependence of $\chi_1^{'}$ for the film with small (001) peak. Whereas (b) shows the $\chi_1^{''}$ at various frequencies. (c) is the real part of ac susceptibility for the film having a large (001) peak and (d) corresponds to its imaginary part. (a) shows a much stronger diamagnetism as compared to (c). High values of imaginary component of susceptibility show strong dissipation in these thin films.

The film glued at the centre of the heater, however showed a low intensity (*001*) peak. Real part ($\chi_1^{'}$) of ac susceptibility for this film (figure 3.18 (a)) showed a much stronger diamagnetism as compared to the film with large (001) peak (figure 3.18(b)). It also

showed a higher T_c. If our assumption is correct then it may be concluded that carbon only helps in modulating the structure of infinite layered $BaCuO_2$ by doubling its *c* lattice parameter. Onset of diamagnetism in superconductors usually indicates the zero resistive state of superconductors. Thus we also find that T_c (zero) increases for films deposited under low CO_2 partial gas pressure. As CO_3^{2-} acts as a "poison" for cuprate superconductors, therefore a very little amount is needed to stabilize the (Cu,C)-1201 thin films. Another remarkable observation in the ac susceptibility is the high value of $\chi_1^{''}$ (imaginary part of susceptibility) with respect to $\chi_1^{'}$. High $\chi_1^{''}$ denotes high dissipation, (figures 3.18(a) and (b)), however it's magnitude usually do not overcome the value of $\chi_1^{'}$.

$MBa_2Ca_{n-1}Cu_nO_{2n+2+\delta}$ (where M = Tl, Hg, (Cu,C)) forms the general formula for most of the HTSCs and represents the basic layered structure in terms of charge layer block (CR) and the IL block (mainly represented by $CaCuO_2$). Depending upon the number (n) of $CaCuO_2$ layers, a family of layered superconducting structures can be derived and can be separated out in the form of two sub-units:

$$MBa_2Ca_{n-1}Cu_nO_{2n+2+\delta} = MBa_2CuO_{4+\delta} + (n-1)CaCuO_2$$

$MBa_2CuO_{4+\delta}$ or M -1201 correspond to the CR block and for n = 1, forms the first member of the whole series. Though the cations in all the three above mentioned families are arranged in a similar fashion, they do differ in oxygen arrangement. The oxygen site in $TlBa_2CuO_{4+\delta}$ (δ = 1) or Tl-1201 in the Tl-O rock salt layer is fully occupied whereas the Hg-O layer is mostly empty in $HgBa_2CuO_{4+\delta}$ (Hg-1201) [29]. The formal valence of

Cu in $TlBa_2CuO_y$ is +3 which implies that it is overcompensated with holes. When annealed in reduced environment, superconductivity is induced in the structure with a T_c (zero) of 9.5 K [30]. Doping the compound with Sr increases the T_c (zero) to 33 K. The cell parameters of superconducting $TlBa_2CuO_{4+\delta}$ or equivalently $TlBa_2CuO_{5-\delta}$ have a lattice parameter: a = 3.86 Å and c = 9.26 Å whereas that of overcompensated $TlBa_2CuO_{5+\delta}$ have a = 3.86 Å and c = 9.56 Å [30]. Thus an increase in oxygen content leads to increase in the c lattice parameter. Hg-1201 on the other hand, is oxygen depleted and shows superconductivity at around 94 K. The lattice parameters are: a = 3.87 Å and c = 9.5 Å respectively [31]. (Cu, C)-1201 also shows superconductivity with a T_c (onset) as high as 60 K and a T_c (zero) at 40 K. However the structure of the compound is completely different from that of Tl-1201 and Hg-1201. Structural analysis through neutron diffraction in (Cu,C)-1234 identifies three non-equivalent oxygen sites of structural importance in the charge reservoir block (formed by (Cu,C)-1201) of this compound [32].

Presence of Ba in the structural unit of charge reservoir, presents a unique reorganization of oxygen atoms (due to large size of Ba ion) giving rise to two non-equivalent Cu-sites in (Cu,C)$Ba_2CuO_{4+\delta}$ or (Cu,C)-1201. One of the Cu sites (Cu2) belong to the CuO_2 planes where superconductivity is observed (figure 3.19). The other Cu (Cu1) assembles along with two non-equivalent oxygen ions (O1 and O2 in figure 19) to form the charge reservoir. Cu1 has chain like oxygen arrangement and resembles CuO_4 square planar chains in YBCO. Some of these CuO_4 planes are partially substituted

by CO_3 group where two of the oxygen atoms of carbon occupy the apical positions (O3) of CuO_6 octahedral consisting the superconducting CuO_2 planes. Small size of CO_3 group (C-O3 bond length is 1.23 Å as compared to the bond length of 1.80 Å for Cu1-O1) gives rise to variation in the apical Cu-O distances for the octahedral CuO_6 units. So there are two Cu2-O (1 and 3) bond lengths, one is 2.39 Å and another is 3.18 Å [32, 33]. In YBCO, the Cu present in the plane has a bond length between 2.30-2.46 Å with its apical oxygen. The Cu and apical oxygen bond length of CuO_6 octahedra is 2.41 Å in $La_2CuO_{4+\delta}$ [34]. A longer bond length between the apical oxygen (O3) and Cu2 in CuO_6 may make the bond weak and more prone to breaking and rearrangement.

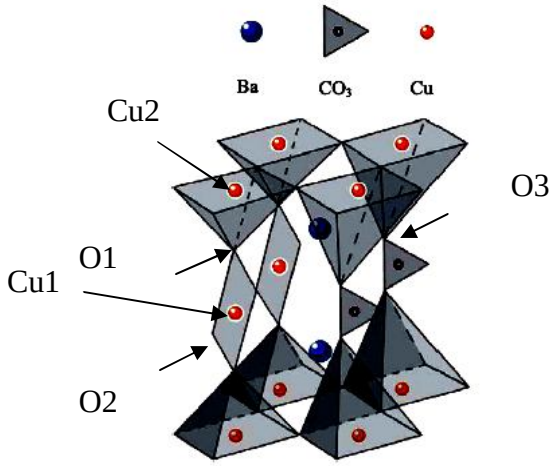

Figure 3.19. Proposed structure of $(Cu_{0.5},C_{0.5})Ba_2CuO_{4+\delta}$ superconductor taken from *Supercond. Sci. Technol.* **20** (2007) S455

It has also been found that the incorporation of CO_3 group in the structure is rather stochastic and its site is mainly dominated by CuO_4 chains. If we consider the CuO_4 chains to be similar to those in YBCO, then (Cu,C)-1201 can be considered to be in the over-doped state [35] when most of the CO_3 sites are occupied by CuO_4 group.

Thus introduction of CO_3 group could help in the following ways:

- Stabilize a modulated structure.
- Bond length variations in the chain and CuO_6 octahedra.
- Optimizing the generation of charge carriers in the CuO_4 chains.

Now the general features of the (Cu,C)-1201 thin films as revealed in our study are as follows:

- Superconductivity is observed in films with *c* lattice parameters ranging between 8.25 Å – 8.33 Å. However the *c*-axis lengths varied between 7.8 Å and 8.4 Å.
- Films which showed the above mentioned *c* lattice parameter were under compressive strain. Whereas the films which were relaxed had an out of plane lattice parameter less than 8 Å.
- Films deposited under less oxygen pressure but later cooled in 1 atm. oxygen pressure showed much better normal state properties.
- Superconducting transition temperature as well as superconducting volume fraction improved with decrease in the carbon content.

The extreme flexibility of the structure due to weakness of the Cu1- O3 bond may be the reason behind variations in the *c*-axis length of (Cu,C)-1201. Increasing substrate temperature may lead to vacancies at CO_3 site, which require apical oxygen rearrangement and ordering. The reordering is done by the substitution of CuO_4 square planes at CO_3 site. And thus there is an elongation along the *c*- axis length which in turn

is compensated by *a*- axis compression. A balanced number of CO_3 and CuO_4 chains can lead to superconductivity. However complete removal of CO_3 leads to overdoped state where (Cu,C)-1201 behaves as an insulator (not metallic) [33]. Therefore at different CO_3 concentration, (Cu,C)-1201 can act as a charge reservoir and a superconductor. There is also a possibility of incorporation of oxygen atoms in the interstitial positions of the two Ba-O layers that can further lead to the optimization of *c*-axis length similar to $La_2CuO_{4+\delta}$ [36]. The control of charge generation and transfer mechanism in these structures are not very obvious as in $La_2CuO_{4+\delta}$, however it should be similar to that in YBCO. Superconductivity in $La_2CuO_{4+\delta}$ with excess oxygen, arises due to elongation of the CuO_6 octahedra along the *c*- direction that are mainly influenced by the repulsion caused by interstitial oxygen. The structural change results in a variation of the overall charge distribution leading to hole doping [36, 37]. In-plane lattice compression in epitaxial thin films introduces the same structural change. As discussed in the introduction, appearance of superconductivity associated with compressed in-plane axis in (Cu,C)-1201 is similar to that observed in $La_2CuO_{4+\delta}$, the mechanism seems to be different. Here the primary cause seems to be the presence of weak bonds and rearrangement of oxygen atoms in (Cu,C)-1201 films deposited at higher substrate temperature. Change in bond-lengths and distortions in the local crystal structure may be a secondary cause that is mostly affected by the prime source. Since superconductivity takes place in the CuO_2 planes, changes in the in-plane bond length which is a measure of hybridization between $Cu3d_{x2-y2}$ and $O2p_{x,y}$ orbitals as well as of super-exchange coupling between neighboring Cu spin in the planes, will correlate with the superconducting parameter. Charge reservoir layers

influence the in-plane electronic parameters of CuO_2 planes through apical oxygen. It is found from the band calculation that the distance of apical oxygen has a substantial effect on the second nearest hopping integral t' between nearest Cu-Cu atoms in the CuO_2 plane and t' has a correlation with the maximum T_c of each cuprate material [38]. The LDA band calculation along with calculation of Madelung potential difference between apical and planar oxygen sites find a general trend that T_c becomes higher as $|t'|$ becomes larger or as the apical oxygen distance becomes longer [38,39]. Figure 3.20 (a) shows the variation of T_c of hole doped superconducting compounds containing single CuO_2 plane with distance between the apical oxygen and in-plane copper. Figure 3.20 (b) shows the variation of T_c of the same compounds with in-plane distance between copper and oxygen.

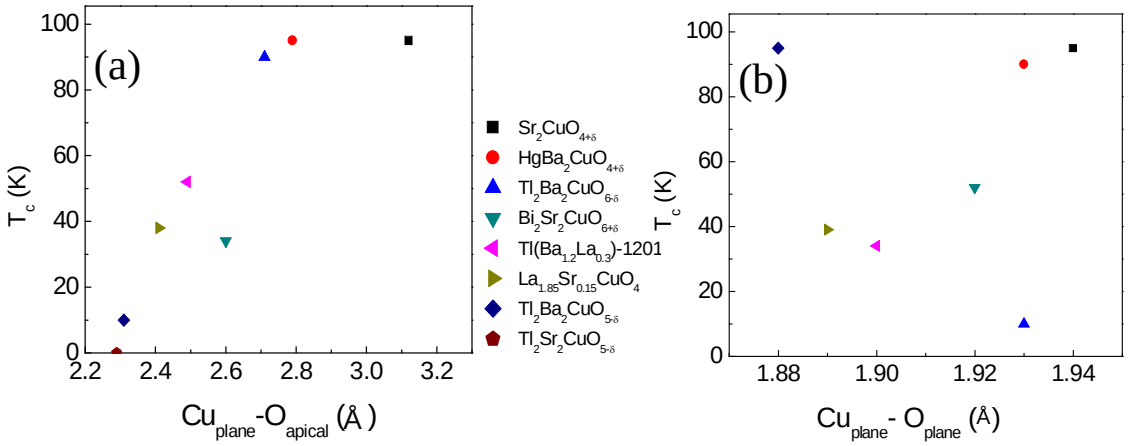

Figure 3.20. (a) shows the bond length between the planar Cu and apical oxygen in cuprate superconductors with single CuO_2 planes. We observe that a large value of the bond length corresponds to a higher T_c. (b) shows the planar Cu and planar oxygen in the CuO_2 planes of the same copper oxide superconductors. The in-plane and out of plane lattice parameters of (Cu,C)-1201 resembles that of $La_{1.85}Sr_{0.15}CuO_4$.

3.5 Conclusions

Incorporation of carbon in the form of CO_3 group doubles the c- axis length of $BaCuO_2$ to give a modulated structure represented by (Cu,C)$Ba_2CuO_{4+\delta}$ or (Cu,C)-1201 which forms the first member of the series: (Cu,C)$Ba_2Ca_{n-1}Cu_nO_{2n+2+\delta}$. The ability of (Cu,C)-1201 thin films to get tuned from an optimally doped superconductor to an overdoped non-superconductor highly depends upon the CO_3 amount in the film and the deposition temperature. Increasing substrate temperature drives the completely relaxed (Cu,C)-1201 thin film to a strained film experiencing a compressed in-plane axis. The out-of-plane axis expands simultaneously with the contracting in-plane axis. Superconductivity is observed only in strained films which are deposited at higher substrate temperature. Elongation along the *c*- axis helps in modulating the local structure near the apical oxygen position, thus helping in achieving superconductivity.

The planar Cu-O bond length (1.95 Å) in strained (Cu,C)-1201 is almost similar to the bond lengths in other Hole doped cuprate superconductors with single CuO_2 layer. Appearance of superconductivity under compressive strain, arise the possibility of further increase in T_c. It would be rather interesting to study the substrate temperature effects in trilayers with the following sequence: STO/(Cu,C)-1201/$CaCuO_2$/(Cu,C)-1201. The terminating (Cu,C)-1201 may further experience more in-plane lattice contraction due to the underlying $CaCuO_2$ layer with in-plane lattice parameter varying between 3.86 and 3.88 Å. Thus we may observe further increase in the T_c [40].

3.6 References

1. D. P. Norton, B. C. Chakaoumakos, J. D. Budai, D. H. Lowndes, B. C. Sales, J. R. Thompson and D. K. Christen, *Science* **265** (1994) 2074.
2. J. L. Allen, B. Mercey, W. Prellier, J. F. Hamet, M. Hervieu and B. Raveau, *Physica C* 241 (1995) 158.
3. H. Adachi, M. Sakai, T. Satoh and K. Setsune, *Physica C* 244 (1995) 282.
4. E. Koller, L. Fábrega, J.-M. Triscone, M. Decroux and Ø. Fischer, *J. Low Temp. Phys.* **105** (1996) 1325.
5. T. Kawashima, Y. Matsui, E. Takayama-Muromachi, *Physica C* **224** (1994) 69.
6. J. –S. Zhou, J. B. Goodenough, H. Sato and M. Naito, *Phys. Rev. B* **59 (1999) 3827.**
7. I. Bozovic, G. Logvenov, I. Belca, B. Narimbetov and I. Sveklo, *Phys. Rev. Lett.* **89** (2002) 107001.
8. F. Hardy, N. J. Hillier, C. Meingast, D. Colson, Y. Li, N. Barišić, G. Yu, X. Zhao, M. Greven and J. S. Schilling, *Phys. Rev. Lett* **105** (2010) 167002.
9. H. Sato, M. Naito and H. Yamamoto, *Physica C* **280 (1997)** 178
10. J. -P. Locquet, J. Perret, J. Fompeyrine and E. Machler, *Nature* 394 (1998) 453.
11. Weidong Si and X. X. Xi, *Appl. Phys. Lett.* 78 (2001) 240.
12. J. P. Locquet, J. Perret, J. W. Seo and J. Fompeyrine, *Proc. SPIE* **3481** (1998) 248.
13. H. Sato, T. Tsukada, M. Naito and A. Matsuda, *Phys. Rev. B* **61** (2000) 12447.

14. J. M. Tranquada, B. J. Sternlieb, J. D. Axe, Y. Nakamura and S. Uchida, *Nature* **375** (1995) 571.
15. J. D. Jorgensen, B. Dabrowski, S. Pei, D. G. Hinks, L. Soderholm, B. Morosin, J. E. Schirber, E. L. Venturini, and D. S. Ginley, *Phys. Rev. B* **38 (1988)** 11337.
16. J. He, R. F. Klie, G. Logvenov, I. Bozovic and Y. Zhu, *J. Appl. Phys.***101** (2007) 073906.
17. T. Yamamoto, K. Kikunaga, M. Mitsunaga, K. Obara, T. Okuda, N. Kikuchi, Y. Tanaka, K. Tokiwa, T. Watanabe and N. Terada, *J. Phys.: Conf. Ser.* **150 (2009)** 052286.
18. M. Kawasaki, K. Takahashi, T. Maeda, R. Tsuchiya, M. Shinohada, O.Ishiyama, T. Yonezawa, M. Yoshimoto, and H. Koinuma, *Science* **266** (1994) 1540.
19. G. Koster, B. L. Kropman, G. J. H. M. Rijnders, D. H. A. Blank, and H. Rogalla, Appl. Phys. Lett. **73** (1998) 2920.
20. G. Balestrino, S. Martellucci, P. G. Medaglia, A. Paoletti, G and Petrocelli, *Physica C* **302** (1998) 78.
21. T. Yamamoto *et. al., Supercond. Sci. Technol.* **20** (2007) S461.
22. A. Yamamoto, K. Hirose, Y. Itoh, T. Kakeshita and S. Tajima, *Physica C* **421** (2005) 1.
23. Y. Masuda, R. Ogawa, Y. Kawate, K. Matsubara, T. Tateishi, S. Sakka, *J. Mater. Res.* **8** (1993) 696.
24. M. Uehara, M. Uoshima, S. Ishiyama, H. Nakata, J. Akimitsu, Y. Matsui, T. Arima, Y. Tokura, N. Mori, *Physica C* **229** (1994) 310.

25. H. Wakamatsu *et. al. J. Phys.Conf. Series* **43** (2006) 289.
26. K. Nakamoto, *Infrared and Raman spectra of Inorganic and co-ordination compounds* (Wiley-Interscience, New York, 1986).
27. T. Timusk and B. Statt, *Rep. Prog. Phys.* **62** (1999) 61.
28. N. Werthamer, E. Helfand, and P. Hohenberg, *Physical Review* **147** (1966) 295.
29. B. Bandopadhyay, J. B. Mandal and B. Ghosh, *Physica C* **298** (1998) 95.
30. I. K. Gopalakrishnan, J. V. Yakhmi and R. M. Iyer, *Physica C* **175** (1991) 183.
31. S. N. Putilin, E. V. Antipov, O. Chmaissem and M. Marezio, *Nature* **362** (1993) 226.
32. Y. Shimakawa *et. al*, *Phys. Rev. B* **50** (1994) 16008.
33. M. N. Iliev, H.-G. Lee, A. P. Litvinchuk, Z. L. Du, Y. S. Wang and C. W.Chu, *Phys. Rev. B* **59** (1999) 9611.
34. R. J. Cava, A. Santro, D. W. Johnson, W. W. Rhodes, *Phys. Rev. B* **35** (1987) 6716.
35. K. Kikunaga *et. al. Supercond. Sci. Technol.* **20** (2007) S455.
36. R. A. Fisher, J. E. Gordon, and N. E. Phillips, *Ann. Rev. Phys. Chem*. **47** (1996) 283.
37. K. H. Lee and R. Hoffmann, *J. Phys. Chem. A* **110** (2006) 609.
38. E. Pavirini *et.al.*, *Phys. Rev. Lett.* **87** (2001) 047003.
39. Y. Ohta *et. al.*, *Phys. Rev. B* **43** (1991) 2968.
40. T. Yamamoto *et. al., Physica C* **470** (2010) S71.

Chapter 4

Preparation and characterization of superconducting $(Cu,C)Ba_2Ca_{n-1}Cu_nO_{2n+2\pm\delta}$ superlattices with n = 2 and 3.

karmanyevaadhikaaraste maa phaleshu kadaachana |
maa karmaphalaheturbhuu maatesangotsvakarmani ||

A person has the right towards action alone and not towards the fruit of action. Let not the fruit of action be the motive for acting. Also, let there not be any attachment to inaction.

- Bhagwad Gita

Summary

By exploiting thin film deposition technique, we have fabricated higher members (*n* = 2, 3) of the superconducting family represented by general formula: $(Cu,C)Ba_2Ca_{n-1}Cu_nO_{2n+2\pm\delta}$ using a multitarget *rf* magnetron sputtering system. We have shown that members of the series with n = 2 and 3 (containing 1 unit cell of (Cu,C)-1201 and 1 or 2 unit cells of $CaCuO_2$) can be prepared by controlling the thickness of (Cu,C)-1201 and $CaCuO_2$ upto 1 unit cell using sputter deposition. Our main aim was to tune the amount of charge carriers in the CuO_2 planes to obtain superlattices with high temperature superconducting transition temperature, we were successful only in getting a T_c of 10 K in (Cu,C)-1212 and no superconductivity was observed in (Cu,C)-1223. But, presence of sharp peaks in XRD pattern showed high quality crystallinity in the superlattice.

4.1. Introduction:

Multilayered superconducting cuprates are remarkable for their exceptionally high critical temperature (T_c) and forms the backbone of ongoing research to realize and understand the underlying microscopic mechanism to achieve room temperature superconductor. The electronic aspects in these layered superconductors are very much influenced by the arrangement of atoms in their unit cell especially the interplay among the Cu–O bond lengths, the cation sizes, and the Cu valence may affect the hole-doping level of the CuO_2 plane [1]. As discussed in previous chapter, the two main sub-units of a cuprate superconductor are the charge reservoir (CR) block and the CuO_2 planes. For a particular type of CR, the number ('*n*') of CuO_2 can be varied to achieve a hierarchy of a superconducting family [1]. It has been found that for most of the superconducting

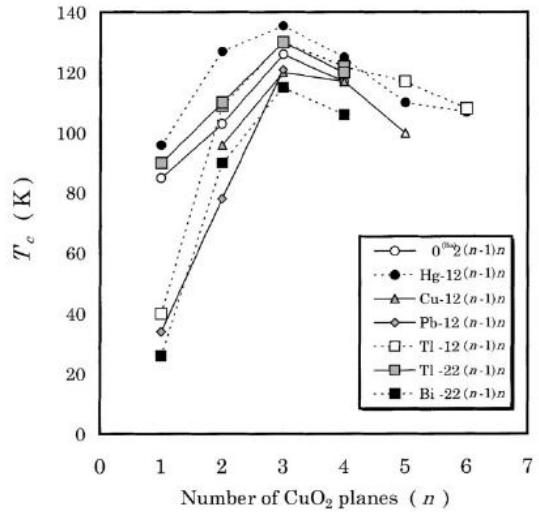

Figure 4.1. Superconducting transition temperature, T_c, versus number of stacked CuO_2 planes, *n*, for various homologous series. The n = 3 member of each homologous series most likely has the highest T_c.

families, the highest T_c is found for n = 2 or 3 and then decreases with further increase of 'n' (figure 4.1). The main reason for such a trend may be the inhomogeneous distribution of charge carriers among the CuO_2 planes. For superconducting materials with n = 3, there exist two different CuO_2 layers which are characterized by different coordination number of Cu with surrounding oxygen ions. There are two pyramidal CuO_5 units whose apical oxygen connects the Cu to the charge reservoir layer and these units are called outer planes (OP). The other one is CuO_2 square oxygen network which is sandwiched between the OP and is termed inner planes (IP) [2]. The outer-planes have been found to be slightly overdoped while the inner planes are found to be optimally or under-doped. The over-doping may be caused by the increased co-ordination of Cu in the OP as compared to the four oxygen co-ordinated Cu in the inner planes. It is rather remarkable to note that T_c remain high even in presence of overdoped region of these multilayered materials [2]. The non-equivalent CuO_2 planes often show different competing phases in multi-layered cuprate superconductors. For e.g. coexistence of electron and hole like band in the Fermi surface mapping of $Ba_2Ca_3Cu_4O_8F_2$ superconductor. Similarly coexistence of antiferromagnetism and superconductivity has been observed in the NMR and μSR studies of $HgBa_2Ca_4Cu_5O_y$. In $(Cu,C)Ba_2Ca_3Cu_4O_y$ ((Cu,C)-1234), analysis of Knight shift and the nuclear spin-lattice relaxation rate ($1/T_1$) of ^{63}Cu suggest that the IP keeps high value of T_c by remaining nearly optimally doped while the OP is predominantly overdoped [3]. (Cu,C)-1234 is the third member (n = 3) of superconducting family described by the general formula: $(Cu,C)Ba_2Ca_{n-1}Cu_nO_{2n+2\pm\delta}$,

(where n is the number of CuO_2 planes per unit cell). These materials are not only interesting because of their high T_c (>116 K) but also important since they exhibit many interesting physics [4–6]. Further they do not have any toxic elements and are iso-structural with single Tl- and Hg-layer based multilayer materials having tetragonal structure with the space group P4/mmm. The chemical formula of the first member of this series (n = 1) is $(Cu,C)Ba_2CuO_{4\pm\delta}$ ((Cu,C)-1201) and shows a T_c between 8 K – 20 K. The detailed study of this compound has already been discussed in the previous chapter. The higher members can be considered as an intergrowth of (Cu,C)-1201, which acts as charge reservoir layer, and the infinite layer (IL) $CaCuO_2$. In the case of n = 2, which is formed from one unit of each (Cu,C)-1201 and $CaCuO_2$, the structure is analogous to $YBa_2Cu_3O_{7-\delta}$ except that some of the Cu O chains are replaced in the present case by carbonate group and Y^{3+} is replaced by Ca^{2+} ion. In this system, copper in the superconducting CuO_2 planes has pyramidal coordination with oxygen neighbors. Electronic band structure calculations suggest that $(Cu,C)\text{-}Ba_2Ca_{n-1}Cu_nO_{2n+2\pm\delta}$ can be considered as multiband superconductor [7]. Due to different carrier concentration in IP and OP and weak interband interaction there are indication for inherent lower T_c of OP that can not be seen in other conventional multiband superconductors. Moreover, weak interband interactions could result in the formation of phase dislocation in the quantum condensation or interband phase difference soliton [8–11]. These interesting properties and the nontoxic nature of these multilayer cuprates are very promising. However, unlike other multilayer cuprates these materials require high pressure to stabilize the phase [4–6].

We thought that it would be interesting from both fundamental and application point of view to fabricate thin films of such multilayer cuprates. There are few reports on the preparation of the first member (n = 1, 2) of the series (Cu,C)$Ba_2Ca_{n-1}Cu_nO_{2n+2\pm\delta}$ using rf-magnetron sputtering and pulsed laser ablation (PLA) techniques using a ceramic target [12–16]. It requires stringent growth conditions and therefore only few groups have succeeded in achieving superconductivity [12–15]. The higher members (n = 3) have not been reported by the conventional thin film fabrication technique i.e. using a single target with the composition (Cu,C)$Ba_2Ca_2Cu_3O_y$. An artificial superlattice method, involving deposition of charge reservoir layer BaCuO2 or (Cu, C)-1201 and CaCuO2 layers alternatively, was applied to grow thin films of such higher members using PLA and Molecular Beam Epitaxy techniques [17–22]. However, the maximum T_c was observed to be around 80 K. The low T_c has been attributed to a possible disorder among the layers [23]. By adapting the superlattice method, our goal is to achieve higher members with T_c higher than 100 K using *rf* magnetron sputtering. The advantage of this technique is, one can prepare large area films with growth rate obtained between Molecular Beam Epitaxy and Pulsed Laser Deposition.

4.2. Scope of present investigation

The goal of the present study is a first step towards the realization of control and preparation of higher members of the superconducting family with structural formula

(Cu,C)$Ba_2Ca_{n-1}Cu_nO_{2n+2\pm\delta}$ where *n = 2, 3* and so on. The preparation technique involved here uses a multitarget sputtering system which can be programmed to make superlattices

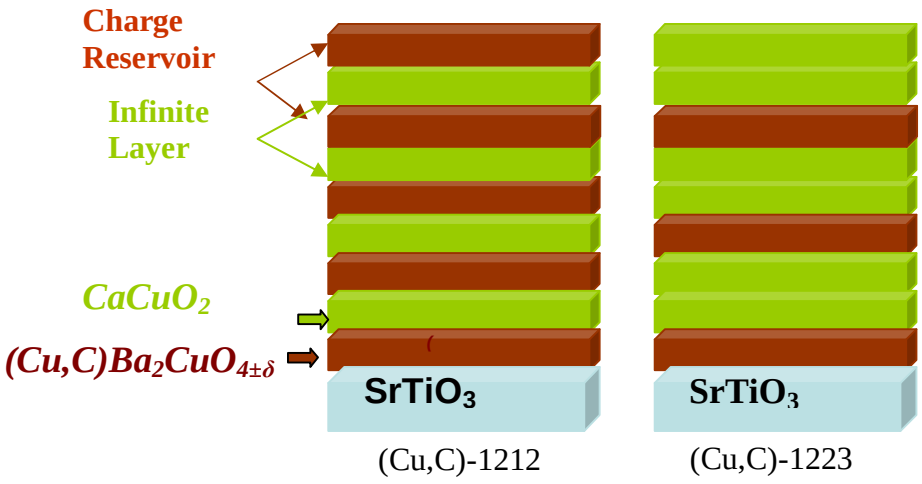

Figure 4.2. Deposition sequence of (Cu,C)$Ba_2CuO_{4+\delta}$ ((Cu,C)-1201) and $CaCuO_2$ to prepare (Cu,C)-1212 and (Cu,C)-1223. (Cu,C)-1212 consists of 1 unit cell each of (Cu,C)-1201 and $CaCuO_2$ while (Cu,C)-1223 has 2 unit cell of $CaCuO_2$

with any desired number of unit cells of (Cu,C)-1201 and $CaCuO_2$. The main focus of the study is emphasize the role of substrate temperature and oxygen partial pressures in getting a good structure and inducing superconductivity in (Cu,C)$Ba_2Ca_1Cu_2O_{6\pm\delta}$ ((Cu,C)-1212) and (Cu,C)$Ba_2Ca_2Cu_3O_{8\pm\delta}$ ((Cu,C)-1223) structures.

4.3. Experimental

Ceramic targets of 50 mm diameter of the composition $BaCu_{0.75}O_y$ and $CaCuO_2$ were fixed on two oppositely placed sputtering sources in the instrument. As mentioned earlier

the shutters in the sputtering system can be programmed according to the desired timings required to deposit layers of preferred thickness. The (100) oriented $SrTiO_3$ (STO) was always kept at an optimum distance of 75 mm from both the targets. The deposition was carried out in a gas mixture of Ar, O_2 and CO_2 where the Ar : O_2 ratio was varied between 1 : 0.5 – 1 : 3 whereas the CO_2 partial gas pressure was fixed at 1 mTorr. After deposition, films were cooled to room temperature in 1 atm O_2 pressure with a rate of 1 °C/min. The rf power to the target was kept constant at 25 W for both the targets. The superlattices were annealed ex-situ in the presence of 1 atm. O_2 pressure in the infra-red annealing system at various annealing temperatures. The substrates that were used for the preparation of superlattices were annealed in air at 1000 °C for 1 hour. Annealing helped crystallization of the as received STO substrate.

Structural characterization of the superlattices was carried out using Rigaku miniflex and Bruker D8 DISCOVER diffractometers. The phase was identified using 2θ/θ scan with 2θ ranging between 5° to 60°. XRD patterns were also used to calculate the individual layer thickness and total periodicity of the superlattices formed from the one or two unit cells of the constituent layers. A rough estimate of deposition rates of the individual layers was obtained from cross-sectional FESEM (NOVA NANO600 – FEI, The Netherlands). All the films were prepared on rectangular cut substrates. Before attaching four point probe leads, 800 nm thick gold pads were deposited on the films masked by aluminium foils. Electrical contacts were made with Cu wires working as leads, were glued on these pads with the help of silver epoxy. Electrical dc resistivity

was measured using the dc transport measurement option in physical property measurement system (PPMS).

4.4 Results and discussion

4.4.1 Structure:

Before depositing the superlattice, it was essential to set the correct temperature ranges where $CaCuO_2$ gets deposited. $CaCuO_2$ (CCO) deposits in a narrow range of substrate temperature and pressure on STO substrate, however it grows easily on (Cu,C)-1201

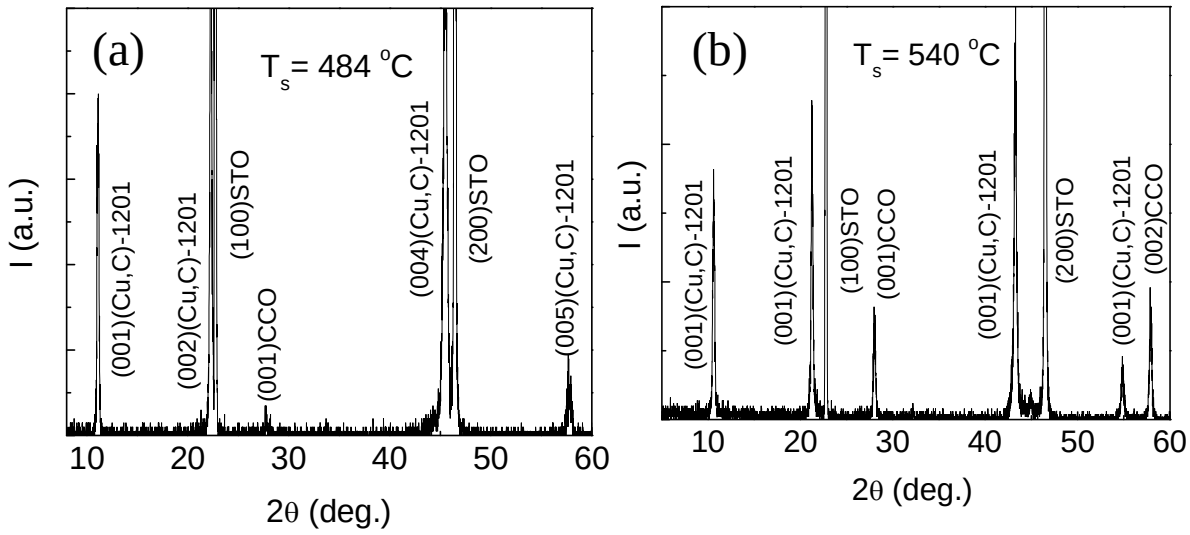

Figure 4.3. (a) and (b) X-ray diffraction patterns of $CaCuO_2$ deposited on (Cu,C)-1201 at two different substrate temperature. At high temperature the in-plane lattice mismatch between the two films decreases as at high substrate temperature the '*a*'-axis length of (Cu,C)-1201 becomes equal to that of $SrTiO_3$.

layer. Figures 4.3 (a) and (b) shows the XRD pattern of CCO films on (Cu,C)-1201 layer deposited at T_s = 480 °C and 540 °C respectively. As observed CCO grows well at 540 ºC with a (001) orientation and a '*c*'- axis length of ~ 3.18 Å. The low value of the out-of -plane lattice parameter of CCO thin film as compared to the bulk value shows that it is compressed along the *c*- axis. High temperature growth may be because of the low in-plane lattice mismatch between CCO and (Cu,C)-1201. As discussed in chapter 3, low substrate temperature facilitates growth of relaxed (Cu,C)-1201 thin film whereas the same film when grown at high substrate temperature experience a compressive strain and shrink the in-plane lattice parameters from 4.08 Å to 3.90 Å. If we consider the reported bulk lattice parameters of $CaCuO_2$ (a = 3.86 Å and c = 3.20Å), the in-plane lattice mismatch between $CaCuO_2$ and (Cu,C)-1201 can be calculated using the following formula:

$$(mismatch)\, f = \frac{a_{CCO} - a_{(Cu,C)-1201}}{a_{(Cu,C)-1201}}$$

The mismatch between relaxed (Cu,C)-1201 and CCO is ~ -0.037 i.e. -3.7 % . Similarly a strained (Cu,C)-1201 gives a mismatch of ~ -0.01 or 1% mismatch between the in plane lattice parameters. To know more about the structure and morphology of $CaCuO_2$ we performed reciprocal space mapping (RSM) of the film deposited on strained (Cu,C)-1201. Figure 4.4 shows the symmetrical RSM about the (100) Bragg peak of $SrTiO_3$ showing the (002) XRD peak of strained (Cu,C)-1201 and and (001) peak of CCO. The *c*- axis length for CCO (c_{CCO}) is calculated to be ~ 3.20 Å using the formula:

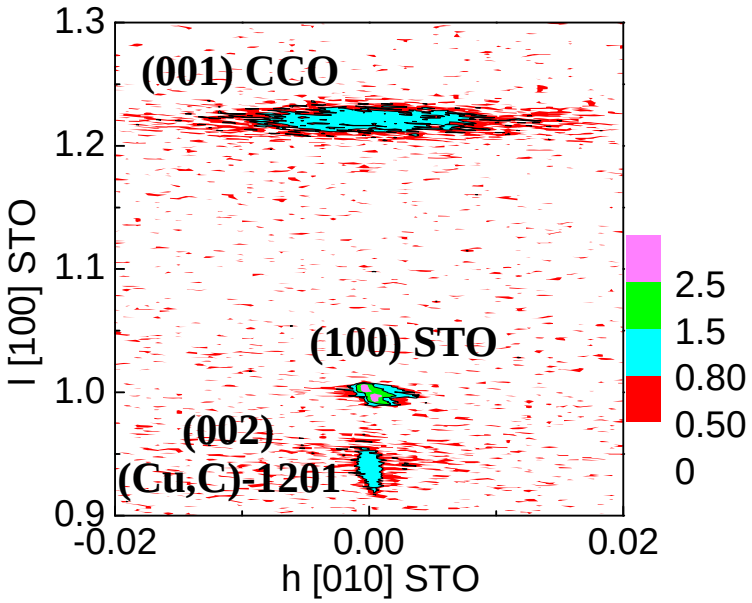

Figure 4.4. Symmetric RSM around the (100) Bragg reflection of $SrTiO_3$ substrate showing the (001) and (002) reciprocal lattice point of $CaCuO_2$ and (Cu,C)-1201 respectively with intensity in log-scale.The spread of (002) Bragg reflection point in the lateral direction shows the mosaic nature of $CaCuO_2$.

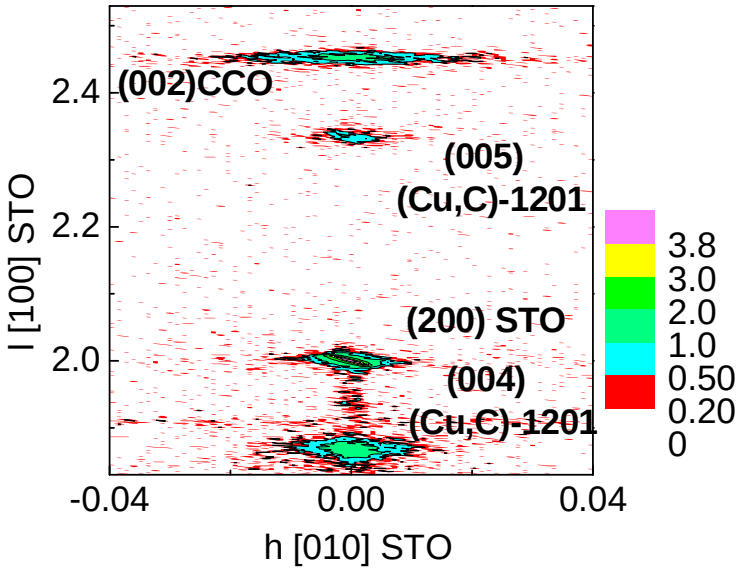

Figure 4.5. Symmetric RSM around the (200) Bragg reflection of $SrTiO_3$ substrate showing the (001) reciprocal lattice point of $CaCuO_2$ where the intensity is in log-scale. The (004) and (005) reflection points of (Cu,C)-1201 can also be observed.

$$c_{CCO} = \frac{c_{STO}}{h_{CCO}} (\text{ from RSM, } h_{CCO} \sim 1.22)$$

The small difference between the c- lattice parameters obtained from the 2θ/ω scan and symmetric RSM, may be due the in-exact identification of exact reciprocal point in the RSM. Another attempt to calculate the *c*- axis length from the (002) Bragg point gave a value of ~ 3.187 Å (figure 4.5). It can also be observed that as compared to (Cu,C)-1201 (002) reflection, the width of CCO (001) reflection is very broad (figure 4.4). The (002) Bragg reflection of CCO is much wider than the (001) reflection and as discussed in chapter 2, this kind of lateral spread shows mosaicity in the CCO film. Information about the in plane lattice parameter of CCO thin film deposited on (Cu,C)-1201 layer was obtained using the asymmetrical RSM. Due to the presence of a lighter Ca atom, the X-ray scattering factor for $CaCuO_2$ is very less and therefore getting a good intensity for

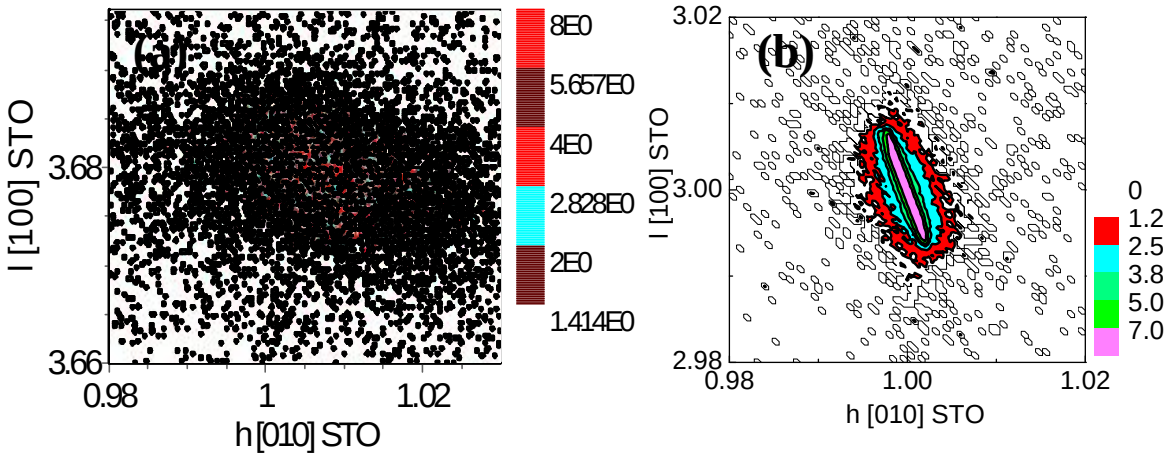

Figure 4.6. (a) corresponds to the (013) Bragg reflection of $CaCuO_2$ while (b) shows the (310) reciprocal lattice point of the $SrTiO_3$. Here also the intensity is in log-scale.

asymmetric Bragg reflection was very difficult. So the (013) Bragg reflection (figure 4.6(a)) was obtained with a very slow scan after selecting a small area around that peak, otherwise it was not visible. The data for (310) reflection of STO was collected separately (figure 4.6(b)).The *a*- axis length was calculated to be between 3.88 Å and 3.86 Å respectively. Thus from here one can conclude that there is an in-plane tensile strain working on the CCO layer which leads to a simultaneous expansion of *a*- lattice parameter and compression of *c*- axis length. The thickness of the film was monitored through cross-sectional FESEM imaging. Figure 4.7(a) shows the cross-section of a strained (Cu,C)-1201 thin film where the layer and the substrates are well distinguished. A bilayer consisting of CCO thin film deposited on top (Cu,C)-1201 is shown in figure 4.7(b). These cross-sectional images are of great help in calculating the rates of

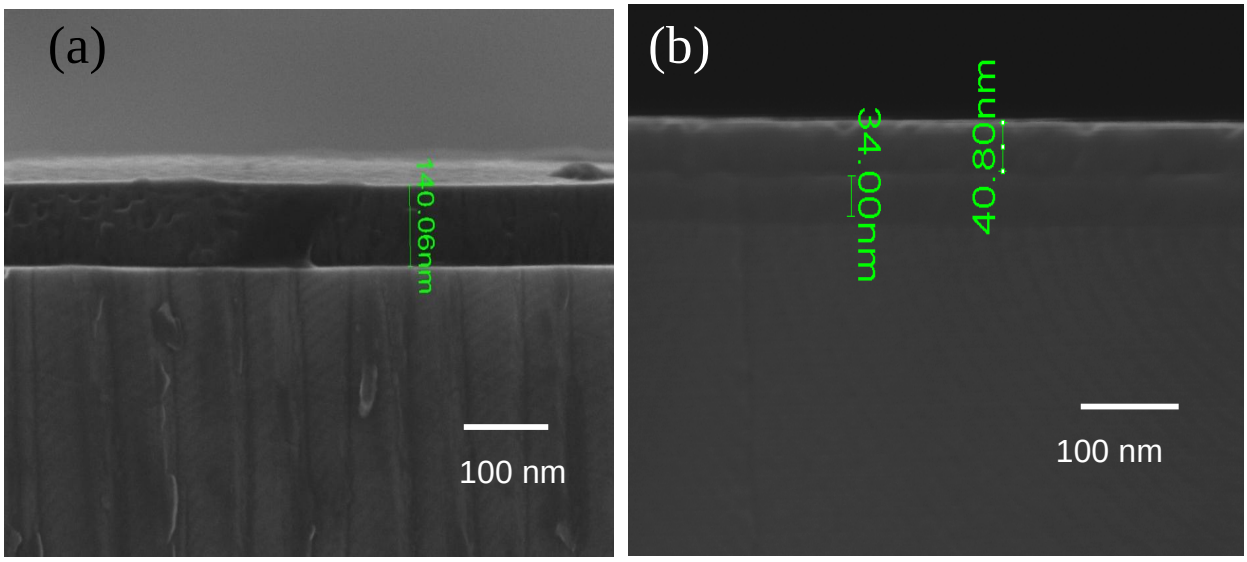

Figure 4.7. (a) shows the cross-sectional FESEM image of a single layered film showing (Cu,C)-1201 layer while (b) is a bi-layered film with $CaCuO_2$ deposited on top of (Cu,C)-1201. The two layeres can be identified separately as there is a sharp boundary between the two and a rough estimate of the film thickness can be determined.

deposition for both layers. Rates were calculated from the thickness of the film and the total time taken to deposit them. Using these rates, superlattices were prepared and their XRD patterns are shown in figure 4.8. Here the thickness of (Cu,C)-1201 was varied to calculate the change in the periodicity (Λ) of superlattices, defined as:

$$\Lambda = n1c1 + n2c2$$

Where *n1* and *n2* are number of unit cells of individual layers in the superlattice and *c1* and *c2* are the *c*- axis widths of the layers. The periodicity can also be determined from the angular distance between the adjacent satellite peaks using the formula:

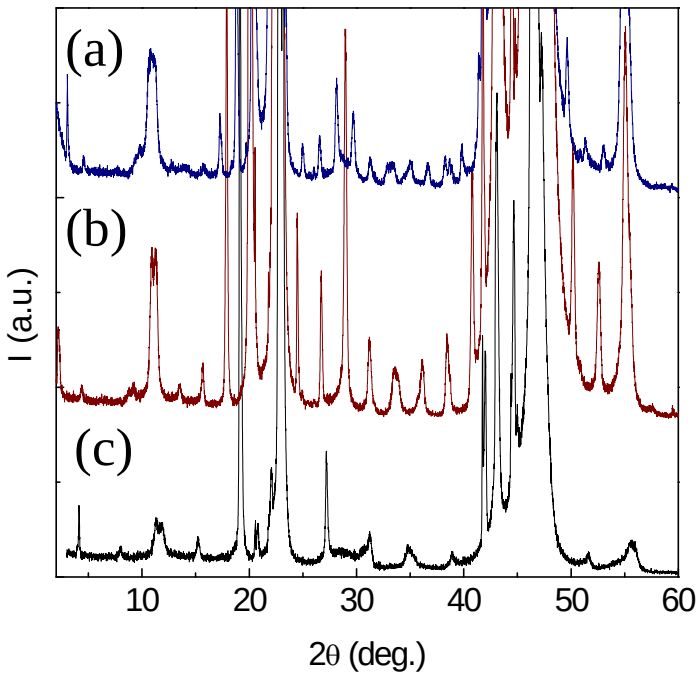

Figure 4.8. XRD patterns of the superlattices with a periodicity of (a) Λ = 56.5 Å corresponding to 5 unit cells of (Cu,C)-1201 and 1.5 unit cell of CaCuO2 , (b) Λ = 39.9 Å corresponding to 3.4 unit cells of (Cu,C)-1201 and 1.5 unit cell of CaCuO2 and (c) Λ = 23.3 Å corresponding to 1.7 unit cell of (Cu,C)-1201 and 1.5 unit cell of CaCuO2 respectively.

$$\Lambda = \frac{\lambda}{2\left|\left(\sin\theta_n - \sin\theta_{n\pm1}\right)\right|}$$

Here λ = 1.54 Å, and θ_n is the nth order satellite peak. Knowledge of Λ, *c1* and *c2* can provide a rough estimate of *n1* and *n2*. In the XRD pattern shown in Figure 4.8, the calculated superlattice periodicity is (a) 56.5 Å, (b) 38.9 Å and (c) 23.3 Å respectively. As in these superlattices, only (Cu,C)-1201 layer thickness was changed, the superlattices correspond to $((Cu,C)\text{-}1201)_m/(CCO)_n$, where *m* = 5 (a), 3.4 (b), 1.7 (c) and *n* = 1.5. Using this method, we were able to get the approximate values of the rates of deposition.

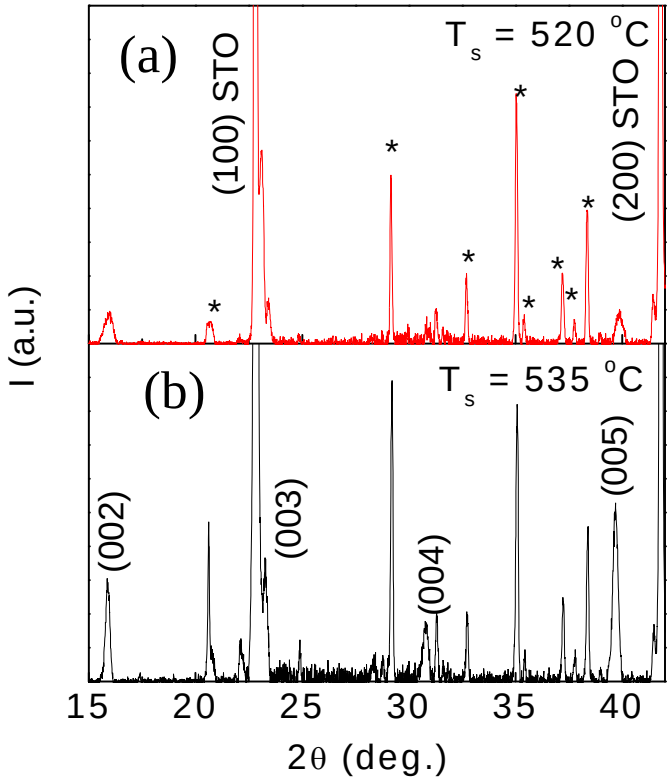

Figure 4.9. XRD patterns of $((Cu,C)\text{-}1201)_1/(CaCuO_2)_1$ superlattice deposited at different substrate temperatures. It can be observed that superlattice grows much better at high substrate temperature (a) as compared to low deposition temperature (b). The peaks marked with * indicates substrate satellite peaks.

Rate of deposition of ((Cu,C)-1201) = 6.2 Å/min

Rate of deposition of ((CCO) = 1.37 Å/min

Figure 4.9 shows temperature dependence of the superlattice films prepared at two different substrate temperatures. The superlattice grows much better at higher temperature which support the earlier observation of epitaxial growth of CCO layer on (Cu,C)-1201 at higher temperatures. Employing these rates of deposition, we were able to get: $\Lambda \sim 12.72$ Å which is ~ 1 Å larger than the expected value. The partial pressures of

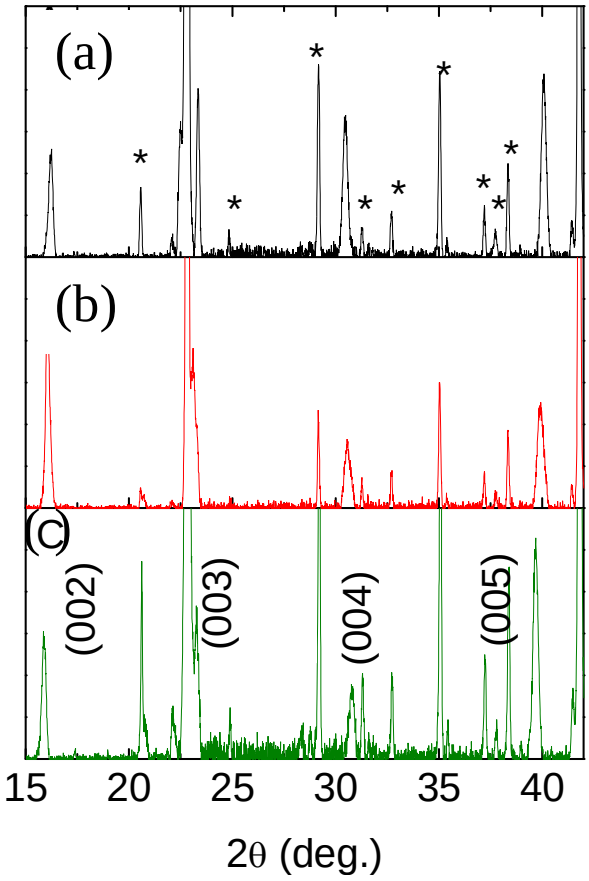

Figure 4.10. XRD patterns of superlattices grown with O_2 partial pressures, assuming rate of deposition for (Cu,C)-1201 to be 6.2 Å/min. The superlattice peaks become very sharp with increasing decreasing pressure. Satellatite peaks of substrate are marked with *.

Ar, O_2 and CO_2 gases are 5 mTorr, 10 mTorr and 1 mTorr respectively. Figure 4.10 shows the evolution of XRD peaks with varying O_2 pressure. The O_2 partial pressures for the XRD patterns shown in figures 4.10 (a), (b) and (c) are 5 mTorr, 7.5 mTorr and 10 mTorr respectively. The substrate temperature is 540 °C. Using the best optimized conditions we were able to get a Λ = 12.05 Å after decreasing the time of deposition for CCO. Figure 4.11 shows the XRD pattern of superlattices formed based on the time taken for depositing 1 unit cell of (Cu,C)-1201 (80 sec) and 1 unit cell of CCO (125 sec).

The rates of deposition were as follows:

Rate of deposition of ((Cu,C)-1201) = 6.2 Å/min

Rate of deposition of ((CCO) = 1.53 Å/min

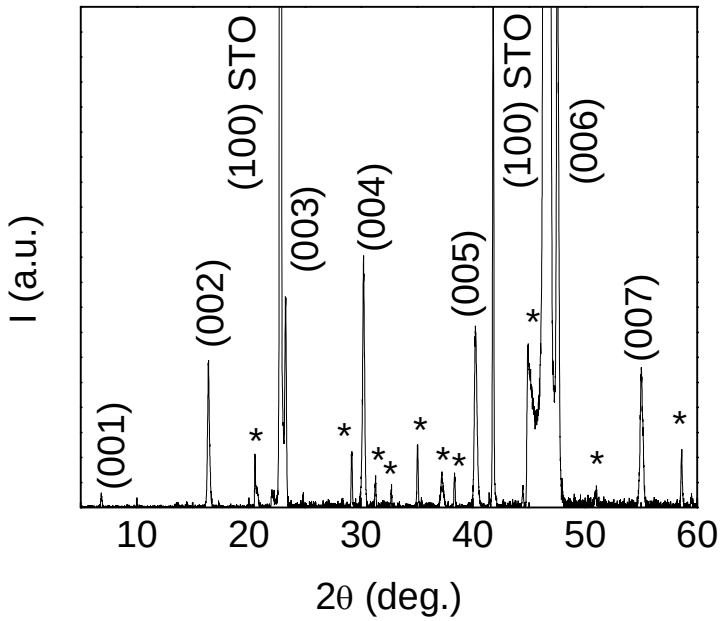

Figure 4.11. XRD pattern of the (Cu,C)$Ba_2CaCu_2O_{6\pm\delta}$ or (Cu,C)-1212 formed by depositing a superlattice of 1 unit cell of (Cu,C)-1201 and 1 unit cell of $CaCuO_2$ respectively with optimized substrate temperature and O_2 partial pressure. The substrate temperature was 540 ºC and O_2 partial pressure was 5 mTorr.

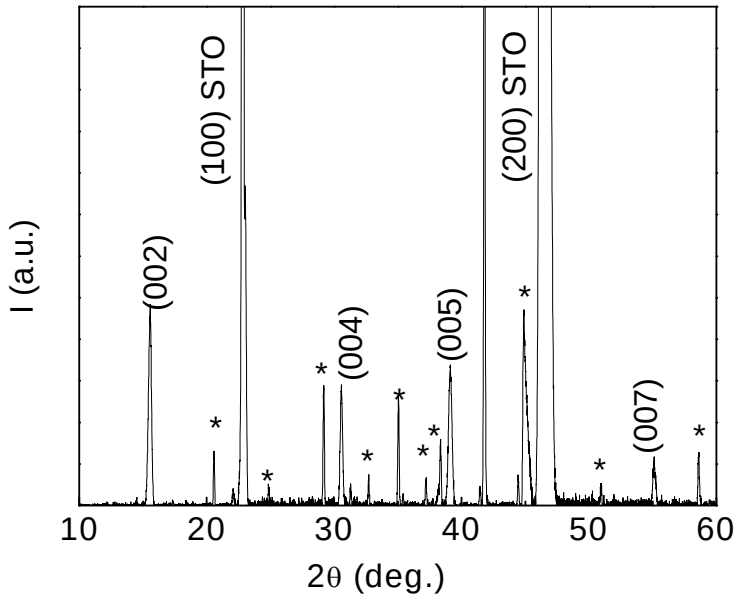

Figure 4.12. XRD pattern of (Cu,C)-1212 superlattie film annealed ex-situ at 650 ºC in an infra-red annealing system under 1 atm. O_2 partial pressure.

Attempts were made to reduce the time for deposition of 1 unit cell of (Cu,C)-1201, but no superlattice peak was observed. Figure 4.12 shows the corresponding XRD pattern of the film which was annealed ex-situ in an infrared annealing system at 650 ºC for 1 hour under flowing oxygen. Using the same conditions, we also tried to deposit the third member of the series with the general structural formula: (Cu,C)$Ba_2Ca_{n-1}Cu_nO_{2n+2\pm\delta}$. (Cu,C)$Ba_2Ca_2Cu_3O_{8\pm\delta}$ or (Cu,C)-1223 can be fabricated using 1 unit cell of (Cu,C)-1201 and two unit cells of CCO. Figure 4.13 shows the XRD pattern of superlattice corresponding to (Cu,C)-1223. The periodicity, Λ, as calculated from the angular positions of the peaks is calculated to be ~ 15.1 Å. The superlattice was grown at a substrate temperature of 540 ºC and the oxygen partial pressure was 5 mTorr. The CO_2 partial pressure was 1 mTorr.

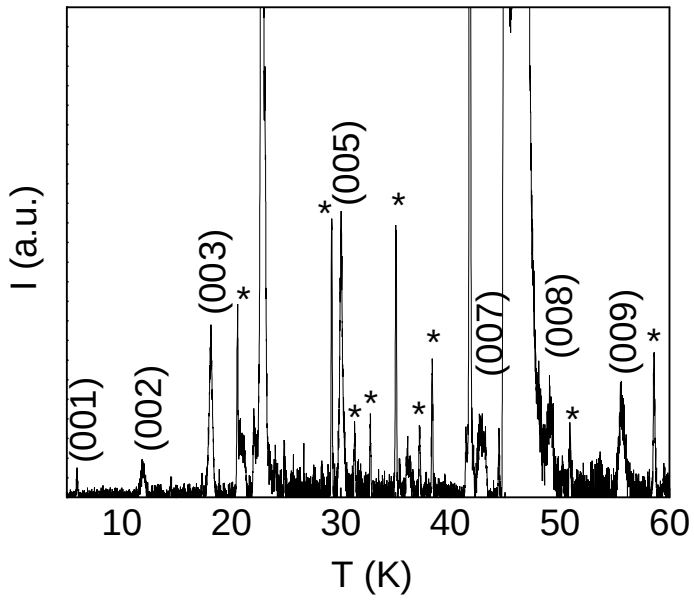

Figure 4.13. XRD pattern of the (Cu,C)$Ba_2Ca_2Cu_3o_{8\pm\delta}$ or (Cu,C)-1223 formed by depositing a superlattice of 1 unit cell of (Cu,C)-1201 and 2 unit cells of $CaCuO_2$ respectively. The substrate temperature was 540 ºC and O_2 partial pressure was 5 mTorr.

4.3.2 Electrical Transport

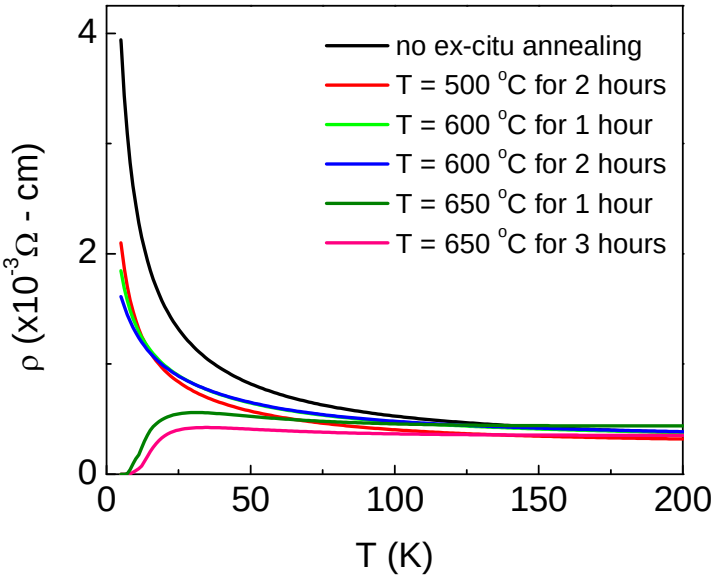

Figure 4.14. Resistivity versus temperature plots of (Cu,C)-1212 superlattice film annealed ex-situ at various temperatures in an infra-red annealing system under 1 atm. O_2 partial pressure.

Almost all the superlattices showed semiconductor behavior. However ex-situ annealing induced superconducting transition in these thin films. A large area film using 10 mm x 10 mm substrate was deposited with a substrate temperature with 540 ^{o}C and 5 mTorr O_2 partial pressures. The CO_2 partial pressure was 1 mTorr. Before taking out the superlattice film, it was slowly cooled in 1atm. of O_2 gas inside the sputtering chamber. The substrate (along with the film) was cut into smaller pieces and then annealed at various temperatures ex-situ in an infra-red annealing system under 1 atm. flowing oxygen. Figure 4.14 shows the $\rho - T$ plots for films annealed at various temperature and time. The normal state resistivity decreases with increasing annealing temperature. A superconducting transition is observed at around 25 K with a T_c (zero) = 10 K for the film annealed at 650 °C for 1 hour. Increase in the time for annealed led to the decrease in the

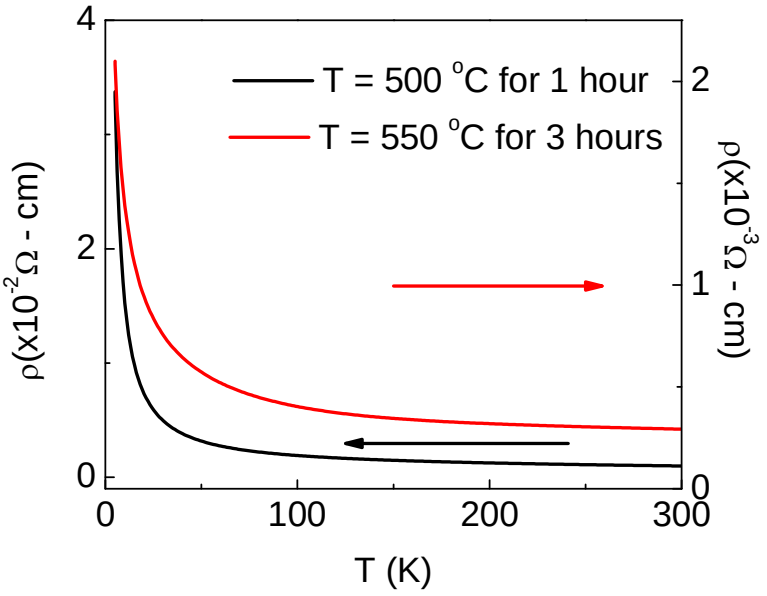

Figure 4.15. Resistivity versus temperature plots of (Cu,C)-1223 superlattice film annealed ex-situ at various temperatures under 1 atm. O_2 partial pressure. The resistivity decreases with increase in annealing temperature.

normal state resistivity without changing the transition temperature. While annealing the films ex-situ, we went up to a temperature of 800 °C. At this temperature we observed increase in the width of the superlattice peaks. This film did not show superconductivity. (Cu,C)-1223 films also showed decrease in their in-plane resistivity after ex-situ annealing, however no superconducting transition (figure 4.15). There is a one order decrease in the resistivity after annealing the superlattice at 550 °C for 3 hours as compared to film annealed at 500 °C for 1 hour. As discussed in chapter 3, the in-plane lattice parameter of (Cu,C)-1201 shrinks with increasing substrate temperature or increasing out-of-plane lattice parameter. The film deposited at high temperature is suitable for growing $CaCuO_2$ as the lattice mismatch between the two layers becomes very less. High temperature also facilitates the growth of superlattice formed using the two layers with sharp XRD peaks. However the superlattices show a very low superconducting transition temperature (T_c) as compared to what is expected in these structures. The main reason behind the low T_c may be high CO_2 gas partial pressure. As we already discussed that charge carriers in the charge reservoir layer i.e. (Cu,C)-1201 can be adjusted by the amount of CO_3 group in it. And therefore the (Cu,C)-1201 layer can be tuned to become a metal or a superconductor or an insulator by just varying the CO_3 content in its structure. To increase its efficiency as a donor of charge carriers to the CuO_2 plane in the superconducting layer, the carbon content should be adjusted to a minimum. Hole redistribution across the interface of $(BaCuO_2)_2/(CaCuO_2)_2$ have been measured from the x-ray absorption spectroscopy [24]. These multilayers were prepared

by pulsed layer deposition technique under very high oxygen partial pressure. No CO_2 gas was introduced in the deposition chamber, however authors believed that some amount of CO_3 group may get incorporated into the film from the target. The redistribution is believed to be because of the bridging between CuO_2 planes through apical oxygen atoms present in the Ba layer. As the numbers of $CaCuO_2$ layers increase, the bridging becomes weak and superconductivity is lost. The inner CuO_2 planes become charge deficient while the outer CuO_2 plane is over-doped. Homogeneous optimum doping for T_c enhancement can be realized by reducing the effect apical oxygen i.e. either by elongating the Cu-apical oxygen bond length or by selective reduction of the charge reservoir [25].

4.5. Conclusions

We have shown that $CaCuO_2$ thin film grow epitaxially on strained (Cu,C)-1201 thin film. The strained (Cu,C)-1201 has an in-plane lattice parameter equal to 3.90 Å which is equal to that of $SrTiO_3$ substrate. This compression helps in the growth of $CaCuO_2$ with a comparatively low mismatch. Moreover from RSM, we have also shown that the '*a*' lattice parameter of $CaCuO_2$ expands leading to the contraction in '*c*' lattice parameter. Using multitarget sputtering system with a programmed controller we were able to control a unit cell thick layer of both (Cu,C)-1201 and $CaCuO_2$ and it was possible to prepare superlattices of (Cu,C)-1212 and (Cu,C)-1223 structures. Superconductivity in (Cu,C) – 1212 was induced by ex-situ annealing at a temperature of 650 °C. The structure

was stable even after annealing at 800 °C, but no superconductivity was observed. (Cu,C)-1223 showed semiconductor behavior.

4.6. References

1. M. Karppinen and H. Yamauchi, *Mater. Sci. Eng., R.* **26** (1999) 51.
2. M. Ogino, T. Watanabe, H. Tokiwa, A. Iyo, H. Ihara, *Physica C* 258 (1996) 384.
3. Y. Tokunaga, K. Ishida, Y. Itaoka, K. Asayam, K. Tokiwa, A. Iyo, H. Ihara, *Phys. Rev. B* 61 (2000) 9707.
4. H. Ihara, K. Tokiwa, H. Ozawa, M. Hirabayashi, H. Matuhata, A. Negishi, Y.S. Song, Jpn. J. Appl. Phys. 33 (1994) L300.
5. H. Ihara, K. Tokiwa, H. Ozawa, M. Hirabayashi, A. Negishi, H. Matuhata, Y.S. Song, Jpn. J. Appl. Phys. 33 (1994) L503.
6. T. Kawashima, Y. Matsui, E. Takayama-Muromachi, Physica C 224 (1994) 69.
7. N. Hamada, H. Ihara, *Physica B* 284 (2000) 1073.
8. K. Kotegawa, Y. Tokunaga, K. Ishida, G.-q. Zheng, Y. Kitaoka, H. Kito, A. Iyo, K. Tokiwa, T. Watanabe, H. Ihara, Phys. Rev. B 64 (2001) 064515.
9. H. Suhl, B.T. Matthias, L.R. Walker, Phys. Rev. Lett. 3 (1959) 552.
10. Y. Tanaka, A. Iyo, N. Shirakawa, M. Ariyama, M. Tokumoto, S.I. Ikeda, H. Ihara, Physica C 357 (2001) 222.
11. Y. Tanaka, J. Phys. Soc. Jpn. 70 (2001) 2844.
12. H. Adachi, M. Sakai, T. Satoh, K. Setsune, Physica C 244 (1995) 282.
13. E. Koller, L. Fa´brega, J.-M. Triscone, M. Decroux, Ø. Fisher, J. Low Temp. Phys. 105 (1996) 1325.

14. H. Wakamatsu, T. Ogata, N. Yamaguchi, S. Mikusu, K. Tokiwa, T. Watanabe, K. Ohki, K. Kikunaga, N. Terada, N. Kikuchi, Y.Tanaka, A. Iyo, J. Phys.: Conf. Series 43 (2006) 289.
15. K. Kikunga, T. Yamamoto, K. Takeshita, K. Oki, T. Okuda, K. Obara, K. Tokiwa, H. Wakamatsu, T. Watanabe, N. Kikuchi, Y. Tanaka, N. Terada, J. Phys.: Conf. Series 43 (2006) 247.
16. N. Kikuchi, A. Sundaresan, N. Terada, M. Hirai, K. Tokiwa, T. Watanabe, Y. Kodama, A. Iyo, Y. Tanaka, Vacuum 74 (2004) 585.
17. D.P. Norton, B.C. Chakoumakos, J.D. Budai, D.H. Lowdnes, B.C.Sales, J.R. Thomson, D.K. Christen, Science 265 (1994) 2074.
18. Tebano, C. Aruta, N.G. Boggio, P.G. Medaglia, G. Balestrinio, Supercond. Sci. Technol. 19 (2006) S45.
19. M. Kanai, T. Kawai, Physica C 235–240 (1994) 174.
20. S. Colonna, F. Arciprete, A. Balzarotti, G. Balestrino, P.G. Medaglia, G. Petrocelli, Physica C 334 (2000) 64.
21. H. Shibata, S. Karimoto, A. Tsukada, T. Makimoto, Physica C 445 (2006) 862.
22. A.Sundaresan, M. Hirai, J.C. Nie, K. Hayashi, Y. Ishiura, H. Ihara, Physica C 357 (2001) 1403.
23. G. Balestrino, A. Crisan, S. Lavanga, P.G. Medaglia, G. Petrocelli, A.A. Varlamov, Phys. Rev. B 60 (1999) 10504.
24. C. Aruta *et. al.*, *Phys. Rev. B* **78** (2008) 205120.
25. H. Ihara, *Physica C* **364-365** (2001) 289.

Chapter 5

Synthesis and characterization of Sub-micron sized superconducting $YBa_2Cu_3O_{7-\delta}$ clusters

karmanyevaadhikaaraste maa phaleshu kadaachana |
maa karmaphalaheturbhuu maatesangotsvakarmani ||

A person has the right towards action alone and not towards the fruit of action. Let not the fruit of action be the motive for acting. Also, let there not be any attachment to inaction.

- Bhagwad Gita

Summary**

Recurring reports on the observation of ferromagnetism in nanoparticles of other-wise nonmagnetic inorganic compounds have added a new flavor to the existing exotic properties of nanomaterials. The origin of this type of ferromagnetic behavior is mainly discussed in terms of surface defects that may include cation or anion vacancies. As superconductivity and ferromagnetism are antagonistic to each other, we have done a complete and systematic study of the magnetic properties of sub-micron sized $YBa_2Cu_3O_{7-\delta}$ superconductors, prepared by sol-gel method, both above and below T_c. The cluster containing sub-micron sized particles exhibit surface ferromagnetism. Magnetic measurements below T_c generate unusual and interesting hysteresis curves which are explained on the basis of the size of individual grains forming the cluster. Further, the hysteresis curves below T_c seem to be influenced by ferromagnetism and therefore a possible coexistence of core superconductivity with surface ferromagnetism cannot be excluded. The inhomogeneous particle size distribution along with sub-micron dimensions of the particle also gave rise to zero imaginary part of ac susceptibility.

A paper based on the present study has been published in *solid state communications* **142 (2007) 685-688.

5.1. Introduction

Synthetic procedure plays an important role in defining the microstructure of high temperature superconductors (HTSCs) which in turn determines the superconducting properties for desirable applications. The most common preparative method is the conventional solid state reaction route using metal–oxides as the starting materials [1 - 3]. However, the associated drawbacks i.e. inhomogeneous mixing of reactants, repeated heating and calcinations for prolonged time intervals makes the ceramic route, an unfavorable choice for the synthesis of HTSCs [4]. Long and high temperature sintering results in large sized superconducting grains which make study of sub-micron sized superconductors, almost impossible. Solution based sol gel method gives an advantage of providing monophasic compounds synthesized at low temperatures with homogeneous mixing of reactants at the atomic level [5]. Low temperature heating prevents agglomeration of grains and therefore helps to control the increase of particle size [6]. There have been regular reports on the magnetic properties of granular superconductors for example the Wohlleben effect [7-9], presence of surface barriers [10-16] and observation of paramagnetic contribution in the magnetic hysteresis measurements of oxygen deficient superconductors [17]. Granularity due to weak link between the grains in these low temperature sintered compound, also introduces double peak loss behavior in the ac magnetic susceptibility measurements of HTSCs [18, 19]. All these properties have been extensively studied for samples having weakly coupled grains but there are very

occasional experimental reports on the response shown by sub-micron sized particles of these compounds.

Recently, there have been lots of exciting results published on the room–temperature ferromagnetism in nanoparticles of nonmagnetic oxides [20]. In these materials, ferromagnetism occurs due to cation or anion defects on the surface of the nanoparticles and thus the ferromagnetism is confined to the surface of the particles. This motivated us to study whether such surface related ferromagnetism can occur in nanoparticles of cuprate superconductors which are otherwise well known Pauli paramagnets above superconducting transition temperature (T_c). For this purpose, we selected $YBa_2Cu_3O_{7-\delta}$ (YBCO) which is a well known high temperature superconductor.

Earlier when HTSCs were discovered, there was common consensus about the origin of paramagnetic Meissner effect, and that it was mainly seen as consequence of *d* – wave symmetry of the Cooper pairs or Josephson junctions. The above effect was mainly observed for small applied fields between 0.1-1 Oe [21]. Later such effects were also observed in *s*-wave and *d*-wave superconductors with range of the applied magnetic fields extending up to few kOe [22, 23]. These were explained on the basis of flux compression near the micro-structural defects in the superconducting material [21]. However, there were few indications in which surface of the sample was found to play an important role both in *s*-wave as well as *d*-wave superconductors [24, 25]. Apart from the observation of Wohlleben effect, granular superconductors also exhibit a crossover from negative magnetization value to a positive value in the field increasing part of the *M-H* curve. The reason for this effect is mainly explained in terms of the presence of

$BaCuO_{2\pm\delta}$ impurity phases in the sample. A clear manifestation of the reasons involved in such observation is yet to be investigated. In our study we were able to retrieve some of these features in the magnetic properties of sub – micron sized YBCO grains, and explained these observations in terms of localized moments on the surface of superconducting grains.

5.2. Scope of present investigation

In this work, we have proposed the coexistence of surface ferromagnetism along with core superconductivity in the sub-miron sized YBCO. A direct implication of such a structure is the study of interfaces between a ferromagnet and a superconductor. Usually such studies require deposition of bilayers using thin film deposition technique. However a system of superconducting grain having a ferromagnetic surface forms a natural system to study such interfaces.

5.3. Experimental

5.3.1 Materials

5.3.1(a) Synthesis

Different batches of sub-micron sized samples were prepared by using polymeric precursor route described by a modified Pechini method in the literature [26]. Stoichiometric amounts of high purity $Y(NO_3)_3.6H_2O$ (99.9%), $BaCO_3$ (99+%) and CuO (99.99%) were taken as starting materials. CuO was converted into its nitrate by dissolving it in conc. HNO_3 while $BaCO_3$ was dissolved in aqueous solution of citric acid. Appropriate amount of ethylene-diamine was added to make the pH of the solution to 7. The solution changed its color from light blue to dark violet after adding the base. Here, citric acid having three carboxylic groups acts as chelating agent. The solution was slowly evaporated at 80ºC to produce a gel. The dried gel was heated at 550 ºC for 2 hours inside a tube furnace in the presence of flowing oxygen to decompose the organic materials. The final heating was done at various temperatures (770, 780, 790, 940 ºC) for 12 hours and at 800 and 830 ºC for 18 hours with a heating and cooling rates of 5 ºC/min. The sample heated at 940 ºC was first pressed in the form of a rectangular bar while other samples were heated in the powder form. The samples are designated as YBCO along with the temperature at which they were heated (e.g. YBCO790). A flowchart regarding the synthesis procedure of sub-micron sized YBCO grains is presented in Figure 5.1.

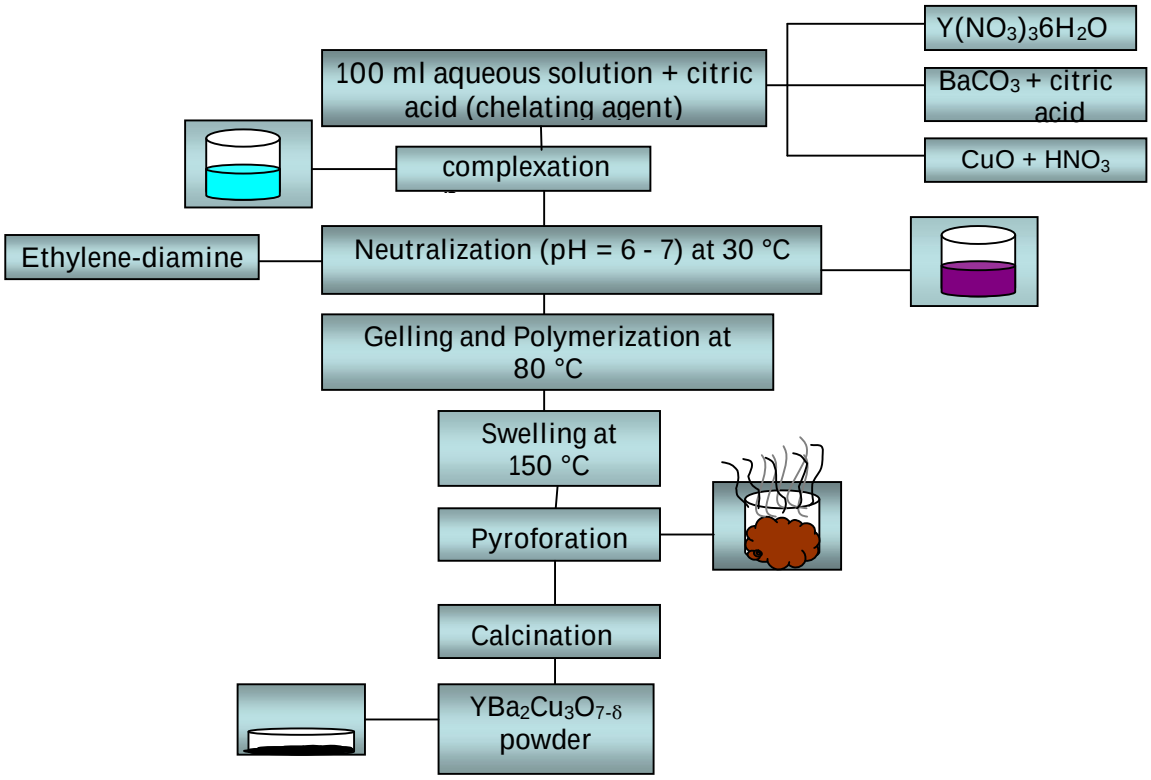

Figure 5.1. A flow chart of the various synthesis phases involved in the preaparation of $YBa_2Cu_3O_{7-\delta}$ superconductor.

5.3.1(b) Reaction mechanism

The citric aid in the sol-gel process acts as a chelating agent and forms Metal-organic acid complex. The two dentate –COOH groups bridges with the metal ions in the metal nitrate solution to form the complex. The complex solution is neutralized with the help of ethylene-diamine which also acts as a chelating agent due to the presence of amine groups. It also helps in restricting the growth of nanoparticles. The pH of the solution should be between 5.6 – 6.1, as at low pH, there are chances of the precipitation

of $Ba(NO_3)_2$. The citrate-nitrate solution in the presence of amine group has very unique properties. First it helps in getting a clear gel and second it facilitates temperature induced pyrolysis. At around 426 ºC, citric acid turns into itaconic acid that upon continued heating polymerizes and swells up with decarboxylation process releasing large amounts of CO_2 gas. The powder obtained, on further heating realeases nascent oxygen, water and nitrogen due to an exothermic reaction involving the decomposition of NH_4NO_3. The heat liberated is sufficient to calcine the respective metal compounds but, further heat treatment is necessary to remove trapped moisture and to gain a crystalline phase with right oxygen stoichimetry [50, 51].

5.3.2 Characterization

The X- ray diffraction (XRD) patterns of the as prepared powdered sample were taken with the help of Bruker's D8 Discover. Lattice parameters of these samples were obtained by matching the XRD profiles of $YBa_2Cu_3O_{7-\delta}$ using the software *Fullprof* . The size and surface morphology of YBCO powder was studied using Field Emission Scanning Electron Microscope (FESEM, NOVA NANO600 – FEI, The Netherlands). For this study, the loose powder was ultra-sonicated and dispersed in ethanol before drop-casting it on an Al stub. DC and AC magnetic measurements were carried out using vibrating sample magnetometer (VSM) and ACMS options, respectively in physical property measurement system (PPMS, Quantum Design, USA). The zero field cooled (ZFC) and field cooled (FC) data were collected by applying a magnetic field of 20 Oe

while warming from 5 K – 100 K. Comparison of the obtained ZFC - FC data with those obtained at higher fields was also done. In order to evaluate the zero field cooled isothermal magnetic hysteresis curves, data was taken at various temperatures below and above T_c. To study the flux dynamics of the powdered sample, ac susceptibility measurements were performed at various frequency, ac and dc fields. To eliminate any effect of remnant magnetic field, the temperature was raised to about 100 K and the field was reduced to zero by oscillating the field from 30 kOe after taking each set of measurements. All measurements were done on pressed powder in the form of pellets. DC electrical transport measurement was performed using the conventional four-point probe technique. The probes were made of Cu wires which were glued to the pressed pellet using a silver epoxy. Transport measurements were taken in the temperature range between 5 K and 100 K.

5.4. Results and discussion

5.4.1 Structure

Figure 5.2(a), compares the XRD patterns of the samples prepared at 770 ºC, 780 ºC and 790 ºC, 830 °C and 920°C respectively. The 2θ/ω scan reveals the presence of Orthorhombic (*Pmmm*) YBCO phase for all the samples. Although the sample prepared at high temperature do not contain any impurity phase, but those prepared at low temperatures contained impure phases like $BaCuO_2$ and Y_2O_3. Figure 5.3, shows the

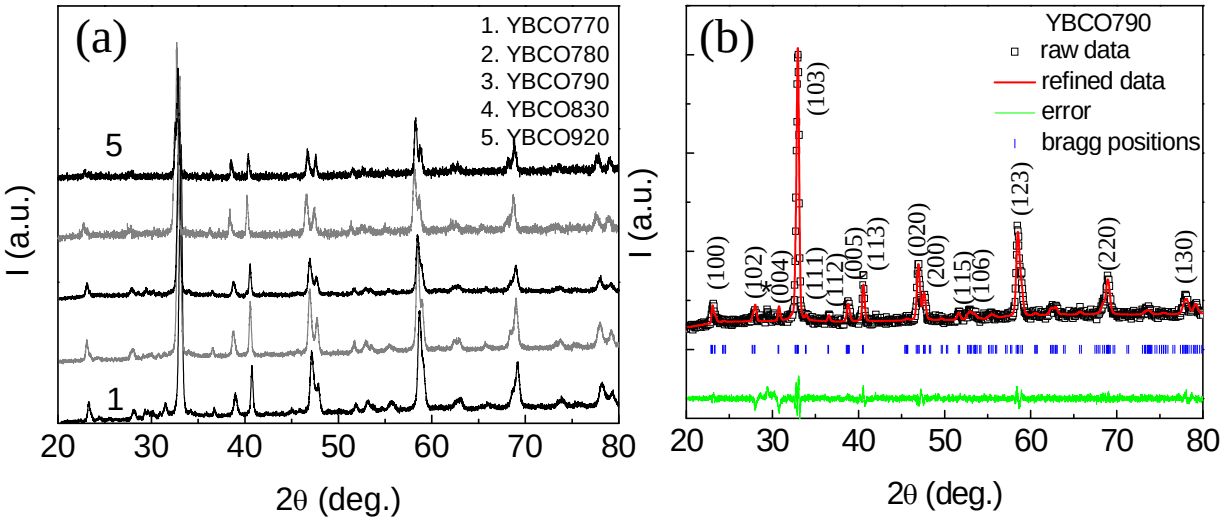

Figure 5.2. (a) shows the X-ray diffraction patterns of sub-micron sized $Y_1Ba_2Cu_3O_{7-\delta}$ powders prepared at different annealing temperatures. The sample prepared at 770 ºC showed impurities like $BaCO_3$ and Y_2O_3. However the sample prepared at 920 ºC showed a pure phase. (b) shows the reitveld refined pattern for the sample prepared at 790 ºC. All the peaks matched with the pure phase of YBCO except a small $BaCO_3$ impurity shown by asterisk (*) mark.

Sample	*a* (Å)	*b* (Å)	*c* (Å)
YBCO770	3.806	3.845	11.643
YBCO780	3.816	3.869	11.666
YBCO790	3.820	3.869	11.658
YBCO800	3.847	3.887	11.626
YBCO830	3.827	3.852	11.616
YBCO850	3.829	3.892	11.716
YBCO920	3.824	3.886	11.688

Table 5.1. (a) Unit cell lattice parameters obtained from the refinement of the XRD patterns in figure 5.2(a)

profile-matching pattern of the sample heated at 790 ºC using the software *fullprof*. The refined unit cell parameters with the accuracy at third decimal, are tabulated in table 5.1. A comparison between the lattice parameters and oxygen content is given in figure 1 of reference 35.

5.4.2 Morphology:

Figure 5.3 shows the FESEM images of (a) YBCO770, (b) YBCO790, (c) YBCO830 and (d) YBCO920 respectively. The particle size as well as the agglomeration of particles

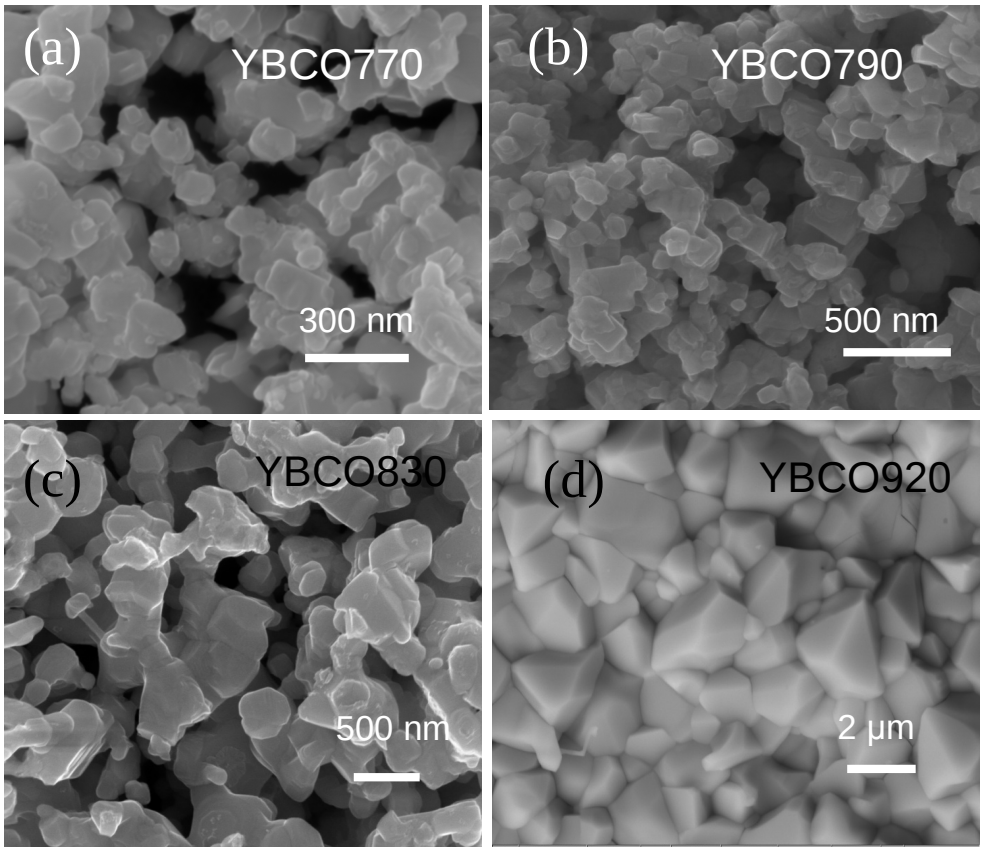

Figure 5.3. (a), (b), (c) and (d) shows the FESEM images of samples prepared at 770 ºC, 790 ºC 830 ºC and 920 ºC respectively. The particles increase in size and agglomerate as the synthesis temperature increases.

increases with increasing synthesis temperature. In all the FESEM images, the irregular shaped grains are highly agglomerated. The typical size of grains in YBCO790 varies between 50 nm and 200 nm while in YBCO920; the size of the grains is between 2 μm and 5 μm. Figure 5.4(a) shows the FESEM image of cold pressed YBCO790 reheated at 790 ºC for two hours while (b) shows the grain size and morphology of reheated cold pressed bar of YBCO790 at 940 ºC. Scales present on the surface indicate the spiral growth which may be due to screw dislocations [27].

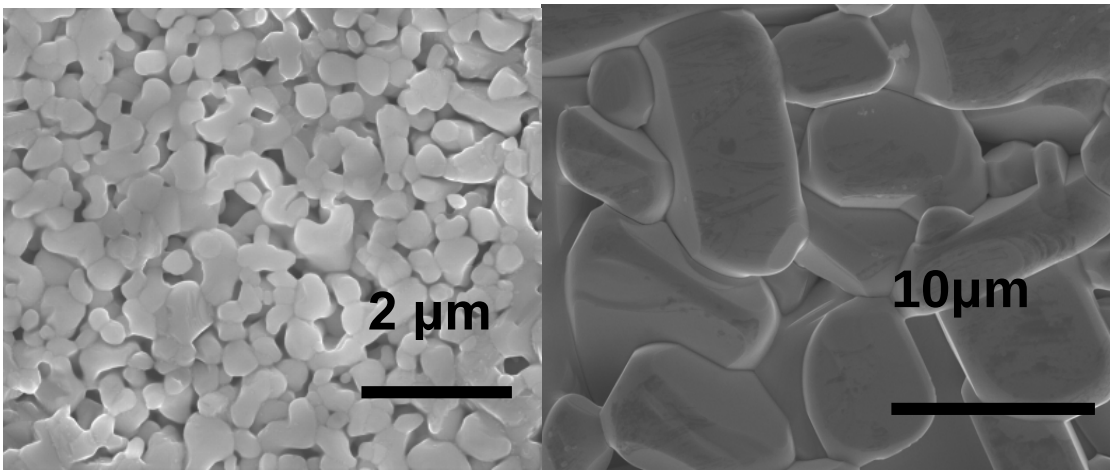

Figure 5.4. (a), (b), (c) and (d) shows the FESEM images of samples prepared at 770 ºC, 790 ºC 830 ºC and 920 ºC respectively. The particles increase in size and agglomerate as the synthesis temperature increases.

The grains are almost transparent to the electron beam in Transmission Electron Microscope (TEM) (figure 5.5(a)) and are highly crystalline as revealed from electron diffraction pattern of a single isolated grain (figure 5.5(b)) of YBCO790 and also

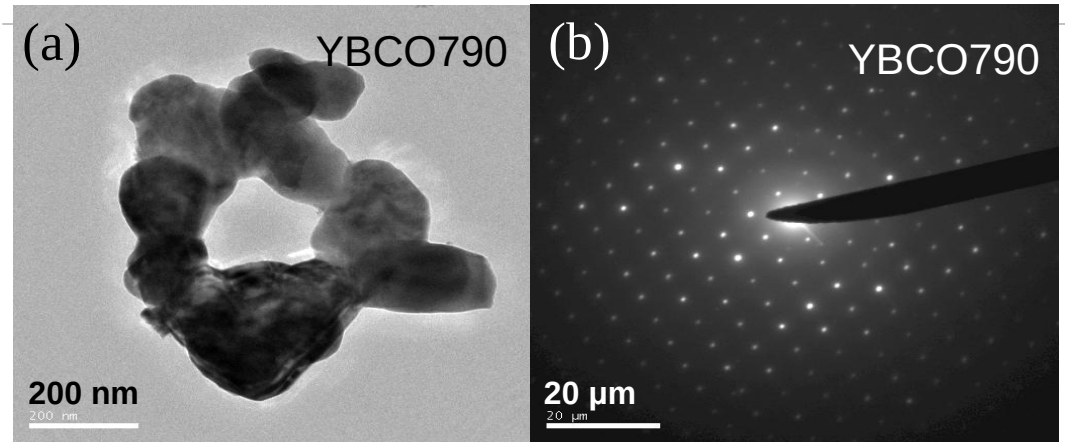

Figure 5.5. (a) Bright field TEM image of the sample synthesized at 790 ºC and (b) is the corresponding ED pattern of the sample.

confirms the orthorhombic crystal symmetry of YBCO. From transparency of the electron beam we can infer that YBCO powder synthesized at low temperature is having thin plate like morphology with thickness smaller than the diameter of the grain. This growth process resembles the shape of $YBa_2Cu_3O_{7-\delta}$ single crystals which grow as thin platelets oriented perpendicular to the *c*-axis [28, 29].

5.4.2 DC Magnetic properties

Fig 5.6(a) shows thermomagnetic measurements on the sample heated at 790 °C. It shows a superconducting transition temperature (T_c) of 90 K similar to that of bulk YBCO (figure 5.6(b)), and shows the fully oxygenated states of YBCO grains. However, the transition is not very sharp which may be due to large size variation of superconducting grains. The ZFC - FC curves almost overlap with each other up to T = 40 K for an applied field (H) of 20 Oe indicating a high degree of reversibility in the

sample. Such observations were also found in earlier literatures on small YBCO superconducting particles [30,31]. The relative reversibility arises from the fact that at low field the inter-vortex spacing is larger than the particle size in mesoscopic superconductor. So the nucleation of vortices and their aggregate bulk pinning is diminished at low fields [19]. Small size also leads to the small values of shielding fraction (ZFC) as well as Meissner fraction (FC) as compared to that of the bulk sample. As the applied field increases, more number of vortices nucleate in the sample and both curves start separating from each other indicating the increase in irreversibility. A very interesting observation is that the FC curve is more diamagnetic than the ZFC curve at 100 Oe. For H = 20 Oe, bulk YBCO in Fig 5.6(b), shows a completely separated ZFC - FC curves with a high superconducting volume fraction with a Meissner fraction of about 0.8. Low value of FC with respect to ZFC value denotes increased effect of bulk

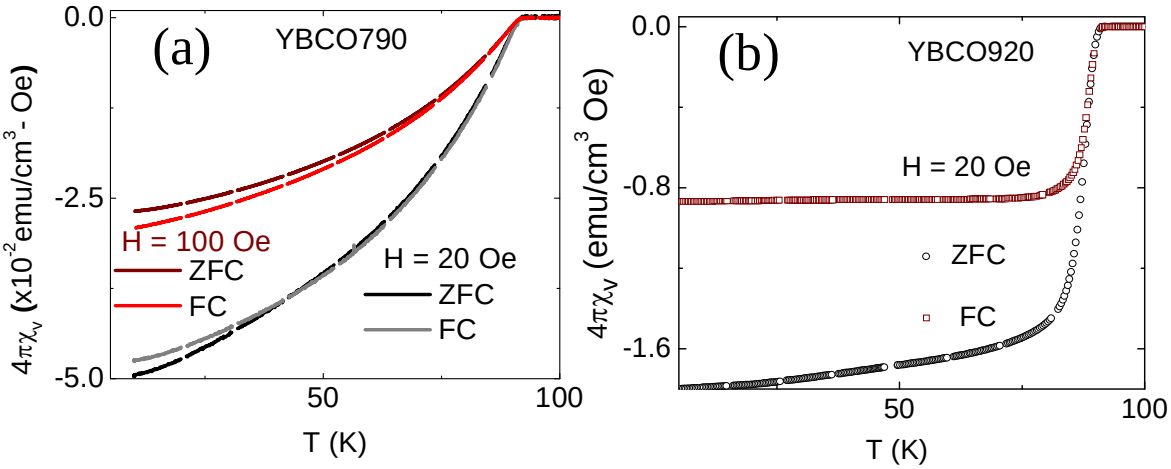

Figure 5.6. (a) ZFC-FC curves of YBCO790 for an applied field (H) of 20 Oe and 100 Oe. The irreversibility increases with increasing H. (b) ZFC-FC curve of the bulk sample prepared at 920 ºC showing irreversibility due to strong pinning of magnetic vortices.

pinning. Isothermal magnetization curves above T_c for YBCO790 are shown in figure 5.7(a). Intriguingly, the room-temperature magnetization of YBCO sub-micron paticles shows hysteresis, with a coercivity of ~ 200 Oe, typical of ferromagnetic behavior. At T = 91 K, just above the T_c, the ferromagnetic hysteresis still remains with increased coercivity (300 Oe). This observation is consistent with the prediction that all oxide nanoparticles would exhibit ferromagnetism [20]. Although grains of YBCO790 are somewhat larger as compared to other simpler oxide, nitride or chalcogenide nanoparticles, however the origin may be involving the same mechanism [32]. The origin of ferromagnetism is likely to be due to magnetic moments arising from the oxygen vacancies at the surfaces of the nanoparticles. Magnetic hysteresis measurement at room temperature for YBCO920 revealed paramagnetic behavior (not shown here) which is typical of bulk YBCO [33]. This supports the suggestion that the ferromagnetism is confined to the surface of the nanoparticles. Figure 5.7(b) shows the virgin magnetization

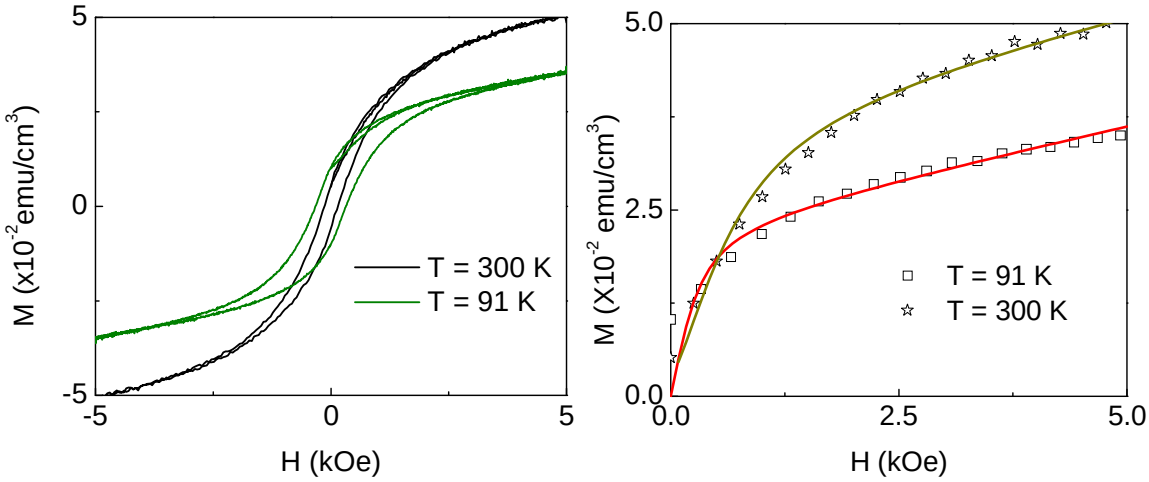

Figure 5.7. (a) Isothermal magnetization curves for YBCO790 at *T* = 300 K and 91 K respectively. (b) the corresponding virgin magnetization curves (symbol) and their fitting a model function(lines) containing the Langevin function plus a paramagnetic term to obtain average particle moment.

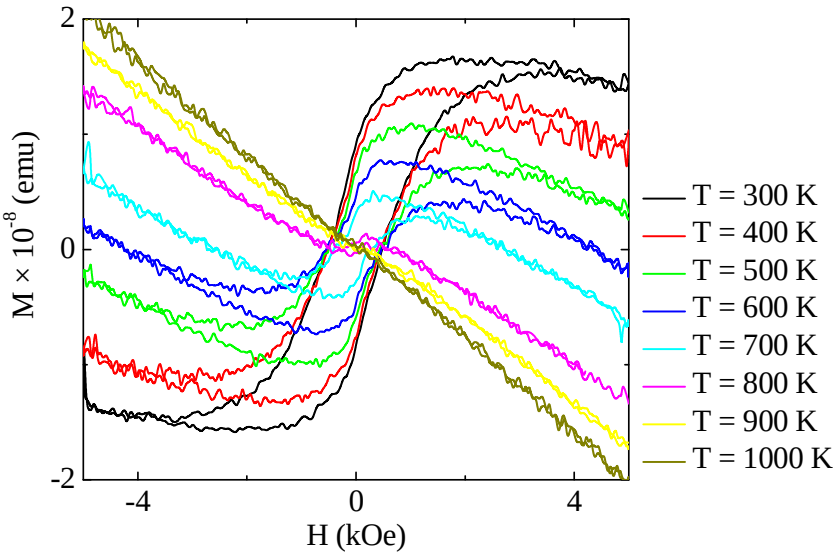

Figure 5.8. Magnetization curves of nanocrystalline YBCO at various temperatures showing the disappearance of ferromagnetic ordering at 800 K. The measurement was performed with the SQUID magnetometer, Quantum Design, USA.

curve of YBCO790. The average particle moment was calculated by fitting (represented by solid line in (b)) the measured virgin magnetization curve (symbol) at 300 K and 91 K, using the formula $M(H,T) = M_S(T)L(x) + \chi_p(T)H$, where $M_S(T)$ is the saturation magnetization and $L(x) = \coth(1/x)-x$ is the Langevin function, $x = \mu_p H/k_BT$, μ_p is the average particle moment, k_B is the Boltzmann constant, and $\chi_p(T)$ is the paramagnetic susceptibility. The values obtained are 13 x 10^{-3} μ_B (Bohr Magneton) and 10 x 10^{-3} μ_B respectively at 300 K and 91 K. These values agree well with the values obtained for Sn nanoparticles [34]. The ferromagnetic Curie temperature determined from temperature-dependent magnetization measurements above room temperature is shown in figure 5.8, where the ferromagnetic Curie temperature is 800 K. The measurement was performed with the SQUID magnetometer, Quantum Design, USA. Above the Curie temperature,

the magnetization shows a linear diamagnetic response instead of paramagnetic at high fields.

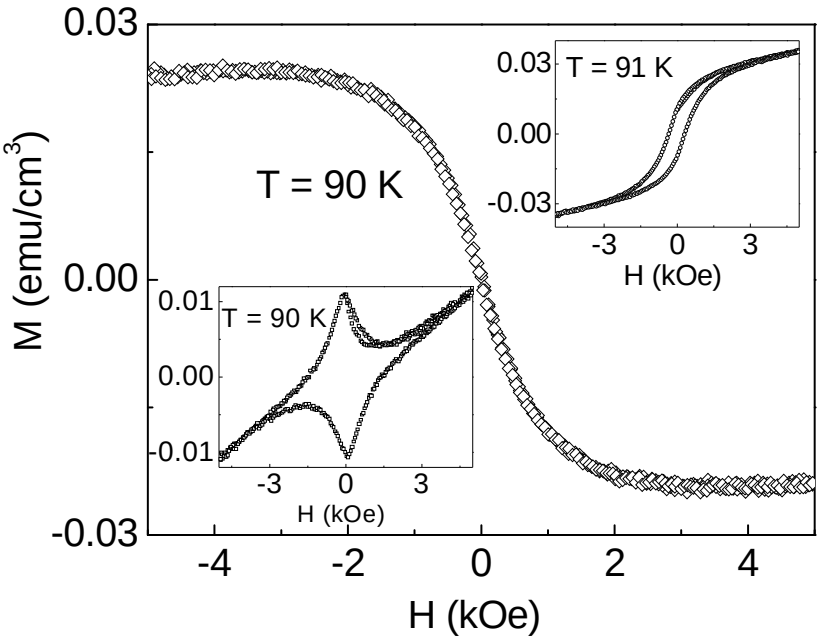

Figure 5.9. shows the *M-H* hysteresis curve for YBCO790 at T = 90 K (T_c) obtained by subtracting the data at 91 K (upper inset) from that of 90 K (lower inset).

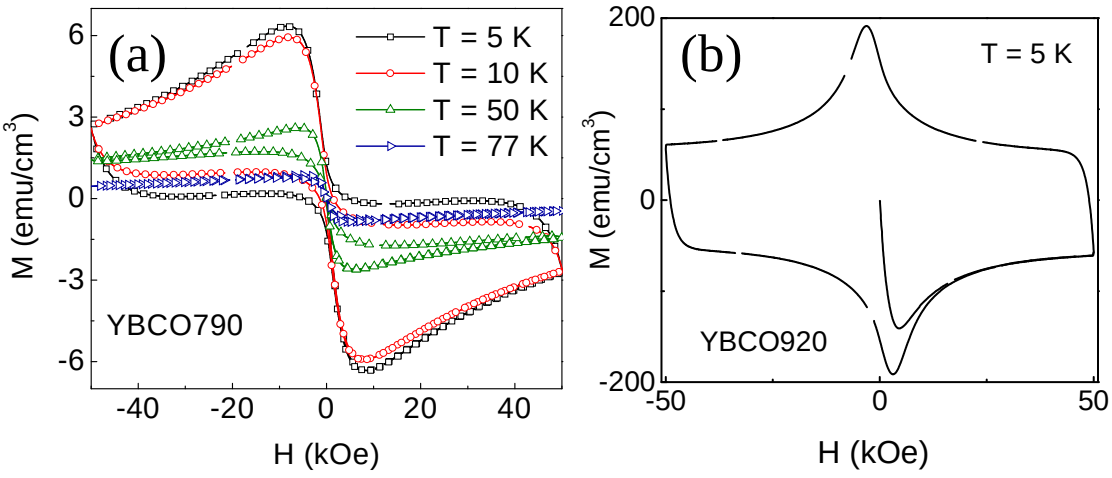

Figure 5.10. (a) Shows the *M-H* curves obtained at various temperatures. The curves are highly asymmetrical about M = 0 axis which shows the dominance of surface barrier. For a comparison, symmetrical M – H curve of bulk sample is shown in (b).

This may be due to the dominant contribution of sample holder. Figure 5.9 shows the isothermal magnetic properties of YBCO790 at T = 90 K. *M* - *H* curves in upper inset shows ferromagnetic behavior at *T* = 91 K. However, just below T_c, a diamagnetic hysteresis curve can be seen in the lower inset. The hysteresis loop is very different from the usual Z - shaped hysteresis loops observed for bulk YBCO superconductors which arises due to high degree of reversibility at temperatures near T_c [35]. Subtracting ferromagnetic contribution gave back the usual Z - shaped hysteresis curve for YBCO790 and therefore we can conclude that at *T* = 90 K, both ferromagnetic as well as diamagnetic contributions are coexisting together. It has been proposed that submicron sized powder can be considered to have a superconducting core and a ferromagnetic shell. Figure 5.10(a) shows Magnetic hysteresis behavior at low temperature for YBCO790. It should be noted that the ferromagnetic contribution above T_c is not subtracted from the data at low temperatures as the width of ferromagnetic hysteresis loops are temperature dependent. But we can neglect ferromagnetic contribution at low temperatures as value of ferromagnetic magnetization is very small as compared to diamagnetic contribution. Figure 5.10(b) shows the *M*-*H* curves of YBCO920 at *T* = 5 K, where we observe that this hysteresis curve is symmetric about *M* = 0 axis. However the hysteresis loops at all temperatures below T_c in YBCO790, loose this symmetry (figure 5.10(a)). The field decreasing part of the magnetization remains negative, consistent with the granular nature of the superconductor where the flux pinning is weak compared to the bulk or single crystals. A negative magnetization in the field decreasing part of hysteresis curve is sometimes associated to the presence Bean-Livingston Surface Barriers [36]. In bulk

samples, the Z-shaped or asymmetric hysteresis curves dominate magnetic properties only at temperatures near T_c where bulk pinning is almost negligible [37, 38]. The hysteresis curves in figure 5.10(a) show a very broad dip which may be because of a large distribution of grain sizes in the sample. Figure 5.11(a) and 5.11(b) shows the prediction of penetration field (H_p) for YBCO790 and YBCO920. There are many reports that suggest that the field at which the initial magnetization curve deviated from linearity gives the value of H_P. In the insets of figure 5.11(a) and 5.11(b), we have shown this deviation for YBCO790 and YBCO920 respectively. However we have adopted the following method to roughly estimate H_P, at which vortices start penetrating the sample. It can be calculated from the isothermal magnetization curves using the graph plotted between $[\mathrm{mod}(\delta M)]^{1/2}$ and H. Here $\delta M = M - (dM/dH)|_{H=0} H$. The field at which $[\mathrm{mod}(\delta M)]^{1/2}$ becomes linear function of applied field gives the value for H_P [39]. However we observe that the data at low fields is scattered and the exact value of H_P is

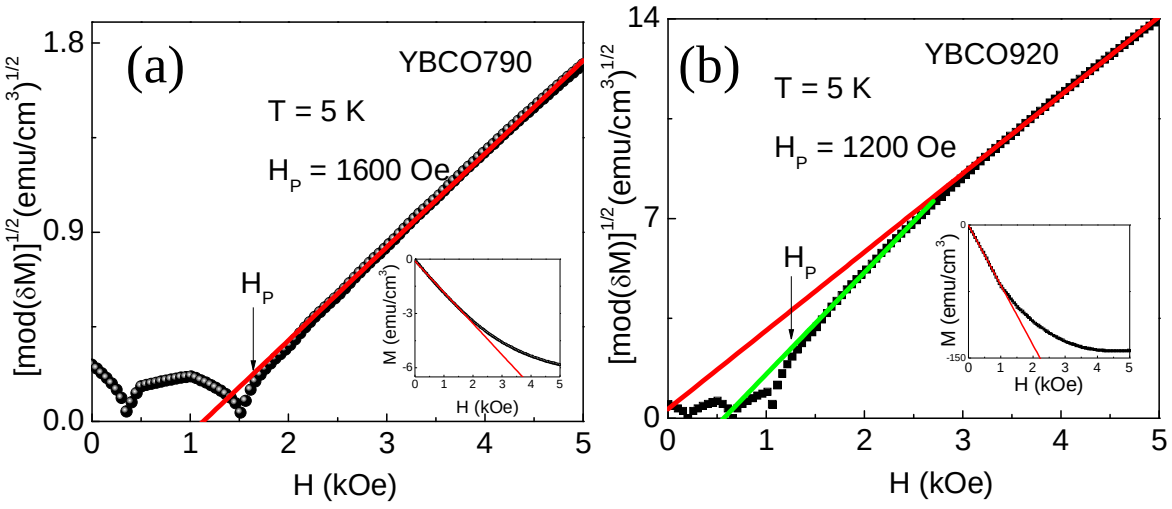

Figure 5.11. (a) and (b) shows the plots of $[\mathrm{mod}\delta M]^{1/2}$ versus H for predicting the penetration field H_P from the M–H curves of YBCO790 and YBCO920 at T = 5 K.

very difficult to obtain. For YBCO920, the slope of $[mod\delta M]^{1/2}$ versus H is high at low fields than as compared to fields above 3 kOe. This difference may occur due to the presence of sharp inter-granular regions between the grains of YBCO920 as observed in figure 5.3(d). An estimation of the intragranular critical current density for the cold pressed rectangular bar of YBCO790 and sintered bar of YBCO920 is given in figures

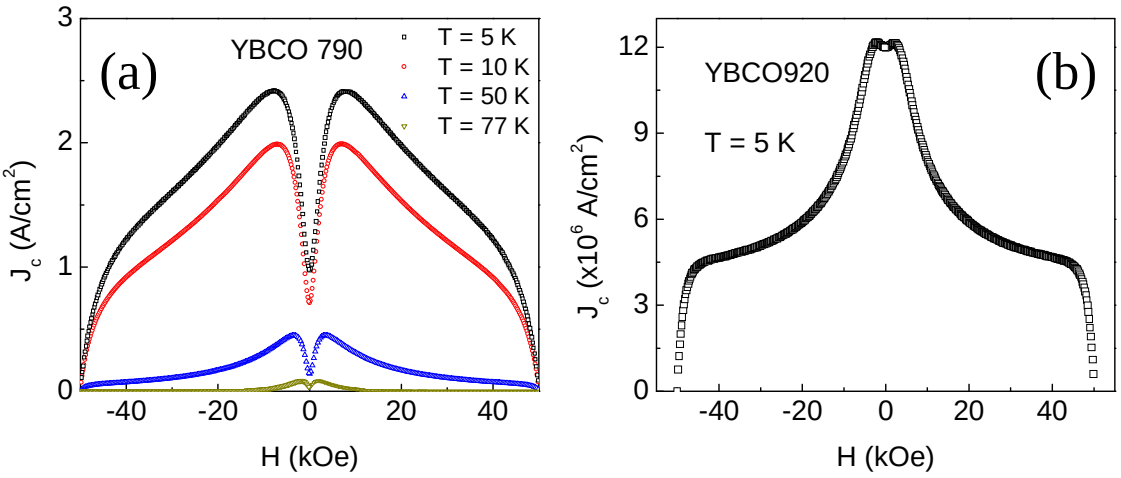

Figure 5.12. (a) and (b) shows the calculated values of J_c for the samples prepared at 790 ºC and 920 ºC respectively.

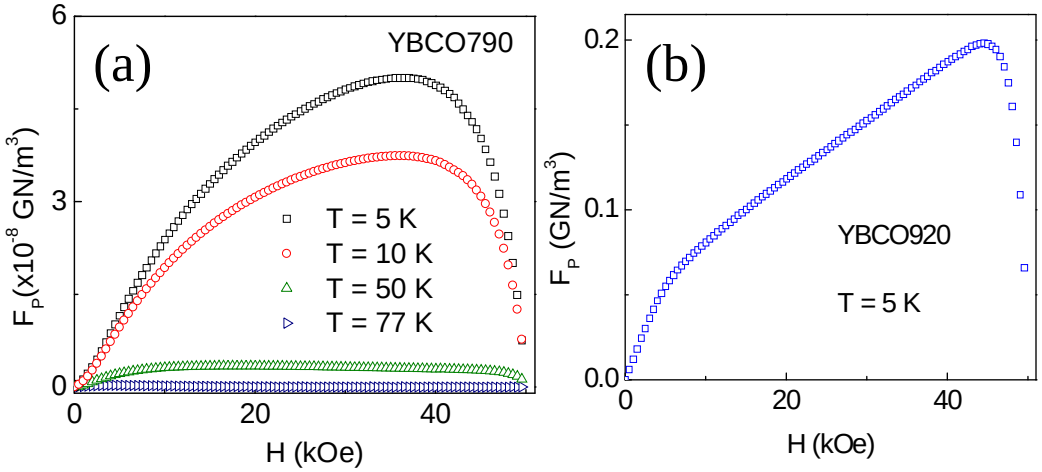

Figure 5.13. (a) and (b) shows the calculated values of F_P for the samples prepared at 790 ºC and 920 ºC respectively.

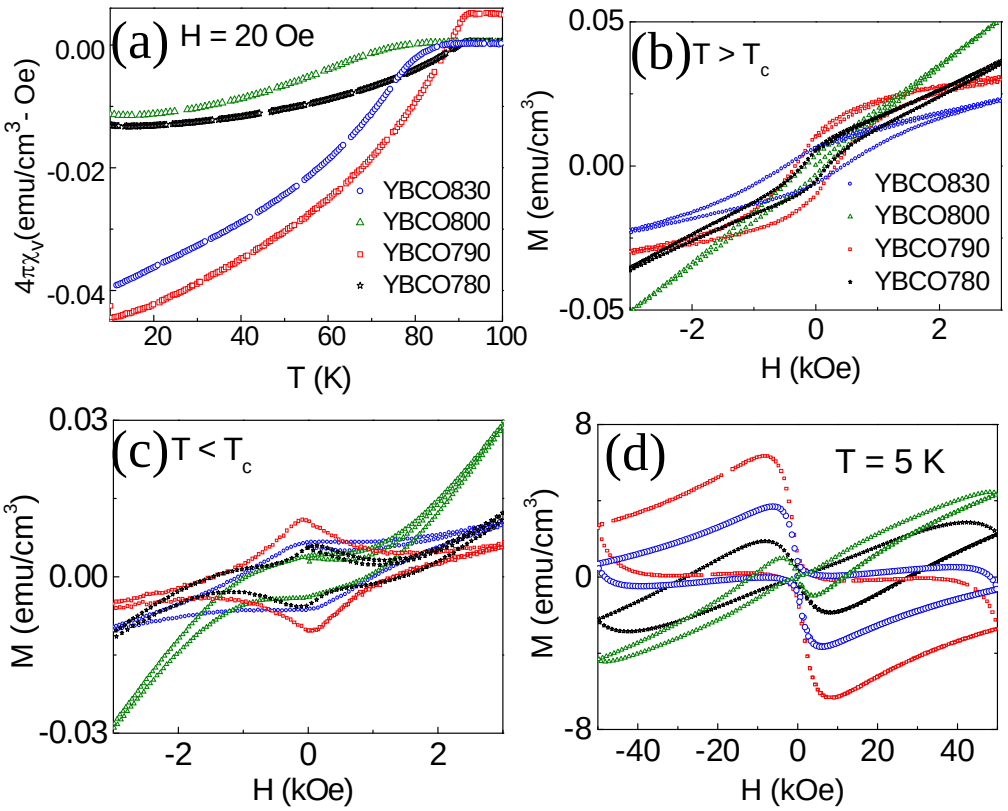

Figure 5.14. (a) shows the ZFC data of the samples prepared at various temperatures whereas (b), (c) and (d) shows the *M-H* hysteresis curves just above T_c, below T_c and at 5 K for the same samples.

5.11(a) and 5.11(b). The value was obtained according to the Bean's formula, $J_C = 20\Delta M \Big/ a\left(1-\frac{a}{3b}\right)$ A/cm^2, where $\left(\Delta M = M^+ - M^-\right)$. Here M^+ is the value of magnetization in the field increasing part of magnetic hysteresis curve while M^- is the the value of magnetization in the field increasing part. At T = 5 K, critical current density of YBCO790 is 5 orders smaller than that of YBCO920. This again may be because of the granular nature of submicron sized YBCO790. The bulk pinning force ($F_p = J_cB$, where $B = \mu_0 H$) in bulk YBCO is eight orders greater than that of submicron sized YBCO as

shown in Fig. 5.12(a) and 5.12(b). Attempts to make homogeneously distributed grains with uniform particle size, prompted us to synthesize samples at various temperatures. However, the results that we obtained were not very encouraging but we found a very interesting relation between the superconducting volume fraction and appearance of ferromagnetism in these samples. It was observed that the samples having superconducting volume fractions higher than 4% (figure 5.13(a)) showed a well distinguished ferromagnetic magnetization curves above T_c (figure 5.13(b)). The superconducting transition temperature for YBCO780 and YBCO790 is 90 K while for YBCO830 and YBCO800, it is 83 K respectively. The samples with low superconducting fraction show a much larger paramagnetic magnetization just below T_c (figure 5.13(c)) [17] which dominates over surface ferromagnetism. This explains the crossover of magnetization curves from negative to positive side of y – axis in the field increasing part itself at very low applied magnetic fields. With these observations, one can argue that, due to low superconducting volume fraction, the superconducting regions in the sample shrink; leaving a large part of the sample, non-superconducting. This in turn gives rise to increased paramagnetism. But, as the superconducting regions expand, paramagnetic moments are suppressed and surface ferromagnetism emerges, as manifested in the magnetization curves.

5.4.3 AC Magnetic properties:

In order to separate out the inter-granular and intra-granular components that may be

influencing the magnetic properties, we performed ac susceptibility of the sample prepared at 790 ºC and heated for 15 hours. In a single phase superconductor, losses ($\chi_n^{"}$) may be due to two different factors: (1) losses associated with flux penetrating the grain boundaries and termed as inter-granular losses and (2) intra-granular losses due to de-pinning of Abrikosov vortices. Here '*n*' denotes the number of harmonics. Correspondingly we should also observe two steps in the real part ($\chi_n^{'}$) of ac

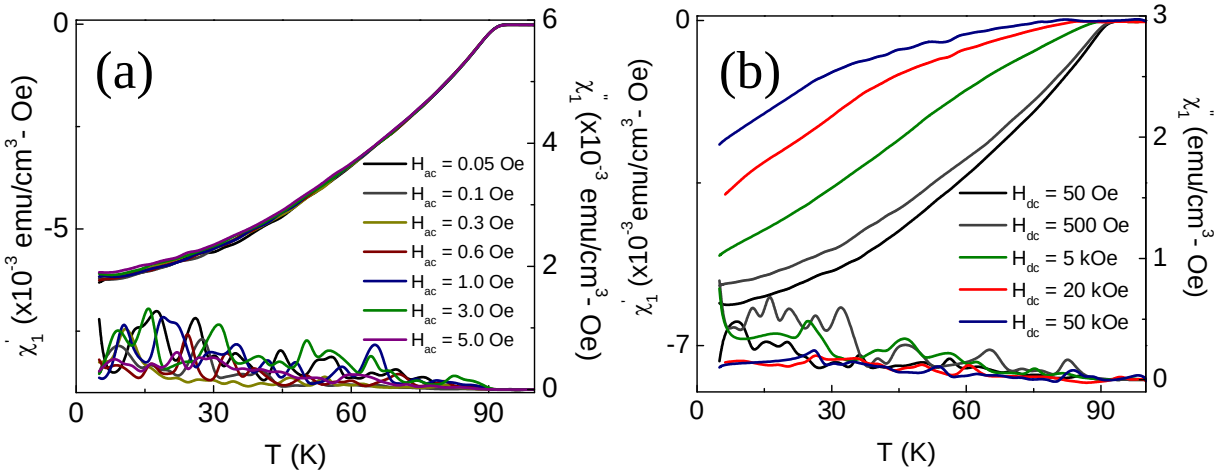

Figure 5.15. (a) and (b) shows the ac and dc field dependence of YBCO790 powder as prepared after 15 hours heating.

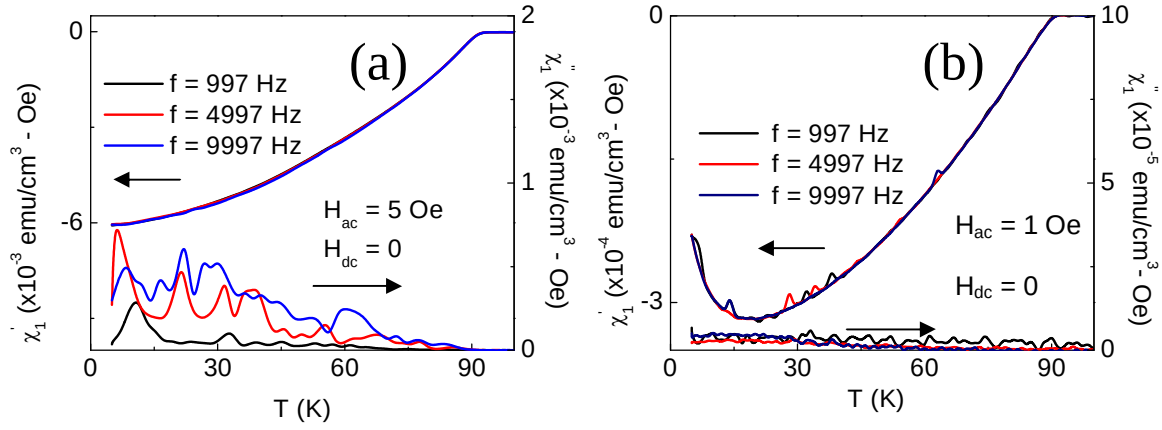

Figure 5.16. (a) and (b) shows the frequency dependence of as prepared YBCO790 powder after 15 hours and 12 hours heating.

susceptibility [40-42]. Figure 5.15(a) shows the temperature dependence of $\chi_1^{'}$ and $\chi_1^{''}$ for YBCO790 at various applied ac fields. It can also be seen that there is no ac field dependence however at a small broadening below 60 K in $\chi_1^{'}$ can be observed. The corresponding $\chi_1^{''}$ do not show any peak related to losses. Suppression of loss peaks may be because of inhomogeneous distribution as well as small size of the sub-micron sized grains. However the real component shows strong dc field dependence as seen in figure 5.15(b)) but no distinguished loss peak is observed here. The dc field dependence may arise from the weak links in the granular sample. It may also be associated with Campbell's reversible screening [41]. Figure 5.16(a) and (b) shows the $\chi_1^{'}$ and $\chi_1^{''}$ of the sample prepared at 790 ºC and annealed for 15 hours and 12 hours respectively. The real component of ac susceptibility does not show any frequency dependence, but the imaginary component though contain fluctuations, show a weak dependence. The real component $\chi^{'}$ for the sample calcined for 12 hours (on which most of the dc measurements are performed and shown here), show a minimum which may result from the combination of surface ferromagnetism and superconducting diamagnetism. This sample also shows no ac field or frequency dependence. To improve the connectivity between the grains, the cold pressed pellet of YBCO790 was heated at the same temperature (790 ºC) for 2 hours under flowing oxygen. For comparison we also heated one pellet at 940 ºC for 12 hours. The FESEM images of these samples are shown in figures 5. 4(a) and (b). Figure 5.17(a) and (b) shows the ac field dependence of $\chi_1^{'}$ and

$\chi_1^{''}$ for the two samples. In the bulk sample that was heated at 940 ºC (figure 5.17(a)), the inter-granular and intra-granular components can be well distinguished in $\chi_1^{'}$. The inter-granular T_c is lower than the intra-granular T_c. The intra-granular part is weakly dependent on the ac field whereas the inter-granular part depends strongly on the ac field [42]. This is consistent with the earlier reports on the ac susceptibility measurements on bulk superconductors. In the imaginary part the two parts are resolved only at high ac fields. The intra-granular losses appear because of the decoupling of individual grains at

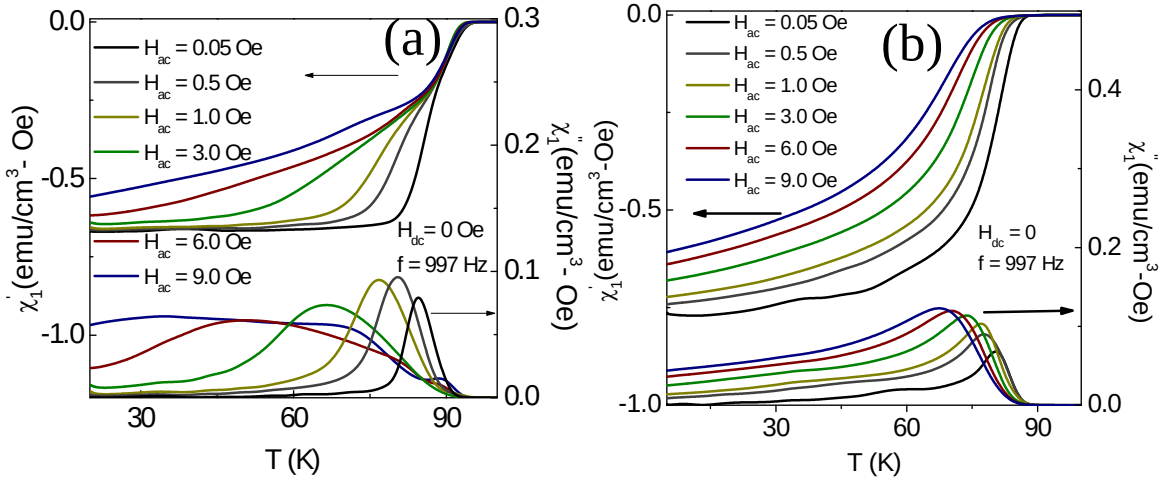

Figure 5.17. (a) and (b) shows the ac field dependence of pressed YBCO790 pellet heated at 940 ºC for 12 hours and at 790 ºC for 2 hours respectively.

high ac fields [19, 42]. The peak in the imaginary component increases and shift to low temperatures. At fields greater than 3 Oe, the peak gets suppressed and but continue to shift. As we know that the peak in the imaginary component appears only when the flux enters at the centre of the sample. So during warming (ZFC measurement in presence of ac field), the flux enters at low temperature when the ac field is high. At much higher

fields the induced current densities exceed the inter-granular critical current density that lead to the breaking of the weak links. This decouples the superconducting grains and the imaginary component only show losses due to the intra-granular regions. The above explanation is depicted in figure 5.18. The inter- and intra-granular parts are very difficult to distinguish in the real as well as imaginary ac susceptibilities of the cold pressed

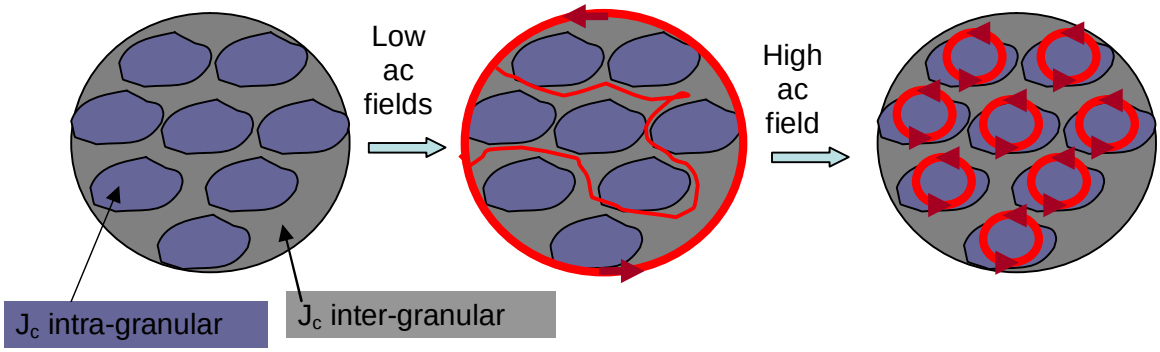

Figure 5.18. Inter-granular and intra-granular critical current with increasing ac fields.

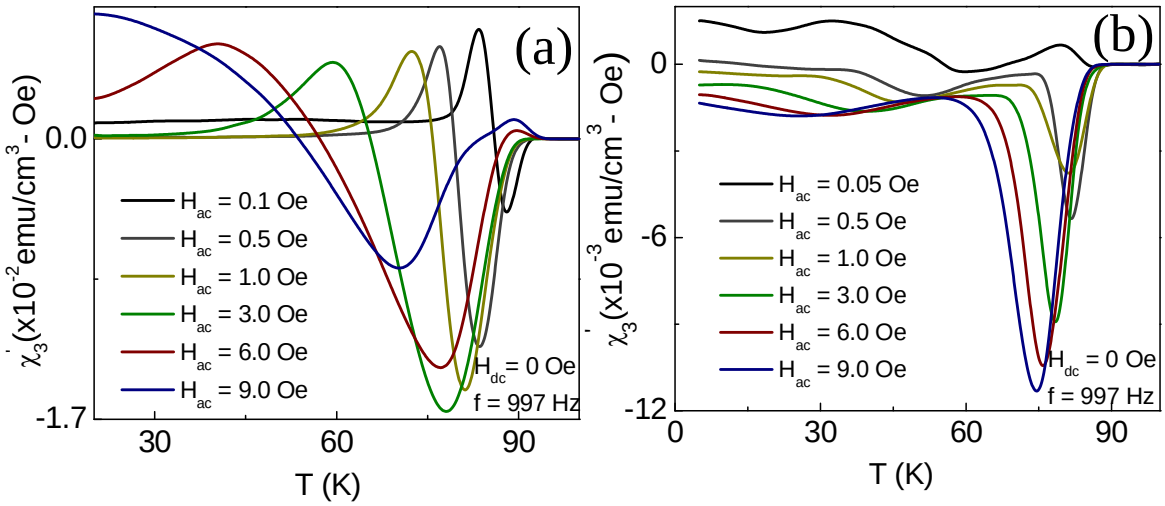

Figure 5.19. (a) and (b) shows the real part of third harmonic of the pressed YBCO790 pellet heated at 940 ºC for 12 hours and at 790 ºC for 2 hours respectively.

YBCO790 reheated at 790 ºC for 2 hours. However strong ac field dependence and appearance of the loss peak at low temperature suggests that the above observations belong to the inter-granular part of the susceptibility measurement on reheated YBCO790 [42]. Although not shown here but the intra-granular T_c, for this sample in dc susceptibility comes out to 90 K whereas the inter- granular T_c, coincides with the temperature (T = 80 K) where the loss peak emerges in the ac susceptibility. Another interesting observation in the above figure is that the loss peak starts getting suppressed at 3 Oe itself in figure 5.16(a) whereas the loss peak keep on increasing with increasing ac field in figure 5.16(b). To further resolve the inter- and intra- granular parts, we analyzed the third harmonic susceptibility of the two samples [43]. Figure 5.19(a) and (b) shows the real component of third harmonic ($\chi_3^{'}$) ac susceptibility for YBCO790 reheated at 940 ºC and 790 ºC. In figure 5.17(a), we observe well distinguished valley in the negative side of Y-axis and a peak on the positive side of Y-axis. The valley corresponds to the mid-point of ascending $\chi_1^{''}$ peak at half maxima while the peak in 3rd harmonic corresponds to mid point of descending $\chi_1^{''}$ peak at half maxima. With increasing ac field, both (peak and valley) move to lower temperatures. At H_{ac} = 3 Oe, a second peak evolves just below T_c with increasing ac field on the positive side of Y-axis and may correspond to the intra-granular loss peak in $\chi_1^{''}$. For the other sample (heated at 790 ºC) $\chi_3^{'}$ shows a valley below T_c, that becomes deeper and shift to lower temperatures with increasing ac field. In contrast to bulk, there is no positive peak, but a broad plateau that remains in the negative side of Y-axis. When YBCO790 was heated at 830 ºC for 5 hours, the positive

peak appeared (not shown here). From the above discussion it can be concluded that the appearance of positive peak indicate stronger inter-granular connection between the superconducting grains. The disappearance of imaginary part of ac susceptibility may be due to the presence of sub-micron sized grains in cold pressed YBCO790 powder. It is a well known fact that as the grain size decreases and become comparable to the London penetration depth, their diamagnetic visibility and the intragranular loss peak is lowered [40]. Similar ac susceptibility response of superconducting sub-micron sized YBCO have been reported by Deimling *et. al.*, which, they attributed to the granular nature of the sample [44]. Strong dc field dependence with a negligible ac field and frequency dependence of the ac susceptibility is an indication of reversible motion of fluxoids [41].

5.4.4 DC transport

Figure 5.20(a) shows the normalized resistance of YBCO790. The curve follows a semiconductor behavior throughout the temperature range. A small step at the T_c corresponding to the intra-granular superconducting regions of the sample can be observed. This small step can be more distinguished from the dR/dT versus T plot where the peak represents the T_c of the sample. One more peak corresponding to the onset inter-granular T_c can be observed at around 5 K. A better understanding of the inter-granular and intra-granular effects can be achieved by comparing transport and ac susceptibility measurements. Ac susceptibility of YBCO790 is shown in figure 5.16(b) where we observe only one step in real part of ac susceptibility corresponding to the intra-granular

superconductivity. Figure 5.20(b) corresponds to the sample that was heated for 15 hours at 790 ºC and corresponds to the ac susceptibility measurements in figures 5.15(a), (b) and

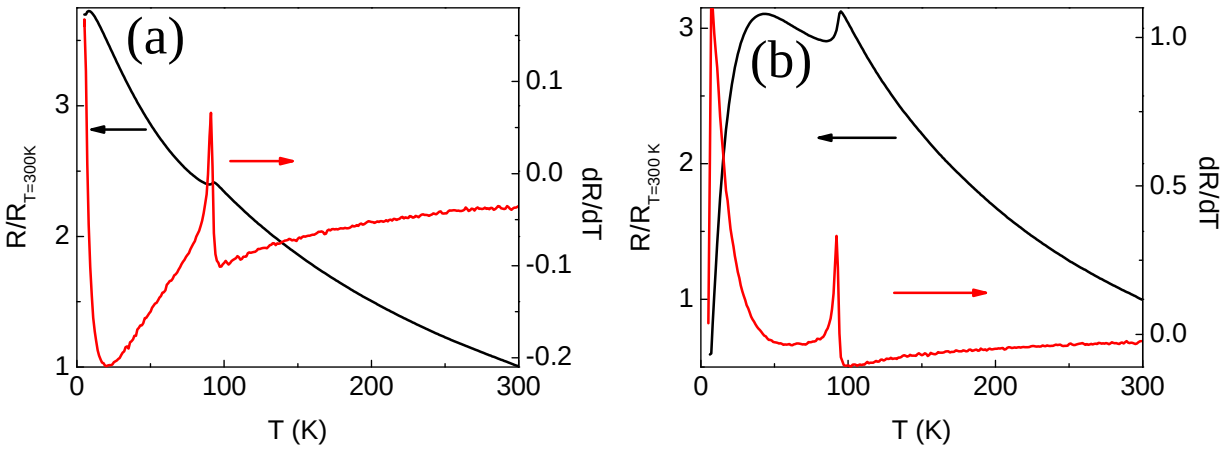

Figure 5.20. (a) and (b) shows the temperature dependent resistivity measurements on the cold pressed pellet of as prepared YBCO790 powder after 15 hours and 12 hours heating.

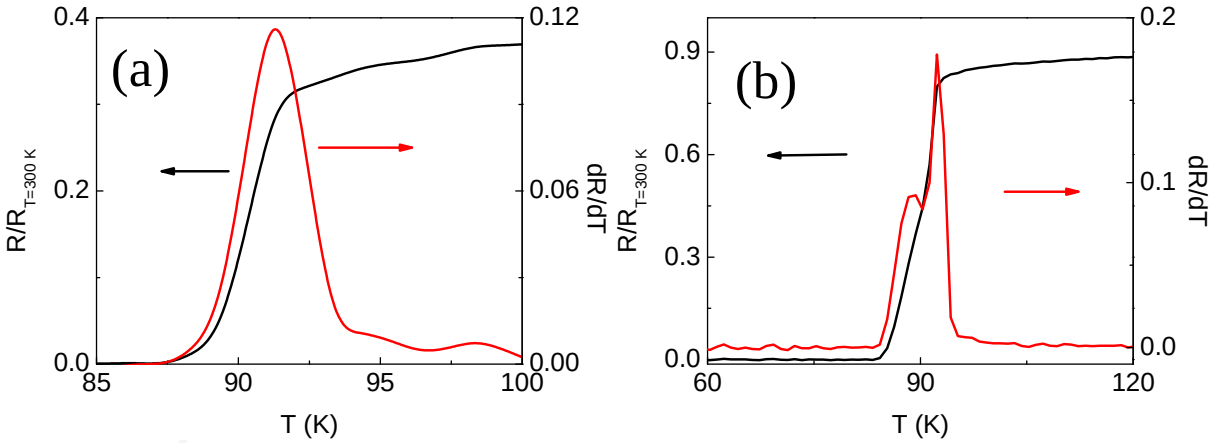

Figure 5.21. (a) and (b) shows the temperature dependent resistivity on cold pressed YBCO790 pellet heated at 940 ºC for 12 hours and at 790 ºC for 2 hours respectively.

5.16(a). As we can observe that the low temperature broadening of χ_1' in figure 5.15(a) coincides with inter-granular T_c (T = 60 K) in figure 5.20(b). The intergranular and intra-granular transitions are well distinguished from dR/dT plot. Figure 5.21(a) shows the

normalized resistance plot corresponding to the ac susceptibility of cold pressed YBCO790 heated at 940 ºC. It shows only one peak that corresponds to intra-granular T_c of the sample. However in figure 5.21(b), two peaks are clearly distinguishable in the sample reheated cold pressed YBCO790 at 790 ºC. In the ac susceptibility measurement, the two components are not clearly visible and the main component comes only from the inter-granular part. The observed differences in the resistivity as well as ac susceptibility data comes from the fact that transport measurement is a one dimensional probe that depends on a single percolation path, however susceptibility measurement involves the whole volume of the sample.

Observation of reversible magnetic properties and peak-less imaginary part of ac susceptibility in YBCO powder prepared by the aforementioned citrate-gel method reveals the mesoscopic granular nature of the sample containing sub-micron sized grains. Further, observation of hysteresis above the T_c confirms that it is a direct implication of size dependent surface induced ferromagnetism in the superconducting grains [20, 45]. The most common defect that occur on the surface of oxides are oxygen vacancies. It is expected that the same is true in the case of YBCO as well. It has been shown theoretically that these trapped electrons at the defect site can lead to extended surface states (more than 1 nm from the surface) that favor long range magnetic order [46]. These trapped electrons come from the cations in proximity to the vacant oxygen site. As a result there is redistribution of charge carriers on the cation site. The electrons associated with defects form impurity band which can mix with the redistributed 3*d* state

of Cu and hence may lead to a spin split *d* band similar to $BaTiO_3$ [47]. As these states are quite extended in the plane of the surface, they allow mediation the magnetic interactions necessary for surface ferromagnetism. One of the theoretical studies also considers cation vacancies as a source of ferromagnetism in case of non-magnetic oxides [48].

From the magnetic hysteresis curves in figure 5.14, it is observed that along with the non-linear rise in the moment for low field, there is a also a linear part to the moment at higher fields which becomes prominent in the samples with low superconducting volume fraction. The dominance of linear moment may be due to the paramagnetic non-superconducting regions resulting from low superconducting volume that implies a shrinking superconducting core with paramagnetic shell. The superconducting volume fraction does not seem to be related to the size of grains here as the grains in YBCO830 as compared to YBCO790, has large size and more agglomeration but low superconducting volume fraction. The T_c of YBCO780 is similar to YBCO790, but the superconducting volume fraction and as observed magnetization related to the field increasing part of hysteresis curve at 5 K goes to the positive side at very low dc fields. The appearance of a well resolved ferromagnetic hysteresis curve for YBCO790 with a high superconducting volume fraction confirms that observed ferromagnetism in this sample is related to the surface of these mesoscopic superconducting grains and not to impurities. Thus in the submicron YBCO particles, ferromagnetism is confined to the surface whereas superconductivity is related to the core of particles, forming like a core-shell structure. This is similar to that reported for $BaTiO_3$ nanoparticles where the core

of the particle is ferroelectric and the surface is ferromagnetic due to oxygen defect [47, 49].

5.5. Conclusions

We have demonstrated the presence of surface ferromagnetism above the superconducting transition temperature (T_c) in mesoscopic YBCO prepared at low temperature by modified citrate-gel route. A well resolved ferromagnetic hysteresis is only visible when the superconducting volume fraction is above a certain threshold otherwise the isothermal magnetization curves are dominated by paramagnetic linear response. The paramagnetic effects also dominate the hysteresis curves below T_c. We observe that in samples with low superconducting volume fraction, a cross-over from negative to positive magnetization occur at very low applied dc fields in the field increasing part of the hysteresis curve. For a high superconducting volume fraction, the magnetization in the field decreasing part remain negative or the field trapping in the superconducting is very weak. Presence of overlapping temperature dependent ZFC-FC curve confirms the reversible nature of the small/mesoscopic grain size in these granular systems. The YBCO790 sample shows a loss-less behavior in the ac susceptibility which has been attributed to the small and inhomogeneous distribution of the grain sizes. AC susceptibility do not show any inter-granular dissipation peak also which means that the related coupling is very weak in these samples. Further, from resistivity measurement it was found that the inter-granular transition temperature is as low as 5 K. Therefore the

above magnetic measurements above or below T_c are very much related to the intra-granular regions, however a weak superposition by inter-granular regions cannot be excluded as the grain not well separated. We also performed ac susceptibility measurements on cold pressed and reheated sample of YBCO790 that show a greater contribution from the inter-granular coupling and the results are compared with the bulk sample heated at 940 ºC respectively for 12 hours. Effect of weak/strong inter-granular coupling was examined by the real part of third harmonic susceptibility.

5.5. References

1. R.J. Cava, B. Battlog, R.B. Vandover, D.W. Murphy, S. Sunshine, T. Siegrist, J.P. Rameika, E.A. Rietnam, S. Zahurak and G.P. Espinosa, Phys. Rev. Lett. 58 (1987) 1676.
2. C.N.R. Rao, P. Ganguly, A.K. Raichaudhari, R.A. Mohan Ram and K. Sreedhar, Mater. Res. Bull. 23 (1987) 1469.
3. A.W. Sleight, Science 242 (1988) 1519.
4. E. Ruckeinstein, S. Narain and N.L. Wu, J. Mater. Res. 4 (1989**)** 267.
5. R. Sangines, K.R. Thampi and J. Kiwi, J. Am. Ceram. Soc. 71 (1988) C512.
6. P. Paturi, J. Raittila, H. Huhtinen, V.-P. Huhtala and R. Laiho, J. Phys. Condens Matter 15 (2003) 2103.
7. N. Knauf, J. Fischer, B. Roden, R. Borowski, B. Freitag, B. Büchner, H. Micklitz, A. Freimuth, V. Kataev and D. I. Khomskii, *Europhys. Lett*. 34 (1996) 541.
8. D. Khomskii, *Physica C* 235-240 (1994) 293.
9. S.V. Bhat, A. Rastogi, N. Kumar, R. Nagaranjan and C.N.R. Rao, Physica C 219 (1994) 87.
10. Y.R. Sun, J.R. Thomson, H.R. Kerchner, M. Paranthaman, J. Brynestad, Phys. Rev. B 50 (1994) 3330.

11. Y.C. Kim, J.R. Thompson, D.K. Christen, Y.R. Sun, M. Paranthaman, E.D. Specht, Phys. Rev. B 52 (1995) 4438.
12. M. Konczykowski, L. Burlachov, Y. Yeshurun, F. Holtzberg, Physica C 194 (1992) 155.
13. E. Zeldov, A.I. Larkin, V.B. Geshkenbein, M. Konczykowski, D. Majer, B. Khaykovich, V.M. Vinokur, H. Shritkman Phys. Rev. Lett. 73 (1994) 1428.
14. N. Morozov, E. Zeldov, M. Konczykowski,
15. R.A. Doyle, Physica C 291 (1997) 113.
16. E.H. Brandt, Physica C 332 (2000) 99.
17. H. Theuss and H. Kronmüller, Physica C 178 (1991) 37.
18. F. Gömory, Supercond. Sci. Technol. 10 (1997) 523.
19. R.A. Hein, T.L. Francavilla and D.H. Liebenberg, 1991 *Magnetic susceptibility of superconductors and other spin systems* (New York: Plenum).
20. A. Sundaresan, R. Bhargavi , N. Rangarajan, U. Siddesh and C.N.R. Rao, Phys. Rev. B **74** (2006)161304 R.
21. M. S. Li, *Physics reports* **376** (2003) 133.
22. P Köstic *et. al., Phys. Rev. B* **53** (1996) 791
23. A. I. Rykov, S. Tajima and F. V. Kusmartsev, *Phys. Rev. B* **55** (1997) 8557.
24. A. K. Geim, S. V. Dubonoj, J. G. S. Lou, M. Heini and J. C. Maan, *Nature* **396** (1998) 144.

25. R. Lucht, H. V. Löhneysen, H Claus, M. Kläser and G. M. Vogt, *Phys.Rev.B* **52** (1995) 9724.
26. E. Blinov, V.G. Fleisher, H. Huhtinen, R. Laiho, E. Lahderanta, P. Paturi, Yu. P. Stepanov and L. Vlasenko, Supercond. Sci. Technol. 10 (1997) 818.
27. H. Stroumbos, P. Odier, C. Lacour and P. Monod, J. Magn. Mag. Mater. 104 – 107 (1992) 633.
28. A.V. Narlikar, P.K. Dutta, S. B. Samanta, O.N. Srivastava, Journal of Crystal growth 121 (1992) 527.
29. Veer Singh, Subhash C. Kashyap, S.K. Agrawal, Physica C 220 (1994) 160.
30. A.V. Narlikar, 1995 *Field penetration and magnetization of High Temperature Superconductors* (New York: Nova Science)
31. P. Paturi, J. Raittila, and H. Huhtinen, *IEEE Trans. Appl. Supercond.***13** (2003) 3133.
32. A. Sundaresan and C.N.R. Rao, Nanotoday 4 (2009) 096.
33. Shipra, A. Gomathi, A. Sundaresan and C.N.R. Rao, Solid State Comm. 142 (2007) 685.
34. W. –H. Li, C. –W. Wang, C. –Y. Li, C.K. Hsu, C.C. Yang and C. –K. Wu, Phys. Rev. B 77 (2008) 094508.
35. D. X. Chen and A. Sanchez, *Phys. Rev. B* **45** (1992) 10793.
36. A.M. Campbell, J.E. Evetts and, Dew-Hughes D, Phil. Mag. 18 (2008) 313.
37. D. –X. Chen, R. B. Goldfarb, R. W. Cross and A. Sanchez, *Phys. Rev. B,* **48** (1993) 6426.

38. R. B. Flippin, T. R. Askew, J. A. Fendrich and C. J. Van der Beek, *Phys. Rev. B* **52** (1995) R9882.

39. R. Liang, P. Dosanjh, D. A. Bonn, W. N. Hardy and A. J. Berlinsky, *Phys. Rev. B* **50** (1994) 4212.

40. Y. Yang, C. Beduz, Z. Yi and R. G. Scurlock, *Physica C* **201** (1992) 325

41. F. Gömöry, *Supercond. Sci. Technol.* **10** (1997) 523.

42. R. V. Sarmago and B. G. Singidas, *Supercond. Sci. Technol.* **17** (2004) S578.

43. E. S. Otabe *et. al., IEEE Trans. Appl. Supercond.* **5** (1995) 1383.

44. C.V. Deimling, M. Motta, P.N. Lisboa-Filho, W.A. Ortiz, Journal of magnetism and magnetic materials 320 (2008) 507.

45. Sundaresan, A. and Rao, C. N. R. Ferromagnetism as a universal feature of inorganic nanoparticles, *Nano Today* **4** (2009) 96.

46. A. M. Stoneham *et. al., J. Phys.: Condens. Matter* **19** (2007) 255208.

47. R.V.K. Mangalam, M. Chakrabrati, D. Sanyal, K. Chakrabrati and A. Sundaresan, J. Phys: Condens. Matter 21 (2009) 445902.

48. J. O. Guillen, S. Lany, S. V. Barabosh and A. Zunger, *Phys. Rev. B* **75** (2007) 184421.

49. R.V.K. Mangalam, M. Chakrabrati, D. Sanyal, K. Chakrabrati and A. Sundaresan, *J. Phys: Condens. Matter* **21** (2009) 445902.

50. M. Kakihana, *Journal of sol-gel science and technology* **6** (1996) 7.

51. L. C. Pathak and S. K. Mishra, *Supercond. Sci. and Technol.***18** (2005) R67.

Chapter 6

Synthesis, characterization and superconducting properties of nanocrystalline δ-NbN

"My philosophy of life is that if we make up our mind what we are going to make of our lives, then work hard toward that goal, we never lose -- somehow we win out."

- Ronald Reagan

Summary**

We synthesized superconducting NbN using urea-nitridation technique and studied effects of topology on magnetic, transport (electrical) and thermal (heat capacity) properties of nanocrystalline δ-NbN. The superconducting transition temperature, T_c (onset) obtained from resistivity measurement on cold-pressed nanocrystalline sample having a larger agglomeration is 16 K with a transition width of 1.8 K. Above T_c, it shows ferromagnetic hysteresis curves which originates from cation/anion defects at the surface of nanoparticles. Below T_c, the isothermal magnetization curves exhibit hysteresis typical of type II superconductors due to irreversibility caused by pinning of magnetic flux lines, which is further evidenced from ac susceptibility measurements. Heat capacity measurements confirm the bulk nature of superconductivity with strong electron – phonon coupling constant. The sample with lesser extent of agglomeration does not show superconductivity down to 2 K but exhibit ferromagnetic hysteresis at room temperature. The normal state resistivity increases with a decrease in agglomeration of particles. The Debye temperature (ϑ_D) of non-superconducting sample is larger than that of the superconducting sample; however the Sommerfeld constant (γ) remains the same for both. These results are discussed on the basis of different lattice parameter of the samples.

**A paper based on the present study has been communicated to Superconductor Science and Technology

6.1. Introduction

Cubic δ-NbN is a low temperature type II superconductor having NaCl (B1) type crystal structure with two interpenetrating fcc lattices where each atom of one type lies at the centre of the octahedral created by the atoms of the other type [1]. It is a strong coupled superconductor with a London penetration depth, $\lambda_L(0) \sim 200$ nm and a coherence length, $\xi(0) \sim 4$ nm. Its superconducting transition temperature (T_c) is the highest (17.3 K) among all binary compounds and has a high critical current density ($J_c \sim 10^{10}$ A/m^2 in thin films at 4.2 K) [2] which is almost near to that of A15 (Nb_3Al or Nb_3Si) superconducting systems. This compound is the most studied binary superconducting system and finds high quality performances in applications like hard coatings [3], high field magnets [4], superconducting quantum interference devices [5], single photon detectors [6] and ultrafast digital logic circuits [7]. However, the phase diagram of this binary compound is rather complex and depending upon the ratio of Nb:N, can lead to various structural polymorphs (ranging from a simple cubic structure to a tetragonally distorted cubic structure) [8, 9] that strongly affects the electronic structure and therefore superconductivity. The density of states above Fermi level (E_F) in δ-NbN consists mainly of Nb 4*d* states and below E_F, mainly consists of a mixture of N *p* and Nb *d* orbitals. Nitrogen vacancy results in the tetragonal distortion of δ-NbN which results into diffused and lowered density of states above E_F [9, 10]. A study on the dependence of T_c on nitrogen content of δ-NbN powders has shown a maximum for the nominal composition, $NbN_{0.98}$ [11]. The method of synthesis for this study involved a very

vigorous route of heating sub-micron sized Nb powder in presence of high purity nitrogen. Thus getting a pure impurity free phase of this compound as well as a high T_c is very difficult by adopting the conventional solid state synthesis procedure. Therefore, most of the reported studies have focused mainly on thin films of δ-NbN [12, 13]. However, chemical routes involving metal – precursors under different reaction environments for synthesizing pure phase of δ-NbN have been substantially successful [14-18]. Gomathi *et al.* used urea for nitridation of $NbCl_5$ to obtain nanoparticles of superconducting δ-NbN and T_c was reported to be lower (8 K)[14]. However this is a single step, simple and versatile procedure that is reproducible, cheap as well as scalable in production and therefore holds promise in large scale applications. In our work, we followed the same synthetic procedure to make δ- NbN with a little modification in the ratios of $NbCl_5$ and urea along with slow heating and cooling rates and achieved the desired T_c. The sample prepared by this method formed clusters with a 3D network of nanoparticles. Such agglomerated clusters may also be assumed as 'islands' of strong superconductivity separated by weak superconducting regions which in our case may be defined by grain boundaries and space between the nanoparticles. Thus the weakly ordered regions introduce disorder in the superconducting cluster. Disorder induces quantum localization of the Cooper pair wavefunction that transforms a superconductor into an insulator with diverging resistance [19-22]. A profound effect of such localization was also observed in our samples where disorder due to decrease in the extent of agglomeration of nanoparticles, drove the system through Superconductor Insulator Transition (SIT).

As mentioned earlier, δ-NbN is mostly studied in the form of thin films, it's worthy to discuss some of the important results. While most of the earlier works mainly focused on the synthesis and characterization of thin films, a more recent contribution comes from the works of Pratap Raychaudhury *et. al.*[13, 23] In their studies they have mainly given a systematic experimental evidence of the effect of disorder (which they have taken in terms of Loffe-Regel parameter, $k_F l$) on the physical parameters (resistivity, Hall coefficient, upper critical field and penetration depth) of δ-NbN. Recently they also emphasized the role of phase fluctuations in the formation of pseudogap in the energy spectrum of δ-NbN that is usually observed at temperatures above the T_c. They clearly mention that the disorder in their films does not result from physical granularity but rather from atomic scale disorder such as Nb vacancies in the crystalline lattice (electronic disorder) [24]. However physical granularity has been observed to induce a gapless superconductivity in the otherwise *s*-wave gapped δ-NbN superconducting textured thin film [25]. Physical granularity is mainly influenced by the presence of weak link (Josephson Junction) between the superconducting grains. Superconductors prepared using substrate or template mediated route, though granular, usually have a very ordered arrangement of grains that are strongly or weakly connected [12, 25]. The superconducting order parameter varies uniformly throughout the sample. However in synthetic methods, where there is no control on the topology of grains, the sample behaves as an array of weak links with different inter-grain couplings and degrees of disorder. The weakening of inter-granular regions induces profound effect not only on the

T_c, but also on the magnetic [14, 26, 27], electrical [28] and thermodynamic properties [29,30] as well. In case of our sample, we have found that a decrease in the agglomeration of these nanoparticles resulted in the suppression of superconductivity though the individual grain size was almost the same for all the samples prepared at different temperatures. The main aim of our work was to prepare nanoparticles with homogeneous size distribution and study size dependent study of surface ferromagnetism in nanoparticles. However as mentioned earlier, grain sizes does not varied much, but the nanoparticles which showed superconductivity were having a higher extent of agglomeration. Attempt to minimize agglomeration resulted in a complete suppression of superconductivity. Therefore we present a brief account of relationship between microstructure and superconducting properties of δ-NbN nanoparticles.

6.2. Scope of present investigation

This work is an amalgam of a much robust chemical route for preparation of δ-NbN nanoparticles and characterization of its superconducting and normal state properties by various measurement techniques. A desired T_c of 16 K was achieved in the present study using a very simple synthetic route. The work emphasizes the role of Josephson coupling between the nanoparticles in affecting superconductivity in the 3D network of nanoparticles in the form of clusters. Josephson coupling induced effective order parameter, helps in overcoming disorder created by defects, vacancies and grain boundaries. While there are number reports on thin films of NbN superconductors, there

is no report on the systematic study of superconducting properties of nanocrystalline NbN which exhibits room temperature surface ferromagnetism.

6.3. Experimental

6.3.1 Materials:

6.3.1(a) Synthesis:

High analytical grade pure $NbCl_5$ was mixed with urea in the molar ratio of 1:12 inside a glove box as $NbCl_5$ is highly hygroscopic. Three samples were prepared by heating the mixture in an alumina boat at 900 ºC (NN900), 800 ºC (NN800) and 700 ºC (NN700) for 3 hrs in flowing nitrogen gas. The heating was done in a quartz tube placed in the furnace. Before start heating the mixture, the quart tube was purged with nitrogen gas so as to remove any humidity or other oxidizing gases. The ramping and cooling rate was kept at 5 ºC/ min. For comparison, a bulk sample was prepared by sintering the pressed nanoparticles at 900 ºC for 3 hours. The sample prepared at high temperature was dark grey which when pressed gave a metallic luster.

6.3.1(b) Reaction mechanism:

Before decomposition urea molecules construct a coordination sphere around metal ion and forms a stable structure compared with the air sensitive metal halide. At around 300 ºC, urea decomposes and react with $NbCl_5$ to form $NbCl_5 \cdot xNH_3$. Above 300 ºC, this

intermediate compound decomposes to give HCl and the following reactions take place:-

$$NbCl_5 \cdot NH_3 \longrightarrow \tfrac{1}{2}\,(Cl_2NbNH_2)_2 + HCl$$

$$\tfrac{1}{2}\,(Cl_2NbNH_2)_2 \longrightarrow \tfrac{1}{4}(Cl_2NbNH_2)_4 + HCl$$

$$\tfrac{1}{4}(Cl_2NbNH_2)_4 \longrightarrow NbN + HCl$$

The final product forms at or above 600 ºC. The NbN monomers obtained, then nucleate and grow into cubic NbN nanoparticles [42].

6.3.2 Characterization

The X- ray diffraction (XRD) patterns of the as prepared powdered sample were taken with the help of Bruker's D8 Discover. Lattice parameters of these samples were obtained by matching the XRD profiles of δ-NbN using the software *Fullprof* with the standard data (PDF # 896042). Transmission electron microscopic (TEM) images were taken using JEOL JEM 3010 fitted with *Gatan* CCD camera operating at accelerating voltage of 300 kV. For taking images the sample was first dispersed in ethanol using ultra-sonication before drop-casting it on to a carbon coated copper grid. DC and AC magnetic measurements were carried out using vibrating sample magnetometer (VSM) and ACMS options, respectively in physical property measurement system (PPMS, Quantum Design, USA). The zero field cooled (ZFC) and field cooled (FC) data were

collected by applying a magnetic field of 5 Oe while warming from 3 K to 25 K. Before taking each magnetic measurement, the field was reduced to a minimum value at temperature well above T_c. DC electrical transport measurement was performed using the conventional four-point probe technique. The probes were made of Cu wires which were glued to the sample using a silver epoxy. Magneto-transport measurements were taken in the temperature range of 5 K to 25 K, with magnetic field varying between 0 to 9 T. Before each measurement the field was zeroed at 25 K which is above the T_c of δ-NbN. Specific heat capacity at constant pressure (C_p) was measured in the heat capacity measurement option in the PPMS. Heat capacity is measured in the PPMS using a relaxation calorimetric method that takes into consideration, the thermal relaxation of sample platform with both sample and the bath. Therefore no corrections are necessary in the data prior to the poor contact between sample and sample platform.

6.4. Results and discussion

6.4.1 Structure:

Figure 6.1, compares the XRD patterns of the samples prepared at 700 ºC, 800 ºC and 900 ºC respectively. The 2θ/ω scan reveals the presence of NaCl type cubic (δ) NbN phase for all the samples without any secondary phase. The peaks shift to lower angles as the reaction temperature changes from 700 ºC to 900 ºC. Figure 6.2, shows the profile-matching pattern of the sample heated at 900 ºC. The lattice parameter for the sample

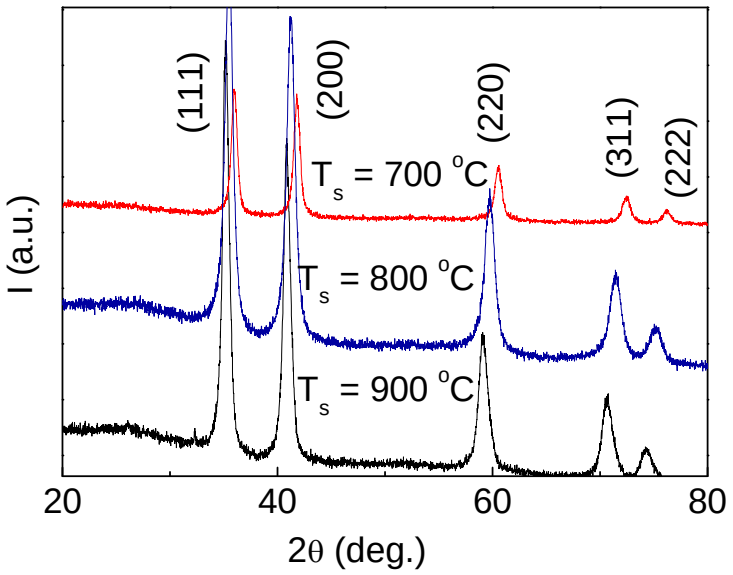

Figure 6.1. X-ray diffraction patterns of samples prepared at various reaction temperatures. The peaks shift to lower angles with increasing temperature. All the observed peaks can be indexed with the cubic (δ) phase of NbN**.**

heated at 900 ºC is 4.418 (1) Å, while for 800 ºC and 700 ºC heated samples it is 4.373 (1) Å and 4.325 (1) Å respectively. Usually the lattice constant decreases with increasing off-stoichiometry between Nb and N content and the highest value (4.428 Å) is found for a ratio of 1:1 [11]. The compound is more prone to N vacancies [31] as compared to that of Nb and it has been observed that T_c is more correlated to a higher extent of hybridization between the N 2*p* states and Nb 4*d* states [8]. Therefore, such a high value of 4.418 (1) Å for the stoichiometric δ-NbN is rarely reported for samples prepared by sold state reaction, except thin films, or samples synthesized by wet chemical route or in theoretical calculations [32]. As discussed in the introduction, a large variation in off-stoichiometry may switch the crystal structure from one polymorph to another.

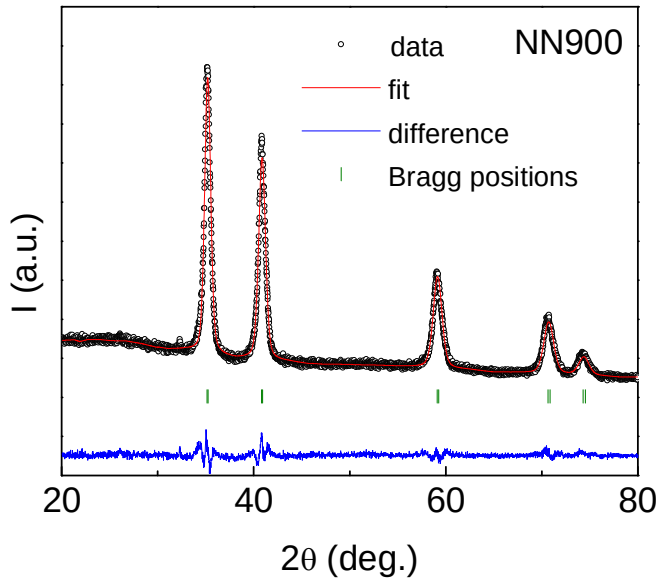

Figure 6.2. Profile matching of sample prepared at 900 ºC using the software *fullprof*. The lattice parameter obtained is 4.418(1) Å. χ^2 is 2.19. Vertical streaks show allowed symmetry reflections of δ-NbN.

The average particle size is calculated from Debye-Scherrer's formula: $d = \frac{0.97 \times \lambda}{B \times \cos\theta}$

where λ is the wavelength of X – ray, B is the FWHM (full width at half maximum) and θ is the angle at which the B is taken [12]. Using the FWHM of the sharpest peak, the crystallite size for sample heated at 700 ºC is 23 nm while for 900 ºC heated sample, it comes out to be 27 nm.

6.4.2 Morphology:

Figure 6.3, shows the morphology of δ-NbN nanoparticles heated at 700 °C (a) and 900 °C (b). We can observe that in 700 °C heated sample the grains are less agglomerated however they agglomerate more when prepared by heating at 900 °C. The grains in

NN700 are almost transparent to the electron beam and the grain boundaries can be clearly distinguished. For NN900, the TEM specimen is almost opaque and the grain boundaries are unclear. Most of the grains in the agglomerated state give an overall impact of a comparatively large size as compared to the individual grain size. The topological arrangement of δ-NbN nano-grains, can therefore be taken as a dense aggregate of weakly connected superconducting grains. Further in terms of charge transport, they can be considered as an ensemble of metallic grains embedded in a matrix of poorly conducting disordered matrix. Consequences of such an ensemble on the physical properties of NN900 are discussed later. Rings in the selected area electron diffraction (SAED) pattern confirm the polycrystalline nature of the sample (inset). Figure 6.4(a), shows the histogram for particle size distribution for NN900. It indicates

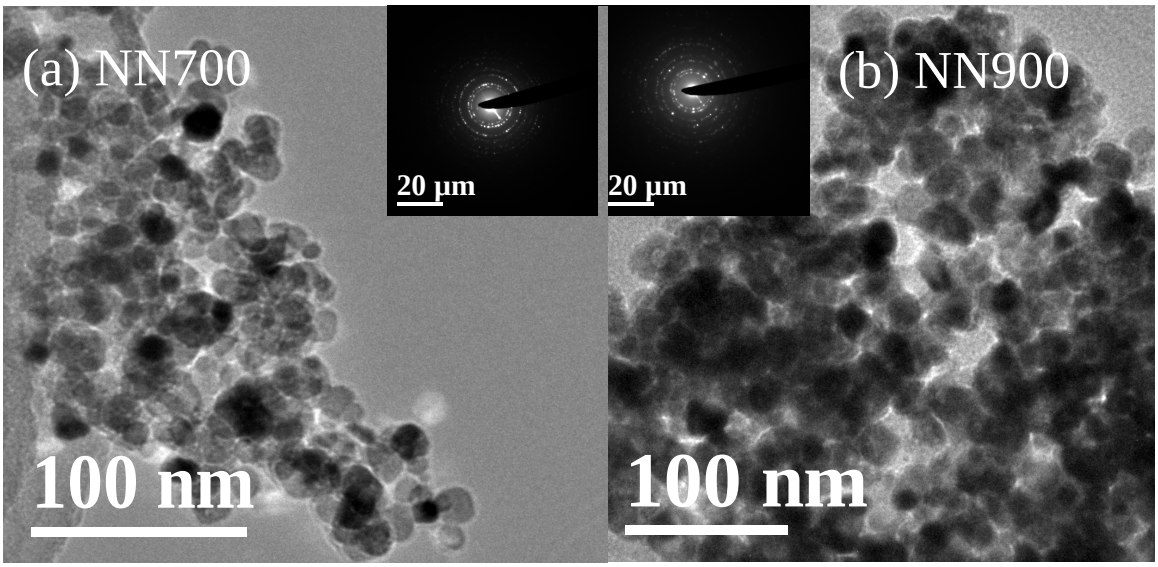

Figure 6.3. (a) Bright field TEM image of sample prepared at 700 °C. Inset shows the electron diffraction (ED) pattern of the sample. (b) Morphology of 900 °C prepared sample as shown in TEM image. Inset shows its ED pattern.

the average particle size to be 23 nm. Figure 6.4(b), shows the HRTEM image of δ-NbN nanoparticles where lattice fringes corresponding to the (200) planes can be seen clearly.

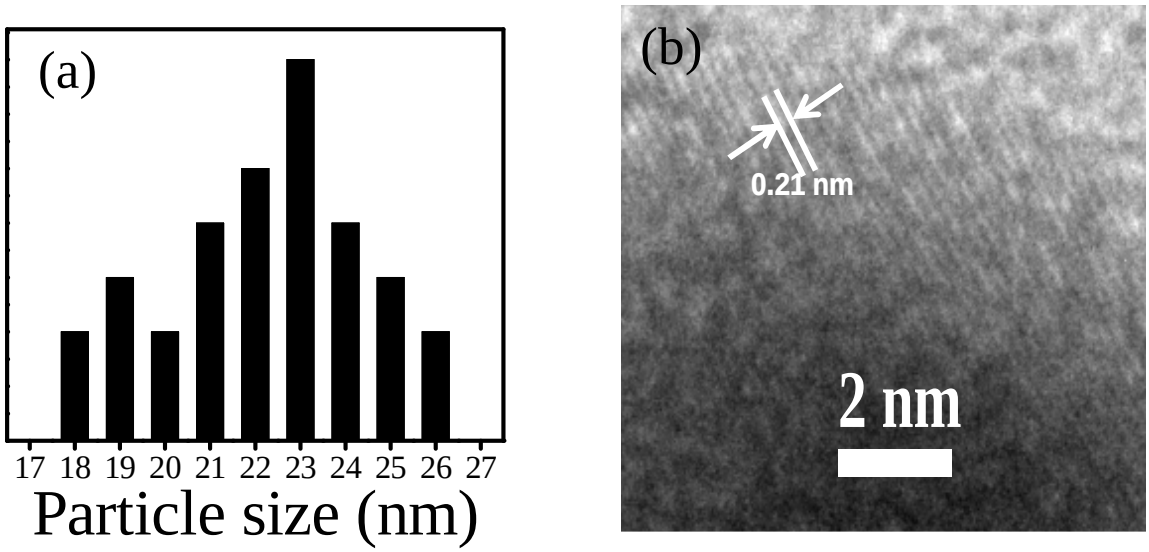

Figure 6.4. (a)Histogram of particle size disbribution of sample prepared at 900 ºC. (b) HRTEM image showing lattice fringes of the same sample.

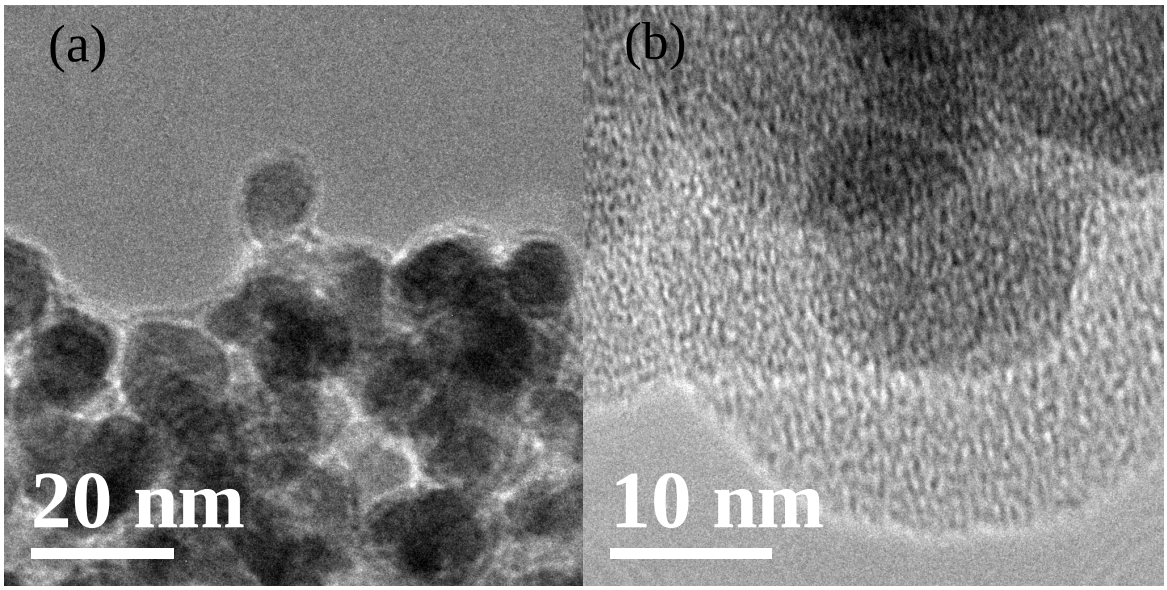

Figure 6.5. (a) and (b) shows the HRTEM image of sample prepared at 700 ºC at different magnifications.

While performing the HRTEM, we found the crystalline grains turned amorphous after interacting with high energy electron beam. The sample NN700 was more prone to turn amorphous as compared to NN900. Figures 6.5 (a) and 6.5 (b) shows highly magnified HRTEM images of NN700. As seen clearly the grains have a crystalline core with a amorphous shell. The shell slowly expands inwards with increasing electron beam exposure time. NN900 grains (figure not shown here) were more resistant to become amorphous. Therefore it was much easier to observe the lattice fringes of this sample. According to the above the above discussions on structure and morphology, we can draw the following conclusions:

- Increase in the lattice parameter of δ-NbN with increasing reaction temperature indicates a more ordered arrangement of Nb and N in their respective sublattices of NaCl type lattice. NN700, therefore has more number of vacancies (mostly N) and more prone to atomistic disorders.
- The grain are more connected in samples prepared at higher temperatures and therefore the effective size of nano-grains increases which should have an impact on the effective superconducting order parameter.
- The sample prepared at 700 °C, therefore suffers not only from the consequences of an effective small grain size but also from scattering of charge carriers by atomistic as well as grain boundary disorder. Vacancies and size have a profound effect on electronic structure that then determines various physical parameters of these nano-structures.

- The inter-granular regions formed by the diffused grain boundaries in NN900 may play an important role in the magnetic and transport properties. As discussed earlier in the introduction, that they can form regions of weak superconductivity.

6.4.3 DC magnetic properties:

Figure 6.6(a), shows the ZFC – FC data of the sample heated at 900 ºC at an applied dc field of 5 Oe. Low values of shielding as well as Meissner fraction may result from nano-sized grains and high porosity (~ 75 %) of the pressed pellet. Irreversibility between the ZFC – FC curves at a low field (5 Oe) indicates pinning of magnetic flux lines that may be occurring in the inter-granular regions and/or surface of the sample. When the applied field was increased to 5000 Oe (figure 6.6(b)), the FC data became positive which indicates, large trapped flux lines in the superconducting state of the sample. The main cause for flux trapping may be the diffused grain boundaries. However the vacancies

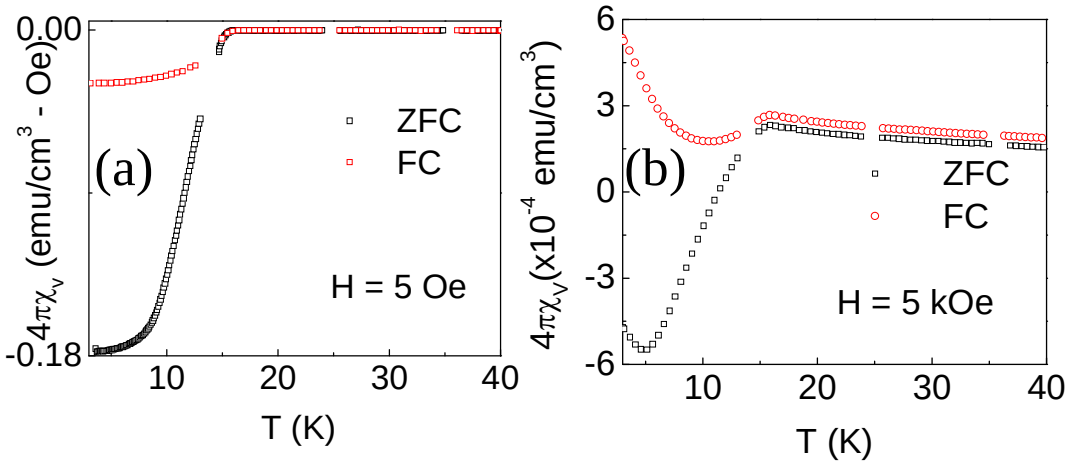

Figure 6.6. (a) shows the ZFC-FC curves of the sample prepared at 900 ºC at an applied field (H) of 5 Oe, whereas (b) shows the data at H = 5 kOe.

present on the surface of nanoparticles responsible for defect induced surface ferromagnetism may be another source of flux pinning. Getting a positive FC curve, issimilar to paramagnetic Meissner effect, observed in many granular superconducting samples where large number of flux lines get compressed near defects [33]. The sample prepared at 800 ºC showed a very small diamagnetic response in ZFC data with a T_c at around 10 K, while no trace of superconductivity was observed in the sample prepared at 700 ºC. The bulk sample also showed a T_c of 16 K similar to NN900 but with a much

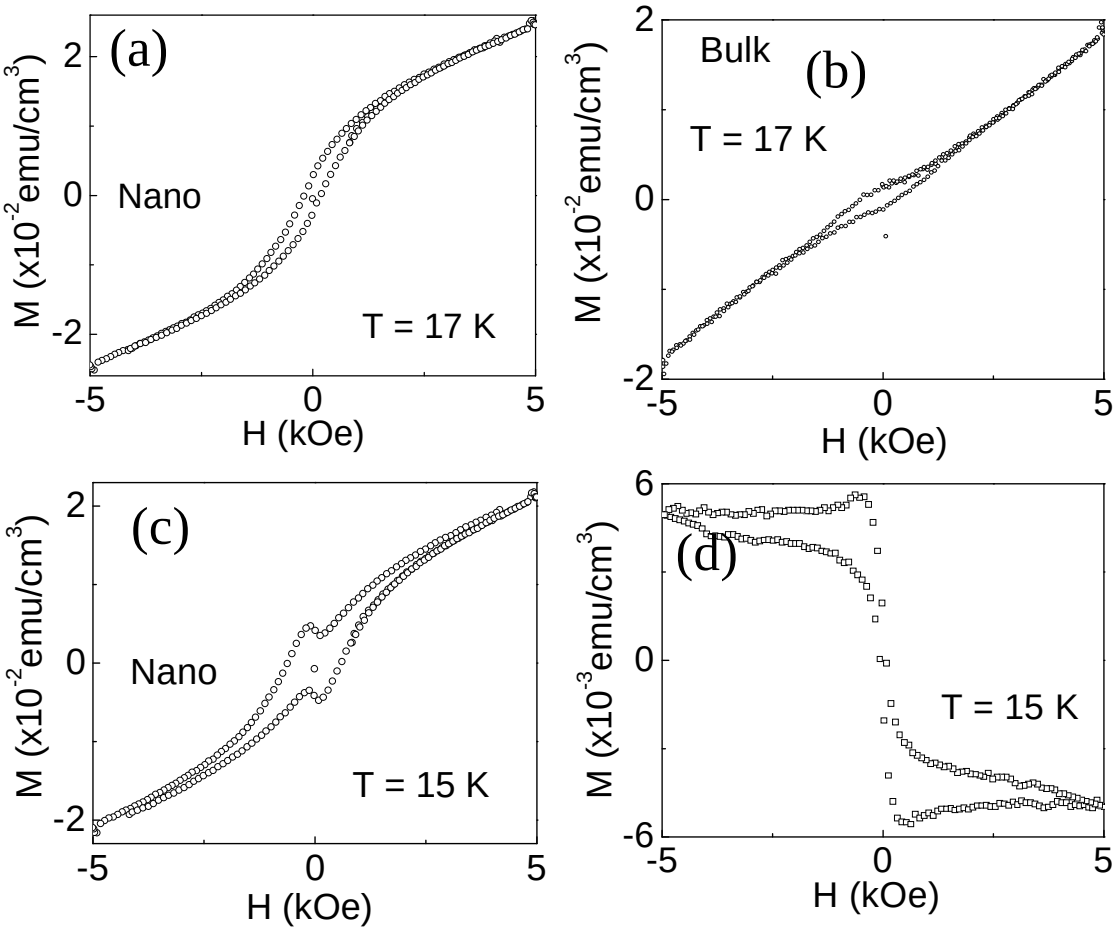

Figure 6.7. Magnetization versus field (*M-H*) curve just above T_c for the sample prepared at 900 ºC. (b) *M-H* curve for bulk sample. (c) Magnetic hysteresis curve for 900 ºC heated sample. (d) corresponds to the hysteresis curve obtained by subtracting the hyteresis curve in (a) from that of (c).

higher value of screening fraction (ZFC). Figure 6.7(a) shows the M – H curve of δ-NbN prepared at 900 °C at T = 17 K. The curve shows a hysteresis typical of soft ferromagnets. The coercive field is around 150 Oe. The curve does not saturate at any field and shows a linear response typical of paramagnets above 2 kOe that may come from the core of the particles as the magnetism is confined to the surface as discussed below. The bulk sample, at the same temperature, however showed an overall paramagnetic behavior in the whole field range. The observation of ferromagnetism in nano-grains of δ-NbN is consistent with the earlier reports of the surface defect induced ferromagnetism in nanoparticles [14,34,35]. Surface ferromagnetism has been suggested to be a universal feature of almost all nanoparticles of otherwise nonmagnetic inorganic materials which arises due to surface cation or anion vacancies resulting in ferromagnetic spin polarizations [35]. As discussed earlier, one of the possible vacancies in δ-NbN may be due to N, which in case of NN900 may be more confined to the surface rather than in the core of the sample. Samples prepared at 800 °C and 700 °C also show ferromagnetic hysteresis curves and as they are non superconducting, the observation of surface ferromagnetism extends well down to low temperature measured (T = 3 K). Figure 6.7(c) is the hysteresis curve for NN900 just below the T_c of the sample. In principle, the magnetization in the increasing field branch of the hysteresis curve should be negative; however, we see a switch from negative values to positive values at a low applied field: H = 2 kOe. An attempt to subtract the hysteresis curve obtained at T = 17 K from that obtained at T = 15 K resulted in a Z- shaped hysteresis curve characteristic of type II superconductors near temperatures below T_c

(figure 6.7(d)). This observation is very similar to what we got in case of sub-micron sized YBCO grains in chapter 5 where we proposed about the possible coexistence of superconductivity and ferromagnetism in superconducting nanoparticles. There are similar reports about such a prospect published by other groups [36, 37]. Coexistence of surface ferromagnetism and a ferromagnet in nanoparticles make them suitable to study interface between a superconductor and a ferromagnet, which is otherwise studied using bi-layered thin films consisting of a ferromagnet and a superconductor [38].

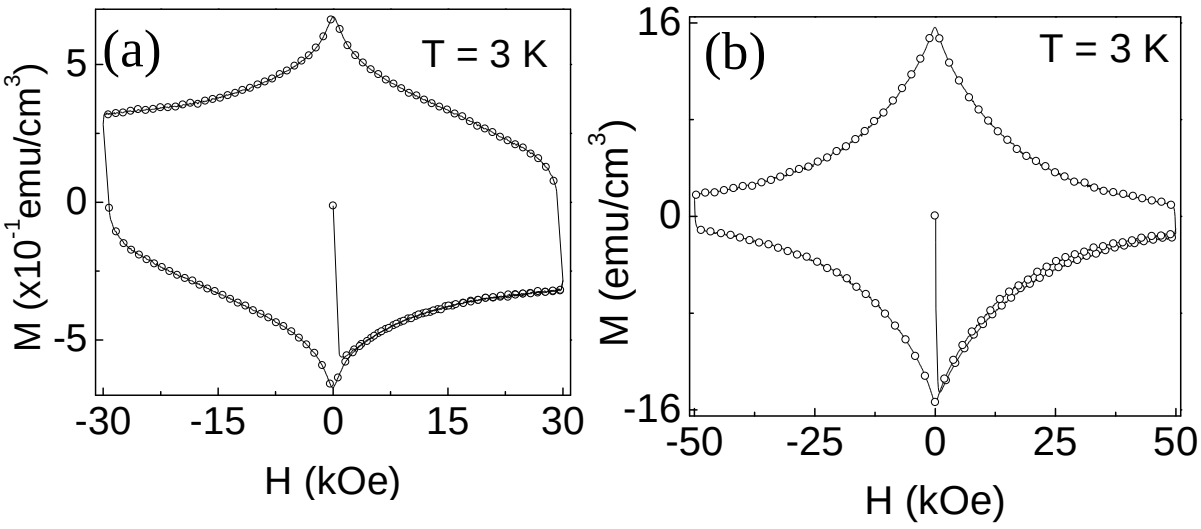

Figure 6.8. (a) *M-H* curve of NN900 nanoparticles at T = 3 K whereas (b) is the M-H curve of the bulk sample

Figure 6.8(a), shows the typical hysteresis curve for NN900. It is to be noted that the curvature of the superconducting hysteresis curve in the 2nd and 4^{rth} quadrant for nanoparticles is different from that of the sintered pellet (figure 6.8(b)). An attempt to subtract the ferromagnetic hysteresis loop obtained for sample synthesized at 800 °C

from the hysteresis curve of 900 °C sample (figure 6.9(b)) resulted in asymmetric hysteresis curve about the field axis. The shape of the curve resembles the hysteresis curve measured when the maximum field applied was only 30 kOe (figure not shown).

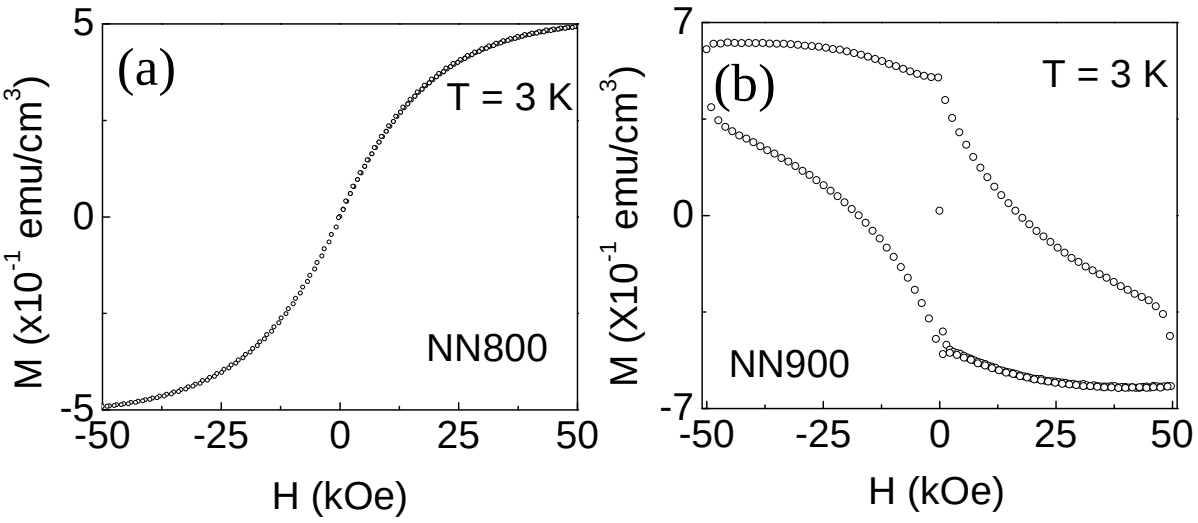

Figure 6.9. (a)*M-H* curve for the sample prepared at 800 ºC. (b) *M-H* curve of NN900 sample obtained by subtracting the curve in figure 6.9(a) from 6.8(a).

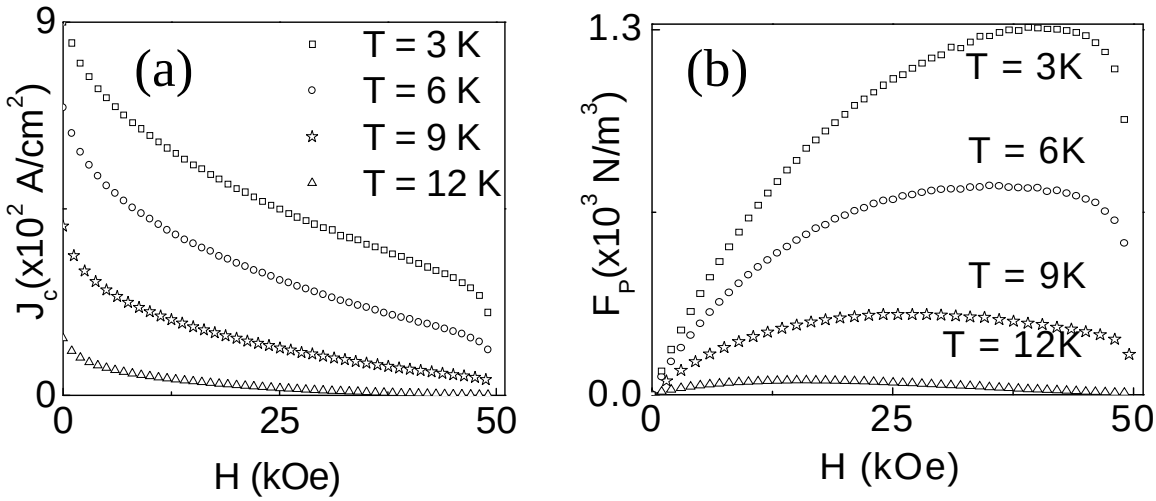

Figure 6.10. (a) Critical current density (J_c) for the sample prepared at 900 ºC and (b) is the pinning force (F_p) obtained using the Bean's critical model.

Figures 6.10(a) and 6.10(b) show the critical current density ($J_c(H)$) and flux pinning energies obtained from hysteresis curves obtained at various temperatures below T_c. Considering the sample to be a rectangular bar, we used Bean's critical state formula $J_c = 20\Delta M/a(1-a/3b)$ with $a < b$. The pinning energy is given as the product of $J_c \times \mu_0 H$. For the bulk sample the J_c and F_p were two and five orders more than that of the nanoparticles respectively.

6.4.4 AC magnetic properties

In order to further investigate the nature of flux pinning, we measured ac susceptibility at various frequencies, dc and ac fields. As discussed earlier, the ac susceptibility is a complex quantity: $\chi_n = \chi_n' - i\chi_n''$, where the real part χ_n' is the in-phase signal and the imaginary part χ_n'' is the out of phase signal [39]. Irreversible superconductors induce nonlinearities which in turn give rise to higher harmonic susceptibilities with n = 2, 3, 4… For Bean's critical state model, where the critical current density is independent of applied magnetic field, only odd harmonics are possible. However, Kim – Anderson model predict possibility of even order harmonics in the presence of superimposed dc fields [40]. The shapes of fundamental harmonic susceptibility do not change with external conditions like frequency, ac field, dc field and temperature. However, higher harmonics do show a change and therefore can be more informative than the first harmonic. Figure 6.11(a), shows the real part of first harmonic susceptibility (χ_1')

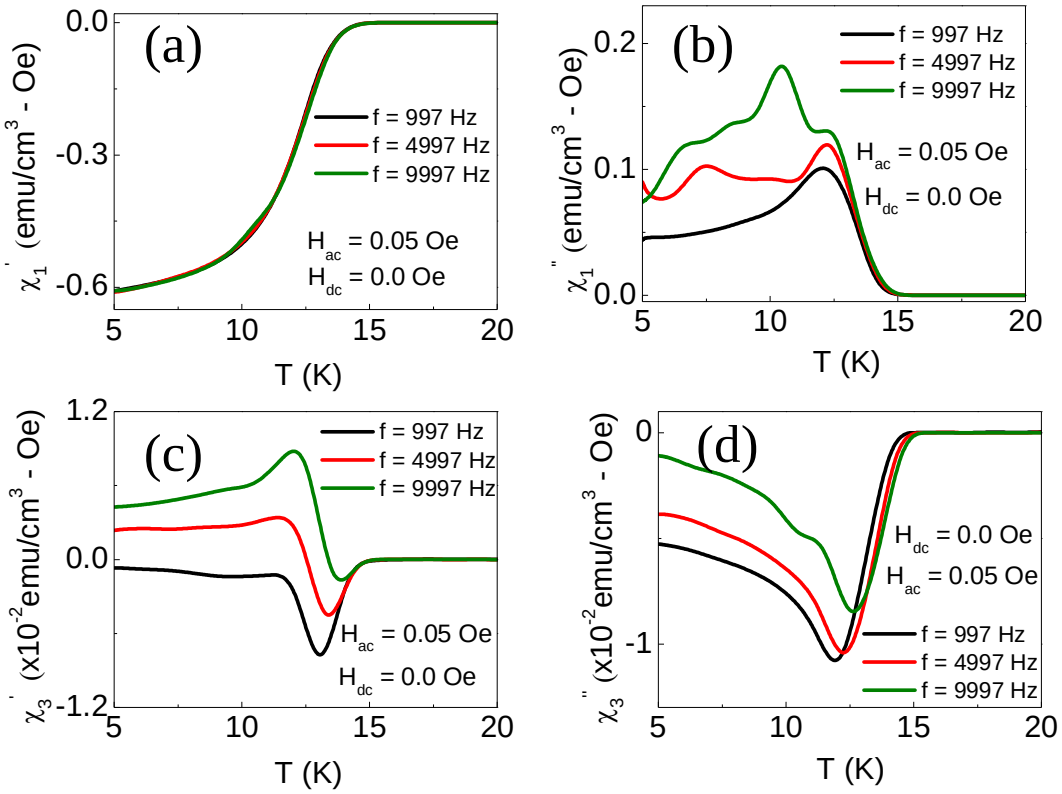

Figure 6.11. (a) and(b) Frequency dependence of the real and imaginary part of first harmonic of ac susceptibility. (c) and (d) corresponding real and imaginary part for third harmonic.

at various frequencies. Typically in granular samples, two steps are observed in the real part of fundamental ac susceptibility ($\chi_1^{'}$). The first step near T_c corresponds to intra-granular currents whereas the second step corresponds to the inter-granular currents. Usually, the inter-granular critical current density is lower as compared to intra-granular J_c due to weak superconducting order parameter in between the grains. During measurement, the ac field first penetrates the inter-granular regions at low temperature. As temperature increases the field penetrates into the intra-granular regions. Figure 6.11(a) shows only one step and no frequency dependence. However if viewed carefully,

we can observe some spread between T = 10 K and T = 12 K. In contrast, $\chi_1^{''}$ shows very strong frequency dependence (figure 6.11(b)). For f = 997 Hz in , there is only one peak below T_c whose magnitude increases and shifts to higher temperature with increasing frequency. At higher frequencies, more number of peaks are visible which may arise due to inhomogeneity in the degree of agglomeration of particles. Such frequency dependence signifies the presence of flux creep [41]. However frequency dependence can also occur for losses due to eddy current at high frequency but this possibility is ruled out due to the presence of higher harmonics. Frequency dependences of real ($\chi_3^{'}$) and imaginary ($\chi_3^{''}$) of third harmonic are shown in figures 6.11(c) and 6.11(d). Figure 6.12(a) shows the temperature dependence of the real part obtained at 997 Hz at various ac fields. There is strong ac field dependence. The corresponding imaginary part is shown in figure 6.12(b). With increasing ac field, the loss peak becomes broad and shifts to lower temperature (T_p). The single broad peak may contain both inter-granular as well as intra-granular contributions coming from the nano-crystalline sample. At high ac field (5 Oe), the loss peak become very broad because of electromagnetic decoupling of grains in the cluster as larger applied ac fields induce larger screening currents which exceed the upper bound imposed by $J_{c\text{-}inter}(T)$. The exact temperature dependence of $J_{c\text{-}inter}(T)$ depends largely upon the type of inter-granular coupling. This can be found by fitting $J_{c\text{-}inter}(T)$ as a function of $(1\text{-}T_p/T_c)^{\beta}$ where β is the fitting parameter. Here, $J_{c\text{-}inter}(T)$ is calculated from the peak value of $\chi_1^{''}$ using the expression $J_c = 2h_0 / xd$. Peak in $\chi_1^{''}$ occurs at x = 1.942 [12]. For our sample, the value of β is 1 which is an indication of Josephson current

associated with *S-I-S* type junctions for the inter-granular matrix. Figure 6.12(c) shows the real part of third harmonic. We observe a dip/valley corresponding to the mid point of the peak in the imaginary part of first harmonic ($\chi_1^{''}$). These valleys are further resolved in the imaginary part of the third harmonic ($\chi_3^{''}$) .

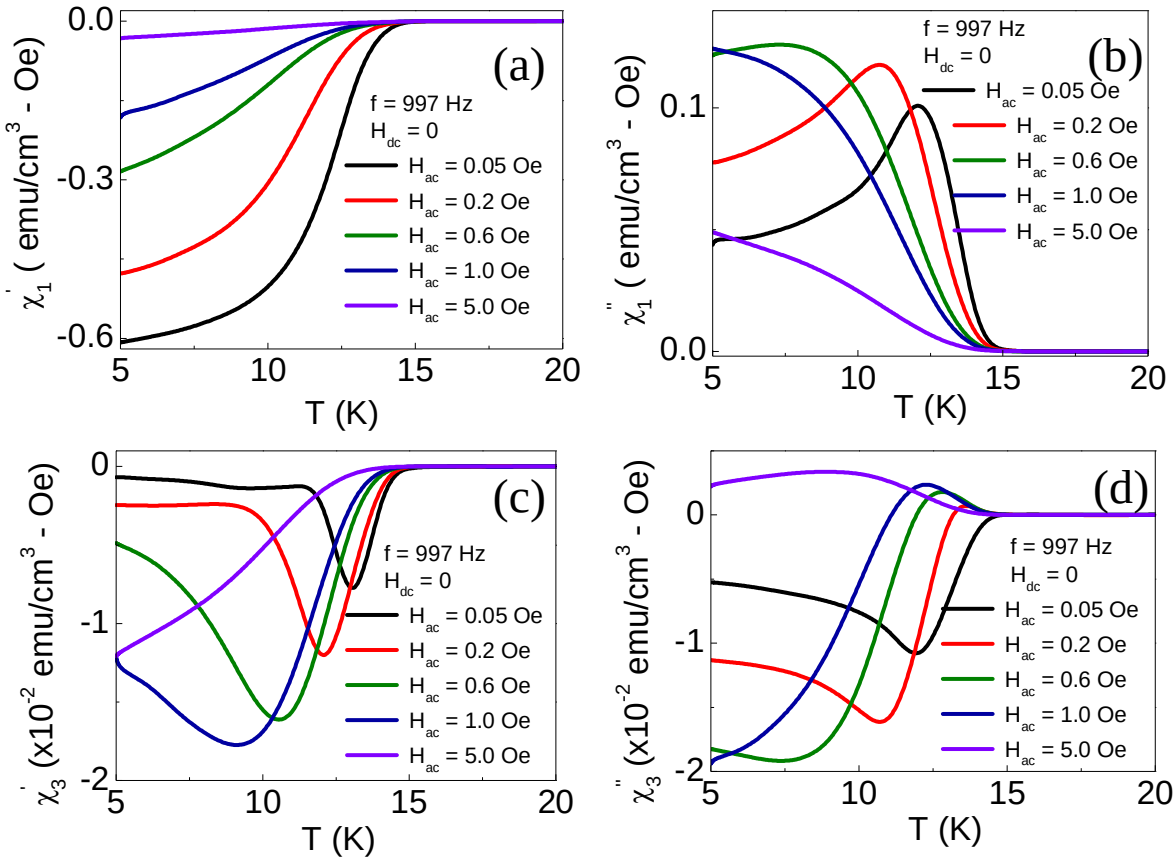

Figure 6.12. (a) and(b) Ac field dependence of the real and imaginary part of first harmonic of ac susceptibility. (c) and (d) corresponding real and imaginary part for third harmonic.

As seen in Figure 6.12(d), the shape of the third harmonic curve is very different from that observed in bulk MgB_2 or YBCO [43, 44] but resembles that of powder and thin

discs [45, 46]. The important observation here is that a positive peak emerges just below T_c with increasing ac field and becomes very broad at high field. Authors in ref. [45] considered the occurrence of positive peak to the reversible fluxoid motion in small grain sized Rb_3C_{60} superconductor. In another discussion, it is associated with intra-granular component. The valley or negative peak observed at low ac fields can be associated with inter-granular component [47]. Figure 6.13(a), shows the dc field dependence of the real

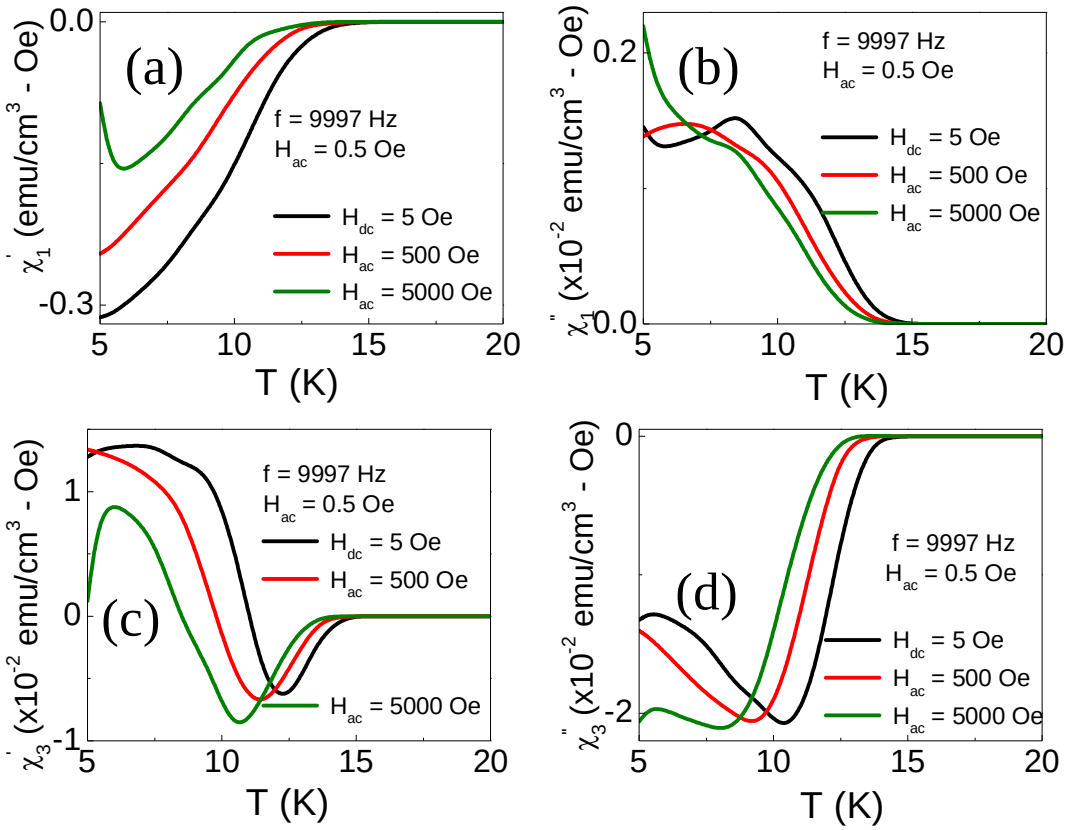

Figure 6.13. (a) and(b) Dc field dependence of the real and imaginary part of first harmonic of ac susceptibility. (c) and (d) corresponding real and imaginary part for third harmonic.

part of fundamental ac susceptibility. As expected, the screening fraction gets reduced with increasing dc field. The peaks in the imaginary part (figure 6.13(a)) were very broad

even for a small (5 Oe) dc field. The corresponding shapes of the real and imaginary parts of ac susceptibility are shown in figures 6.13(c) and 6.13(d). The above observations in the ac susceptibility fit well with Ishida – Mazaki model where a multi-connected network behaves as a single screening current loop due to coherency maintained between individual Josephson Junctions throughout the sample [48]. The pinning of flux lines is very weak in the inter-granular region and therefore we almost get a reversible fluxoid motion at low magnetic (dc or ac fields). Another interesting feature of the nanocrystalline sample is the presence of second harmonic susceptibility without any

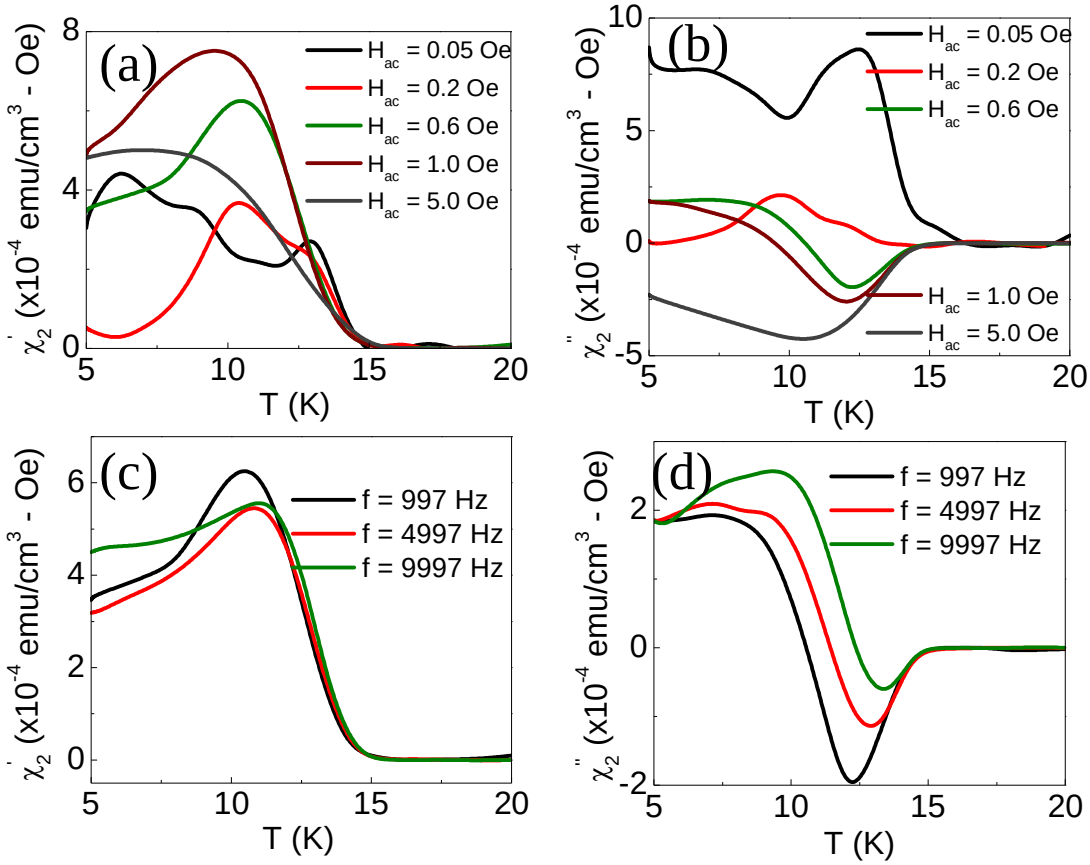

Figure 6.14. (a) and(b) Ac dependence of the real and imaginary part of second harmonic of ac susceptibility. (c) and (d) corresponds to the frequency dependence of the real and imaginary part for second harmonic.

applied dc field; however, the magnitude is two orders less than that of the third harmonic susceptibility. Figures 6.14(a) and 6.14(b) show the ac field dependence of $\chi_2^{'}$ and $\chi_2^{''}$, whereas figures 6.14(c) and 6.14(d). According to Kim, second harmonics are generated only in the presence of a superimposed dc field on the ac field. No dc field was applied during the measurements. Presence of second harmonics indicates trapping of magnetic flux either in the sample or the PPMS magnet.

6.4.5 Electrical transport

As the nanoparticles are agglomerated, we found it interesting to perform the resistivity measurements on the cold pressed rectangular bar. Figure 6.15(a), shows the temperature dependence of zero field resistivity for the sample prepared at 900 ºC. As expected for cold pressed nanoparticles, the temperature dependent resistivity profile above T_c shows a

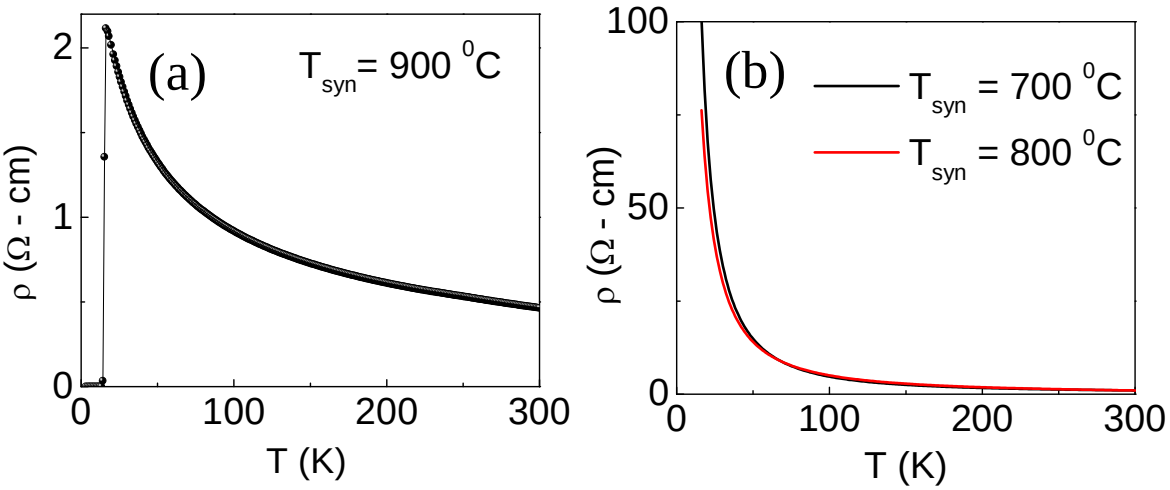

Figure 6.13. (a) and(b) Resistivity versus temperature plots for samples synthesized at 900 ºC, 800 ºC, 700 ºC respectively.

negative temperature dependence for the entire temperature range. However, at T = 16.2 K, a sharp drop in resistivity is observed and it becomes zero at 14.4 K with a narrow transition width ΔT_c = 1.8 K. Figure 6.15(b) shows the ρ-T curve for samples prepared at 800 ºC and 700 ºC respectively. We see that the resistivity increases with decreasing synthesis temperature consistent with decrease in agglomeration for the samples prepared at lower temperatures. The temperature dependence of conductivity in 3D disordered granular systems mainly follow Mott variable range hopping (VRH) model [49, 50]. According to VRH model, it is energetically favorable that the charge carriers can hop over a larger distance. In a simple activated transport, the charge carriers often hop to nearest neighbors. In VRH model, the temperature dependence of conductivity is given as: $\sigma = A(T)\exp\left(-\left(T_0/T\right)^{1/4}\right)$, where $A(T)$ is the temperature dependent pre-factor and T_0 is the Mott temperature. T_0 depends upon the density of states near Fermi level ($N(E_F)$) as: $T_0 = \lambda\alpha^3/k_B N(E_F)$. Here, λ is a dimensionless constant, α is the Bohr radius and k_B is the Boltzmann constant. Attempt to fit the data with this model resulted in a curve with positive curvature between $ln\ [\sigma]$ and $T^{-1/4}$. The VRH model takes into account a constant $N(E_F)$ and negligible electronic correlation effects which is not always true in real systems. According to Ambegoaker, Halperin and Langer (AHL) model, $ln\ [\sigma]$, when plotted against $T^{-1/4}$, has a positive curvature if the second derivative of $N(E_F)$ with respect to energy is positive [51]. On taking a linear temperature dependence of the pre-factor for fitting the conductivity curve we found a linear relation between $ln\ [\sigma T^{-1}]$ and $T^{-1/4}$ (figure 6.16(a)). This relation is also found to be valid for 800 ºC and 700 ºC

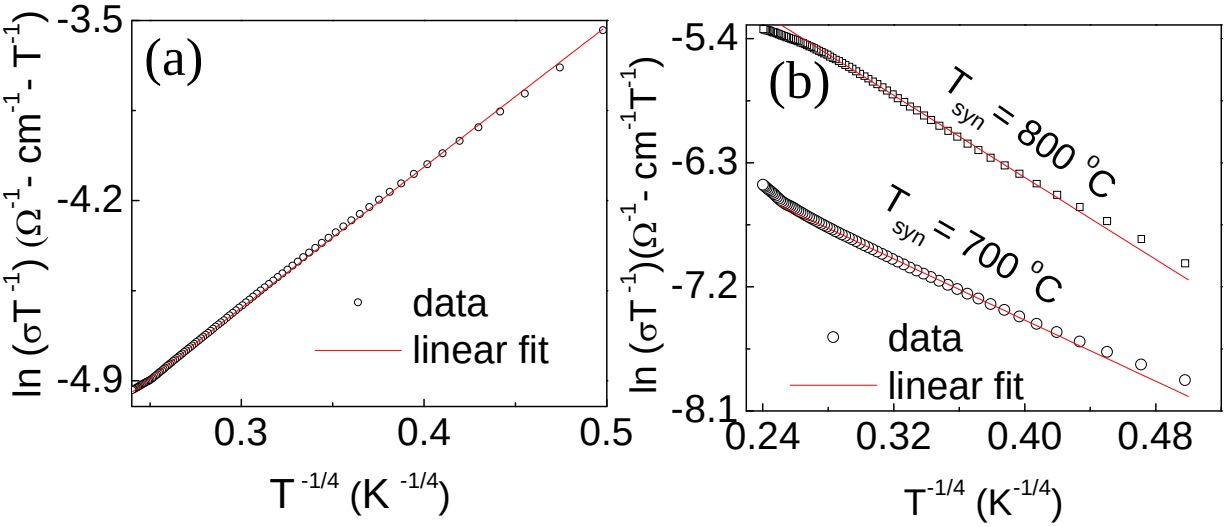

Figure 6.16. (a) and (b) are the plots of $\ln(\sigma T^{-1})$ versus $T^{-1/4}$ for samples synthesized at 900 ºC, 800 ºC, 700 ºC respectively.

samples (figure 6.16(b)). AHL viewed the medium as a resistance network where regions of high conductivity are connected by less conductive resistors through which electrons are able to move by phonon assisted tunneling. Figure 6.17 shows a cartoon of the AHL model for granular systems. In such a medium, AHL proposed that the overall

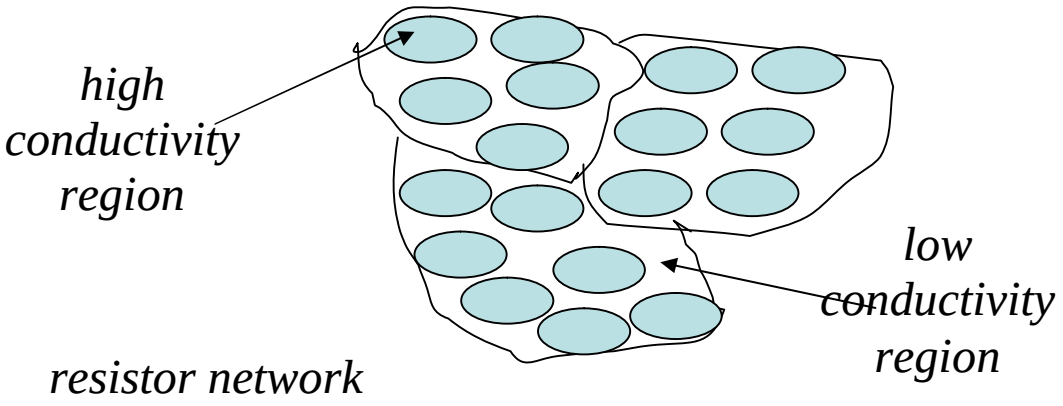

Figure 6.17. A cartoon showing a resistor network comprising low and high conductivity regions.

conductivity of the medium can be written as $\sigma = G_c/\check{R}$, where G_c is the critical percolation conductance and $\check{R}$ is some characteristic length scale of the system. Here G_c varies exponentially according to VRH theory while the pre-factor, $A(T) = \check{R}^{-1}$ is some power of $(T/T_0)^{\beta}$. For our sample, we found $\beta = 1$. The main obstacle to the percolation of charge carriers in granular compounds is the buildup of Coulomb charging energy (E_C) when high conductivity region decreases with respect to the non-conducting region. A superconducting transition occurs if the Josephson coupling (E_J) energy is larger than E_C [19]. In 700 °C and 800 °C heated samples, it is possible that $E_C > E_J$ and therefore, they do not exhibit superconductivity. Figure 6.18(a), shows the temperature dependent resistivity at various applied magnetic fields (H = 0, 5, 10, 20, 30…..90 kOe). In the normal state, resistivity is almost independent of the applied magnetic field. Below T_c, the superconducting transition width (ΔT_c) becomes broader with increasing magnetic

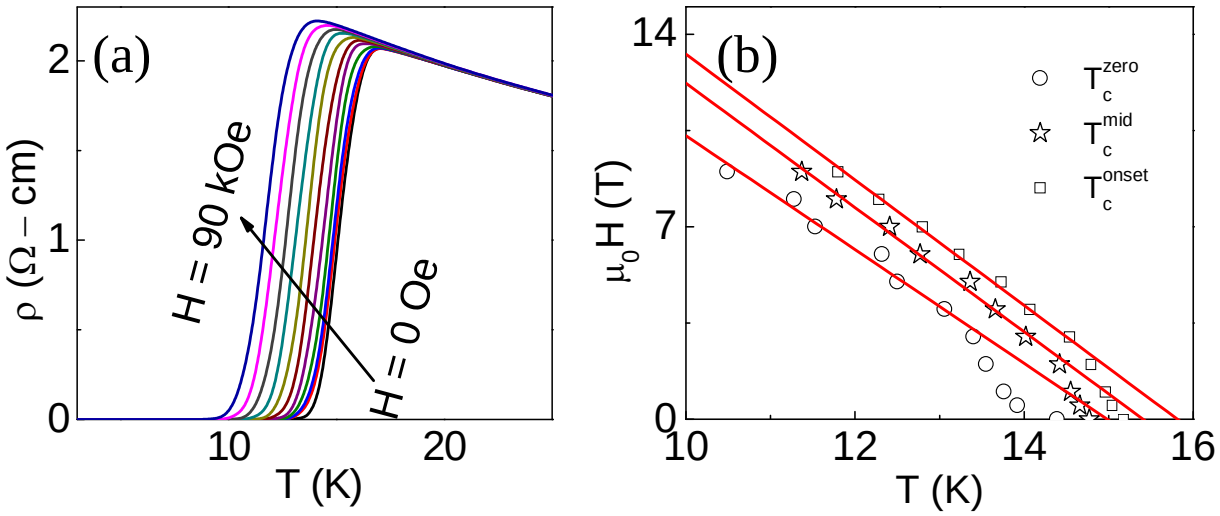

Figure 6.18. (a) Shows the magnetic field dependence of ρ-T for sample synthesized at 900 ºC, and (b) is the corresponding H – T diagram.

field as expected. The onset temperature of superconductivity, $T_{c\text{-onset}}$ (defined as temperature at which there is 90 % decrease in normal resistivity) decreases at a rate $\partial H_{c2}/\partial T_c$= -22.839 Oe K^{-1} (figure 5(d)). The upper critical field (B_{c2}) was calculated to be 24 T at T = 0, using the standard Werthamer-Helfand-Hohenberg (WHH) relationship for a dirty type-II superconductor [52]. The Ginzburg-Landau coherence length is ξ_{GL} = 3.74 nm. The lower critical field was calculated as 101 Oe from the relation $H_{c1}(0)/H_{c2}(0) = 2\kappa^2(0)/\ln\kappa(0)$ using $\kappa(0)$ = 71 [53].

6.4.6 Heat Capacity

Figure 6.19(a), shows the ratio of specific heat capacity to temperature (C_P/T) as a function of T^2 for the sample prepared at 900 ºC. It displays a jump at T_c confirming the bulk nature of superconductivity. The data were fitted with the relation $C_P(T) = \gamma T + \beta T^3$ and the value of γ and β obtained from the fit is 0.028 $Jmol^{-1}K^{-2}$ and 8.96 x 10^{-5} $Jmol^{-1}K^{-4}$ respectively. Heat capacity data for 700 ºC heated sample is shown in figure 6.19(b), the value of β comes out to be 7.06 x 10^{-5} $Jmol^{-1}K^{-4}$, however, the value of γ is almost the same as that of 900 °C sample. The value of θ_D for 900 ºC and 700 ºC samples was calculated to be 278 K and 301 K respectively using the formula $\theta_D = \left(12\pi^4 R/5\beta\right)^{1/3}$ where R is the gas constant. The pairing potential V is related to T_c via the relation

$$T_c = 1.14\theta_D exp(-1/N(E_F)V).$$

where the value for $N(E_F)V$ comes out to *be* 0.33. A superconductor is considered to

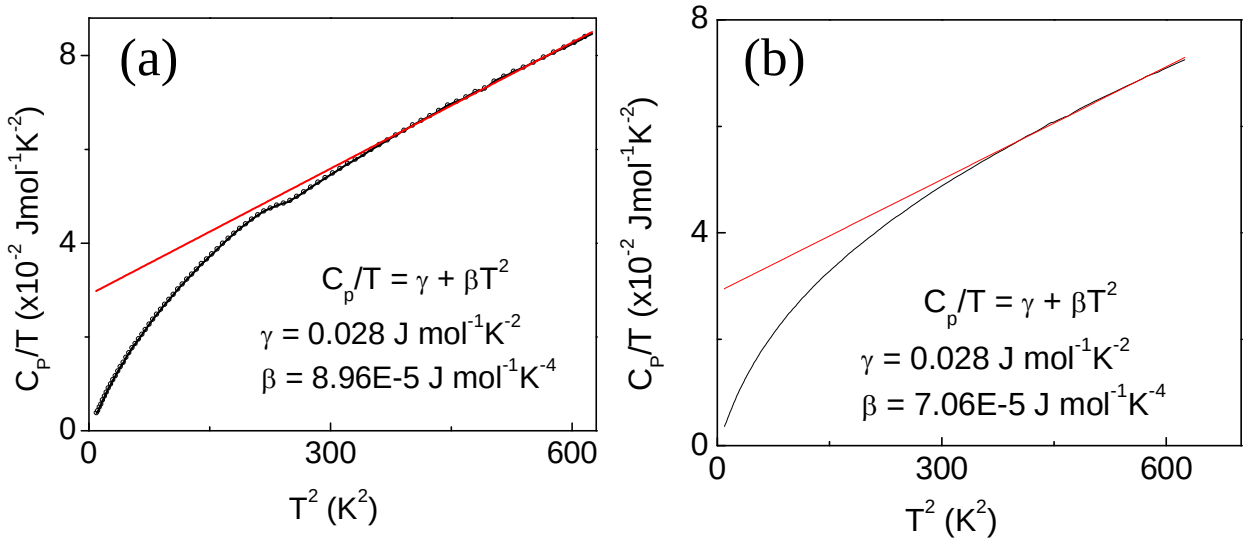

Figure 6.19. (a) and (b) Plots of C_P/T versus T^2 for samples prepared at 900 ºC and 700 ºC respectively.

have a strong pairing potential when $N(E_F)V > 0.25$ [54, 55]. Information about the strength of the electron–phonon coupling can be obtained by evaluating the average electron–phonon coupling constant $\lambda_{e\text{-}ph}$ from MacMillan equation

$$\lambda_{e-ph} = 1.04 + \mu^* \ln(\theta_D/1.45T_c)/[(1-0.62\mu^*)\ln(\theta_D/1.45T_c) - 1.04]$$

where μ^* is the electron – electron repulsion constant [39]. For transition metal compound it is taken as 0.13. The value of $\lambda_{e\text{-}ph}$ for NN900 comes out to be 1.29 which is almost equal to the value of a disordered NbN film reported earlier [13]. Figure 6.20 shows the electronic components of superconducting sample and the non-superconducting sample which were obtained by subtracting βT^3 from $C_P(T)$. The value of molar heat capacity jump for the superconducting sample is very less due to nano-size of the material [56]. Apart from the jump in the specific heat capacity for superconducting sample, the

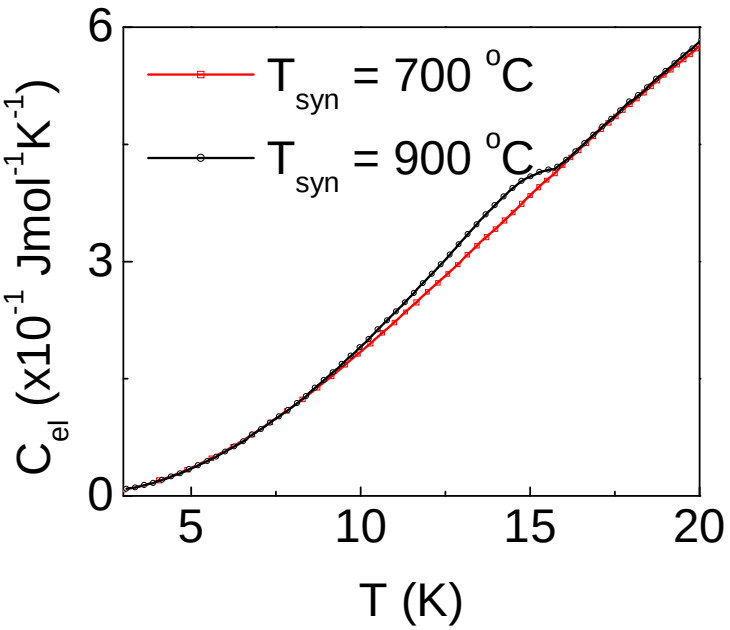

Figure 6.20. Electronic part of the specific heat capacity for the samples prepared at 900 °C and 700 °C obtained by subtracting the phonon part from the total specifi heat capacity.

electronic molar heat capacity is almost the same for both the samples at low temperature. Electronic heat capacity is related mainly to the change in entropy due to thermal excitations of electrons above Fermi level at $T > 0$. It is also directly related to the density of states near the Fermi level which in turn depends upon the size of the superconducting grains. The density of states near Fermi level in δ - NbN is mainly occupied by the Nb 4*d* states [9, 57], therefore a change in the nitrogen content in the sample may not affect the electronic state much, although it can change the lattice parameter and thereby change the phonon contribution to the heat capacity. This is also clear from the values of γ and β for the two samples as discussed earlier. As δ- NbN is a BCS superconductor with a strong pairing potential, phonons can play a prominent role in inducing superconductivity into the material. To have an idea about the BCS gap, the electronic heat capacity in the range

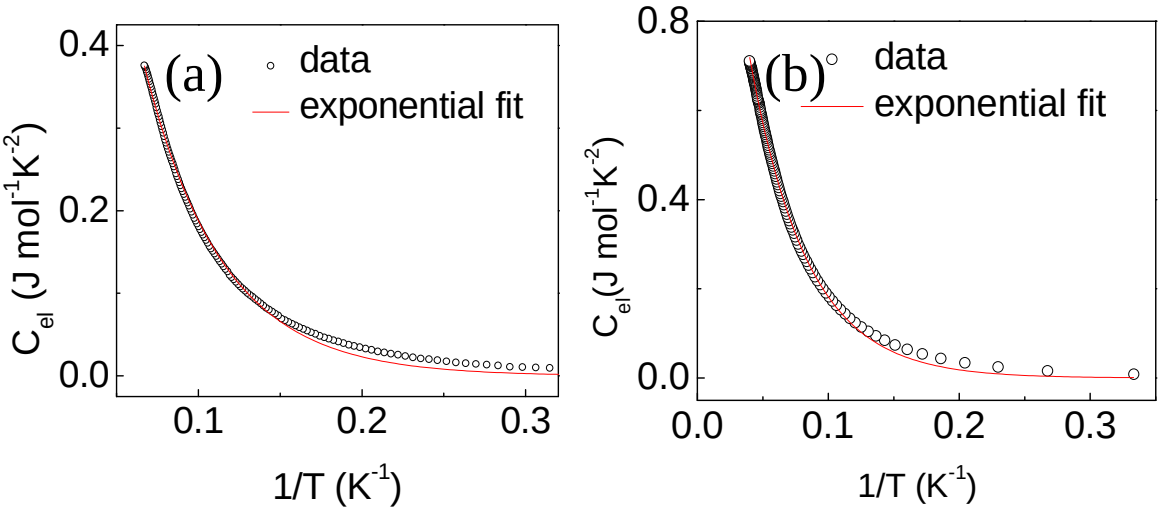

Figure 6.21. (a) and (b) to the low temperature electronic heat capacities below the superconducting transition temperature (T_c) for samples prepared at 900 ºC and 700 ºC.

between 3 K to 15 K was fitted using the formula $C_{el} = A\gamma T_c exp(-BT_c/T)$. Fig. 6.21(a) shows the plot of electronic heat capacity for NN900 versus 1/T. The value of B = 1.37, while the value of A is much less than that (8.5) predicted by BCS theory and may be due to the nano-size of the sample [58]. Figure 6.21(b) is the inverse temperature dependence of electronic heat capacity of non-superconducting sample. It can be observed that it fits well with an exponential function.

6.5 Conclusions

Urea method for the nitridation of Niobium is an extremely efficient method of synthesizing nanoparticles of δ - NbN superconductor. The sample prepared at 900 °C showed bulk superconductivity with a T_c at around 16 K whereas those prepared at lower temperatures do not show superconductivity. Presence of bulk superconductivity in 900 °C sample shows that inter-granular network of diffused region between the grains

play an important role. The superconducting sample shows ferromagnetic hysteresis curve above T_c due to the nano-size of the grains. A possibility of the coexistence of superconductivity and surface ferromagnetism cannot be ruled out similar to that of Sn nanoparticles [36]. Presence of positive peak below T_c in the third harmonic ac susceptibility may be regarded as a signature of granularity in the sample. Granularity also induces semiconducting nature in resistivity versus temperature plot in the normal state of all the samples which is mainly governed by AHL model with a linear temperature dependence of the pre-factor. Jump in the heat capacity measurement, although small due to nano-size of the superconducting grains, confirm the bulk nature of superconductivity.

6.6 References:

1. C. P. Poole, H. A. Farach, and R. J. Creswick, *Superconductivity,* Academic Press, 1995, Chap. 3.
2. J. Gavaler, A. Santhanam, A. Braginski, M. Ashkin, M. Janocko, IEEE Trans. Mag. **17** (1981) 573.
3. G. I. Kerber, *IEEE Trans. Appl. Supercond.* **7** (1997) 2638.
4. D.W. Capone II, K.E. Gray, R.T. Kampwirth and H.L. Ho, *Journal of Nuclear Materials* **141-143** (1986) 73.
5. A. Ire *et. al., IEEE Trans. Appl.Magnetics* **27** (1991) 2967
6. A. D. Semenov and Hubers, *IEEE Trans. Appl. Supercond.* **11** (2001) 196.
7. Masoud Radparvar and Sergey Ralov, *IEEE Trans. Appl. Supercond.* **4** (1994) 92.
8. R. Kaiser, W. Spengler, S. Shicktanz and C. Politis, *Phys. Stat. Sol (b)* **87** (1976) 565.
9. E. C. Ethridge, S. C. Erwin and W. E. Pickett, *Phys. Rev. B* **53** (1996) 12563.
10. D. J. Chad and M. L. Chen, *Phys. Rev. B* **10** (1974) 496.
11. A. V. Linde, R. –M. Marin-Ayral, F. Bosc-Rouessac and V. V. Grachev, *International Journal of Self Propagating High-Temperature Synthesis* **19 (**2010) 9
12. K. Senapati, N. K. Pandey, R. Nagar and R. C. Budhani *Phys. Rev. B* **74** (2006) 104514.
13. S. P. Chockalingam *et al., Phys. Rev. B*, **77 (**2008**)** 214503.

14. A. Gomathi, A. Sundaresan, C. N. R. Rao, *J. Solid State Chem*. **180** (2007)291.

15. K. Sardar M. Dan, B. Schwenzer, C. N. R. Rao, *J. Mater. Chem.* **15** (2005) 2175.

16. Y. Qiu, L. Gao, *Chem. Lett.*, 32 (2003) 774.

17. Y.Qiu, L.Gao, *J. Am. Ceram. Soc.* **87** (2004) 352.

18. C. Giordano, C. Erpen, W. Yao, B Milke, and M. Antonietti, *Chem. Mater*. **21** (2009) 5136.

19. I. S. Boloboredov, A. V. Lopatin and V. M. Vinokur, *Rev. Mod. Phys.* **79** (2007) 469

20. A. V. Lopatin and V. M. Vinokur, *Phys. Rev. B,* **75** (2007) 092201.

21. D. Guetcher *et. al,* **44** (1980) 1150.

22. A. Gerber, A. Milner, G. Deutscher, M. Karpovsky, and A. Gladkikh, *Phys. Rev. Lett.* **78** (1997) 4277.

23. M. Chand *et. al., Phys. Rev. B.* **80** (2009) 134514.

24. M. Mondal *et. al.,Phys. Rev. Lett.* **106** (2011) 047001; arxiv:/1005.1628v3.

25. A. Lascialfari, A. Rigamonti, E. Bernardi, M. Corti, A. Gauzzi, and J. C. Villegier, Phys. Rev. B **80** (2009) 104505.

26. A.Schindler, R. Konig, T. Herrmannsdorfer, and H. F. Braun, *Phys. Rev. B* **62** (2000) 14350.

27. M. Baenitz *et. al.,Physica C* **228** (1994) 181.

28. R. Cabanel *et. al.,J. Phys. France* **49** (1988) 795.

29. F. R. Ong and O. Bourgeois, *Eur. Phys. Lett.,* **79** (2007) 67003.

30. A.M. Gabovich *et. al., J. Phys.: Condens. Matter* **14** (2002) 9621.

31. J. Redinger *et. al., Z. Phys. B*, **63** (1986) 321.

32. C. Stampfl, W. Mannstad, Asahi R and Freeman A J 2001 *Phys. Rev. B.* **63** 155106

33. D. J. Thompson, L. E. Wenger and J. T. Chen *Phys. Rev. B* **54** (1996)16096 .

34. Shipra, A. Gomathi, A. Sundaresan and C. N. R. Rao *Solid State Comm.* **142** (2007) 685.

35. A. Sundaresan and C. N. R. Rao *Solid State Comm.* **149 (**2009) 1197; A. Sundaresan and C. N. R. Rao *Nanotoday* **4** (2009) 096.

36. W.-H. Li, C. –W. Wang, C. –Y. Li, C. K. Hsu, C. C. Yang and C. –M. Wu *Phys. Rev. B* **77 (**2008**)** 094508

37. C. -K. Hsu, D. Hsu, C.-M. Wu, C.-Y Li, C.-H. Hung, C.-H. Lee, and W.-H. Li, *J. Appl. Phys.* **109** (2011) 07B528.

38. H. Wu, J. Ni, J. Cai, Z. Cheng, and Y. Sun, *Phys. Rev. B* **76** (2007) 024416.

39. Bean C P 1964 *Rev. Mod. Phys.* **36** 31

40. Ji L, Sohn R H, Spalding G C, Lobb C J and Tinkham M 1989 *Phys. Rev. B* **40** 10936

41. Jin M J and Xao X X 1997 *Physica C* **282 – 287** 2229

42. Y. Qiu and L. Gao, J. Am. Ceram. Soc., 87 (2004) 352.

43. M. Polichetti, M. G. Adesso, A. Vecchione and S. Pace, *Physica B* **284 – 288 (**2000**)** 909

44. A. Gencer *Supercon. Sci. Technol.* **15** (2002) 247.

45. John R. Clem, A. Sanchez, *Phys. Rev. B* **50** (1994) 9355.

46. E. S. Otabe, T. Matsushita, M. Heinz, M. Baenitz and K Lüders, *IEEE Trans. Appl. Supercond.* **5 (**1995**)** 1383.

47. M. Polichetti, M. G. Adesso, D. Zola, J. Luo, G. F. Chen, Z. Li, N. L. Wang, C. Noce and S. Pace, *Phys. Rev. B* **78** (2008) 224523.

48. T. Ishida and M. Mazaki, *J. Appl. Phys.* **52** (1981) 6798.

49. N. F. Mott, *Phil. Mag.* **26** (1972) 1015.

50. R. Cabanel, J. Chaussy, J. Mazuer and J. C. Villegier *J. Phys. France* **49** (1988)795.

51. V. Ambegaokar, B. I. Halperin and J. S. Langer, *Phys. Rev. B* **4 (**1971**)** 2612.

52. N. R. Werthamer, E. Helfland and P. C. Hohenberg, *Phys. Rev.* **147** (1966) 295.

53. M. P. Mathur, D. W. Deis, and J. R. Gavaler, *J. Appl. Phys.* **43 (**1972**)** 3158.

54. S. M. Pattalwar, R. N. Dixit, S. Y. Shete and B. K. Basu, *Phys. Rev. B* **38 (**1988**)** 7067

55. P. Roedhammer and E. Gmelin, *Phys. Rev. B* **15** (1977) 711

56. B. Mühlschlegel, D. J. Scalapino and R. Denton, *Phys. Rev. B* **6** (1972) 1767.

57. L. F. Mattheiss, *Phys. Rev. B* **5** (1972) 315.

58. V. H. Tran, W. Miller, Z. Bukowski, *Acta Materialia* **56** (2008) 5694.

Chapter 7

Synthesis and characterization of $FeSe_{1-x}Te_x$ and $Fe_{1-x}M_xSe_{0.5}Te_{0.5}$ (M = Co and Ni) superconductors

"False facts are highly injurious to the progress of science, for they often endure long; but false views, if supported by some evidence, do little harm, for every one takes a salutary pleasure in proving their falseness."

- Charles Darwin

Summary**

Substitution of isoelectronic Tellurium (Te) for Selenium (Se) in the tetragonal phase, known as β-FeSe, increases the superconducting transition temperature (T_c) by causing a negative pressure on the lattice. With increasing Te concentration, the T_c increases and reaches a maximum to ~ 14 K for $FeSe_{0.5}Te_{0.5}$ and then decreases with further increase of Te. However, the normal state resistivity increases and shows an anomalous semi-metallic behavior for samples with higher Te concentration especially for $FeSe_{0.5}Te_{0.5}$. We further observed that substitution of Cobalt (Co) and Nickel (Ni) for Fe, in $FeSe_{0.5}Te_{0.5}$ with nominal composition, $Fe_{1-x}TM_xSe_{0.5}Te_{0.5}$ (TM = Co (x = 0.05, 0.1, 0.15, 0.2) and Ni (x = 0.05, 0.1)) suppresses the normal state resistivity anomaly. We have investigated these observations with the help of Hall measurements where we found that the multiband character of the Fermi surface influences both the normal state and the superconducting states. Both Co and Ni substitution suppress T_c and drives the system to metal–insulator transition. The in-plane ('*a*') and out-of-plane ('*c*') lattice constants decrease with increasing substitution.

A paper based on the present study has been published in *Physica C* **470 (2010) 528-532.

7.1. Introduction

The discovery of new iron-based high T_c superconductors has ignited immense excitement in the material science community from past 3 years. Immediately after the discovery of $LaFeAsO_{1-x}F_x$ with a critical temperature (T_c) of 26 K, efforts were made to increase the T_c in isostructural compounds by substituting La with different rare earth metals of smaller radii [1–5]. The highest T_c in these oxypnictides was reported at 56 K for $SmFeAsO_{0.85}$ and $Gd_{0.8}Th_{0.2}FeAsO$ [6,7]. The family of Fe-based superconductors has expanded to have oxygen free systems including K or Na doped AFe_2As_2 (A = Ba, Sr, Ca) [8], (A,RE)FeAsF (A = Sr, Ca; RE = rare earth metals) [9] and $(Li, Na)_x$ FeAs [10]. The common structural element of all these compounds is based on Fe_2X_2 (X = P, As) layers of edge sharing FeX_4 tetrahedra [11]. It is considered that this layer is electronically active while other layers stabilize the structure and serve as charge reservoirs to dope the active layer [2]. Iron based chalcogenides (FeSe, $FeSe_{1-x}Te_x$, $FeTe_{1-x}S_x$) having similar Fe_2Se_2 layers (as shown in figures 7.1 (a) and (b)), have also registered their distinct presence in this family

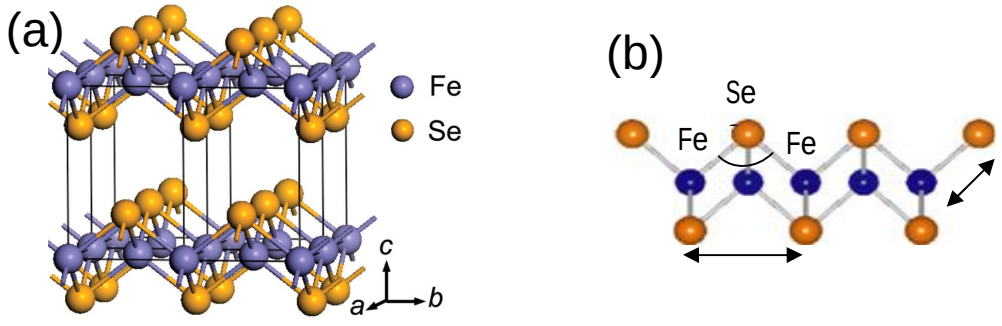

Figure 7.1. (a) Crystal structure of $FeSe_{1-\delta}$ showing Fe atoms arranged forming a 2D sheet. Each Fe is bonded tetrahedrally to Se atoms. Fe-Fe, Fe-Se bond lengths and Fe-Se-Fe bond angles are shown in (b). The figure is adapted from Hsu.F *et. al. PNAS* 105 (2008)14262.

[12–15]. The self doped anion deficient binary superconductor β-$FeSe_{1-\delta}$ shows a T_c of 8 K which increases to 37 K by mere applying a hydrostatic pressure of 8.9 GPa [16,17]. Recently a new superconductor was added to the family of Fe based chalcogenides (*FeChs*) by alkali metal intercalation between Fe_2Se_2 layers with a nominal composition of $K_{0.8}Fe_2Se_2$ with a T_c of 30 K [35]. A high T_c , similar structure and band filling as that of FeAs layer found in the quaternary iron arsenide makes *FeChs* [18,19] a simple suitable model to study the interplay of structure, magnetism and superconductivity within iron based superconducting materials family. Extreme dependence of T_c on selenium content [20], pressure and different chemical substitution at both iron and selenium sites is remarkable in *FeChs* [21,12–15]. Isovalent substitution of Te for Se modifies the crystal structure by lowering the local symmetry from the average P4/nmm crystal symmetry by decreasing the Fe–Se–Fe bond angle from 104° to lower values. The T_c increases without any change in carrier concentration when Se^{2-} is replaced by Te^{2-} on the assumption of ionic crystal of $FeSe_{1-x}Te_x$ [22]. The solid solution of $FeSe_{1-x}Te_x$ shows superconductivity for a wide range of Te substitution for Se with a maximum T_c(zero) of 14 K [14]. The first and last members of this family are $FeSe_{1-\delta}$ and $FeTe_{1-\delta}$. Although, they are isostructural at room temperature, they show very different behavior when cooled down to low temperatures. It is usually found that $FeSe_{1-\delta}$ is mainly Se deficient, while $FeSe_{1-x}Te_x$ and $FeTe_{1-\delta}$ have excess Fe in the interstitial positions [36, 37]. $FeTe_{1-\delta}$ undergoes both structural (tetragonal to monoclinic) as well as magnetic transitions at the same

temperature T_N = 67 K [23, 24]. It has been suggested that superconductivity occurs in nearly stoichiometric $Fe_{1.01}Se$ which undergoes a structural transition at T = 90 K to an orthorhombic space group, C*mma* [25] without any accompanying magnetic transition. More recently however, pressure induced short order magnetic fluctuations were observed in this system [38]. It was also observed that samples containing higher selenium deficiency show a very complex magnetic behavior which was earlier attributed to a structural transition (T = 70 K) and the impurities present in the sample [12]. $FeSe_{1-x}Te_x$ does not undergo any structural or magnetic transition, however magnetic order is found to survive as short range correlation, that can be resonant or dispersive depending upon the excess interstitial 'Fe' in this solid solution [28,29]. Density functional theory predicts the existence of spin density wave ground state through Fermi surface nesting in $FeSe_{1-\delta}$ and $FeTe_{1-\delta}$, but recent neutron diffraction studies ruled out such possibilities and an alternate fluctuating local moment model has been predicted [39]. Although simple in structure, understanding magnetic and electronic properties of *FeChs* are very debatable and greatly influenced by excess Fe in the interstitial positions. The excess Fe ions randomly get distributed in the chalcogenide layer. DFT calculations focused on $FeTe_{1-\delta}$ show that the excess of Fe occurs in +1 state with each Fe^+ donating electrons to $FeTe_{1-\delta}$ [40] Further Fe^+ was also found to be strongly magnetic with a local moment of $2.4\mu_B$ to influence the overall magnetism in *FeChs*. Depending upon the amount of excess Fe, the nature of short range magnetic fluctuations can be resonant and dispersive [28, 29]. The interstitial Fe induce pair breaking effect in the superconducting state and show

suppression of superconductivity and localization effects [41]. Multiband iron chalcogenides are low carrier density metals with high density of states where the electronic structure near Fermi level is mainly influenced by Fe derived bands. Se derived bands lie well below the Fermi Level and Fe–Se hybridization is weak as compared to Fe–Fe interaction [18]. However, recent spectroscopic measurements performed at room temperature suggest that hybridization significantly influence the electronic structure of Fe*Ch* superconductors and is controlled by the chalcogen height above the Fe-sheet [42]. It was found that the coupling between chalcogen *p* states and the Fe *d* states is stronger in $FeSe_{1-\delta}$ as compared to $FeSe_{1-x}Te_x$ which is consistent with the difference observed in the chalcogen height between $FeSe_{0.88}$ (1.46 Å) and $FeSe_{0.5}Te_{0.5}$ (1.60 Å) [43]. As we know that self doping in $FeSe_{1-\delta}$ is usually achieved by Se deficiency, the charge balance between Fe and Se is assigned to itinerant electrons formed due to hybridized Fe-Se bond that are located mostly on the Fe site [36]. Usually Te substitution weakens the hybridization [44] and these effects become further complicated due to local structural variation in $FeSe_{1-x}Te_x$ superconductor where Fe-Te bond length (2.57 Å) is large as compared to Fe-Se bond length (2.39 Å). The Fe-Te bond in $FeSe_{1-x}Te_x$ is shorter than in pure $FeTe_{1-\delta}$. Influenced by hybridization, superconductivity mainly occur within the Fe-Fe sheets, it would be interesting to study the development of various physical properties with increasing disorder in the in-plane Fe-sheet. In the present work, we first tried to synthesize samples with the nominal composition $FeSe_{1-x}Te_x$ (x = 0, 0.2, 0.5, 0.8, 1) and then studied the effect of substitution of Cobalt (Co) and Nickel (Ni) for Fe in

$FeSe_{0.5}Te_{0.5}$ on the physical properties. When the work was started, there were very few studies on such substitutions have been reported in FeSe system [30, 34] and there was no report for $FeSe_{1-x}Te_x$ system. However recently few reports are published on the transition metal substitution in $FeSe_{1-x}Te_x$ system [47-49]. Although, Co and Ni substitutions in undoped Fe based oxypnictides induce superconductivity by providing charge carriers, the T_c is relatively low compared to fluorine doping [31–33]. Similarly, in self doped *FeChs* samples there is a negative impact of Co and Ni substitution on T_c which indicates that Fe is an essential element for obtaining high temperature superconductivity in the pnictide or chalcogenide superconductors [21,34].

7.2. Scope of present investigation:

The present study mainly covers the aspects of substitution effects on the cation and anion sites of $FeSe_{1-\delta}$ superconductors with a nominal composition of $FeSe_{1-x}Te_x$ (x = 0, 0.2, 0.5, 0.8 and 1), $Fe_{1-x}Co_xSe_{0.5}Te_{0.5}$ (Co = 0, 0.05, 0.1, 0.15, 0.2) and $Fe_{1-x}Ni_xSe_{0.5}Te_{0.5}$ (x = 0, 0.05, 0.1). We have mainly focused on the structural and transport properties of these substitutions. Te substitution increases the Fe-*Ch* bond lengths and therefore decreases the effect of hybridization on the electronic properties of $FeSe_{1-x}Te_x$. Substitution of Co and Ni not only provide local structural disorders in the Fe layer but also provide extra electrons into the structure. These disorders

although suppresses superconductivity however it was observed that normal state resistivity shows a much better metallic behavior.

7.3. Experimental

7.3.1 Material synthesis

Figure7.2 shows the schematic of the synthesis procedure. Three series of compounds with the nominal compositions $FeSe_{1-x}Te_x$ (x = 0, 0.2, 0.5, 0.8, 1), $Fe_{1-x}Co_xSe_{0.5}Te_{0.5}$ (x = 0.05, 0.1, 0.15, 0.2) and $Fe_{1-x}Ni_xSe_{0.5}Te_{0.5}$ (x = 0.05, 0.1) were synthesized. First

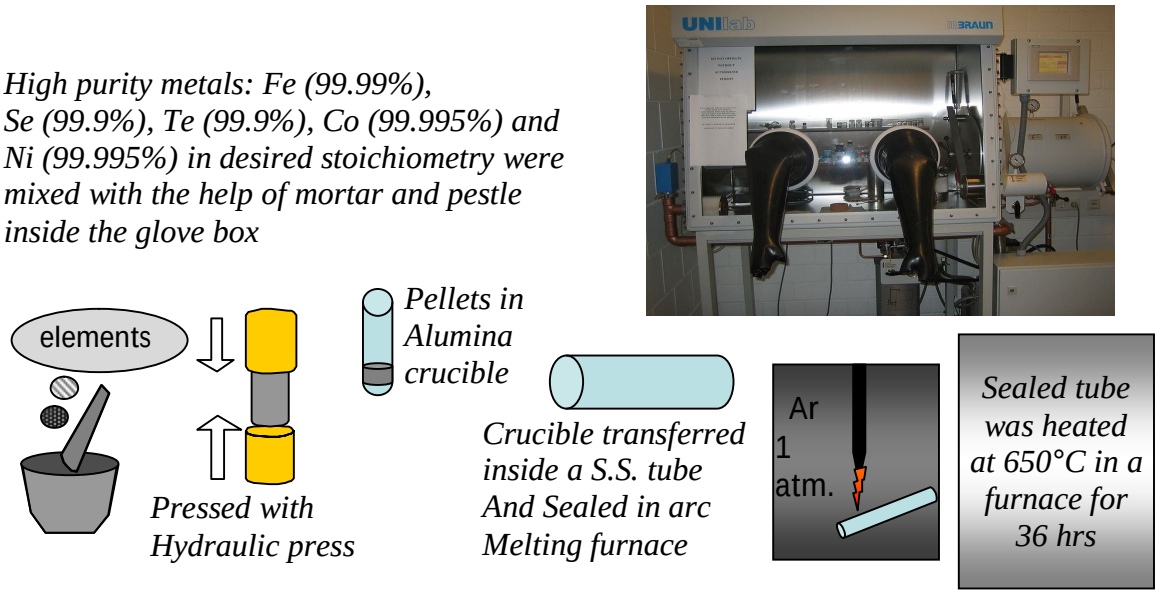

Figure 7.2. Schematic of the synthesis procedure for preparing pure or transition metal substituted $FeSe_{1-x}Te_x$ superconductors. The described procedure not only protects Se and Fe from being oxidized but also protects from the toxicity of selenium oxides.

of all, stoichiometric amounts of Fe (*3N*), Se (*3N*), Te (*5N*), Co (*5N*) and Ni (*5N*) were ground, pressed and kept in alumina crucibles that were sealed inside stainless steel tubes under 1 atm. pressure of argon. Then the starting mixtures were heated at 650 °C for 10 h after which they were reground, pressed, sealed and reheated at 680 °C for 36 h. All grindings were done in Argon filled glove-box. The samples prepared were stable in air but stored in evacuated desiccators to protect them from moisture.

7.3.2 Characterization

The structural characterization was done by powder X-ray diffraction (XRD) using Bruker D8 Discover employing CuKα and graphite diffracted beam monochromator. Rietveld refinements of the XRD patterns were performed using Fullprof software. Impurity phases were taken into consideration during refinement. Crystalline nature of the compound was further studied by electron diffraction (ED) using Transmission Electron Microscopy (TEM – JEOL JEM 3010). The morphology of the sample was studied by Field Emission Scanning Electron Microscopy (FESEM–FEI NOVA NANOSEM 600). The sample was ground and dispersed in ethanol by ultrasonication and then drop cast on the Cu-grid. Temperature dependent linear resistivity was measured using Quantum Design (QD) physical property measurement system (PPMS). Field dependent Hall measurements were done at T = 300 K and T = 20 K using the AC transport option in the PPMS. The applied excitation was 103 mA at a frequency of 103

Hz. Various DC magnetic measurements were performed using the VSM option in the PPMS

7.4 Results and discussion

7.4.1 Structure

Figure 7.3(a) shows the XRD pattern of the $FeSe_{1-x}Te_x$ superconductor belonging to the

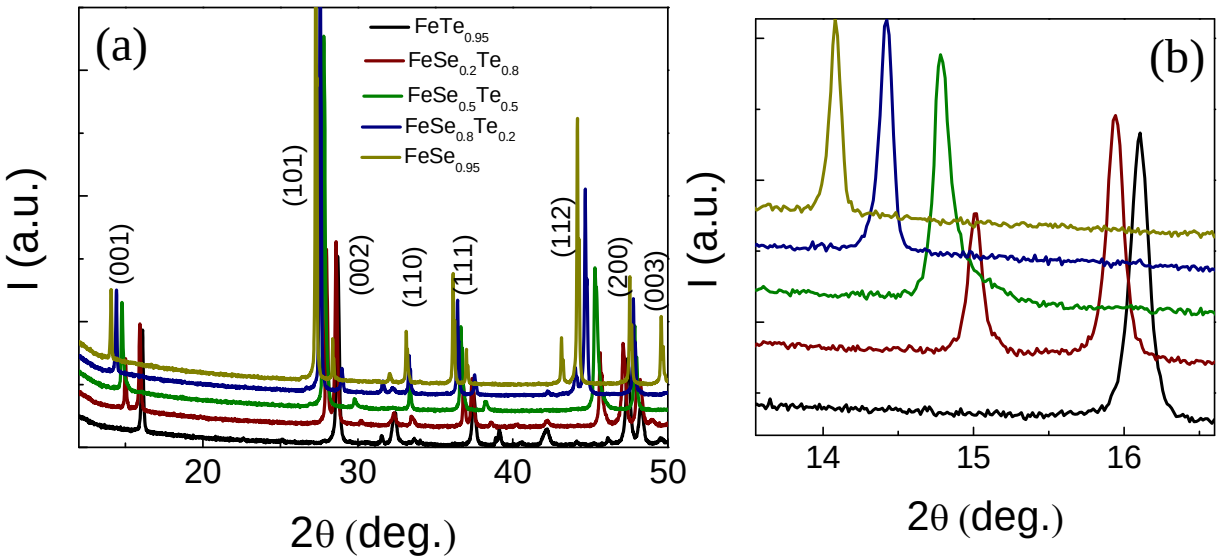

Figure 7.3. (a) X-ray diffraction patterns of $FeSe_{1-x}Te_x$. With increasing Te concentration, the peaks shift to lower 2θ values indicating the increase in the lattice constants. (b) shows the enlarged view of the (001) peak. Splitting of peaks corresponding to two different phases with different Te content for $FeSe_{0.8}Te_{0.2}$ is clearly visible.

space group (SG) P4/nmm. The peak corresponding to (001) Bragg plane shifts to lower *2θ* values with increasing Te content in the sample that is more clearly observed in figure 7.3(b). The sample with 20 % Te content shows a split in the XRD peaks which indicate

the presence of two different phases in the sample. One of the phases contains high Te content while the other has a lower concentration. The main impurity phase in all these samples is hexagonal Fe_7Se_8 (ferrimagnetic, T_c = 455 K). Figure 7.4 shows the

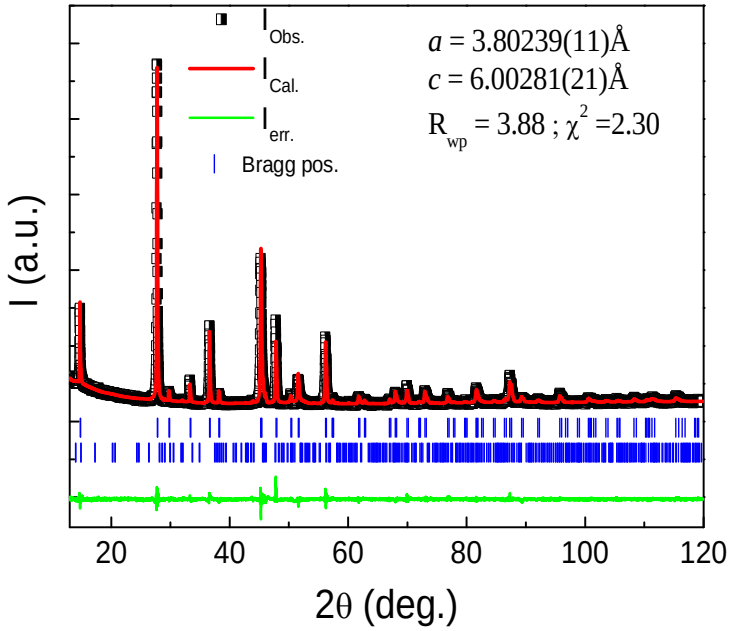

Figure 7.4. XRD pattern of FeSe0.5Te0.5 as obtained from Rietveld refinement. The main phase was fitted with a tetragonal lattice P4/nmm (Fe, 2a (0.75, 0.25, 0); Se/Te, 2b (0.25,0.25, 27667(16)). The lattice parameters are a = 3.8024(1) Å and c = 6.0028(2) Å, respectively with χ^2= 2.44.

the result of Rietveld refinement on the XRD pattern of $FeSe_{0.5}Te_{0.5.}$ The main phase was fitted with a tetragonal lattice P4/*nmm* (Fe, 2a (0.75, 0.25, 0); Se/Te, 2b (0.25, 0.25, 27667(16)). The lattice parameters are *a* = 3.8024(1) Å and *c* =6.0027(2) Å, respectively with χ^2 = 2.44. The occupancy for Fe was fixed to be 1 and after refinement, the obtained value for occupancy of Se is 0.416(8) and for Te, it is 0.584(8).Figure 7.5(a) shows the evolution of the *a*-axis and *c*-axis lattice parameters and unit cell volume for the

$FeSe_{1-x}Te_x$ system as a function of the *Te* content (x). The crystal lattice parameters, the unit cell volume as well as the Fe-Se-Fe bond angle increase almost linearly as the Te concentration is increased (figure 7.5(b)). It is important to note that, due to the larger ionic radius of Te, as compared to that of Se, the Fe–Fe and Fe–Se or Fe-Te bond lengths also increase (figure 7.5(c)). It is worth mentioning that X-ray diffraction technique for structure determination usually gives the average structure of any compound. But the

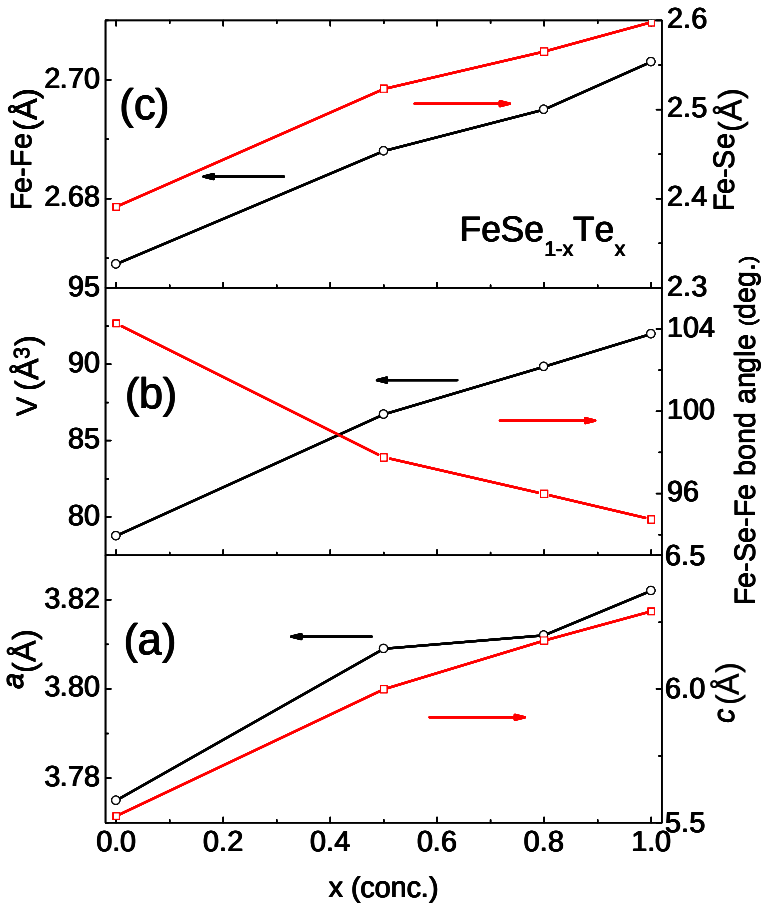

Figure 7.5. (a) shows the '*a*' and '*c*' lattice parameters of $FeSe_{1-x}Te_x$ with increasing x. Due to large size of Te, both the lattice parameters increase as 'x' increases. The unit cell volume also increases along with Fe-Se-Fe bond angle as shown in (b). (c) shows the increasing Fe-Fe and Fe-Se bond lengths as a function of increasing '*x*'.

local structure may differ from the average structure which has been observed in case of $FeSe_{1-x}Te_x$. From EXAFS measurements on $FeSe_{0.5}Te_{0.5}$, it was found that Fe-Se bond length is is usually shorter than Fe-Te bond length. As a result the local structure is very different from the average structure. Due to difference in bond lengths, Se and Te share different z coordinates [44, 46]. However we assigned the same z-coordinates to both Se and Te during structure refinement. Figure 7.6 shows the XRD patterns of $Fe_{1-x}Co_xSe_{0.5}Te_{0.5}$ (x = 0, 0.05, 0.1, 0.15, 0.2) and $Fe_{1-x}Ni_xSe_{0.5}Te_{0.5}$ (x = 0.05, 0.1). The peak marked by * denotes the hexagonal Fe_7Se_8 or $CoTe_2$ impurity phase. In $Fe_{1-x}Co_xSe_{0.5}Te_{0.5}$, for x = 0.05, the main impurity is Fe_7Se_8, whereas for x > 0.05, the impurity phase is identified to be $CoTe_2$, which is paramagnetic. For $Fe_{1-x}Ni_xSe_{0.5}Te_{0.5}$, the main impurity is Fe_7Se_8. Figure 7(a) shows the variation of '*a*' and '*c*' lattice parameters with Co and Ni

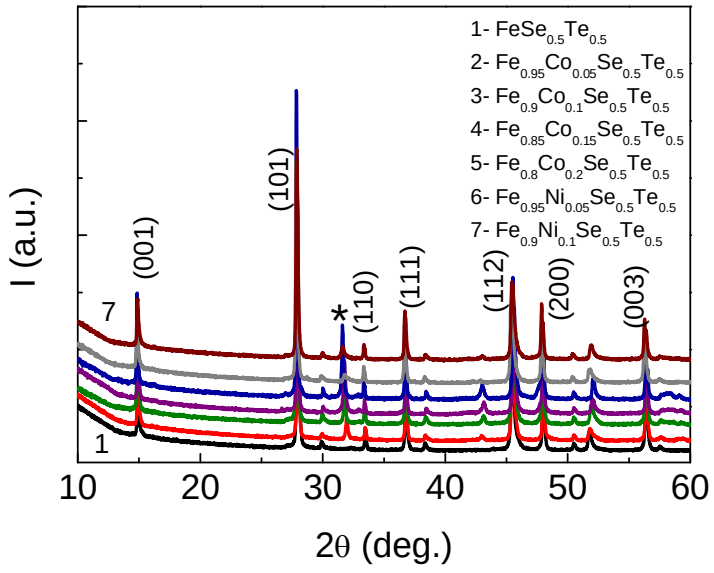

Figure 7.6. X-ray diffraction pattern $Fe_{1-x}Co_xSe_{0.5}Te_{0.5}$ (x = 0.05, 0.1, 0.15 and 0.2) and $Fe_{1-x}Ni_xSe_{0.5}Te_{0.5}$ (Ni = 0.05 and 0.1). The impurity phase is marked with asterisk (*). It is found that impurities are more in case of Co substituted samples as compared to Ni substituted samples.

substitution in $Fe_{1-x}Co_xSe_{0.5}Te_{0.5}$ and $Fe_{1-x}Ni_xSe_{0.5}Te_{0.5}$, respectively. Both '*a*' and '*c*' decreases with increasing Co (0.58 Å for Co^{2+}) and Ni (0.55 Å for Ni^{2+}) concentration according to Vegard's law indicating the substitution of smaller cations compared to Fe^{2+} (0.64 Å) in the tetrahedral coordination. The values completely agree with other reported values [47, 49]. Comparing the variation of lattice parameters of these two systems (figure 7.7(a)), it was observed that '*a*' lattice parameter of Ni substituted sample is

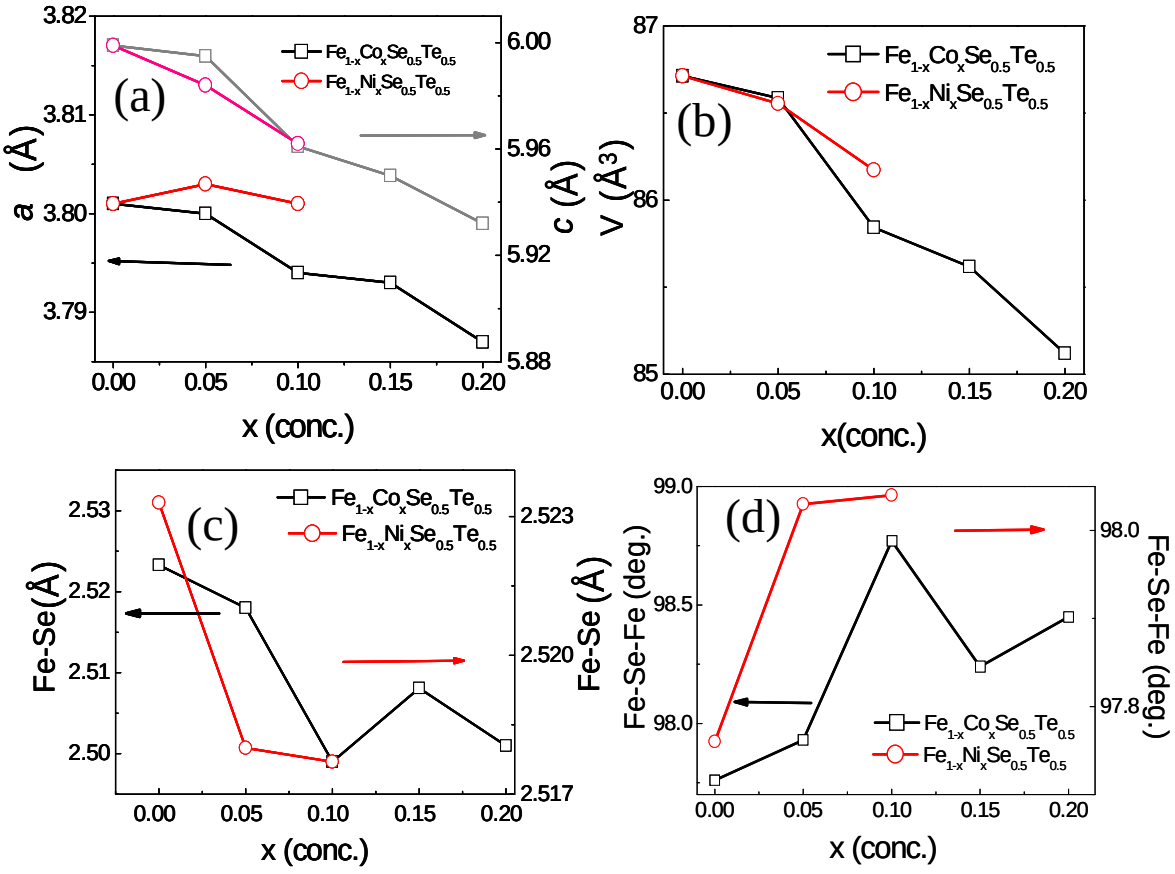

Figure 7.7. (a) Variation of 'a' and 'c' lattice parameters of Co and Ni substituted samples. (b) Variation of lattice volume as a function 'x'. (c) and (d) show the variation of bond length and Fe–Se–Fe bond angle with increasing 'x'. The angle is shown in figure 7.1(b). All quantities decrease except the bond angle which show an increase with increasing substituent.

slightly larger that of the Co substituted sample. This is similar to what was observed in $FeSe_{1-\delta}$ where substitution of Co results in decrease '*a*' and '*c*' lattice parameters whereas Ni substitution increases the '*a*' lattice parameter and decreases the '*c*' lattice parameter [50]. It should also be noted that in the case of Cu substituted FeSe samples, the '*a*' lattice parameter increases while there is a decrease in the '*c*' lattice parameter [30]. The lattice parameter changes are also consistent with the values obtained by D. J. Gawryluk *et. al.* [49] in FeSe. Figure 7.7(b) shows the variation of lattice volume 'V' which decreases with both Co and Ni doping. Figure 7.7(c) shows the variation of Fe–Se–Fe bond angle with increasing Co or Ni concentration. Substitution opens up the tetrahedra i.e. increases the Fe–Se–Fe bond angle while compressing the $FeSe_4$ tetrahedra along both '*c*' and '*a*' axes [21,34,35]. Figure 7.7(d) shows the compression of Fe–Se bond length with increasing 'x'. Though not shown here, the Fe-Fe bond length also decreases with increasing Co and Ni concentration.

7.4.2 Microstructure

Figure 7.8(a) shows the bright field TEM image of $FeSe_{0.5}Te_{0.5}$ and 7.8(b) is the corresponding HRTEM image where lattice fringes can be seen. The high crystallinity and four fold symmetry of the sample is confirmed from selected area electron diffraction (SAED) pattern shown in figure 7.8(c) The reciprocal lattice point corresponding to (110) plane is shown. The FESEM image in figure 7.8(d) shows the stacking of the crystalline $FeSe_{0.5}Te_{0.5}$ layers.

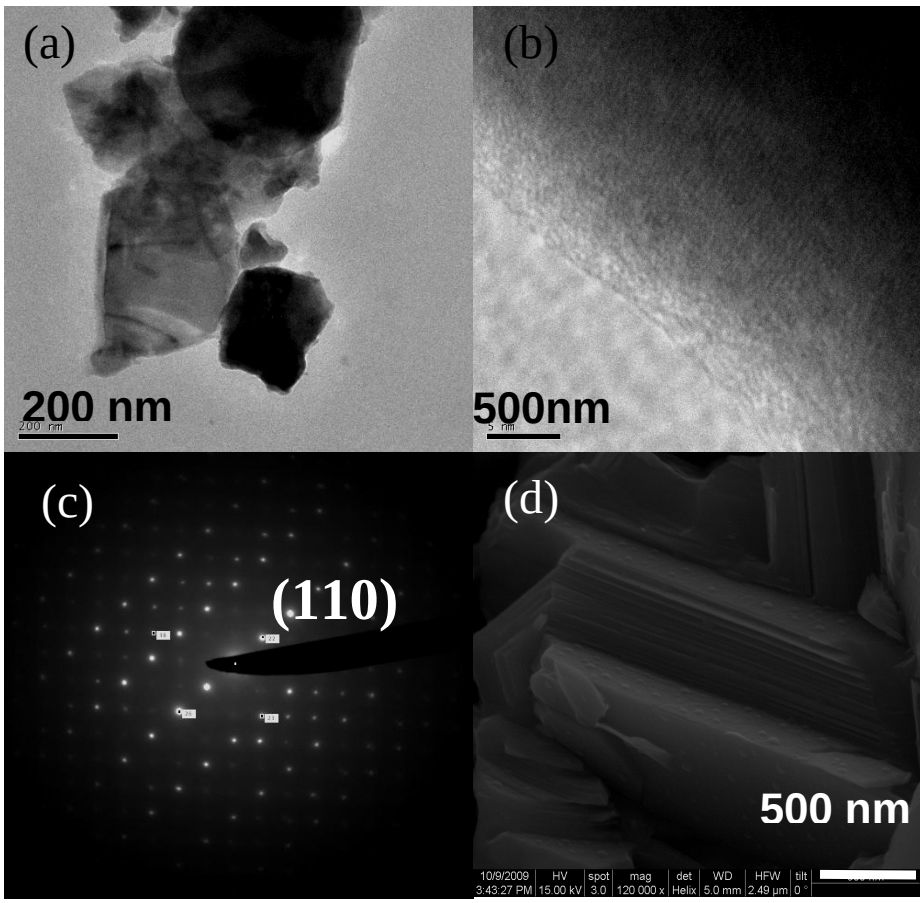

Figure 7.8. (a) TEM image of $FeSe_{0.5}Te_{0.5}$ showing thin plate like morphology. (b) HRTEM image showing the lattice fringes. (c) Selected area electron diffraction (SAED) pattern which confirms the high quality crystalline nature of the sample with tetragonal structure.(d) shows the FESEM image of $FeSe_{0.5}Te_{0.5}$. The morphology shows plate like features stacked on top of each other.

7.4.3 Linear resistivity

Figure 7.9, shows the linear resistivity plot for $FeSe_{1-x}Te_x$ samples versus temperature. For $FeSe_{1-\delta}$, the resistivity varies linearly with temperature below T = 240 K before the onset of superconductivity at (T_c (onset)) at 8 K. The onset of transition temperature as well as the normal state resistivity increases with increasing Te content. The maximum T_c

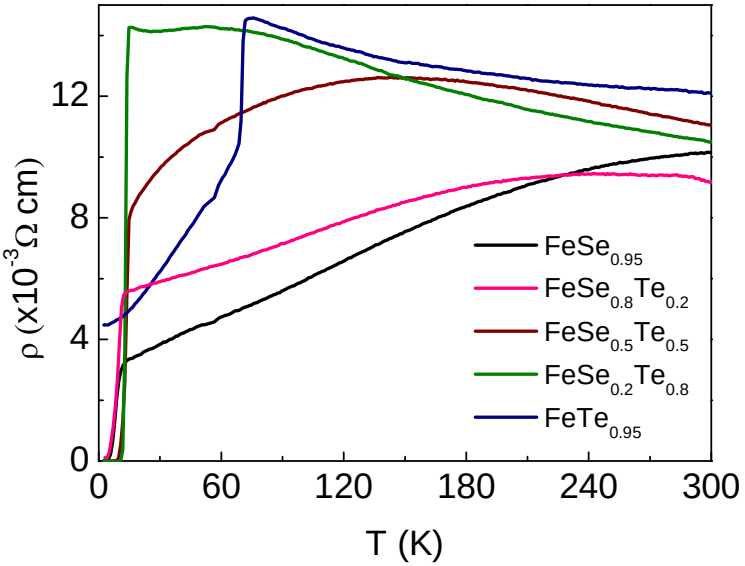

Figure 7.9. Resistivity versus temperature plot for $FeSe_{1-x}Te_x$ superconductors. Normal state resistivity and superconducting transition temperature increases with increasing Te content. The maximum T_c (onset) is 14 K displayed by $FeSe_{0.5}Te_{0.5}$. $FeTe_{1-\delta}$ shows a sharp drop in resistivity corresponding to structural and magnetic transition at T = 67 K.

(onset) was shown by $FeSe_{0.5}Te_{0.5}$ at T = 14 K. For $FeSe_{0.5}Te_{0.5}$, three regions that can be identified in the $\rho - T$ graph. At high temperature, resistivity increases with decreasing temperature i.e. $\frac{d\rho}{dT} < 0$, then a very broad dome is observed after which the resistivity decreases with decreasing temperature i.e. $\frac{d\rho}{dT} > 0$ before entering into a superconducting state. For $FeSe_{0.95}$ and $FeSe_{0.8}Te_{0.2}$ the linear temperature dependence between ρ and T at low temperatures changes to an exponential dependence for $FeSe_{0.5}Te_{0.5}$ depicting the increase in localization. Although Te substitution, by causing a negative pressure on the lattice, increases the T_c, however, the normal state resistivity above T_c (onset) increases with increasing Te concentration. The dome present in the

normal state resistivity broadens and shifts to lower temperatures with increasing Te content. $FeTe_{1-\delta}$ shows a negative temperature dependence above T = 67 K, where the structural and magnetic transition occur simultaneously [13]. At the transition, resistivity undergoes an abrupt jump to a lower value and exhibits a metallic behavior down to the lowest temperatures. The dome is completely suppressed by the structural/magnetic transition. The observed dome in $FeSe_{0.5}Te_{0.5}$ also gets flattened with Co or Ni substitution. Figure 7.10 shows the temperature dependence of electrical resistivity for Co and Ni substituted $FeSe_{0.5}Te_{0.5}$. When Co is substituted at the Fe site, the normal state resistivity decreases, but the critical temperature is suppressed very rapidly and the compound $Fe_{0.85}Co_{0.15}Se_{0.5}Te_{0.5}$ is no more a superconductor down to 4 K, although it shows an onset at around T = 7 K. The sample with 5% Ni substituted sample also shows a T_c (onset) at around 5.2 K but no superconductivity is observed. The resistivity is higher than the corresponding Co substituted samples. However for 10% Ni substitution, the value of normal state resistivity is lower as compared to 5% Ni substitution. This behavior is in agreement with reported results in substituted $FeSe_{1-\delta}$ [34, 35] and in $FeSe_{0.5}Te_{0.5}$ [47]. Superconductivity in $FeSe_{1-\delta}$ is destroyed completely at 5% Co and Ni substitution but in $FeSe_{0.5}Te_{0.5}$ it is destroyed at relatively higher concentration of cobalt (15%). The sudden increase in resistivity of $Fe_{0.85}Co_{0.15}Se_{0.5}Te_{0.5}$ is not understood, however it may either be related to the amount of $CoTe_2$ impurity phase or a sudden increase in the Fe-Se/Te bond length as shown in figure 7.6(c). Increase due to higher

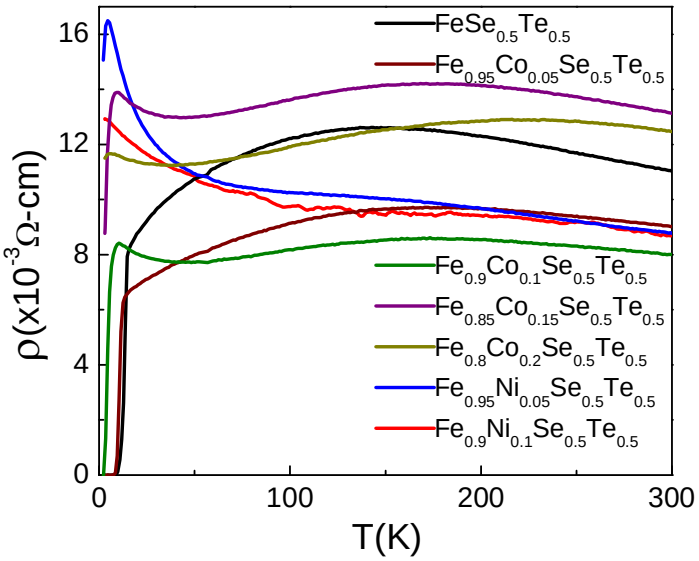

Figure 7.10. Resistivity versus temperature plots for the $Fe_{1-x}M_xSe_{0.5}Te_{0.5}$ with M = Co (x = 0, 0.05, 0.1, 0.15, 0.2) and Ni (x = 0.05, 0.1). Superconductivity is suppressed by Co and Ni substitution.

$CoTe_2$ content can be ruled out as its intensity in $Fe_{0.8}Co_{0.2}Se_{0.5}Te_{0.5}$ is large but still resistivity is low. Figure 7.11 shows the temperature dependence of resistivity normalized to the value of resistivity at T = 300 K. As discussed earlier the normal state resistivity shows a resistive dome for $FeSe_{0.5}Te_{0.5}$ that shifts to higher temperatures with increasing Te content. However we observed that the dome not only gets suppressed by Co and Ni substitution but also shifts to higher temperature. If viewed carefully, the ρ-T plot can be divided into three regions of interest: region I (T < 100 K), region II (100 K < T < 200 K) and region III (T > 200 K). Region III for all the samples shows a semiconducting behavior, while region II is mainly influenced by the dome that shows a shift towards region III with increasing substituent. Region I with 0 and 5 % Co substitution shows a

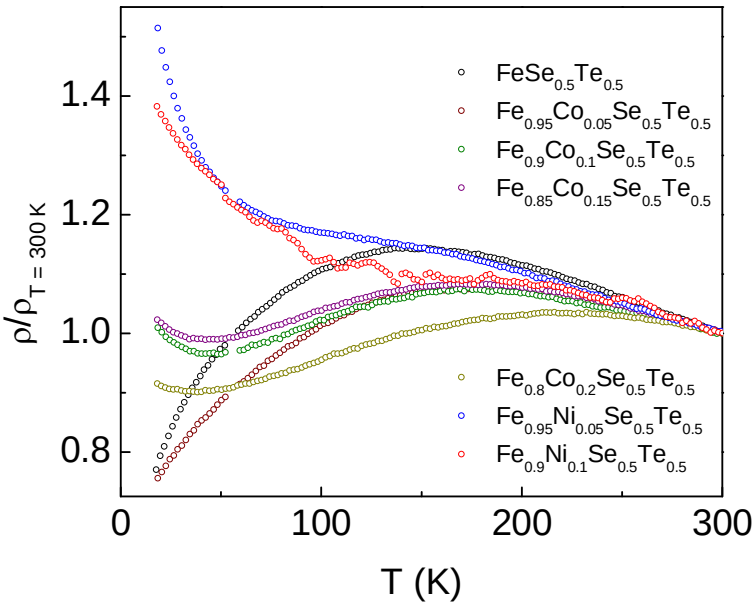

Figure 7.11. Temperature dependent resistivity for $Fe_{1-x}M_xSe_{0.5}Te_{0.5}$ (M = Co, Ni) normalized to the value at T = 300 K. The resistivity dome seen in $FeSe_{0.5}Te_{0.5}$ is suppressed with Co and Ni substitution.

positive ($\frac{d\rho}{dT} > 0$) temperature dependent resistivity profile and has an exponential temperature dependence characteristic of charge carrier localization. With increasing substitution/disorder at the Fe-site, localizations effects prevail in the transport and resistivity curve in region I shows a sign change from $\frac{d\rho}{dT} > 0$ to $\frac{d\rho}{dT} < 0$. For $Fe_{1-x}Ni_xSe_{0.5}Te_{0.5}$, this region spans the whole temperature range. It may be argued that observed resistivity broadening may be due to scattering by magnetic impurities present at different concentrations in the sample. However this possibility was ruled out by the overlap of ρ-T data collected at H = 80 kOe onto the ρ-T data collected at zero field (figure 7.12). Thus the resistivity dome is independent of the applied magnetic field and therefore it is not caused by scattering due to magnetic impurities rather they have some

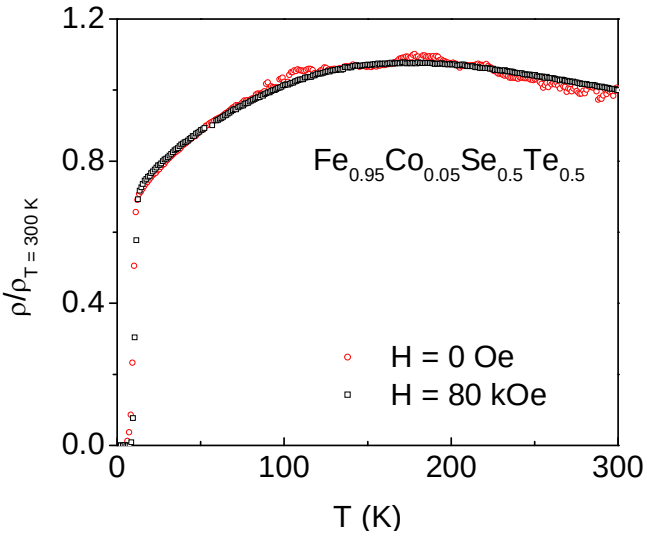

Figure 7.12. Temperature dependent normalized resistivity at H = 0 Oe and 80 kOe. Both curves overlap on each other indicating that the observed broadening is not due to scattering by magnetic impurities and has electronic origin.

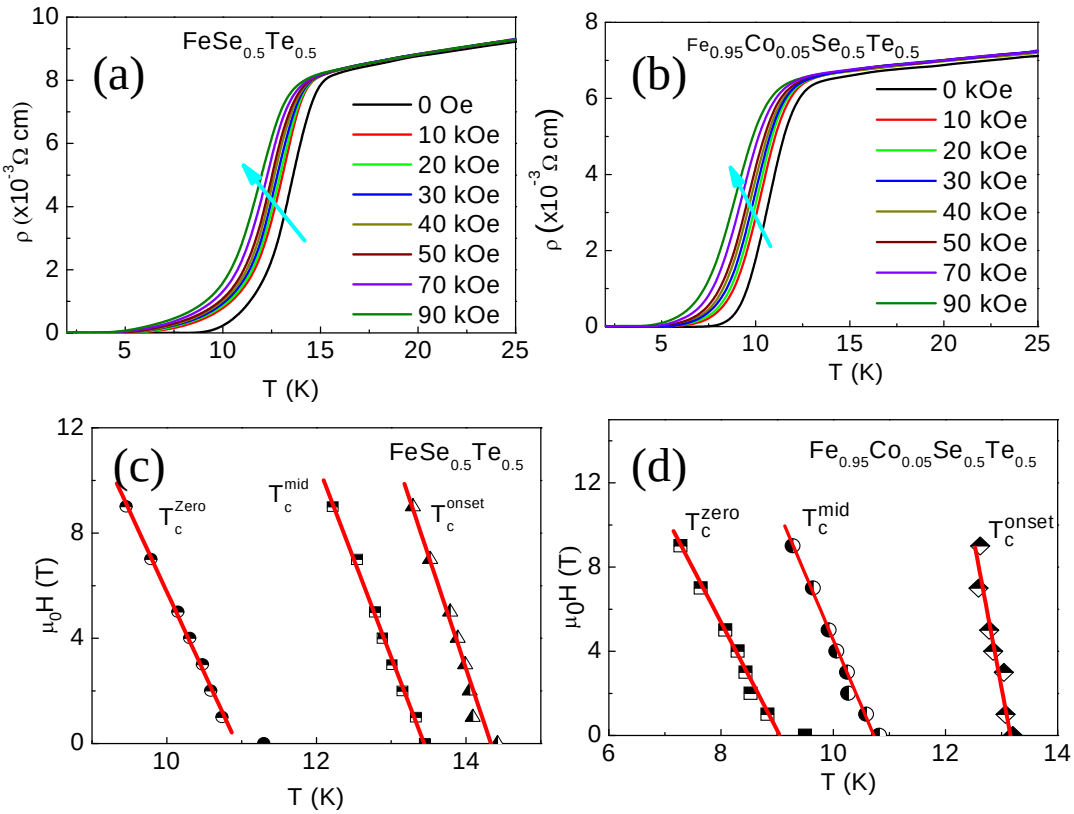

Figure 7.13. Temperature dependence of resistivity at various magnetic fields below T_c (onset) in (a) $FeSe_{0.5}Te_{0.5}$ and (b) $Fe_{0.95}Co_{0.05}Se_{0.5}Te_{0.5}$. The observed broadening is due to interaction of supercurrent with magnetic vortices. (c) and (d) are the corresponds the *H – T* diagram.

intrinsic origin related to the electronic structure of *FeCh* superconductors. Magnetic field dependence of resistivity for $FeSe_{0.5}Te_{0.5}$ and $Fe_{0.95}Co_{0.05}Se_{0.5}Te_{0.5}$ below T_c is shown in figures 7.13(a) and 7.13(b) respectively. An estimate of upper critical fields can be calculated from *H* to *T* phase diagram (figures 7.13(c) and 7.13(d)) corresponding to the temperatures where the resistivity drops to 90% of normal state resistivity (ρ_n at *T* = 25 K), 50% of ρ_n and 10% of ρ_n. Using the Werthamer–Helfand–Hohenberg (WHH) formula:

$$\mu_0 H_{c2}(T = 0\ K) = -0.693\mu_0(dH_{c2}/dT)T_c \big|_{Tc},$$

upper critical fields can be calculated[40]. The coherence lengths corresponding to these upper critical values can be calculated using the Ginzburg–Landau (GL) relation $\xi(T = 0\ K) = (\varphi_0/2\pi\mu_0 H_{c2})^{1/2}$. The upper critical fields ($\mu_0 H$ (*T*=0 K)) and the corresponding

Compound	$T_c(\rho = 0)$ *(K)*	$\mu_0 H_{c2}(T)$ *(T = 0 K)*	ξ*(Å)* *(T = 0 K)*
$FeSe_{0.95}$	*6.04*	*14.69*	*83.9*
$FeSe_{0.8}Te_{0.2}$	*12.13*	*55*	*43.3*
$FeSe_{0.5}Te_{0.5}$	*11.3*	*48*	*46.3*
$FeSe_{0.2}Te_{0.8}$	*12.12*	*54.2*	*43.3*
$Fe_{0.95}Co_{0.05}Se_{0.5}Te_{0.5}$	*9.47*	40	*50.7*
$Fe_{0.9}Co_{0.1}Se_{0.5}Te_{0.5}$	*2.33*	*8*	*113.5*

Table I Shows the values of T_c(zero) corresponding to zero resistivity and related upper critical field and coherence lengths at *T* ~ 0 K.

coherence lengths for 10 % ρ_n are tabulated in table I along with superconducting transition temperature at zero applied field $T_c(\rho=0)$ (corresponds to 10 % ρ_n).

7.4.4 Transverse resistivity

To know more about the intrinsic factors that governs the normal state transport of *FeCh* superconductors, we performed Hall measurements on the samples. Figure 7.14(a) shows the magnetic field (H) dependence of transverse resistivity (ρ_{xy}) for $FeSe_{1-x}Te_x$ at T = 300 K, and figure 7.14(b) shows ρ_{xy} as a function of H at T = 20 K. The Hall resistivity,

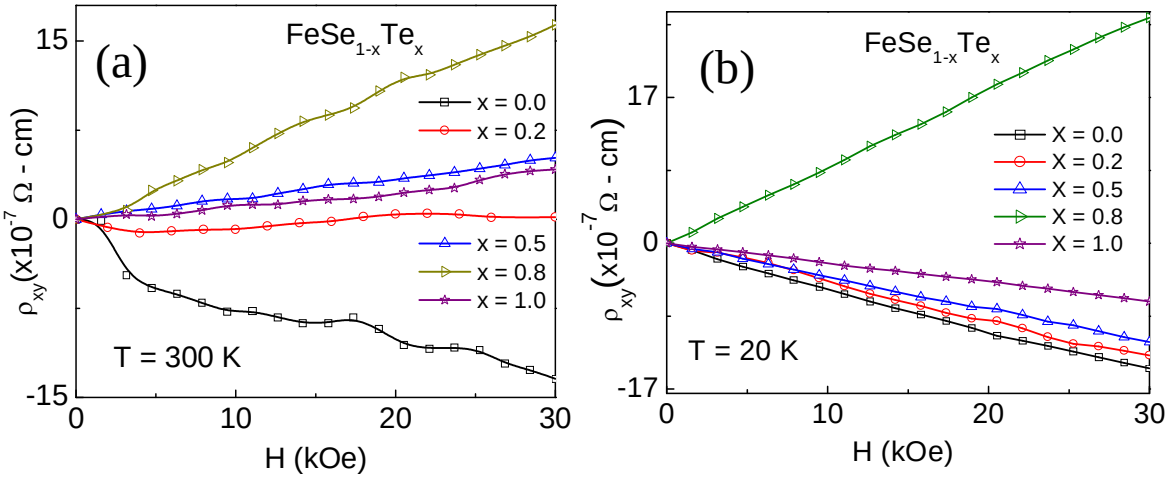

Figure 7.14. Hall resitivity as a function of field for $FeSe_{1-x}Te_x$ at (a) T = 300 K and (b) 20 K respectively.

ρ_{xy} varies linearly with the magnetic field at both temperatures measured from H = 0 kOe to 3 kOe. To avoid the effects of anomalous Hall effect (AHE), Hall coefficient (R_H) was calculated in the high field limit (H = 30 kOe) using the relation: $\rho_{xy} = R_H B$. As the

sample was pill shaped, so the calculated R_H can have an error of $\pm 6l/\pi D^2$, where '*l*' is the length of spread of the probe on the surface of the sample. '*D*' is the diameter of the

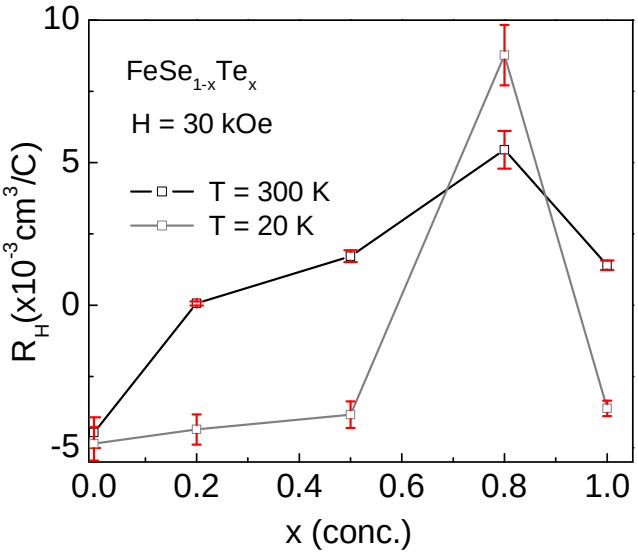

Figure 7.15. Hall coefficient (R_H) for $FeSe_{1-x}Te_x$ at *T* = 300 and 20 K. At *T* = 300 K, R_H is positive, however at *T* = 20 K, R_H is negative. The corresponding field is 30 kOe.

Sample [50]. The type of majority charge carriers is determined from the sign of R_H (figure 7.15). The charge carrier density can be calculated using the relation: $n = 1/e|R_H|$, where '*n*' is the carrier concentration in terms of cm^3/C and '*e*' is the electronic charge. The Hall mobility of the majority charge carriers was calculated as $\mu_H = R_H/\rho$. The calculated values of all the physical quantities are tabulated in Table II. At *T* = 300 K, the majority carriers are holes for all the samples. Although $FeSe_{1-\delta}$ showed electrons as the majority charge carriers, however, the observed carrier concentration is small as compared to other samples. At *T* = 20 K, the majority charge carriers are electrons with an exception for $FeSe_{0.2}Te_{0.8}$, where the carrier concentration is again small. We have not

compound	type of majority charge carrier (T = 300 K)	n ($x10^{21}$ cm^{-3}) (T = 300 K)	μ_H (cm^2/V-S) (T = 300 K)	type of majority charge carrier (T = 20 K)	n ($x10^{21}$ cm^{-3}) (T = 20 K)	μ_H (cm^2/V-S) (T = 20 K)
$FeSe_{0.96}$	-ve	1.396	0.447	-ve	1.28	1.38
$FeSe_{0.5}Te_{0.5}$	+ve	3.631	0.156	-ve	1.62	0.43
$FeSe_{0.2}Te_{0.8}$	+ve	1.141	0.519	+ve	0.71	0.61
$FeTe_{0.96}$	+ve	4.468	0.116	-ve	2.76	0.67

Table II. shows the sign of prevailing charge carrier, calculated charge carrier density and mobility at T = 300 K and 20 K respectively in $FeSe_{1-x}Te_x$. Holes dominate transport at T = 300 K while electrons dominate at T = 20 K.

performed temperature dependent Hall measurement, so it is difficult to correlate it with the linear resistivity measurement data. But, we can have a rough estimate of the prevailing charge carriers at the two measured temperatures. Considering the different temperature dependences of the mobility and density of holes and electrons, the electrical transport could be either dominated by either electrons or holes at different temperatures (e.g. MnAs) [52]. Sign reversals in the Hall coefficient of *FeChs* present a strong evidence of the multiband nature of the Fermi surface. Observed *n* type to *p* type conductivity reversion can be attributed to a two carrier transport nature of *FeCh* superconductors consistent with the reported multiband electronic structure in Fe*Chs***.** The classical expression for the Hall coefficient in the presence of both electron and hole type carriers is given by the expression:

$$R_H = \frac{\left(n_h - n_e b^2\right) + b^2 \mu_h^2 B^2 (n_h - n_e)}{e\left[\left(bn_e + n_h\right)^2 + b^2 \mu_h^2 B^2 (n_h - n_e)^2\right]}$$

Here $b = \mu_e/\mu_h$ and B = μ_0H is the applied magnetic flux. In the limit B→∞, $R_H = \frac{1}{e(n_h - n_e)}$. Therefore the charge carrier density shown in table 2 and 3 is actually: $n = n_h - n_e$ [53]. The number of majority charge carriers is consistent with the reported values. Figure 7.16(a) and 7.16(b) show the Hall resistivity for $Fe_{1-x}M_xSe_{0.5}Te_{0.5}$ (M = Co, Ni). Figure 7.17(a) shows the Hall coefficient (R_H) for $Fe_{1-x}Co_xSe_{0.5}Te_{0.5}$ (x = 0, 0.05, 0.1, 0.15, 0.2) and $Fe_{1-x}Ni_xSe_{0.5}Te_{0.5}$ (x = 0, 0.05, 0.1) as a function of x is shown in figure 7.17(b). The various physical quantities calculated through Hall measurement on these samples are tabulated in table III. The majority charge carriers at T = 300 K for lower Co concentration are holes while for 15 and 20 % Co concentration, negative charge carriers prevail the Hall transport. Substitution 10 % Ni also change the sign of dominant charge carriers from holes (5 % Ni doping) to electrons. At T = 20 K, the Hall

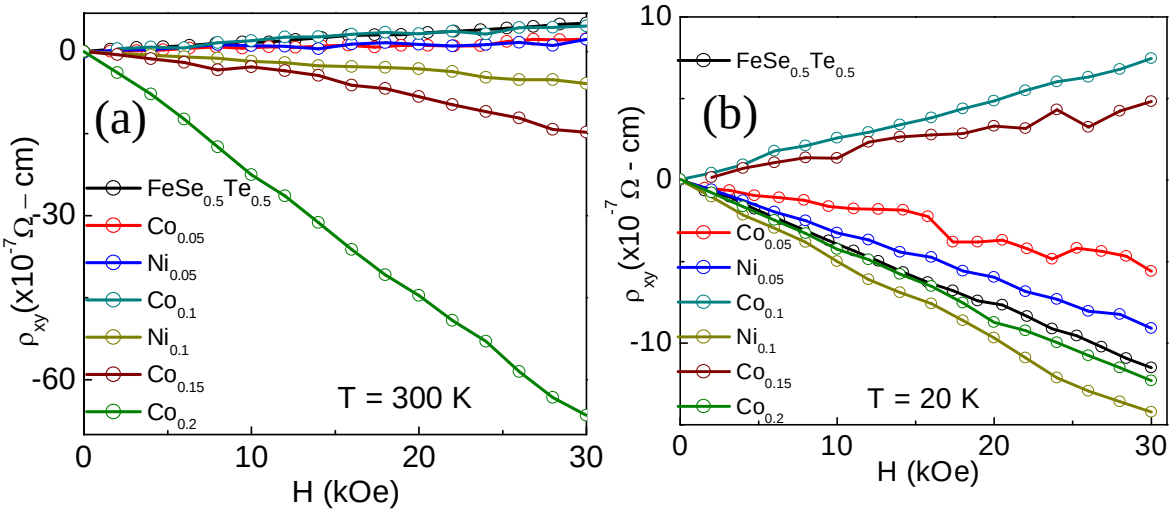

Figure 7.16. Hall resistivity of (a) $Fe_{1-x}Co_xSe_{0.5}Te_{0.5}$ (x = 0.05, 0.1, 0.15 and 0.2) and (b) $Fe_{1-x}Ni_xSe_{0.5}Te_{0.5}$ (Ni = 0.05 and 0.1) as a function of applied field H at T = 300 K and 20 K respectively.

transport is mainly dominated by electrons with the exceptions for 10 % and 15 % Co substituted $Fe_{1-x}M_xSe_{0.5}Te_{0.5}$. The trends shown in table III do not led us to any concrete conclusion, however we found that increasing Co and Ni concentration increases the dominance of electrons at T = 300 K.

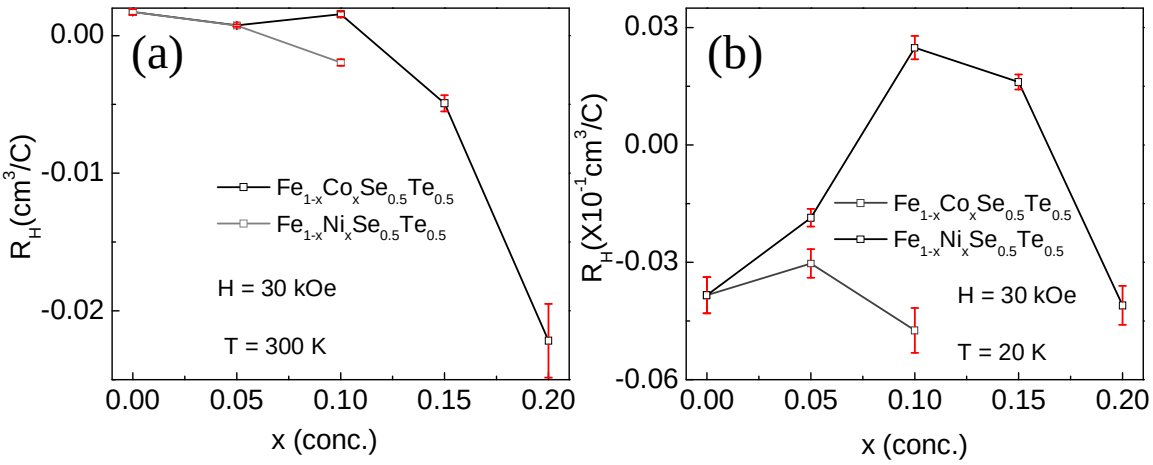

Figure 7.17. Hall coefficient at T = 300 K and 20 K for (a) $Fe_{1-x}Co_xSe_{0.5}Te_{0.5}$ (x = 0.05, 0.1, 0.15 and 0.2) and (b) $Fe_{1-x}Ni_xSe_{0.5}Te_{0.5}$ (Ni = 0.05 and 0.1) as a function of 'x' at H = 30 kOe

7.4.5 Magnetic properties

Figure 7.18(a) shows magnetization as a function of temperature ($M - T$) for $FeSe_{0.5}Te_{0.5}$ which shows a superconducting volume fraction of 0.12 % only at T = 5 K. Similarly, the superconducting volume fraction estimated for $Fe_{0.95}Co_{0.05}Se_{0.5}Te_{0.5}$ is 0.09 % (Figure 7.18(b)). $M - H$ curves for these two samples recorded at 5 K and 17 K are shown in figures 7.18(c) and 7.18(d), respectively. Hysteresis loop above T_c may be due to the presence of ferrimagnetic Fe_7Se_8 impurity or excess Fe in these samples. Figure 7.19(a) shows the zero field cooled (ZFC) $\chi - T$ curves at various magnetic fields for $FeSe_{0.5}Te_{0.5}$.

Compound	type of majority charge carrier (T = 300 K)	*n* ($x10^{21}$ cm^{-3}) (T = 300 K)	μ_H (cm^2/V-S) (T = 300 K)	type of majority charge carrier (T = 20 K)	*n* ($x10^{21}$ cm^{-3}) (T = 20 K)	μ_H (cm2/V-S) (T = 20 K)
$FeSe_{0.5}Te_{0.5}$	+ve	3.63	0.15	-ve	1.62	0.43
$Fe_{0.95}Co_{0.05}Se_{0.5}Te_{0.5}$	+ve	8.25	0.08	-ve	3.35	0.27
$Fe_{0.9}Co_{0.1}Se_{0.5}Te_{0.5}$	+ve	4.00	0.19	+ve	2.51	0.31
$Fe_{0.85}Co_{0.15}Se_{0.5}Te_{0.5}$	-ve	1.27	0.37	+ve	3.88	0.12
$Fe_{0.8}Co_{0.2}Se_{0.5}Te_{0.5}$	-ve	0.28	1.77	-ve	1.52	0.36
$Fe_{0.95}Ni_{0.05}Se_{0.5}Te_{0.5}$	+ve	8.46	0.08	-ve	2.06	0.23
$Fe_{0.9}Ni_{0.1}Se_{0.5}Te_{0.5}$	-ve	3.19	0.22	-ve	1.31	0.39

Table III Calculated carrier density mobility at *T* = 300 K and 20 K for majority charge carriers respectively for $Fe_{1-x}Co_xSe_{0.5}Te_{0.5}$ (x = 0.05, 0.1, 0.15 and 0.2) and $Fe_{1-x}Ni_xSe_{0.5}Te_{0.5}$ (Ni = 0.05 and 0.1).

The curve at an applied field of 10 kOe shows a broadening in the normal state which is suppressed by the application of an applied field of 70 kOe. A small hump also appears at around 54 K with increased magnetic field. The same hump appears in all the samples of Co and Ni substituted $Fe_{1-x}M_xSe_{0.5}Te_{0.5}$ (figure 7.19(b)). ZFC *M* - *T* plots for $Fe_{1-x}M_xSe_{0.5}Te_{0.5}$, where M = Co (x =0, 0.05, 0.1, 0.2) and Ni (0, 0.05, 0.1) as shown in figure 7.19(b). The data is normalized to the value at *T* = 300 K. It can be seen that the magnetization in the normal state increases with increasing Co concentration. However, it is less for Ni substituted samples as compared to Co doped samples. It has been shown

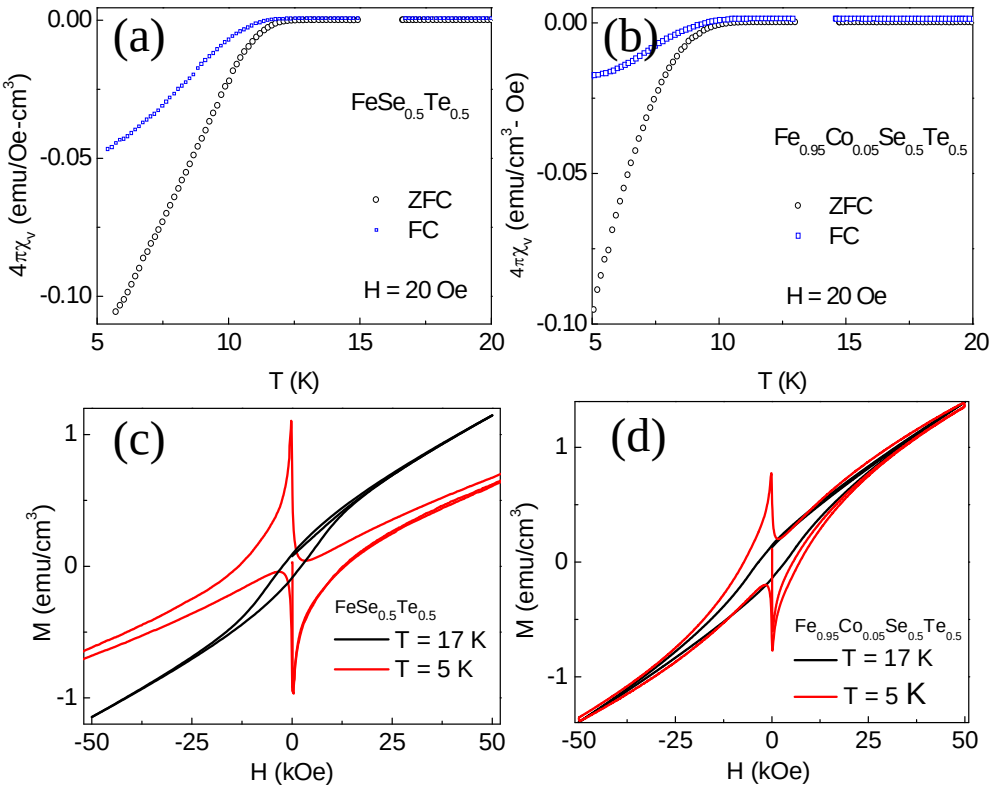

Figure 7.18. Superconducting volume fractions for $FeSe_{0.5}Te_{0.5}$ and $Fe_{0.95}Co_{0.05}Se_{0.5}Te_{0.5}$ are shown in (a) and (b). χ–T plots show the onset of diamagnetism at T = 12 K for $FeSe_{0.5}Te_{0.5}$ and T = 10 K $Fe_{0.95}Co_{0.05}Se_{0.5}Te_{0.5}$, respectively. (c) and (d) shows the hysteresis loops for both the samples above and below T_c.

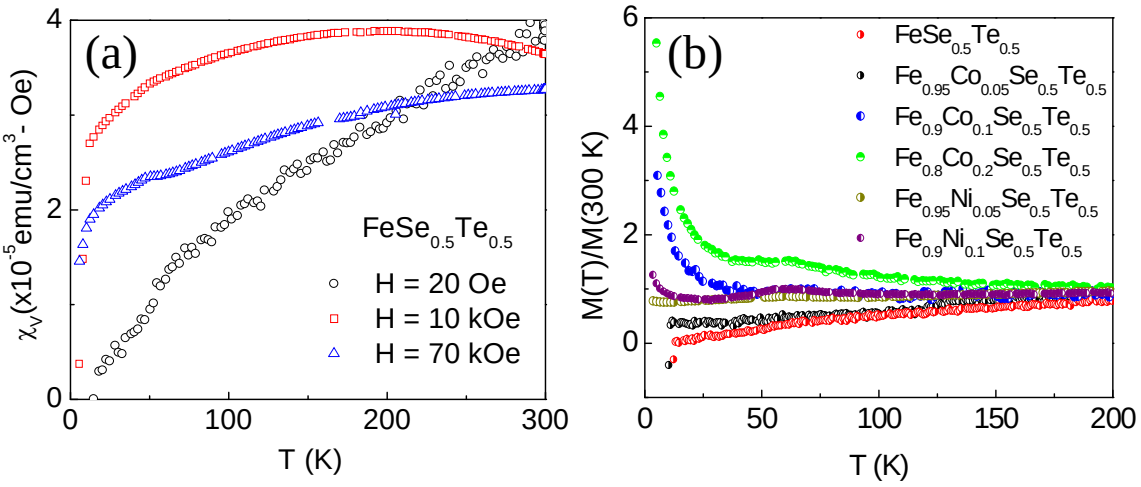

Figure 7.19. (a) shows the temperature dependent variation of ZFC volume susceptibility at different magnetic fields. (b) is the normalized volume magnetization for different Co and Ni concentration.

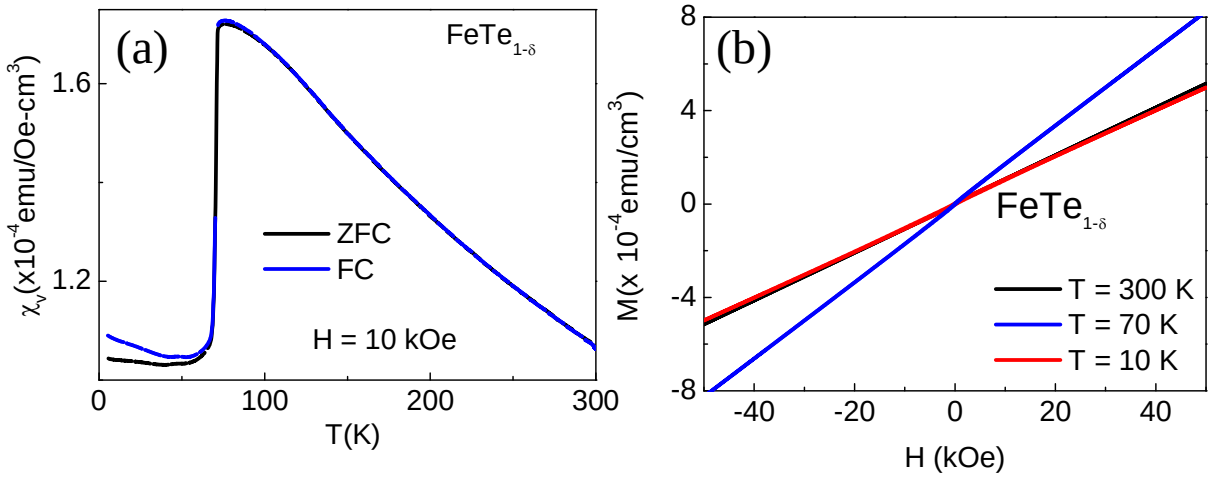

Figure 7.20. ZFC and FC susceptibility curve as a function of temperature for $FeTe_{1-\delta}$ at an applied field of 10 kOe is shown in (a). M – H plot in (b) show no hystereis.

from Mössbauer studies that in FeSe based superconductors, Fe^{+2} ions in a tetrahedral environment are in low spin state. Thus, there are two unpaired electrons in the t_2 orbitals. As Co is having one extra electron in its *d* – orbital than Fe, so the moment per Co^{+2} ion increases due to the presence of three unpaired electrons. Whereas Ni has four electrons in the t_2 orbital and so the moment decreases due to pairing of electrons. The hump at around T = 54 K in all the ZFC plots was also observed in the FC data and can be associated to the presence of impurities. The hump becomes sharper as we apply a much higher dc fields, however, it was not observed in the AC susceptibility measurements. Figure 7.20(a) shows the ZFC-FC susceptibility data of $FeTe_{1-\delta}$ at an applied field of 10 kOe. At low dc field, ZFC and FC shows a very complex behavior above 100 K, which can be related to the impurity phase. A high field of 10 kOe suppresses the effect of the anomaly. The transition at T = 67 K belongs to structural as well as antiferromagnetic transition [23, 24]. Magnetization versus field plots show no hysteresis, however the

slope at T = 70 K show an increase as compared to the slope of the linear plots obtained at T = 10 K and 300 K.

Magnetic measurements performed on $FeSe_{1-x}Te_x$ superconductor shows the presence of secondary phase magnetic impurities in the sample that shadow the impact of superconductivity. There is also a high chance of the presence of interstitial 'Fe' along with the impure phases revealed in the XRD patterns. Though the non-magnetic secondary phases may influence the superconducting properties and to some extent scatter the charge carriers during transport measurements, they do not influence the electronic structure. Interstitial 'Fe' however does have a greater influence on the electronic properties of FeChs as discussed in the introduction. Coming to the electronic structure of $FeTe_{1-\delta}$, both DFT calculations and ARPES measurements confirm and reveal one inner hole like closed Fermi pocket and two outer hole like cylindrical Fermi surface at the Γ – point along with two electron like Fermi surface at the M – point. The inner hole like closed pocket vanishes with increasing Se substitution in $FeSe_{1-x}Te_x$. Such a topology especially in $FeSe_{1-x}Te_x$, fulfills the condition of nesting and proposed to give rise to a spin density wave (SDW) ground state. It was also suggested that doping of electrons and holes suppress the SDW transition and superconductivity arises. However it is found that the antiferromagnetic ordering vector is not the same as the nesting vector and there is no SDW gap in $FeTe_{1-\delta}$, which can be regarded as the parent compound of *FeChs*. In contrast to the spin density wave (SDW) transition usually observed in the parent compounds of the iron arsenides, $Fe_{1.068}Te$ develops a double-stripe

antiferromagnetic (AFM) order with a propagation vector that rotates 45° compared to the nesting vector, and is parallel to the direction of the Fe–Fe connections in the Fe square lattice [54]. Theoretical calculations suggest FeSe exhibits a propagation vector along the nesting direction [23]. It has also been suggested that increasing Se content in $FeTe_{1-x}Se_x$, changes the angle from 45º to 0º, when the distance between the Te atom and Fe plane falls below a critical value in the crystal structure [23, 55]. Explaining magnetic transitions is beyond the limits of this discussion, and the main focus will be on the relation between the electronic structure and transport properties. For the time being it is assumed that the Fermi surfaces of *FeChs* consists of compensating electron and hole bands and assume that nesting plays an important role in inducing superconductivity in *FeChs* similar to *FePns* (Fe based Pnictides) [18, 19, 56]. DFT calculations as well as spectroscopic measurements at room temperature show high Te substitution in $FeSe_{1-x}Te_x$ disorders the Se derived bands thereby affecting the hybridization; however as an exception, for $FeSe_{0.5}Te_{0.5}$, possibility of nesting is enhanced [42, 56]. So we observe an enhanced T_c as compared to $FeSe_{1-\delta}$. These competing effects may also influence the number and type of majority charge carriers in these multiband superconductors as shown in table 7.2. As discussed earlier, the high temperature Hall transport is dominated by holes and electrons dominate at low temperature due to difference in their mobility. The crossover temperature increases with increasing Se content [57]. Thermal transport measurements on Co substituted $FeSe_{1-\delta}$ show that the crossover temperature further shifts to higher temperature with increasing Co concentration and electrons become the dominant charge carrier [58]. Nevertheless, it was also observed that the resistivity dome

observed in $FeSe_{1-\delta}$ was fully suppressed with increasing Co concentration suppressed and the majority charge carriers are electrons through out the temperature range [58]. A natural question arise whether the resistivity dome acts a transition region between the dominant hole type and electron type charge transports. From our measurements we also found suppression of resistivity dome with Co and Ni substitution and suppression in the number of holes at room temperature with evolution of electrons as the dominant charge carrier. DFT calculations show that Co and Ni substitution actually destroys hole pockets on the Fermi surface [56]. The extra electrons in Co and Ni do not act as a dopant but are localized near the substituted site and act as scatterers. Due to increased disorder, the system shows metal-insulator transition [59]. This kind of resistivity broadening has also been observed in LiFeAs and $K_{0.8}Fe_{2-\delta}Se_2$, though both of them show a high T_c but also a much larger broadening. The Fe-As and Fe-Fe bond lengths in LiFeAs (T_c = 18 K) are 2.41 Å and 2.68 Å respectively [60]. The Fe-Se and Fe-Fe bond lengths in $K_{0.8}Fe_{2-\delta}Se_2$ (T_c = 30 K) are 2.44 Å and 2.76 Å [35], whereas in $FeSe_{1-\delta}$ (T_c = 8 K), the corresponding bond lengths are 2.39 Å and 2.66 Å respectively. The Fe-Se/Te and Fe-Fe bond lengths in $FeSe_{0.5}Te_{0.5}$ (T_c = 14 K) are roughly 2.47 Å and 2.69 Å. The room temperature Fe-Se and Fe-Fe bond lengths in $FeSe_{1-\delta}$ (T_c = 37 K at 8.9 GPa) are 2.44 Å and 2.57 Å respectively. The low temperature phase (SG: C*mma*) of $FeSe_{1-\delta}$ with T_c = 8 K, has the same Fe-Fe distance (2.66 Å), however a much smaller Fe-Se bond length (2.32 Å) [61]. If a strong hybridization is important for more efficient charge transfer between Fe and Se, then a decrease in Fe-Se bond length should decrease the dominance of holes in the low temperature along with fact that mobility of holes gets suppressed. It was also found that

the normal state resistivity dome gets suppressed on increasing pressure in $FeSe_{1-\delta}$, however there is no data on the type of charge carriers that dominate the transport. Comparing the high pressure (8.9 GPa) phase of $FeSe_{1-\delta}$ and ambient pressure $K_{0.8}Fe_{2-\delta}Se_2$, we find that although the Fe-Se bond length is almost the same, $K_{0.8}Fe_{2-\delta}Se_2$ has a much larger Fe-Fe bond length as compared to high pressure phase of $FeSe_{1-\delta}$. In $K_{0.8}Fe_{2-\delta}Se_2$, there are no hole pockets at the zone centre and transport is mainly dominated by electrons [62]. The resistive dome in $K_{0.8}Fe_{2-\delta}Se_2$ is sensitive to Fe content. With decreasing δ, the dome shifts to higher temperatures [63]. It has also been shown that

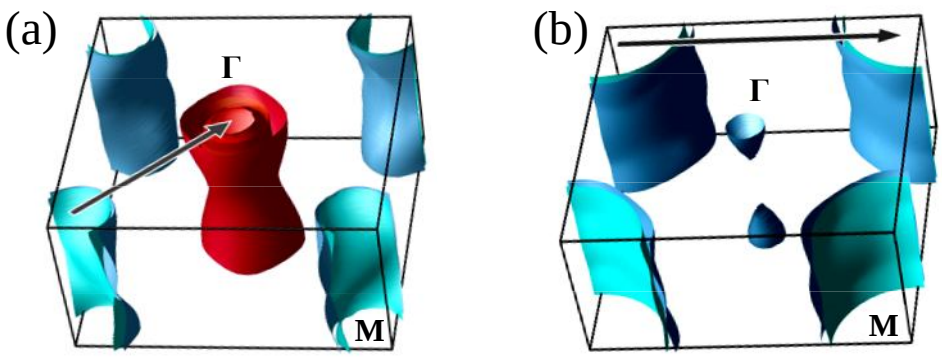

Figure 7.21. Proposed Fermi surfaces of $FeSe_{1-\delta}$ (a) and $K_{0.8}Fe_{1-\delta}Se_2$ (b) superconductors. The arrows indicate the quasi-nesting vector direction.

a very small amount of Co doping is sufficient to suppress superconductivity in $K_{0.8}Fe_{2-\delta}Se_2$ [64]. From above discussion it may be concluded that any weakening in the Fe-Fe interaction or disorder in the Fe- sheet that may include both Fe deficiency and presence of other substituent can lead to destruction of hole pockets. The resistivity dome in $K_{0.8}Fe_{2-\delta}Se_2$ and $FeSe_{0.5}Te_{0.5}$ is also suppressed with increasing pressure however the

samples also loose their high T_c. Therefore a better hybridization also enhances the dominance of negative charge carriers. High pressure cycle studies on $Cs_{0.8}Fe_{2-\delta}Se_2$ reveals that the electronic origin of "dome" and superconductivity are entirely influenced by different mechanisms [65].

7.5 Conclusions

The main features of *FeChs* that were presented in this study are:

- An increase in the Te content in $FeSe_{1-x}Te_x$ not only increases the Fe-Se distance but also the Fe-Fe bond length.
- At the optimum Fe-Fe in-plane distance and Fe-*Ch* out of plane distance, the T_c is highest for $FeSe_{0.5}Te_{0.5}$, however the normal state resistivity display a non-metallic behavior, usually a very broad dome, which shifts to higher temperature with decreasing Te content.
- Co and Ni substitution also decreases the '*a*' as well as '*c*' lattice parameters and therefore not only changes the local structure but also the introduce disorder in Fe sheet.
- Co and Ni doping suppresses the dome in the normal state as well as the superconducting transition temperature.

- The dominant charge carriers at T = 300 K are holes whereas at T = 20 K, electrons dominate the Hall measurements in $FeSe_{1-x}Te_x$. It has usually been observed that holes mostly dominate the transport measurements above T = 100 K and electrons below this temperature.
- High Co and Ni content changes the type of dominant charge carriers to electrons at T = 300 K which also sees the suppression of broad resistivity dome.
- A major hurdle in studying the electronic structure of Fe-based superconductors is the presence of off-stoichiometry between the constituent elements which has a great impact on the physical properties of *FeChs.*
- Temperature dependent measurement of the thermal and electrical (linear and transverse) properties of *FeChs* and their relation to the structural changes with decreasing temperature can present a good description of the electronic structure. The quality of such studies can be enhanced by high pressure synthesis or measurement.

7.6 References

1. Y. Kamihara, T. Watanabe, M. Hirano, H. Hosono, *J. Am. Chem. Soc.* **130** (2008) 3296.
2. H. Takahashi, K. Igawa, K. Arii, Y. Kamihara, M. Hirano, H. Hosono, *Nature* **45** (2008) 376.
3. G.F. Chen, Z. Li, D. Wu, G. Li, W.Z. Hu, J. Dong, P. Zheng, J.L. Luo, N.L. *Phys.Rev. Lett.* **100** (2008) 247002.
4. Z.A. Ren, J. Yang, W. Lu, W. Yi, G.C. Che, X.L. Dong, L.L. Sun, Z.X. Zhao, *arXiv*:/0803.4283.
5. Z.A. Ren et al., *Chin. Phys. Lett*. **25** (2008) 2215.
6. Z.A. Ren et al., *Eur. Phys. Lett.* **83** (2008) 17002.
7. C. Wang et al., *Eur. Phys. Lett* **83** (2008) 67006.
8. M. Rotter, M. Tegel, D. Johrendt, *Phys. Rev. Lett.* **101** (2008) 107006.
9. G. Wu, Y.L. Xie, H. Chen, M. Zhong, R.H. Liu, B.C. Shi, Q.J. Li, X.F. Wang, T. Wu, Y.J. Yan, J.J. Ying, X.H. Chen, *arxiv*:/0811.0761.
10. J.H. Tapp, Z. Tang, B. Lv, K. Sasmal, B. Lorenz, P.C.W. Chu, A.M. Guloy, *Phys. Rev.B* **78** (2008) 060505.
11. Y. Kamihara, H. Hiramatsu, M. Hirano, R. Kawamura, H. Yanagi, T. Kamiya, H. Hosono, *J. Am. Chem. Soc.* **128** (2006) 10012.

12. F.C. Hsu, J.Y. Luo, K.W. Yeh, T.K. Chen, T.W. Huang, P.M. Wu, Y.C. Lee, Y.L. Huang, Y.Y. Chu, D.C. Yan, M.K. Wu, *PNAS* **105** (2008) 14262.
13. M.H. Fang, H.M. Pham, B. Qian, T.J. Liu, E.K. Vehstedt, Y. Liu, L. Spinu, Z.Q. Mao, *Phys. Rev. B* **78** (2008) 224503.
14. K.W. Yeh, T.W. Huang, Y.L. Huang, T.K. Chen, F.C. Hsu, P.M. Wu, Y.C. Lee, Y.Y. Chu, C.L. Chen, J.Y. Luo, D.C. Yan, M.K. Wu, *EPL* **84** (2008) 37002.
15. Y. Mizuguchi, F. Tomioka, S. Tsuda, T. Yamaguchi, Y. Takano, *Appl. Phys. Lett.* **94** (2009) 012503.
16. S. Medvedev et al., *Nat. Mater.* **8** (2009) 630.
17. G. Garbarino, A. Sow, P. Lejay, A. Sulpice, P. Toulemonde, M. Mezouar, M. Núñez-Regueiro, *EPL* **86** (2009) 27001.
18. A. Subedi, L. Zhang, D.J. Singh, M.H. Du, *Phys. Rev. B* **78** (2008) 134514.
19. R. Yoshida, T. Wakita, H. Okazaki, Y. Mizuguchi, S. Tsuda, Y. Takano, H. Takeya, K. Hirata, T. Muro, M. Okawa, K. Ishizaka, S. Shin, H. Harima, M. Hirai, Y.Muraoka, T. Yokoya, *J. Phys. Soc. Jpn.* **78** (2009) 034708.
20. T.M. McQueen, Q. Huang, V. Ksenofontov, C. Felser, Q. Xu, H. Zandbergen, Y.S.Hor, J. Allred, A.J. Williams, D. Qu, J. Checkelsky, N.P. Ong, R.J. Cava, *Phys. Rev. B* **79** (2009) 014522.
21. M.K. Wu et al., *Physica C* **469** (2009) 340.
22. K. Horigane, H. Hiraka, K. Ohoyama, *J. Phys. Soc. Jpn.* **78** (2009) 074718.
23. W. Bao et al., *Phys. Rev. Lett.* **102** (2009) 247001.

24. S. Li et al., *Phys. Rev. B* **79** (2009) 054503.

25. T.M. McQueen, A.J. Williams, P.W. Stephens, J. Tao, Y. Zhu, V. Ksenofontov, F. Casper, C. Felser, R.J. Cava, *Phys. Rev. Lett.* **103** (2009) 057002.

26. Shiliang Li et al., *Phys. Rev. B* **79** (2009) 054503.

27. K Horigane *et. al., J. Phys. Soc. Jpn.* **78** (2009) 074718.

28. M.D. Lumsden et al., *Nat. Phys.* **6** (2010) 182.

29. P. Babkevich et al., *J. Phys.: Condens. Matter* **22** (2010) 142202.

30. A.J. Williams, T.M. McQueen, V. Ksenofontov, C. Felser, R.J. Cava, *J. Phys.: Condens. Matter* **21** (2009) 305701.

31. J. Prakash, S.J. Singh, S. Patnaik, A.K. Ganguli, *arxiv*:0810.1364.

32. C. Wang, Y.K. Li, Z.W. Zhu, S. Jiang, X. Lin, Y.K. Luo, S. Chi, L.J. Li, Z. Ren, M. He, H. Chen, Y.T. Wang, Q. Tao, G.H. Cao, Z.A. Xu, *Phys. Rev. B* **79** (2009) 054521.

33. Y. Qi, Z. Gao, L. Wang, D. Wang, X. Zhang, Y. Ma, *Supercond. Sci. Technol.* **21** (2008) 115016.

34. S.B. Zhang, H.C. Lei, X.D. Zhu, G. Li, B.S. Wang, L.J. Li, X.B. Zhu, W.H. Song, Z.R. Yang, Y.P. Sun, *Physica C* **469** (2009) 1958.

35. J. Guo *et. al., Phys. Rev. B* **82** (2010) 180520.

36. C. L. Chen *et. al., Eur.Phys.Lett.* **93** (2011) 47003.

37. T. J. Liu *et. al., Phys. Rev. B* **80** (2009) 174509.

38. M. Bendele *et. al., Phys. Rev. Lett.* **104** (2010) 087003.

39. M. D. Johannes and I. I. Mazin, *Phys. Rev. B* **79** (2009) 220510.

40. L. Zhang, D. J. Singh and M. H. Du, *Phys. Rev.B* **79** (2009) 012506.

41. S. Röβler *et. al. Phys. Rev. B* **82** (2010) 144523.

42. N. L. Saini *et. al., Phys. Rev. B* **83** (2011) 052502.

43. B. Joseph *et. al., Phys. Rev. B* **82** (2010) 020502.

44. C.Y. Moon and H. J. Choi, *Phys. Rev. Lett.* **104** (2010) 057003.

45. R.D. Shannon, *Acta Cryst.* **A32** (1976) 751.

46. D. Louca *et. al. Phys. Rev. B* **81** (2010) 134524.

47. A. M. Zhang, T. L. Xia, L. R. Kong, J. H. Xiao and Q. M. Zhan, *J. Phys.: Condens. Matter* **22** (2010) 24570.

48. A. Gunther *et. al.,Supercond. Sci. Technol.* **24** (2011) 04500.

49. D. J. Gawrylu *et. al. Supercond. Sci. Technol.* **24** (2011) 065011.

50. Y. Mizuguchi, F. Tomioka, S. Tsuda, T. Yamaguchi, Y. Takano, *J. Phys. Soc. Jpn.* **78** (2009) 074712.

51. L. J. Van der pauw, *Philips Technical Review* **20** (1958) 220.

52. X. J. Wu *et. al., Appl. Phys. Lett* **90** (2007) 112105.

53. I. Tsukada *et. al., Phys. Rev.B* **81** (2010) 054515.

54. C. de la Cruz *et. al., Nature* **453** (2008) 899.

55. T. J. Liu *et. al., Nature Materials* **9** (2010) 716.

56. P.P. Singh, *J. Phys.: Condens. Matter* **22** (2010) 13550.

57. I. Pallecchi, G. Lamura, M. Tropeano and M. Putti, *Phys. Rev. B* **80** (2009) 214511.

58. E. L. Thomas et. al. *J. Appl. Phys* **105** (2009) 073906.

59. H. Wadati, I. Elfimov, G. A. Sawatzky, *Phys. Rev. B* **105** (2010) 157004.

60. L. Zhang *et. al. Phys. Rev. B* **78** (2008) 174520.

61. R. S. Kumar, *J. Phys. Chem B* **114** (2010) 12597.

62. T. Qian *et. al., arxiv:*/1012.6017.

63. R. Hu *et. al. arxiv:*/1102.1931.

64. T. Zhou *et. al. arxiv:*/1102.3506.

65. G. Seyfarth *et. al. arxiv:*/1102.2464.